366-4000

PHOTOGRAPH THIS SHEET

LEVEL

8 th INTERNATIONAL AEROSPACE
and GROUND CONFERENCE ON
LIGHTNING AND STATIC
ELECTRICITY
ADDENDUM
DOT/FAA/CT-83/25A
LIGHTNING TECHNOLOGY ROUNDUP

INVENTORY

①

DOCUMENT IDENTIFICATION

DISTRIBUTION STATEMENT

ACCESSION FOR	
NTIS GRA&I	☑
DTIC TAB	☐
UNANNOUNCED	☐
JUSTIFICATION	

BY
DISTRIBUTION /
AVAILABILITY CODES

DIST	AVAIL AND/OR SPECIAL
A-1	

DISTRIBUTION STAMP

DTIC
SELECTED
JUL 0 2 1986
D

D

DATE ACCESSIONED

DATE RETURNED

86 7 1 061

DATE RECEIVED IN DTIC

REGISTERED OR CERTIFIED NO.

PHOTOGRAPH THIS SHEET AND RETURN TO DTIC-DDAC

DTIC FORM 70A
DEC 83

DOCUMENT PROCESSING SHEET

PREVIOUS EDITION MAY BE USED UNTIL
STOCK IS EXHAUSTED.

DISCLAIMER NOTICE
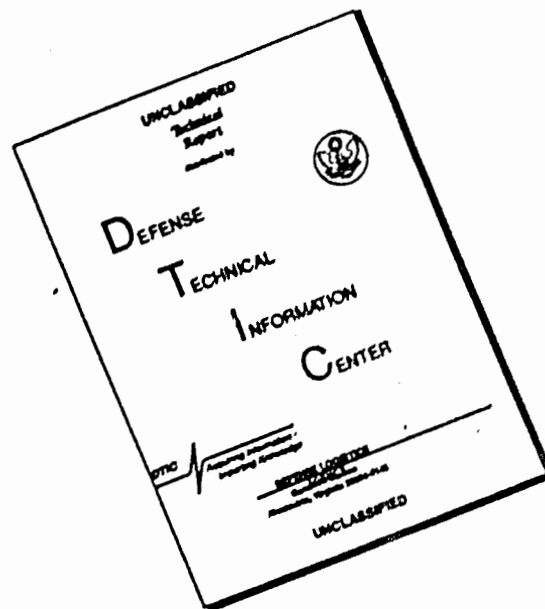
THIS DOCUMENT IS BEST QUALITY AVAILABLE. THE COPY FURNISHED TO DTIC CONTAINED A SIGNIFICANT NUMBER OF PAGES WHICH DO NOT REPRODUCE LEGIBLY.

AD-A169 049

8th
INTERNATIONAL AFROSPACE and GROUND CONFERENCE
on
LIGHTNING and STATIC ELECTRICITY

ADDENDUM

LIGHTNING TECHNOLOGY ROUNDUP

June 21-23, 1983

Fort Worth, Texas, U.S.A.

1983

INTERNATIONAL

AEROSPACE AND GROUND CONFERENCE

ON

LIGHTNING AND STATIC ELECTRICITY

June 21 - 23, 1983

Fort Worth, Texas

LIGHTNING TECHNOLOGY ROUNDUP

ADDENDUM

1. Report No.	2. Government Accession No.	3. Recipient's Catalog No.
DOT/FAA/CT-83/25		

4. Title and Subtitle	5. Report Date
ADDENDUM TO INTERNATIONAL AEROSPACE AND GROUND CONFERENCE ON LIGHTNING AND STATIC ELECTRICITY	October 1983
	6. Performing Organization Code

7. Author's)	8. Performing Organization Report No.

9. Performing Organization Name and Address	10. Work Unit No. (TRAIS)
Federal Aviation Administration Technical Center Atlantic City Airport, New Jersey 08405	
	11. Contract or Grant No.
	13. Type of Report and Period Covered

12. Sponsoring Agency Name and Address	
National Interagency Coordination Group (NICG) of the National Atmospheric Electricity Hazards Protection Program Atlantic City Airport, New Jersey 08405	Addendum to Conference Publication
	14. Sponsoring Agency Code

15. Supplementary Notes

The NICG consists of members from the U.S. Air Force, U.S. Army, U.S. Navy, NASA, NOAA, and the FAA.

16. Abstract

This addendum is a compilation of papers presented at the 1983 International Aerospace and Ground Conference on Lightning and Static Electricity, held at the Fort Worth Hilton Hotel, Fort Worth Texas, June 21-23, 1983, but not available for publication in the original conference proceedings.

The conference was sponsored by the NICG in concert with the Florida Institute of Technology and in association with the Institute of Electrical and Electronic Engineers, SAE-AE4 committee, the United Kingdom Civil Aviation Authority, Royal Aircraft Establishment, Farnsborough, Culham Laboratory.

17. Key Words	18. Distribution Statement
Phenomonology Lightning Locators 'P' Static and Corona Lightning Simulation	

19. Security Classif. (of this report)	20. Security Classif. (of this page)	21. No. of Pages	22. Price
Unclassified	Unclassified		

Form DOT F 1700.7 (8-72)   Reproduction of completed page authorized

Contents

*   Paper incorporated in this addendum

** Abstract only · paper not submitted for publication

IMPROVED ESTIMATES OF THE AREA DENSITY
OF CLOUD-TO-GROUND LIGHTNING OVER
THE UNITED STATES

Michael W. Maier
Lightning Location and Protection, Inc.
Tucson, Arizona

and

Jackie M. Piotrowicz
NOAA/NHRL
Coral Gables, Florida

ABSTRACT

A key element for any successful and cost-effective lightning protection design is an accurate estimate of the frequency of direct lightning strikes to ground. For example, an effective protection system for an electric power transmission line in Florida (an area of high lightning incidence) would be far too costly and not necessary for an area such as California (an area of low lightning incidence). In order to estimate the frequency of lightning strikes the local area density of lightning flashes to ground, i.e. the number of strikes per unit area per month or per year, must be known. In the USA, ground flash density is often assumed to be a relatively simple function of the mean number of thunderstorm days per month or per year. Many design handbooks give formulas which relate ground flash density to thunderstorm days, but no formula is generally accepted as standard. All too often, the actual lightning strike incidence is considerably different from the lightning strike projections based on the thunderstorm day statistics. The resulting over or under design of lightning protection systems ultimately leads to greater costs.

Here we show that the thunderstorm duration statistics are a much better indicator of true ground flash densities than the number of thunderstorm days. Maps of mean annual ground flash density are presented which have been inferred from long term thunderstorm duration observations. The thunderstorm duration data were obtained by the relatively dense network of existing aviation weather reporting stations. Approximately 450 stations are used, each with an uninterrupted 20 year period of record. The station density available here is essentially twice that of any previous thunderstorm frequency analysis of the United States.

Our analyses show that maximum annual ground flash densities of $18/km^2$ are found in the western interior of Florida from Naples to Cross City. High flash density values ($> 12/km^2$) are found over much of the Florida peninsula, the Florida panhandle, and westward through the southern gulf states to eastern Texas. A large area of flash densities $> 8/km^2$ are found over most of Oklahoma, Kansas, Missouri, Arkansas, Louisiana, Mississippi, and Tennessee. High flash densities ($> 8/km^2$) in the western states are limited to south central Colorado, northeastern New Mexico, northern Arizona and extreme southeastern Arizona. Pronounced flash density minima are found over the southern half of Texas and in the southeastern states from central Alabama northeastward through western Virginia. Most of the western and northeastern states have flash densities $< 4/km^2$. Maps of the 95% and 5% probability flash density values are also presented. Verification of these maps awaits a nationwide direct measurement program or successful practical application.

This paper was not available for incorporation into this book.

Lightning and Transient Protection of Radio Systems

By

Prof. S. Lundquist
Institute of High Voltage Research
Uppsala University, S-755 90 Uppsala,
Sweden

ABSTRACT

Protection of important radio systems against electromagnetic transients from lightning discharges and nuclear explosions (NEMP) nowadays is more or less a standard procedure. However, the problem of coordinating different protective measures and selection of the most suitable components still are problems deserving further studies. Tests have therefore been performed to evaluate some important parameters of individual components and of radio systems for frequencies up to 75 MHz. At the testing both standard test pulses as well as fast rising pulses in the nanosecond range has been used. Gas discharge tubes, cables etc. have been tested separately and as part of a system. In this way it is possible to study the effect of different counterpoise and grounding systems, different cable lengths and different locations of the cables as well as the location and properties of gas discharge tubes and semiconductor protection elements on the amplitude and energy of the transient reaching the sensitive parts of the system. The results are also used to estimate the necessary intervals for routine maintenance and to predict the MTBF for faults caused by lightning. A technique for field tests in actual installations will also be discussed.

This paper was not available for incorporation into this book.

Coupling of Natural Atmospheric Interference Through Apertures

By

J. Hamm, W. Graf, and E. F. Vance
SRI International
Menlo Park, CA 94025

ABSTRACT

The coupling of electromagnetic energy through apertures has received a great deal of attention in recent years. This recent research has been both theoretical and experimental in nature and has been focussed on the problems associated with apertures which are small compared to a wavelength.

The results of this research can be applied to the problem of determining the transient signals induced on conductors behind an aperture by lightning and static charging. While the problem of determining induced transients in complex systems (such as aircraft or ground-based facilities) cannot be solved exactly, the research of the past few years indicates that upper bounds can be determined for these transients. This paper reviews our recent work on aperture coupling and applies the results to models of airborne and ground-based facilities.

The nature of this recent work is such that reasonable upper bounds can be determined without the use of extensive computer codes. The system designer can determine quickly whether or not a particular aperture presents a problem for electronic systems located behind the aperture. The analysis performed in recent years has been of two different types: transmission line modeling of canonical circuits behind the aperture, and matrix formulation of Maxwell's equations. Both approches lead to relatively straightforward expressions for bounds on transient voltages and currents on conductors behind the aperture. Our laboratory measurements on test apertures are used to investigate the suitability of these bounds.

The results of this research can also be applied to the problem of generating realistic specifications, standards, and test procedures for certifying systems which must operate in the natural electrical environment.

ATMOSPHERIC ELECTRICITY INTERACTS with aircraft to produce transient electric and magnetic fields at the outer surface of the aircraft. These surface fields and the signals induced on wire penetrations of the surface act as equivalent sources for the transient electromagnetic environment inside the aircraft. A companion paper[1*] describes this problem and shows that wire penetrations of the surface are usually the most significant contributors to the internal transient environment. If all wire penetrations of an aircraft surface have been properly treated, the apertures on the exterior surface of the barrier can become significant points of entry for electromagnetic interference. These apertures may be in the form of holes or openings on the surface or in the form of seams and joints.

To solve the aperture problem, the system designer must: (1) determine quantitatively the effects of the apertures on the internal voltages and currents, and (2) develop measures for "closing" those apertures that affect system performance.

THEORETICAL BACKGROUND

The types of apertures encountered with typical aircraft are holes with maximum dimensions of a few meters, long narrow slots, structural seams and access hatches. For analysis purposes, these apertures can be considered "small;" that is, the characteristic dimension is smaller than a wavelength. Long narrow slots and seams are considered as distributed small apertures, and their coupling properties can be expressed per unit length. With the discussion being limited to "small" apertures as defined above, the following discussion of the theoretical background is generally valid for frequencies below 100 MHz. This is not a severe restriction, since the spectral content and coupling transfer functions appropriate for lightning are usually not important above 100 MHz.

Two recent publications[2,3] present excellent reviews of the literature describing aperture coupling. These problems ae difficult to analyze, especially the case of an aperture on a cavity containing equipment and wiring. The only configuration for which analytically rigorous results are available is that of a small circular aperture on a conducting plane of infinite extent. Numerically "accurate" results are available for some cavity and aperture configurations.[3] These were obtained by a numerical solution of integral equations in terms of the unknown aperture field components. The aperture fields were then considered as sources for the fields existing behind the aperture.

The mechanisms of field leakage through an aperture are described in Figures 1 and 2. The normal electric field and the tangential magnetic field couple through the aperture to interact with conductors and wiring loops behind the plane. As the figures imply, this coupling problem is equivalent to the problem of electric and magnetic dipole sources located at the aperture with the aperture shorted. These sources, radiating in the presence of the conducting plane, produce the same fields in the shadow region as do the original external sources. Formally, the problem is reduced to finding the dipole moments of the equivalent sources and computing the fields produced by these sources.

Figure 3 shows the general aperture coupling problem of interest for electromagnetic interference control. An external electromagnetic field is assumed to be incident on a volume containing electronic equipment and wiring. The volume is assumed to be enclosed by a metallic surface containing holes and seams. The interaction of the incident field with the outer surface produces a surface surrent density J_s and a normal electric field component E_n at the apertures. These surface fields couple through the aperture to produce transients on conductors inside. The internal transients may be in the form of (1) surface current densities on equipment enclosures or (2) voltages and currents on exposed equipment wiring. The internal surface current densities J_i can interact through apertures on the enclosures with conductors at the next topological level, and the voltages and currents can drive these inner levels directly.

The practical problems of interest usually concern volumes that are rather densely packed with equipment and wiring, where the wires are often routed in harnessed bundles. These coupling problems cannot be solved rigorously because of the complexity of the internal configuration of wires and conducting surfaces. Recent research into this problem has concentrated on determining upper bounds on the internal transients, and significant progress has been made in the past few years. Davis[4] has investigated bounds on coupling through an aperture to a single-wire circuit loaded at each end, and other work has addressed the more important multiconductor problem.[5,6] Both problems are formulated in the same way. The aperture excitation is modeled by the usual electric and magnetic dipoles radiating at the aperture location with the aperture shorted, i.e. closed. The single-wire and multiconductor circuits are modeled as transmission lines above a ground plane, with impedance loads at each end. The transmission lines are driven by the fields of the equivalent dipole sources, and this excitation is modeled by inserting equivalent voltage and current sources in the transmission line. Figure 4 describes this model, a key requirement of which is that the

---

*Numbers in parentheses designate references
listed at the end of the paper.

circuit be separated from the aperture by at least a few aperture radii.

The dipole moments can be bounded by bounding the aperture polarizabilities, and the induced currents and voltages can be bounded by applying the usual transmission line equations to the receiving circuit. For the single-wire receiving circuit, the mathematics is straightforward. Analysis of the multiconductor circuit requires a matrix formulation to generate bounds. The single-wire case is a special case of the more general matrix formulation.

The aperture coupling experiments described in this paper have investigated coupling to circuits very near the aperture, as well as circuits distant from the aperture. The results of these experiments are used to verify recent theoretical models.

MEASUREMENT CONFIGURATION

A metal box was constructed with dimensions of 1.22 m by 1.83 m by 0.91 m. The box was excited by a parallel plate transmission line with a source and a matched load at the two ends of the line, as shown in Figure 5. The upper surface of the box was designed so that a variety of apertures could be located under the upper plate of the transmission line. This excitation resulted in a field distribution at the aperture as shown in Figure 6. The source driving the parallel plate line is shown in Figure 7. This pulser circuit supplied an incident electric field with a peak value of 18 kV/m, with a risetime (zero to peak) of about 10 ns, and a pulse duration of approximately 8 µs (to 1/e of the peak). Figure 8 shows the electric field in the center of the parallel plate region.

APERTURE VOLTAGE MEASUREMENTS

The theoretical study by Casey[7] indicated that a small circular aperture can be considered as an inductance, and that the voltage induced across the aperture by magnetic field coupling is the product of the inductance and the time derivative of the external surface current intercepted by the aperture. Figure 9 shows the external current driven over the aperture and the resulting voltage measured across the aperture on the inside of the test volume. The table in the figure indicates the accuracy of Casey's quasi-static model for the aperture sizes used in the experiment. The waveshape of the aperture voltage is very close to that of the time derivative of the external surface current.

Another important contribution of Casey's work is the development of a simple model for predicting the effectiveness of a mesh screen placed over the aperture. With the untreated aperture modeled as an inductance, a wire mesh cover can be modeled as a parallel impedance element, as shown in Figure 10, where Z_{eff} is the effective impedance of the mesh. This

impedance can be evaluated using the expressions developed by Casey. The table on Figure 10 describes the effectiveness of various mesh screens in reducing the aperture voltage and indicates the accuracy of Casey's model.

These quasi-static models are useful for a quantitative understanding of coupling through an aperture and are formally valid only for a circular aperture on an infinite ground plane. The formal extension to noncircular apertures backed by partially filled cavities is a difficult problem that has not been solved. Certain bounding statements can be made, however, that relate to the usefulness of the results of the analysis of a circular aperture in an infinite plane. Both Casey and Davis state that the characteristics of noncircular apertures can be bounded from a knowledge of coupling through circular apertures, and that coupling through an aperture on an infinite plane is an upper bound on coupling to an aperture in a cavity.

INTERNAL TRANSIENT MEASUREMENTS

A single wire was inserted in the test volume in the configuration shown in Figure 11. The dimensions W and D were varied, and the wire currents were measured under a variety of loading conditions. When the wire was short-circuited at each end, the observed current waveshape was similar to the waveshape of the incident electric and magnetic fields. When the wire was terminated in the characteristic impedance of the wire-to-surface transmission line (approximately 240 Ω), the current observed on the wire had a waveshape similar to the derivative of the incident (external) fields. Figure 12 displays these measured currents for one set of wire locations. The tables in the figure contain the peak amplitudes of the currents for two values of the parameter W and for a range of values of the parameter D.

The internal current measurement configurations were used with the analytical results of Davis in order to investigate the bounding process.

Table 1 shows that the computed currents are indeed larger than the measured currents, generally by less than a factor of 10. The first entry in the table (D = 0.007, W = 0) describes a configuration in which the internal wire is right in the aperture, a case for which the theory breaks down; i.e., the wire is well within an aperture radius of the aperture. However, the computed upper bounds are reasonable for the other cases listed for W = 0. As the wire is moved away from the aperture (W = 0.23 m), the agreement improves somewhat.

SUMMARY

This paper has reported on an experimental investigation of recent theoretical developments concerning aperture coupling. Continued development of bounding theories, especially for the multiconductor configuration, will allow

system designers to assess the importance of apertures to the lightning immunity of aircraft. These theoretical developments may also be reflected in the structure of new electromagnetic specifications and standards used for aircraft procurement.

REFERENCES

1. W. Graf, J. Hamm, and E. Vance, "Relative Importance of Electromagnetic Shield Violations," International Conference on Lightning and Static Electricity, Fort Worth, Texas (21-23 June 1983).

2. C. M. Butler, Y. Rahmat-Samii, and R. Mittra, "Electromagnetic Penetration Through Apertures in Conducting Surfaces," IEEE Trans. Electromagnetic Compatibility, Vol. EMC-20, No. 1 (February 1978).

3. K. S. H. Lee, editor, "EMP Interaction: Principles, Techniques, and Reference Data," EMP Interaction 2-1, Air Force Weapons Laboratory Report AFWL-TR-80-402 (December 1980).

4. W. A. Davis, "Bounding EMP Interaction and Coupling," IEEE Trans. Antennas and Propagation, Vol. AP-29, No. 6 (November 1981).

5. W. A. Davis and M. K. Sistanizadeh, "Bounding Signal Levels at Terminations of a Multiconductor Transmission Line Behind an Aperture," Interaction Note 412, Air Force Weapons Laboratory, Kirtland Air Force Base, New Mexico (June 1981).

6. W. A. Davis and M. K. Sistanizadeh, "Frequency Domain Upper Bounds for Signals on Multiconductor Transmission Line Beind an Aperture," IEEE Trans. Antennas and Propagation, Vol. AP-30, No. 4 (July 1982).

7. K. F. Casey, "Low Frequency Electromagnetic Penetration of Loaded Apertures," IEEE Trans. Electromagnetic Compatibility, Vol. EMC-23, No. 4 (November 1981).

Table 1

MEASURED CURRENTS AND CALCULATED UPPER BOUNDS

(Aperture Radius = 0.1 m

$R_1 = R_2 = 240 \ \Omega$)

D (m)	W (m)	I_{mea} (ma)	I_{cal} (ma)	Ratio I_c/I_m
0.007	0	48	1400	29.2
0.050	0	22	197	8.9
0.100	0	13.2	98.5	7.6
0.007	0.23	0.3	1.3	4.3
0.100	0.23	2.8	15.6	5.6
0.200	0.23	3.8	21.2	5.6
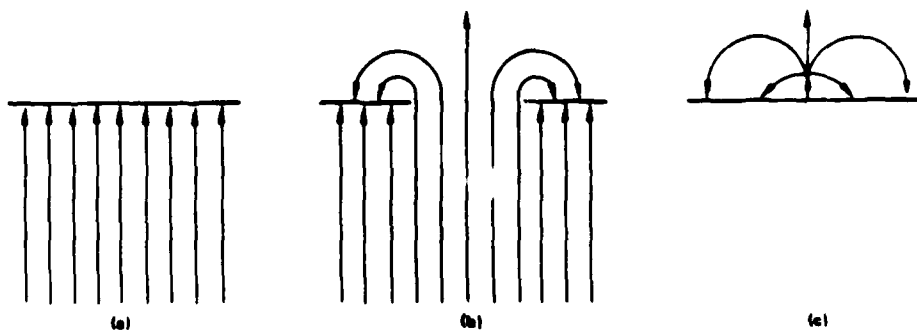
FIGURE 1   ELECTRIC FIELD APERTURE-COUPLING GEOMETRY.   (a) Impressed
electric field perpendicular to screen with no aperture. (b) Electric field
near aperture in screen. (c) Equivalent electric dipole (on screen with no
aperture) and its electric field far from aperture.
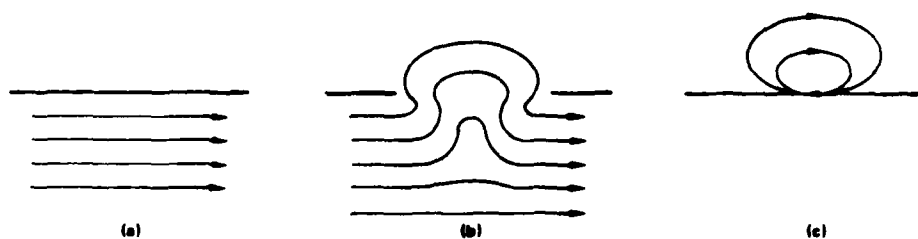
FIGURE 2   MAGNETIC FIELD APERTURE-COUPLING GEOMETRY.   (a) Impressed
magnetic field parallel to screen with no aperture. (b) Magnetic field
near aperture in screen. (c) Equivalent magnetic dipole (on screen with
no aperture) and its magnetic field far from aperture.
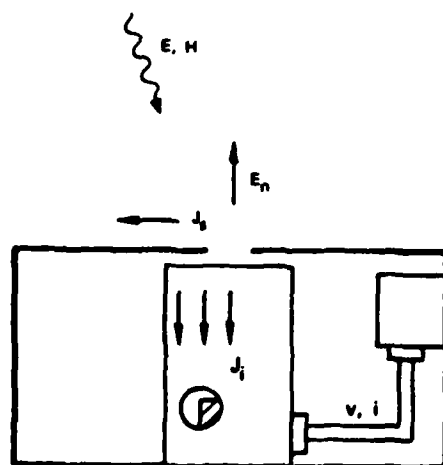
E, H = INCIDENT FIELDS
J_s = SKIN CURRENT
E_n = NORMAL ELECTRIC FIELD
J_i = SURFACE CURRENT DENSITY ON INTERNAL CONDUCTOR
v, i = INDUCED TRANSIENTS AT EQUIPMENT CONNECTOR

FIGURE 3   APERTURE COUPLING EXAMPLE

18-5
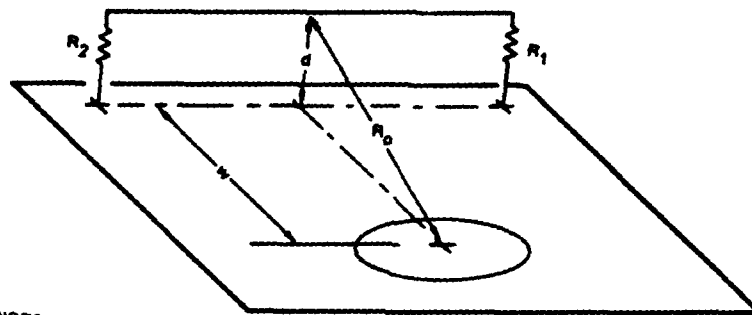
NOTE: This plane is infinite.
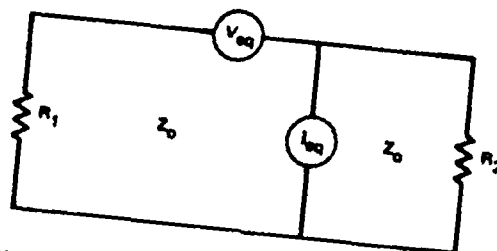
FIGURE 4 GEOMETRY OF WIRE BEHIND APERTURE AND TRANSMISSION LINE COUPLING MODEL
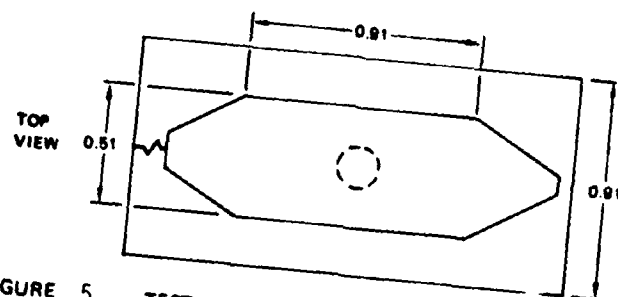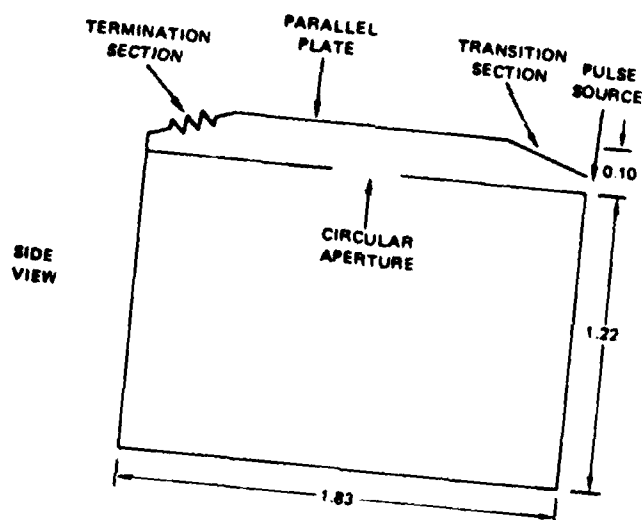
FIGURE 5 TEST CONFIGURATION (all dimensions in meters)

18-6

- - - ► SURFACE CURRENT DENSITY, J_s
———► MAGNETIC FIELD, H_s
———► ELECTRIC FIELD, E_n

NOTE: This plane is infinite.
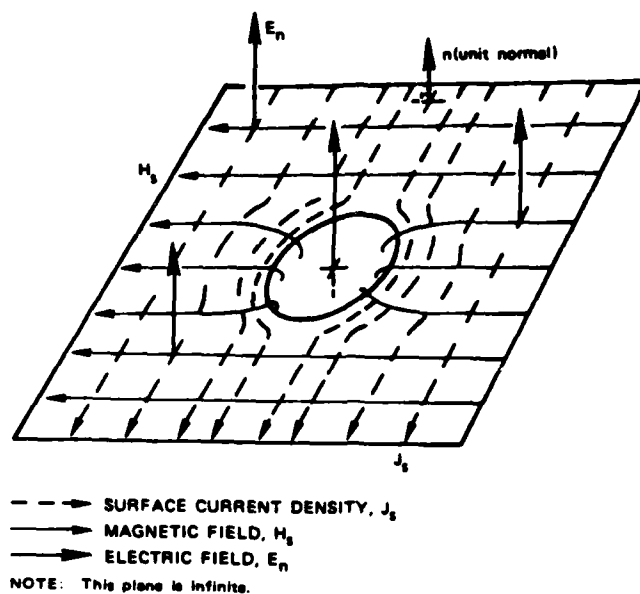
FIGURE 6   FIELD VECTORS AND SURFACE CURRENT AT APERTURE
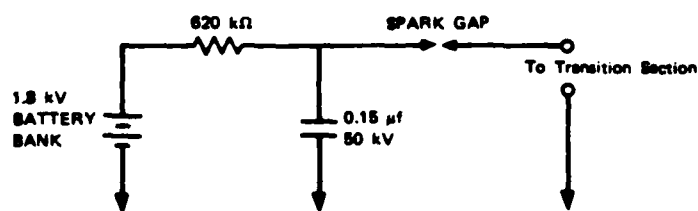
FIGURE 7   PULSE SOURCE FOR PARALLEL PLATE REGION

PEAK FIELD = 18 kV/m

PEAK $\dfrac{dE}{dt}$ = 2.2 kV/m/ns

20 ns/div

2 μs/div
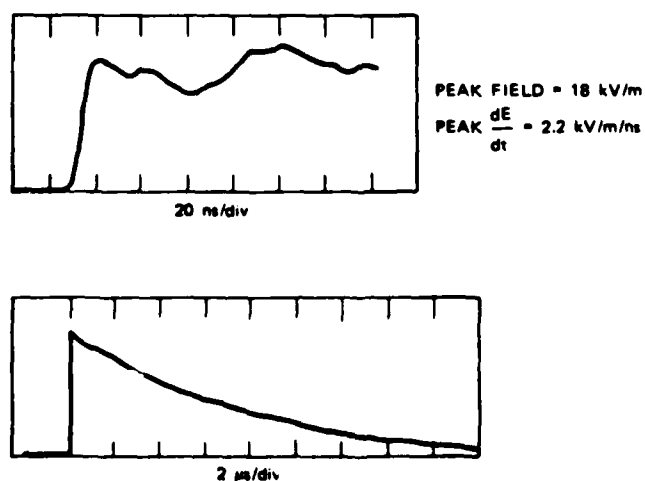
FIGURE 8   ELECTRIC FIELD IN CENTER OF PARALLEL PLATE REGION

18-7
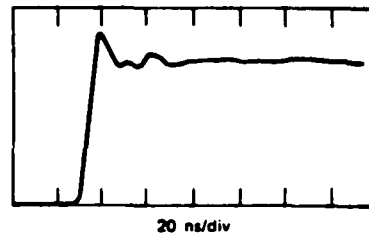
Peak J_s = 40 Am^{-1}

Peak $\dot{j}_s$ = 6 $Am^{-1}ns^{-1}$

20 ns/div

(a) SURFACE CURRENT DENSITY AT APERTURE
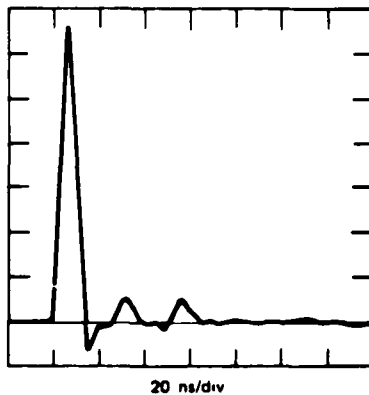
APERTURE RADIUS (m)	PEAK VOLTAGE (V)	
	MEAS.	THEORY
0.10	66.5	67.9
0.05	17.7	16.9
0.025	5.2	4.2

20 ns/div

(b) VOLTAGE ACROSS APERTURE

FIGURE 9   EXTERNAL SURFACE CURRENT DENSITY AND INDUCED APERTURE VOLTAGE (waveshapes shown are typical)
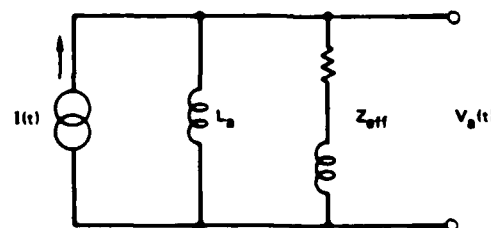
L_a = EQUIVALENT APERTURE INDUCTANCE

Z_{eff} = EFFECTIVE SCREEN (mesh) IMPEDANCE

APERTURE RADIUS (cm)	MESH SIZE (cm)	APERTURE VOLTAGE REDUCTION	
		PREDICTED	MEASURED
10.0	2.54	0.129	0.119
	1.27	0.064	0.043
	0.64	0.028	0.020
2.5	2.54	0.375	
	1.27	0.215	
	0.64	0.102	0.084

FIGURE 10   EQUIVALENT CIRCUIT FOR MESH-COVERED APERTURE WITH MEASURED AND PREDICTED APERTURE VOLTAGE REDUCTION FACTORS

TOP VIEW

SIDE VIEW
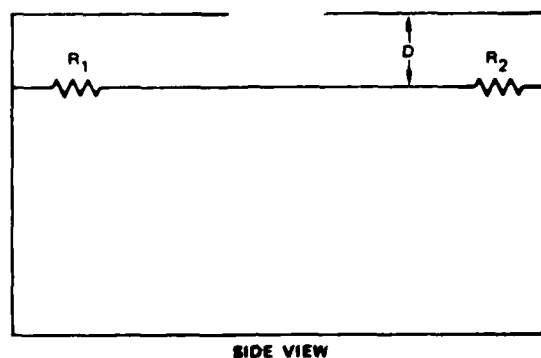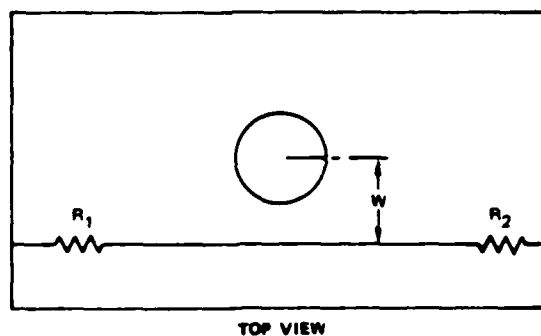
FIGURE 11 LOADED WIRE IN TEST VOLUME

20 ns/div
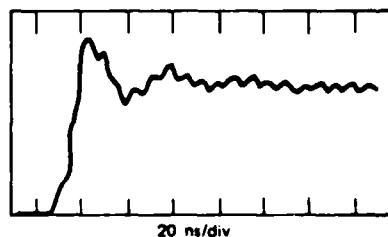
(a) $R_1 = R_2 = 0 \, \Omega$

D (m)	I_{peak} (ma)	
	W = 0	W = 0.23 m
0.007	400	3.3
0.050	160	—
0.100	92	16.8
0.500	42	19.6
0.500	12.4	7.6

20 ns/div
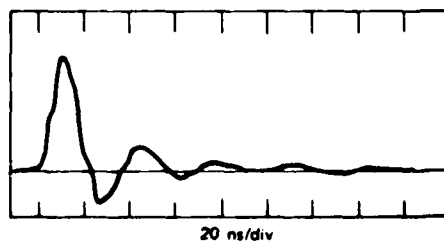
(b) $R_1 = R_2 = 240 \, \Omega$

D (m)	I_{peak} (ma)	
	W = 0	W = 0.23 m
0.007	48	0.3
0.050	22	—
0.100	13.2	2.8
0.200	—	3.8

FIGURE 12 CURRENTS MEASURED ON WIRE IN TEST VOLUME
(circular aperture with 0.10 m radius; waveshapes shown
are typical)

18-9

MULTIPLE LAUNCH ROCKET SYSTEM, (MLRS)
LIGHTNING TEST

by

Dr. George R. Edlin, MICOM

Mr. John D. Robb, LTRI

Mr. Ron Tomme, Vought Corp.

LIGHTNING TESTS HAVE been carried out on the MLRS System including tests of the launcher/loader pod and complete tests of the vehicle in the field. The tests include high voltage long arc strikes to determine the distribution of the strike points, and also high current tests to check for possible damage and accidental ignition of the rockets.

The purpose of the tests was to assure that no accidental ignition would occur under the worse conditions of lightning strike point and current magnitude.

The laboratory tests of the LPC were carried out in the Miami laboratory of LTRI and the field tests were carried out at White Sands Proving Grounds, New Mexico.

Initial tests of the LPC showed that strikes could occur to the metal protection cap over the igniter on the upper center launch pod, and high current tests showed that ignition of the launch igniter squib could occur. Additional protection was therefore added in the form of a protection bar across the top of the frame above the igniter area to prevent this type of strike from occurring. Additional discharges were fired into this area and no indications of ignition occurred.

Tests of the complete vehicle including the long arc high voltage tests and the high current damage tests showed no ignition occurring nor did the system upset which could cause ignition.

These tests included 150 high voltage long arc discharges and over fifty 200,000 ampere discharges to the complete MLRS launch pod system. These tests constitute, to the best of our knowledge, the most severe sequence of tests ever carried out on a complete vehicle of any type.

LABORATORY TESTS OF THE LAUNCHER LOADER POD (LPC)

TEST ARRANGEMENT - The test arrangement, as shown in (Fig. 1), consists of the high voltage 2.5 megavolt Marx impulse generator, the test area, the test electrode and the test object, the launcher loader pod. The LPC consists essentially of a metal frame in which are mounted six rockets inside of launch tubes. The pod of the assembly is used for storage, transportation

and also for loading into the launch vehicle.

The test discharges were fired from the expected angles of approach of a natural lightning discharge.

TEST RESULTS - The tests included approximately 100 test discharges and only one area of the LPC was found to present a possible problem. A strike did occur to the metal cover on the back of the upper central launch pod. A drawing showing both a strike to the metal cover and also streamering off the metal cover from strikes to either of the upper side rails are shown in (Fig. 2).

In order to preclude this, a metal bar was placed across the top above the metal covers. An additional sequence of tests was carried out and no strikes occurred to the metal cover and no streamering was observed.

One other possibility which was evaluated was that a lightning strike would strike the center bar and flash over to the cap by virtue of an inductive impedance voltage. Consideration, however, of this possibility on the basis of simple linear circuit theory indicates that it is of low inductance voltage - $V2$ L * di/dt probability. The length of the bar is approximately one meter and a strike to the center of the bar would present two one-half meter paths to the basic LPC structure. With an inductance of one microhenry per meter estimated, the paths from the center of the bar to each side would constitute, in effect, two one-half microhenry inductors in parallel or one-quarter microhenry. With a rate of rise of 100,000 amperes per microsecond, the di/dt voltage would only be equal to 25,000 volts which would fire approximately only 1/4 inch distance. Therefore, with the cap underneath the bar and spaced away from it, the probability of strikes to the cap would be extremely low. Thus, the tests showed no strikes to the caps after installation of the protection bar above them and even if a stroke did occur to the center of the protection bar which is a relatively low probability, the tests thus indicated that no strikes would occur to the igniter covers.

FIELD TESTS OF THE MLRS COMPLETE VEHICLE LAUNCHER ASSEMBLY

HIGH VOLTAGE LONG ARC - The test arrangement for the high voltage long arc tests are shown in the drawing and photograph of (Fig. 3 and 4). A 1.5 million volt Marx generator was constructed in the field at White Sands Proving Grounds and a ground screen was placed on the ground in front of the Marx generator. Because the Marx generator was not mobile, the MLRS test vehicle was driven into the various positions for firing lightning strokes to it from the expected approach directions of a natural lightning strike. The vehicle was moved rather than the large Marx generator. The test electrode positions as indicated in (Fig. 3), covered the front, middle and rear of the launch pod and also the cab of the vehicle.

The tests indicated that nearly any part of the top of the launch pod could be struck and the launch pod or control cab could be struck.

No strikes were fired to the antennas as the antenna tuner and radio were critical for other tests and possible damage was not acceptable. Therefore the antenna and tuner tests were planned for a separate series of laboratory tests. A rough review of the antenna lead lengths and the fields calculated inside the cab indicated that the induced currents would probably be less than that which would result from strikes to the center dividing posts on the windshield of the cab.

The tests thus indicated no unusual strike-points in this series of tests.

HIGH CURRENT DAMAGE TESTS - The test generator for the high current tests consisted of a large bank of capacitors charged in series - parallel and discharged in the same configuration in the vehicle. The screen mat underneath the vehicle was carried up to the base of the current generator which was located on a truck bed in order to minimize inductance and with this arrangement currents exceeding 200,000 amperes could be fired to the vehicle. Discharges were fired to all the major strike points and no upsets of the launch system occurred in any of the test strikepoints with any of the test strikepoint locations.

CONCLUSIONS

In a series of tests on the LPC and the MLRS vehicle with the LPC installed no upset or damage occurred which would cause an inadvertent launch with the exception of the early tests before the protection bar was installed on the LPC. Thus the system withstood approximately 150 high voltage long arc lightning discharges and 50 discharges between 150,000 and 200,000 amperes. This constitutes one of the most severe tests of a complete vehicle assembly that has been run to our knowledge to date.
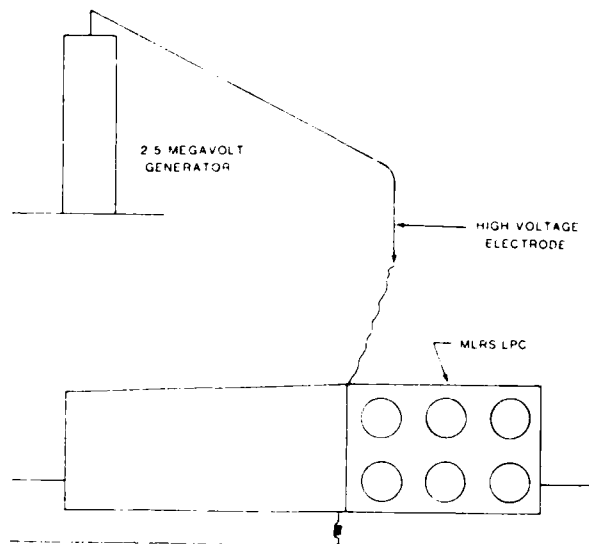
Fig. 1 - Test arrangement for high voltage long arc tests
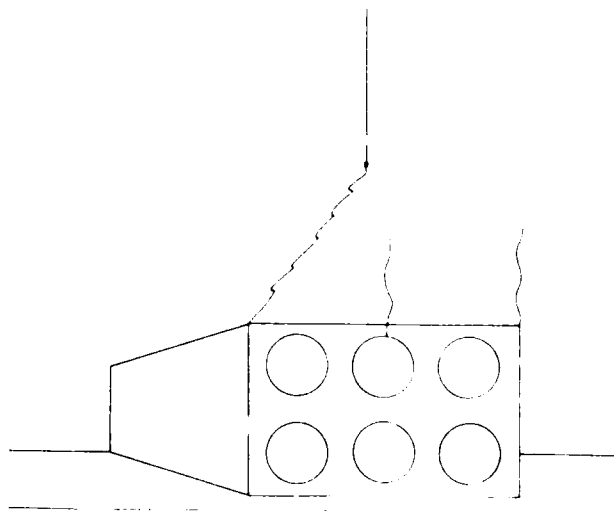
Fig. 2 - Strike to LPC shows streamers of center pod and right rail

Fig. 3 - Illustration of high voltage long arc
field tests of MLRS system
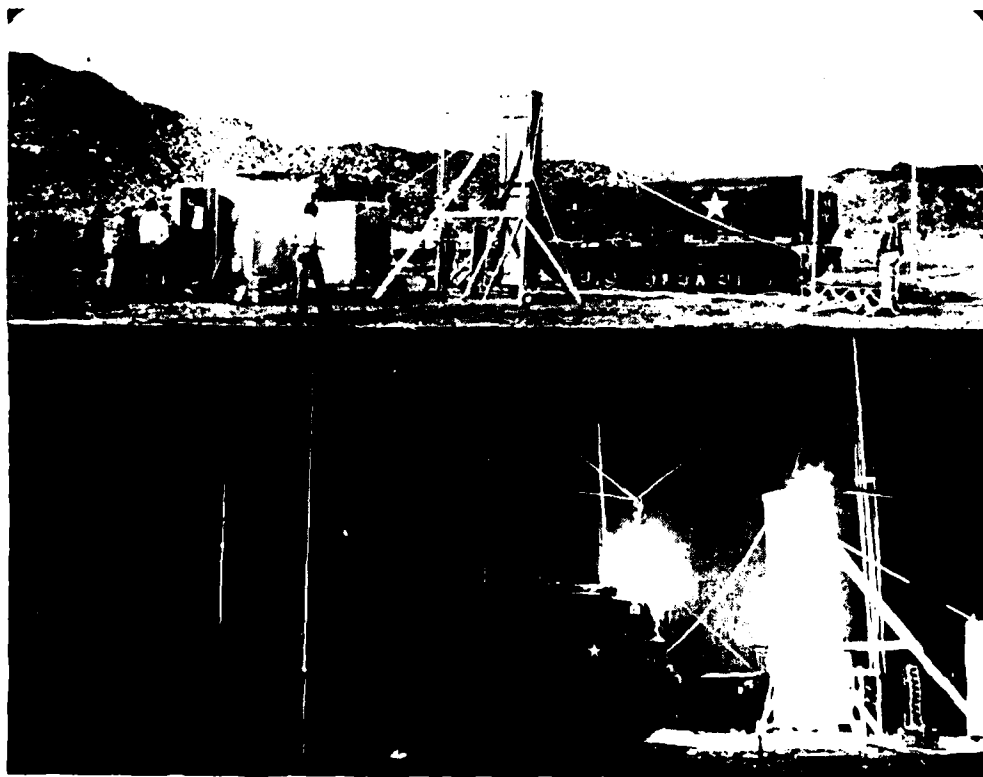
Fig. 4 - Test arrangement shown above with test
discharge shown below

A CONTRIBUTION TO THE ANALYSIS OF TRIGGERED LIGHTNING :
FIRST RESULTS OBTAINED DURING THE TRIP 82 EXPERIMENT

by P. Laroche*, A. Eybert-Berard**, P. Richard*, P. Hubert***,
G. Labaune*, L. Barret**

*Office National d'Etudes et de Recherches Aérospatiales (ONERA)
BP 72 92322 CHATILLON CEDEX (France)

**Centre d'Etudes Nucélaires de Grenoble, rue des Martyrs,
38000 GRENOBLE (France)

***Centre d'Etudes Nucléaires de Saclay
91191 GIF-SUR-YVETTE CEDEX (France)

ABSTRACT

This paper presents a preliminary analysis of the data concerning triggered lightning flashes obtained at the Langmuir Laboratory in 1982. Discharge currents, visible light emitted by return strokes channel and nearby magnetic fields detected at ground are correlated. Measurements of distant VHF radiation by means of a spectrum analyser and a two dimensional interferometer location system at 300 MHz are discussed.

DURING THE SUMMER OF 1982, an experiment on triggered lightning was held at the Langmuir Laboratory of the New-Mexico Institute of Mining and Technology (USA). This experiment was conducted by investigators from the US Air Force (FDL laboratory - WPAFB), New Mexico Tech, ONERA (Office National d'Etude et de Recherches Aérospatiales - France) and CEA (Commissariat à l'Energie Atomique - France). It had two main objectives :
- studies of the behaviour of a hemispherical ended cylinder that simulated an aircraft fuselage when strucked by lightning ;
- analysis of the electrical properties of triggered lightning.

In addition to development and testing of the equipment associated with the instrumented cylinder, the main experiments, to which this article is primarily related, are as follows :
a) current measuring at flash foot ;
b) detection of the visible light emitted by the lower part of return strokes channel ;
c) measurement of magnetic field at ground produce by nearby flashes ;
d) measurement of distant VHF radiation by means of a spectrum analyser and a two dimensional interferometer location system at 300 MHz. Also, a high time resolved measurement of the electromagnetic radiation during a storm was performed.

A preliminary analysis of some of the data procured during the summer is conducted in order to clarify the origin of VHF radiation during lightning.

For that purpose we examine the properties of short pulses observed during a storm and then discusse emission characteristics from triggered lightning as related to flash phase and as deduced from various measurements.

EXPERIMENTS

A diagram giving the location of all measuring equipment is shown in figure 1.

TRIGGERING SITE - Current is Measured by means of a coaxial shunt connected to the triggering device. The resistance of this shunt is 0.001 Ω and its rise time is shorter than 80 ns. The signal is recorded on a wide dynamic range. The bandwidth of the current recording equipment is DC to about 1 MHz.

Triggering Equipment - Lightning flashes are triggered beneath stormy clouds, using the well-known wire and rocket technique [1]* [2]. A small rocket, of the anti-hail type, unspools a steel wire, 0.2 mm diameter. The lower-part of the wire is connected to ground through the current shunt device. Triggered flashes are obtained when the rocket reaches heights between 50 and 500 m depending of the electrostatic field strength created by the cloud.

Light Sensor - A light probe is installed about 300 m away from the triggering site ; it is directed toward the lower part of the channel that corresponds to the conducting wire which is vaporized at the beginning of the event. With an 8 degrees light acceptance angle, the measured optical signal

*Numbers in parentheses designate References at end of paper.

covers about 35 m of channel length. The probe gives information in the visible range (400 to 700 nm).

Magnetic Sensor at Ground - A magnetic sensor is installed about 200 meters from the triggering site. Its bandwidth is 100 Hz-20 MHz and the receiving signal is connected to a battery operated videotape recorder with a 1 MHz bandwidth [3]. Its dynamic range is adjusted in order to record the effect of large current pulse passing through the flash channel.

ELECTROMAGNETIC MEASURING SITE - Experiments are performed at the West-Knoll site located about 1300 m south of the triggering site (see figure 1). They include the following measurements :

Wide Band Measurement - The instrumental device is made of a wide bande antenna connected to a fast transient digitizer (Tektronix 7912 AD) which is controlled by a computer (Tektronix 4052). The bandwidth of the antenna is 20-200 MHz but we have verified that it can be use to 500 MHz. Concerning the response of the system to impulse signals, we must note that due to mismatching of the antenna with the recorder, only the first 10 ns can be considered to represent the actual shape of the incoming pulse.

The transient digitizer is used with an amplifier that has a 600 MHz bandwidth and a detectable signal level of 1 mV. The computer is programmed to record about one event per minute.

300 MHz Interferometer System [4] - The principle of the experiment is to measure the phase difference of an incident electromagnetic wave on two different antennae that are separated by a distance which is a fraction to a few tens of a wavelength. This principle is valid only for a plane wave.

The system used for these experiments is made of two parts : a large system and a smaller one. Each is constituted by three equidistant antennae that provide an angular location of the radiating sources. Antenna dimensions are optimized in such a way that the largest set gives precise but non definite locations (modulo parts of 2π) and the small one imprecise but definite locations. The optimization of instrumental parameters has provided dimensions of 0.5λ and 10λ baseline lengths for the small and the large system respectively. Temporal resolution of the system is 1 µs and the nominal location accuracy is better than 10^{-2} rad. Signal sensitivity is -60 dBm.

Spectrum Analyser - A system of six narrow-band receivers is provided by CNET (Centre National d'Etudes des Télécommunications - France). This equipment is used to study the electromagnetic spectrum of VHF-UHF radiation during lightning flashes. Receiving frequencies are regularly spaced, on a log-scale, from 60 to 900 MHz : 60, 100, 175, 300, 500 and 900 MHz. The dynamic range of each channel is 80 dB. The six antennae are

$\lambda/2$ dipoles, installed at $\lambda/4$ of a vertical supporting mast. We have verified that the coupling between antennae is negligible ; the 3 dB bandwidth of each channel is 370 kHz. The sensitivity of each channel is adjusted following results obtained by other experimentalists [5] : E.T. Pierce gathered the results concerning different measurements, normalized at 10 km for a 1 kHz bandwidth. On figure 2, we have indicated the threshold of the interferometer and of the spectrum analyser, in regards of others results which magnitudes are gathered around the following characteristic :

$$S_{(\mu V/m.kHz)} = \frac{1000}{f_{(MHz)}}$$

RESULTS

WIDE-BAND MEASUREMENTS [6] - These measurements are not synchronized with other data and correspond to natural lightning as well as triggered events. The results obtained during the 82 campaign, bring out the following points :
- the records exhibit mainly short pulses whose shape and rise time are almost identical regardless of the type of flash ;
- the rise time is few ns ;
- the pulses are emitted at a rate between 1 and 20 per µs.

Figure 3 gives the shape of a typical pulse ; the table, shown on figure 4, indicates the characteristics of 20 different pulses obtained during a single storm. It must be keep in mind that the distance between the radiating sources and the antenna is not known.

RESULTS CONCERNING TRIGGERED FLASHES - There were 24 attempts to trigger lightning among which 14 were successfull. Triggered events may be of three types [3] :
- the classical type corresponds to an upward branching flash that produces a continuous current, for the first tens of ms due to an upward positive leader ; however, fast and large current pulses may be observed, superimposed simultaneously with the continuous current component ;
- the "anomalous" type has a channel which does not follow the path of the wire ; there is initially an upward moving positive leader but the current in the shunt falls to zero when the wire is vaporized ; the first return stroke is often initiated by a downward stepped leader whose lower parts follow the branch of the initial upward moving positive leader ; the flash produces few strokes before the beginning of the continuous current component ;
- the "pseudo-anomalous" type has the same current characteristics as the anomalous one, but it strikes the measuring equipment because it follows the lower part of the vaporized wire. Events A and B discussed in what follows are of that type (event A : 17h30mm

46s, day 8.5.1982 ; event B : 12h51mm46s, day 8.7.1982).

Event A - The first radiation detected by the interferometer occurs 32 ms before the first return stroke and a few ms after the vaporization of the wire. Angular location of the VHF sources may not be obtained before the radiation associated with the first stroke, because the signal received is too weak to allow for a full reduction of data.

Figure 5a shows the current versus time variation ; figure 5b shows the angular (elevation-azimuth) locations of the sources corresponding to the flash. Suitable interferometer information indicates several spatial continuous organizations of emitting sources. Associated with the first stroke is an upward propagation of sources, from the location of the triggering site. These move with a mean velocity of 4.10^7 m.s^{-1} if it is assumed that all the events happen in a vertical plane containing the triggering site. Other organized locations of sources, indicate downward propagations that are probably associated with dart leaders. These have a mean velocity between 10^7 and 5.10^7 m.s^{-1}. Figure 6 shows, for the first stroke and a dart leader, the time evolution of the elevation angle of the sources. These curves clearly indicate the upwards or downwards propagation of the phenomenon.

Event B - This negative triggered flash exhibits 16 large current pulses as recorded by the magnetic sensor close to the channel. However, during the same time, the optical sensor indicates 46 fast luminous pulses. After evaporation of the wire, the flash strikes the measuring equipment but the lower part of the channel is diverted so that we only have measurements before vaporization and for the four last strokes. The overall duration of the flash is 412 ms.

The first stroke occurs about 12 ms after wire vaporization. The magnetic sensor at ground indicates a corresponding current of 16 kA with a rise time of 15 µs. The maximum current amplitude during the flash, as deduced from this sensor, is that of the last stroke : 19 kA, rise time 1 µs.

The radiation first detected at 300 MHz by the interferometer is simultaneous with the first stroke ; angular locations associated with it are scattered above the triggering site. Most of the angular locations obtained during this flash are spatially scattered ; they correspond to bursts of a few hundred µs duration, that are generally associated with current or light pulses. On two cases, we observe a downwards organized propagation which may correspond to two dart leaders ; The velocities are 10^7 m.s^{-1} and 8.10^6 m.s^{-1}.

We have drawn on figure 7, current and light emitted by the flash versus time ; we have indicated the bursts of radiation detected by the interferometer and by the spectrum analyser. Figure 8 is a drawing of the

angular location of three different downwards propagation sources defined on figure 7 (points O_1, O_2, O_3).

VHF radiation is detected by the spectrum analyser just before the beginning of current flow due to the upwards positive leader from the wire. Radiation is gathered in burst corresponding to light pulses. One of the most general results concerning this measurement is that the magnitude of the radiated field stays within a short dynamic range, whatever the actual component of the flash. Nevertheless, the temporal evolution of the radiation seems closely related to the flash to ground phase ; we have drawn, on figure 9, radiation associated with the stepped leader before the first stroke O_4 and, on figure 10, the radiation associated with the dart leader preceding the last stroke.

The stepped leader radiation begins by a bursts of 77 µs duration, 1.9 ms before the stroke O_3 (fig. 9). It is followed by short bursts of 5 to 10 µs width that are rather regularly spaced by blanks of 50 to 80 µs. The strongest radiation corresponds to the return stroke.

The duration of radiation from this first return stroke is 140 µs and corresponds to the duration of current deduced by the magnetic sensor. However, the main current pulse, as recorded by the current shunt, lasts only 40 µs.

The dart leader before the last return stroke exhibits very different VHF characteristics. As shown in figure 10, radiation is more continuous and increases slightly as the radiation sources (300 MHz) approach the ground in 600 µs time. All radiation ends at the start of the current pulse from the return stroke.

DISCUSSION

Data reduction of TRIP 82 measurements is still, in a preliminary stage and must be improved in the future.

Nevertheless, it is now possible to point out some interesting facts concerning electromagnetic radiation produced by lightning discharges.

Regarding electromagnetic measurements, we are not able to see big differences between triggered lightning and initially upwards directed natural flashes. Anyway, the most significative result is that VHF radiation due to an upwards positive leader is weak (less than 50 µV/m.kHz at 10 km at 300 MHz). It is just detected by the spectrum analyser which sensitivity is greater than the interferometer one.

We have observed, during natural or triggered lightning, short radiation pulses with a typically 2 to 5 ns rise time, and a maximum rate of 20 per µs. The frequency spectrum of these pulses has the same shape, in the VHF range, as this which corresponds

to well known results on lightning (fig. 3) ; this strengthen the idea of the impulsive nature of VHF radiation due to lightning.

Results indicated by the interferometer have the same general characteristics as those concerning natural flashes observed during a previous campaign and presented in an other paper [7] :
- radiation is, most of the time, constituted by pulses of less than 1 μs duration ;
- those pulses are gathered within longer radiation bursts of few hundreds μs duration ;
- the corresponding locations of the radiation sources are either scattered in a wide angular range or gathered, to indicate a one way propagation which is associated with a mean velocity of few 10^7 m.s^{-1} for both dart leader and return stroke. These velocity values are not in disagreement with results obtained by other authors [8] [9].

Our 1982 measurements include new complementary and simultaneous indications obtained with the VHF spectrum analyser. The main results are the following :
- at any given frequency the strength of the radiation seems not to be strongly dependent on the flash component (leader, return stroke...) ;
- the temporal variation of the radiating field is typical of the flash component as already mentioned by others [10] ;
- VHF spectrum is analogue to the curve on figure 2, but the level obtained is a little less than the mean value.

Comparison of two return strokes indicates that one is associated with propagating radiation sources but that these are completely absent in the second stroke. In both cases, there is no VHF radiation after the strokes. This strongly suggests that the radiation that we observe is not directly associated with the current wave of the return stroke but with some other mechanisms.

The continuous propagations, indicated by the interferometer, for certain bursts of pulses, show that the emission zone within the μs is probably limited to a few m to tens of m large.

CONCLUSIONS

Measurements of VHF radiation, simultaneous with other measurements that identify each flash component, are basic for an understanding of the radiation associated with lightning.

A preliminary analysis of the data obtained during the summer of 1982 raises important questions regarding the origin of the radiation recorded. It appears that strong VHF radiation is not always associated exclusively with the propagation and location of the return stroke.

Triggered flashes, in particular the frequently obtained "anomalous" flashes that deviate from the evaporated wire, exhibit behaviour that is close to that of naturally occuring upward initiated discharges. This makes triggered lightning a powerful tool for all lightning studies including more technically oriented effects such as their interactions, with aircraft.

All these considerations imply the need to improve the instrumentation in future program. A three dimensional, more sensitive, interferometer should be used in conjunction with a spectrum analyser and a wide-band antenna system.

REFERENCES

1. N.N. Newman, "Problems of Atmospheric and Space Electricity." Elsevier, p. 482-490, 1965.

2. R. Fieux, C. Gary and P. Hubert, "Artificial Triggering of Lightning above Ground." NATURE n° 257, p. 212-214, 1975.

3. P. Hubert, "Triggered Lightning at Langmuir Laboratory in July-August 1982." CENS, IRF/SEP/82-077.

4. P. Richard and G. Auffray, "VHF-UHF Interferometric Imagery. Application to Lightning." Submitted to Radio-Sciences.

5. R.H. Golde, "Lightning", Vol. 1, Academic Press, 1977.

6. G. Labaune, A. Delannoy, P. Richard et P. Laroche, "Hypothèse sur les mécanismes physiques du rayonnement VHF-UHF de l'éclair". Presented at 2nd Colloque National sur la Compatibilité Electromagnétique, Trégastel (France), June, 1983.

7. P. Richard, A. Delannoy, G. Labaune et P. Laroche, "UHF Interferometric Imaging of Lightning". Presented at International Conference on Lightning and Static Electricity, Fort Worth (USA), June, 1983.

8. P. Hubert and G. Mouget, "Return Stroke Velocity Measurements in two Triggered Lightning Flashes". JGR, vol. 86, pp. 5253-5261, 1981.

9. W. Beasley, M.A. Uman and P.L. Rustan Jr., "Electric Fields Precedings Cloud to Ground Lightning Flashes". JGR, Vol. 87, No C7, pp. 4883-4902, june 20, 1982.
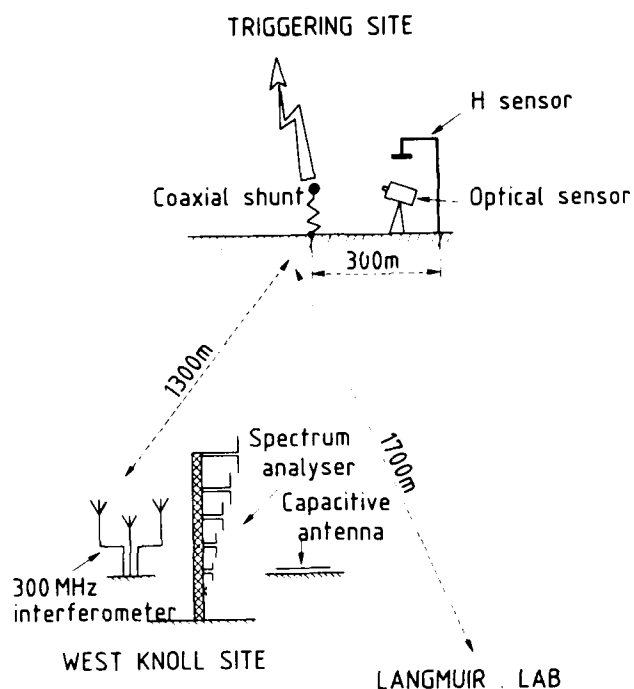
Fig. 1 - Measuring site diagram
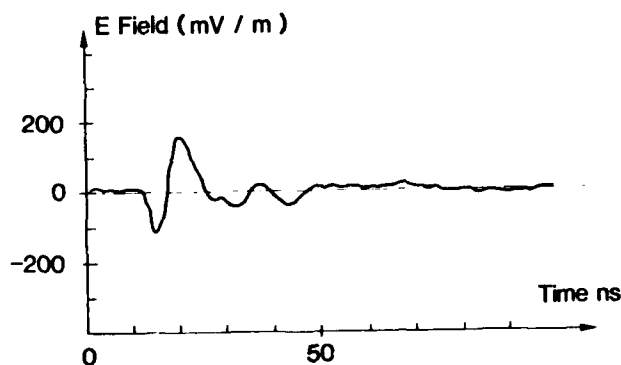
Fig. 3 - Typical pulse detected by a wide band system

↓S300: Threshold of 300 MHz spectrum
        analyser channel
↓I300: Threshold of interferometer
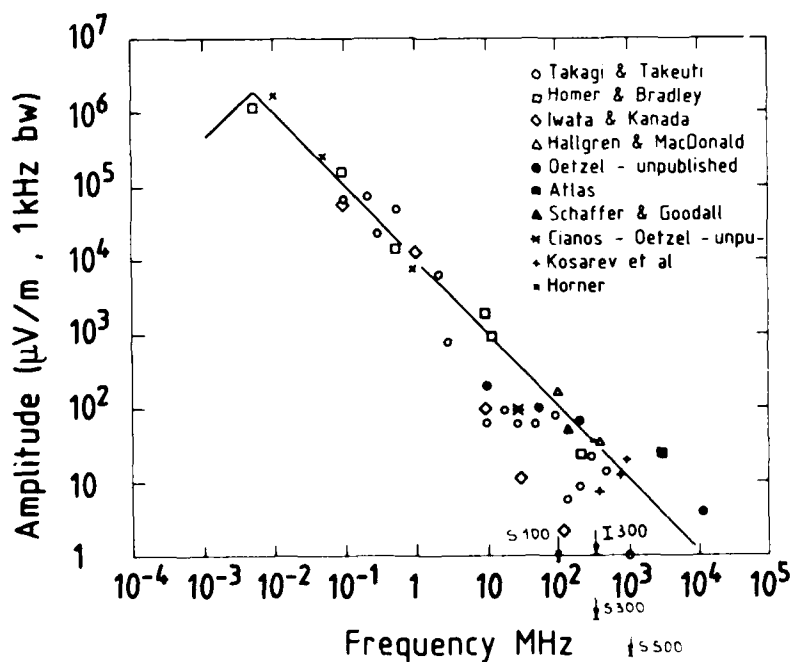
Fig. 2 - General results on lightning radiation

PEAK VALUES mV/m	RISE TIME 10% – 90% ns
290	3.3
300	2.9
300	2.9
60	4.8
65	4.3
100	4.8
171	2.2
37	2.9
100	4.3
45	4.3
33	2.0
60	5.2
45	4.0
230	5.7
210	2.0
345	2.4
355	3.3
155	1.5
177	1.9
230	2.9

Fig. 4 – Characteristic of 20 pulses
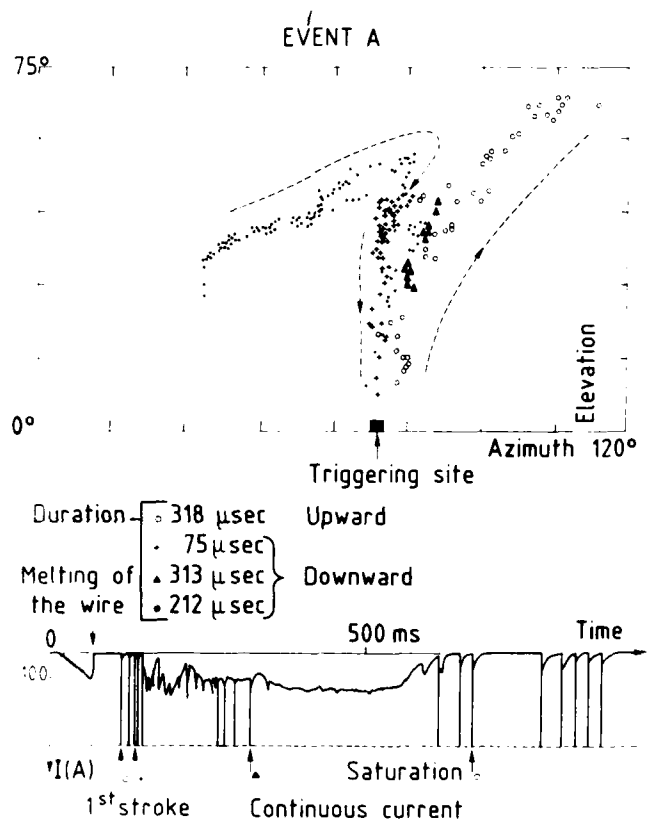
Fig. 5 – Event A : current and 300 MHz sources locations

Mean velocity $4.10^7 m.s^{-1}$

Elevation

$-50°$

0   50 µs   Time

1st stroke

Elevation

Mean velocity
$5.10^7 m.s^{-1}$

$-50°$

Mean velocity
$9.10^6 m.s^{-1}$

0   50 µs   Time

Dart leader preceeding 3rd stroke
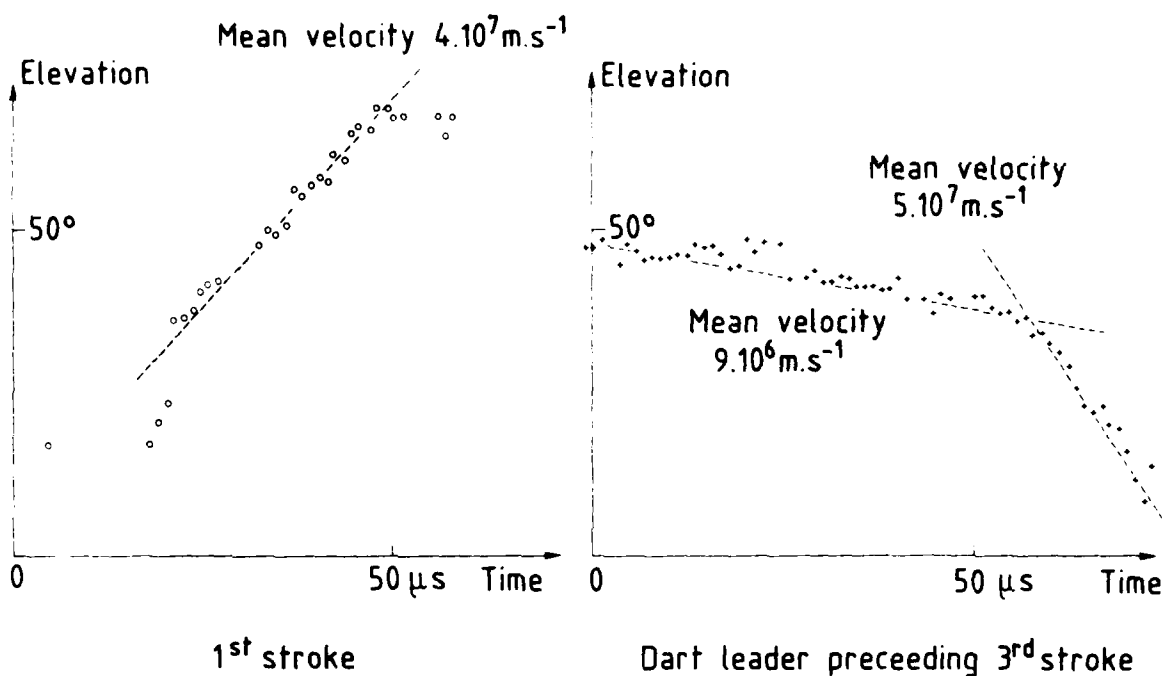
EVENT A

Fig. 6 - Propagation source : elevation
versus time

EVENT B

Melting of
the wire

Current in the shunt

(Current is diverted)

0

-100

I(A)

Optical sensor

0   100

Time (ms)

‡ Burst observed by interferometer

▲ Burst observed by analyser
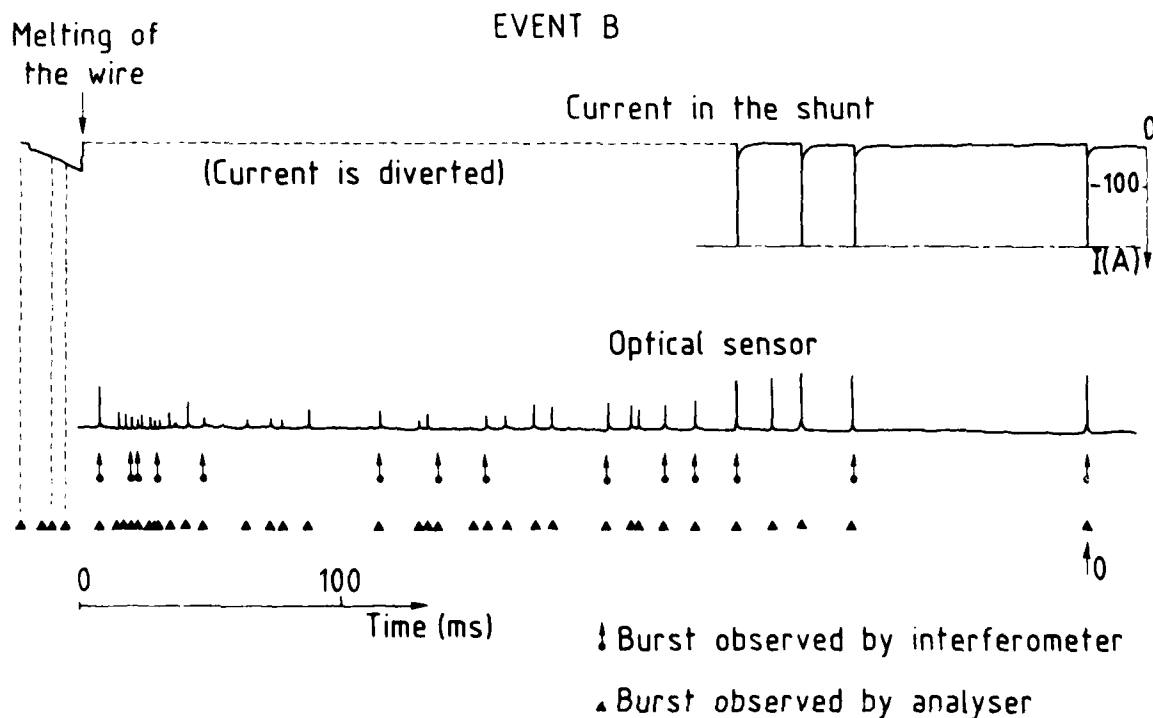
Fig. 7 - Main components of event B

EVENT B

Burst duration: ○ 200 μsec
· 100 μsec
. 120 μsec
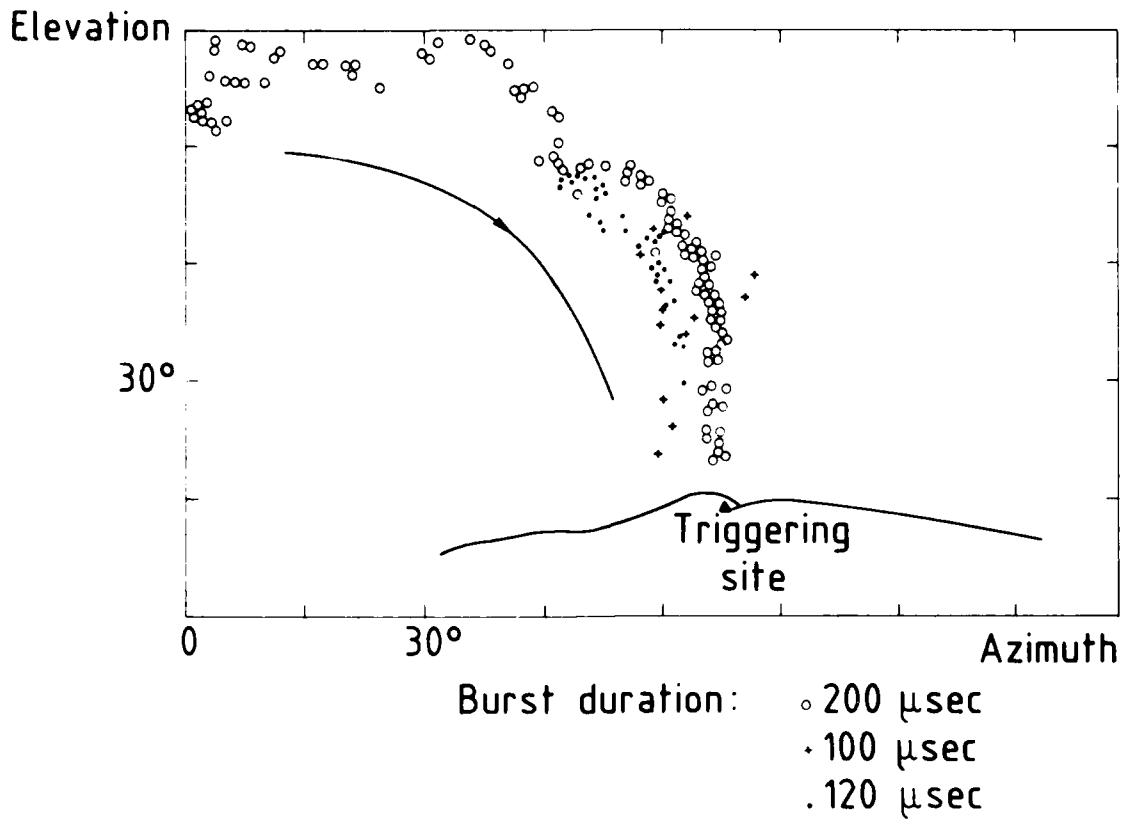
Fig. 8 - Organized propagating sources at 300
MHz
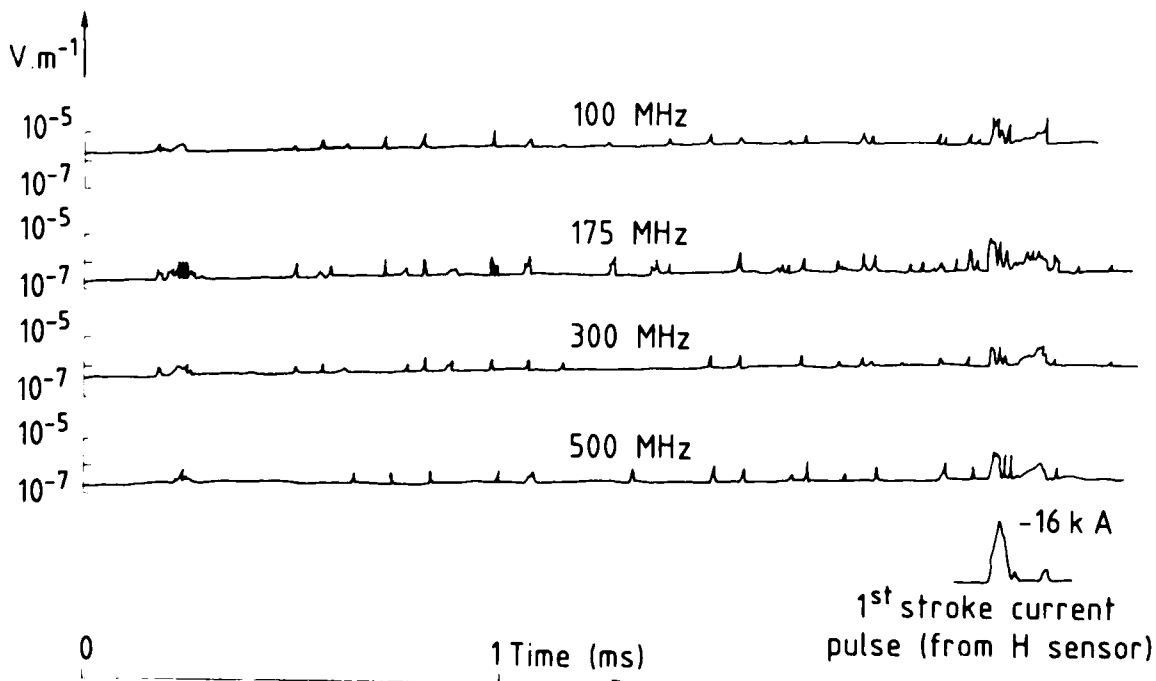
Fig. 9 - Event B : 1st stroke ; spectrum
analyser signal
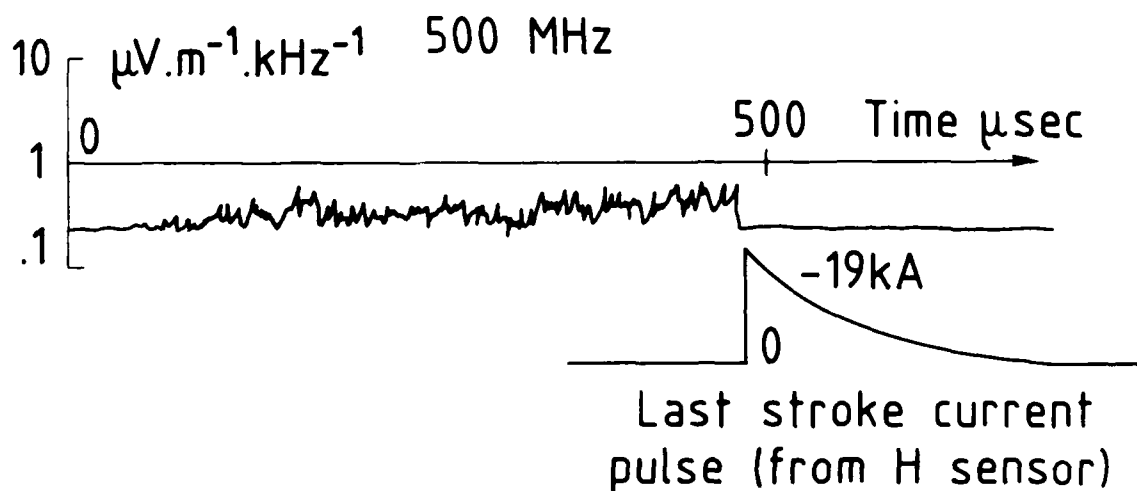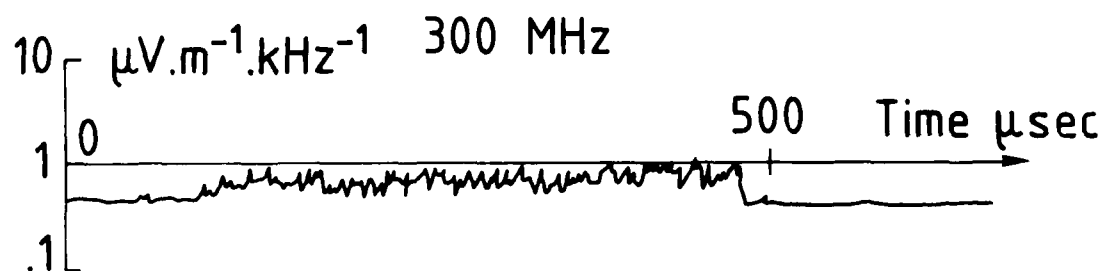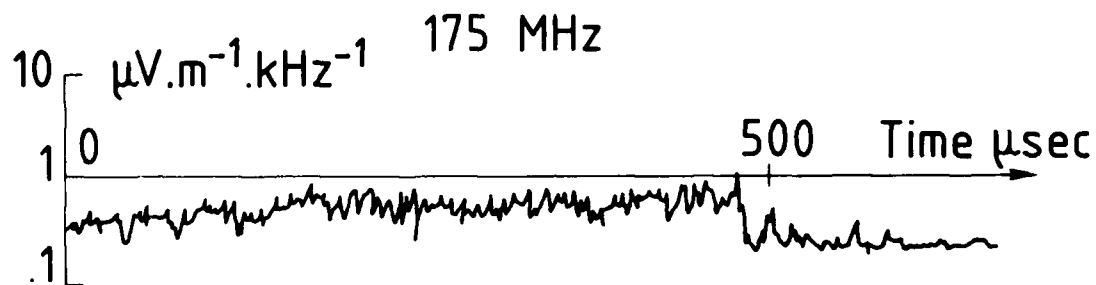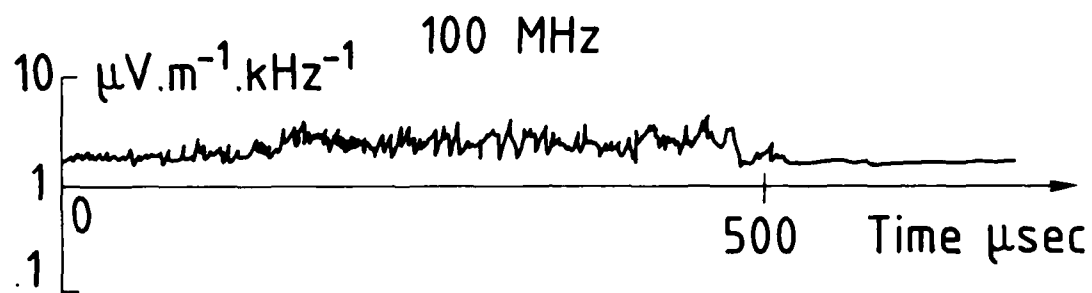
Fig. 10 – Event B : last stroke spectrum
analyser signal

LIGHTNING ATTACHMENT PATTERNS AND FLIGHT CONDITIONS
EXPERIENCED BY THE NASA F-106B AIRPLANE

Bruce D. Fisher
NASA Langley Research Center

J. Anderson Plumer
Lightning Technologies, Inc.

Abstract

During the NASA Langley Research Center Storm Hazards Program, thunderstorm penetrations have been made during three summers by an extensively instrumented F-106B research airplane in order to record direct lightning strike data and the associated flight conditions. The penetrations were made in Oklahoma and Virginia in conjunction with ground-based weather radar measurements by the NOAA-National Severe Storms Laboratory and NASA Wallops Flight Center, respectively. In 1980 and 1981, the airplane received 10 direct lightning strikes each year, with most penetrations occurring near the freezing level. In 1982, 239 penetrations were made during which 156 direct lightning strikes occurred. Most of the penetrations in 1982 were made at higher altitudes and colder ambient temperatures than in 1980 and 1981. Following each flight, the airplane was thoroughly inspected for evidence of lightning attachment, and the individual lightning attachment spots were plotted on isometric projections of the airplane to identify swept flash patterns.

This paper presents samples of the strike attachment patterns that were found, and discusses the implications of the patterns with respect to airplane protection design. The altitudes, ambient temperatures, turbulence, and precipitation at which the strikes occurred are also summarized. The significance of these findings with respect to lightning avoidance by airplanes is also discussed. Finally, lightning strikes to several U.S. Air Force airplanes struck during routine operations are discussed in relation to the Storm Hazards flight experience.

THE NASA LANGLEY RESEARCH CENTER STORM HAZARDS PROGRAM is being conducted to improve the state of the art of severe storm hazards protection, detection, and avoidance, and design of aircraft for those hazards which cannot reasonably be avoided. Although hazards such as turbulence and windshear are being studied, the primary emphasis of the Storm Hazards Program is being placed on lightning hazard research. Lightning is of special interest because the projected use of digital avionics systems and composite aircraft structures will require incorporating appropriate lightning protection design features.

The flight program began in 1978 when a Twin Otter airplane equipped with an airborne lightning locator system was flown on the periphery of thunderstorms in Oklahoma and Virginia (1).[*] The program continued in 1979 when operations began with an F-106B airplane, which was flown on the periphery of thunderstorms in Virginia (2). From 1980-1982 419 thunderstorm penetrations were made with the F-106B in Oklahoma and Virginia during which 176 direct lightning strikes were experienced. The lightning attachment patterns and flight conditions for 1980 are presented in (3).

Since new aircraft are being designed with large areas of skin and structure to be made of composite materials, improved knowledge of the susceptibility of various parts of the aircraft surface to lightning strikes is necessary. For the purpose of establishing surfaces of different susceptibility to lightning strikes on aircraft, the Federal Aviation Administration has defined lightning strike zones (4). These definitions were later refined by Society of Automotive Engineers Committee AE4L (5) to accommodate the different lightning environments at forward and trailing-edge regions of the airplane. These definitions, however, do not establish the actual locations of the various zones on a particular airplane. At present this is accomplished by comparing new designs with actual experience (when available) of similar-shaped airplanes, or by tests in which scale models are subjected to simulated lightning strikes. Uncertainties still exist, and one purpose of the Storm Hazards Program is to clarify some of the more questionable aspects of establishing lightning strike zones. The purpose of this paper is to summarize the results of the Storm Hazards lightning-attachment-point analysis and to present the flight conditions associated with the direct lightning strikes experienced during 1980-1982.

TEST EQUIPMENT AND PROCEDURES

The fifteen airborne experiments on the F-106B in 1980-1982 are described in (6-10). Table 1 summarizes the experiments performed, and the locations of the data systems are shown in Fig. 1.

_____
[*]Numbers in parentheses designate References at end of paper.

TEST EQUIPMENT

F-106B Research Airplane - A thoroughly instrumented F-106B "Delta Dart" airplane (Fig. 1) is used to make thunderstorm penetrations in the Storm Hazards Program. The two-seat cockpit and large internal weapons bay for carrying the research instrumentation systems make it well suited for thunderstorm research. Details on the F-106B airplane and the criteria used in choosing the airplane for this mission can be found in (2 and 3).

An extensive "lightning hardening" program has been carried out on the airplane and the onboard data systems (2 and 11). Prior to each thunderstorm season, the lightning hardening procedures were verified by ground tests (11) in which simulated lightning currents and voltages of greater-than-average intensity were conducted through the airplane with the airplane manned and all systems operating. In addition, all systems were monitored during ground tests in which simulated lightning waveforms were injected into the airplane for calibration of the direct-strike lightning sensors (12). Finally, the paint has been stripped from the top and bottom wing surfaces of the integral wing fuel tanks to reduce lightning dwell times in those areas.

Airborne Data Systems - The F-106B airplane is equipped with a number of data systems to measure the electromagnetic and environmental characteristics of thunderstorms during penetrations. The direct-strike lightning instrumentation system (DLite) (6 and 13) documents the electromagnetic characteristics of direct lightning strikes and nearby lightning flashes at normal airplane flight altitudes. It consists of twelve electromagnetic sensors mounted on the surface of the airplane, a shielded recording system in the weapons bay, and a control panel in the aft cockpit. The DLite recording system consists of two digital, expanded-memory, wide-band, transient-waveform recorders coupled to a 14-track analog tape recorder, and one wide-band, 2-channel, analog tape recorder. In addition, outputs of a current transformer attached to the nose boom and a shunt attached to the Kevlar/epoxy vertical fin cap were recorded on a Boeing Data Logger system mounted in the weapons bay (6 and 7).

The lateral and vertical components of the ambient electric field were measured by a system of three field mills (6). The field mill data were recorded on the 14-track analog tape recorder in the shielded enclosure and were also telemetered in real-time to the mission control room at NASA Langley to help provide real-time guidance to areas of lightning activity.

The lightning attachments to the airplane were filmed by two 16mm color movie cameras (6) running at a frame rate of 14 frames per second (the shutter is open 1/28 sec for each frame). One movie camera was installed forward of the windshield, focused on the nose boom. The second camera was mounted on the left side of the fuselage, looking aft. The field of view of this camera included the left wingtip and vertical tail as shown in Fig. 2.

Environmental parameters and flight conditions were measured by the Aircraft Instrumentation System (AIS) and the Inertial Navigation System (INS). Among the parameters measured by the AIS were the following: static pressure, dynamic pressure, angles of attack and sideslip, total air temperature, and normal acceleration. Interphone conversations and VHF radio transmissions to the mission controllers were recorded on a separate tape track. The separate AIS 14-track analog tape recorder also recorded the outputs of the INS, which included latitude, longitude, and heading. Time was provided to the DLite and AIS tape recorders by a battery-operated time-code generator in the AIS. The descriptions of the lightning flashes by the crew and contacts with the mission controllers were recorded on an onboard voice recorder which ran continually throughout the flight.

Ground-Based Radars - For the research flights in Oklahoma (1980 and 1981), the NSSL Doppler radar at Norman (14) was used to measure the precipitation reflectivity data. Additionally, an incoherent 10-cm-wavelength surveillance radar (14) was used to provide air traffic control guidance to the airplane.

For those flights which occurred in Virginia, four separate radars were used. First, precipitation reflectivity was measured with the NASA Wallops Space Range Radar (SPANDAR). Second, an FPS-16 tracking radar at NASA Wallops was used to track the C-band transponder mounted on the airplane in order to provide the SPANDAR crew with real-time information on the location of the airplane. On those occasions when the INS was not used onboard the airplane, the FPS-16 radar data were used to produce plots of the airplane ground track. Third, the precipitation data from the National Weather Service WSR-57 radar at Patuxent River, Md., were transmitted in real time to a color video display in the SPANDAR control room to assist the SPANDAR crew in providing real-time airplane-penetration guidance. Finally, a 70-cm-wavelength UHF radar at NASA Wallops was used to detect lightning channels in order to provide real-time lightning location information to the airplane (15). The seven ground-based experiments associated with the Storm Hazards Program in 1980-1982 are summarized in Table 2 and described in (15-18).

TEST PROCEDURES

Flight Procedures - The thunderstorm penetration procedures, given in detail in (11) are outlined briefly in this section. Two guidelines adopted from previous thunderstorm programs were that all flights be limited to daylight hours to minimize the threat of flash blindness, and that penetrations not be made through storm areas having precipitation reflectivity contours over 50 dBZ to minimize the chances of encountering hail. In 1980 and 1981, the freezing level was chosen as the altitude for penetration whenever possible. In 1982, however, higher altitudes were chosen, with the

specific altitude determined from the indications of lightning from the NASA Wallops UHF radar. Generally, the pilot set power and indicated airspeed for 300 knots prior to storm entry and maintained a constant pitch attitude during the penetration, accepting the resulting altitude and speed excursions. This procedure was the best technique for flight control and provided a more accurate measurement of turbulence. The flight observer operated all the data systems from the rear cockpit, allowing the pilot to give his undivided attention to flying the airplane. At any time during the mission, the pilot could elect to terminate a penetration by using a predetermined escape vector.

Definition of Penetrations, Direct Strikes, and Nearby Flashes - A thunderstorm penetration is defined as a data run through a thunderstorm, usually at a constant nominal altitude and heading, with the time duration computed from cloud entry to cloud exit. In 1982, the penetration data have been supplemented with two cloud passes, which are data runs through light, indistinct clouds with no discernible precipitation and turbulence and indefinite cloud entry and cloud exit conditions. The two cloud passes were included because three lightning events occurred during them.

The lightning events experienced by the F-106B airplane are categorized as direct strikes or nearby flashes. A direct lightning strike in the Storm Hazards Program is defined as a lightning flash which has been confirmed to have hit the airplane based on lightning attachment points, cockpit voice comments, lightning movies, or direct strike waveforms on the onboard lightning data systems. A nearby flash is defined as a lightning flash which has triggered a sensor in the DLite system without attaching to the F-106B airplane.

Following each flight, a determination was made of the number of direct lightning strikes and nearby flashes which had occurred. The procedure was as follows:

1. Conduct an external inspection of the airplane to check for lightning attachment points.

2. Determine, from the voice transcripts, the times of direct strikes and possible nearby flashes called by the flight crew.

3. Review movie camera films to determine the times of direct strikes seen by the two onboard cameras.

4. Review Data Logger data for times of valid direct-strike waveforms from the nose boom current transformer and vertical fin cap shunt (used with Kevlar/epoxy fin cap only).

5. Review DLite data for times of valid waveforms from the sensors.

6. Compile a list of unique direct strike times from sources 1-5 above.

When no other data were available, the number of strikes was estimated from the geometry of the strike patterns. This was done on several occasions in 1980 and 1981.

It is possible for many of the DLite sensors to trigger on lightning electromagnetic pulse from a nearby flash as well as from a direct attachment. Therefore, uncorroborated triggers in the DLite system (except from the current sensors which could only trigger from a direct strike) were counted as nearby flashes, not as direct strikes. A crew call of a nearby flash without a corresponding DLite sensor trigger was not counted.

Determination of Lightning Attachment Points - Following each flight in which there were direct lightning strikes, the lightning attachment points were located by careful inspection of the airplane surface. The procedure was as follows:

1. Inspect each airplane extremity for evidence of lightning attachment. The evidence was usually manifested by spots of molten and resolidified metal ranging in diameter from 0.01 to 1.00 cm (0.004 to 0.4 in.),* usually surrounded by a region of discolored paint.

2. Closely inspect all surfaces that lie aft of the nose boom for additional lightning attachment points that indicate the swept-flash path(s) taken following initial attachments to the nose beam. This often required the use of a 4 power magnifying glass because the diameters of some of the swept-flash attachment points were very small and the points were hard to distinguish from other blemishes on the airplane surface.

3. Record the location of each attachment point and plot the points on isometric drawings of the airplane.

4. Calculate the dwell time t that elapsed between attachment points, assuming the airplane was travelling at a constant velocity V of 182.9 m/sec (600 ft/sec), with the expression $t = d/V$, where d is the longitudinal distance between successive attachment points.

5. Review and correlate findings with the pilot's and observer's observations. This step was particularly important in separating the attachment points produced by each strike after a flight in which more than one strike was received.

6. Postulate, based on the attachment points, films from the two onboard movie cameras, sensor triggers, and flight crew observations, the probable direction from which the strike initially approached the airplane, the initial and final attachment points, the swept-flash path(s), and the point(s) and direction(s) from which the flash exited the airplane.

Reduction of Airplane-Measured Flight Parameters - Static temperature and pressure altitude were computed from parameters measured and recorded by the AIS. The values of pressure altitude were computed from the static pressure values and corrected for position error (19).

---

*Dimensional quantities are presented in both the International System of Units (SI) and U.S. Customary Units. Measurements and calculations were made in U.S. Customary Units.

The ambient temperature was determined from the total temperature measurement (19). The relative intensities of turbulence and precipitation at the times of the lightning strikes and nearby flashes were extracted from the cockpit voice transcripts.

DISCUSSION OF RESULTS

FLIGHT CONDITIONS - The direct strikes and nearby flashes for the Storm Hazards '80-'82 Programs are summarized by year in Table 3, in which the number of events having corresponding waveforms on the DLite and Data Logger systems, camera views, crew calls, and altitude and temperature data are indicated. As shown in Table 3, 10 direct strikes and 6 nearby flashes occurred in 1980; 10 direct strikes and 22 nearby flashes occurred in 1981; and 156 direct strikes and 26 nearby flashes occurred in 1982. The numbers of thunderstorm penetrations are summarized in Table 3(c).

Prior to beginning thunderstorm penetrations with the F-106B airplane in 1980, published aircraft strike statistics such as those shown in Fig. 3 (from (20)) were used to estimate the best penetration altitudes to use for maximizing direct-strike lightning data. The data in Fig. 3 show the altitudes at which aircraft were struck during routine operations, as compared with a typical cumulonimbus cloud. Based upon those data, most penetrations in 1980 and 1981 were made at altitudes corresponding to ambient temperatures between $\pm 10^{\circ}C$.

The penetrations, strikes, and nearby flashes experienced during 1980-1982 are plotted as a function of altitude in 0.6-km (2000-ft) altitude bands in Fig. 4, and as a function of ambient temperature in $5^{\circ}C$ temperature bands in Fig. 5. A total of 419 penetrations and two cloud passes were made at altitudes ranging from 2.4 km to 11 km (8000 to 36,000 ft), with a mean penetration altitude of 6.5 km (21,400 ft). A mean penetration temperature was available for 322 penetrations (see Table 3(c)), with mean penetration temperatures ranging from $10^{\circ}C$ to $-50^{\circ}C$, with an overall mean value of $-18^{\circ}C$ (see Fig. 5). The 419 penetrations and two cloud passes resulted in a total of 1208 minutes of thunderstorm duration (the 322 penetrations with mean ambient temperature values produced 980 minutes of duration). The distributions of penetration time with altitude and temperature (Figs. 4 and 5) are very similar to the corresponding penetration distributions.

Direct strikes were found at altitudes from 4.3 km to 11.6 km (14,000 ft to 38,000 ft) with a mean value of 8.7 km (28,400 ft) (Fig. 4); the corresponding strike temperatures ranged from $5^{\circ}C$ to $-50^{\circ}C$ with a mean value of $-32^{\circ}C$. Although the peak lightning strike activity was expected to occur at or near the freezing level ($0^{\circ}C$) (20), most of the strikes occurred at altitudes above 7.6 km (25,000 ft) and at ambient temperatures colder than $-25^{\circ}C$. Although 194 minutes of penetration time was spent at

ambient temperatures between $\pm 10^{\circ}C$, only 7 of the 176 strikes occurred at these ambient temperatures. In 1980 and 1981, when the majority of the penetration time was spent at ambient temperatures between $\pm 10^{\circ}C$, only 5 of the 20 strikes occurred at these temperatures. In fact, the peak strike rates per penetration and per minute of duration occurred not at the freezing level, but between the altitudes of 10.4 km and 11 km (34,000 ft and 36,000 ft) (Fig. 4), or between $-40^{\circ}C$ and $-45^{\circ}C$ (Fig. 5). Whereas the highest lightning strike rates were related to penetrations at higher altitudes and colder ambient temperatures, the nearby flashes occurred at altitudes from 4.3 km to 11 km (14,000 ft to 36,000 ft) (Fig. 4), corresponding to ambient temperatures from $0^{\circ}C$ to $-50^{\circ}C$ (Fig. 5), with no apparent pattern of occurrence.

In 1982, there were 156 lightning strikes compared to only 10 strikes per year during 1980 and 1981. This order of magnitude increase in strikes was accomplished without an equal increase in the number of penetrations that were made or in the duration of time spent in the storms. Specifically, 239 penetrations and two cloud passes were made in 1982 in comparison to 180 penetrations in 1980-81 (see Table 3(c)); and 749 minutes were spent in thunderstorms in 1982, while 459 minutes were accumulated in 1980-81. The success of the 1982 program was produced by concentrating on higher altitude penetrations in 1982 than before, and by using the NASA Wallops UHF radar to direct the F-106B airplane to areas of high lightning flash rates in 1982 (15).

The lightning strike statistics gathered in the Storm Hazards '80-'82 Programs are in general agreement with the results of several other research programs, including those of the U.S. Air Force Rough Rider Program (21). In this earlier flight program, the maximum lightning activity in thunderstorms was found to occur near 9.2 km (30,000 ft) altitude at about $-40^{\circ}C$. In addition, ground-based instrumentation systems (22 and 23) have detected two layers of lightning activity in active thunderstorms. For the Florida thunderstorm studied in (22), the temperature of the lower boundary of the higher altitude layer of activity occurred at $-39^{\circ}C$. This higher altitude layer of activity is described in (23) as a new class of small intercloud lightning activity which forms a canopy over the main updraft region of a storm, producing a near continuum of lightning activity centered at 12 to 13 km (39,370 to 42,650 ft) height. Although there are some differences between the altitudes of peak lightning activity found in (23) and by the F-106B airplane, the differences may be due to the difference in the height of the cloud tops of the storms sampled, with tops in Oklahoma generally exceeding those of storms in Virginia. Finally, lightning echoes have been detected by the NASA Wallops UHF radar at the higher altitudes flown by the F-106B airplane in 1982 (15 and 24). Therefore, it seems likely that many of the Storm Hazards

26-4

'82 strikes were taken during flights through the upper lightning activity center of thunderstorms.

The lightning strike statistics shown in this paper differ significantly from the published strike data for commercial aircraft, such as in (20) for several reasons. First, each set of data was accumulated from different meteorological and operational conditions. The NASA data presented herein were taken from intentional penetrations through active thunderstorms, while the operational data include lightning events which occurred in a variety of storm conditions. In addition, the altitudes at which commercial aircraft penetrate thunderstorms were found in (21) to be related to three factors: avoidance of obvious thunderstorm areas; the duration of lower altitude holding patterns in bad terminal weather; and frequency of instrument flight rules (IFR) altitude assignments. In other words, commercial aircraft will normally deviate from course when enroute to avoid thunderstorms which have tops that reach to cruise altitudes, and only penetrate when required to do so in the terminal area, where typical assigned altitudes are near the freezing level. Therefore, the lightning event distribution with temperature found in the Storm Hazards Program is the result of the higher percentage of time spent by the F-106B research airplane at altitudes with high rates of lightning activity above the freezing level, compared with the low percentage of time spent in storms at these altitudes by commercial aircraft in routine operations.

The Storm Hazards data contain several implications for aircraft operations in and around thunderstorms. First, the use of lightning strike statistics, such as those in Fig. 3, to avoid lightning strikes can lead to the opposite effect if the data are not fully understood. Published strike data have been used to prepare pilot briefings that indicate that aircraft should fly at altitudes where the temperature is colder than -10°C in order to avoid lightning strikes. Two examples of such operations are given in (2), in which strikes to three U.S. Air Force F-106A airplanes on routine missions are described. In one case, a pair of airplanes was at an altitude of 7.6 km (25,000 ft) and 7.9 km (26,000 ft) when the airplanes were struck in non-thunderstorm clouds. In the other case, a single F-106A airplane received multiple strikes while penetrating a line of thunderstorms at an altitude of 13.7 km (45,000 ft). In yet another (unpublished) case, a U.S. Air Force F-15A airplane penetrated a thunderstorm in the same general area, altitude, and time as the NASA F-106B airplane. The NASA airplane took six intentional direct strikes (strikes 151-156 in 1982) without incident, while the F-15A sustained one direct strike which caused considerable damage to the airplane. None of the pilots of these USAF airplanes were anticipating a direct lightning strike since they were using accepted lightning avoidance techniques.

A second common misconception among pilots has been that lightning, turbulence, and precipitation occur at the same place and time in thunderstorms. The Storm Hazards data contradict this belief. The number of direct strikes to the F-106B airplane are plotted as a function of the relative turbulence and precipitation intensities, as called by the flight crew, in Fig. 6. In the majority of cases, the direct strikes occurred in areas of the thunderstorms in which the crew characterized the turbulence and precipitation as negligible to light. However, a few strikes occurred where the conditions were described as being heavy. The nearby flash data (not shown) are nearly identical to those shown in Fig. 6. In addition, three lightning events did not occur during penetrations. Two nearby flashes and a direct strike (nearby flashes 2 and 16 and strike 56 of 1982) occurred in what were called "cloud passes," in which the only notable feature was light clouds. In fact, three strikes occurred when the aircraft was at the edge of the clouds, or actually in the clear. Specifically, one direct lightning strike (strike 5 in 1980) occurred only 2 seconds after cloud entry, another (strike 77 in 1982) occurred only when the forward one third of the fuselage was in the cloud, and yet another (strike 3 in 1981) occurred while the airplane was in clear air underneath an overhanging cloud.

For safety reasons, the F-106B airplane was not flown into the reflectivity cores of storms where the precipitation reflectivity values exceeded 50 dBZ. Therefore, no comments can be made on the probability of direct lightning strikes occurring in such areas. However, the data show that, for the thunderstorm areas studied in the Storm Hazards Program to date, lightning strikes may be encountered at nearly all temperatures and altitudes by aircraft in the vicinity of thunderstorms, usually where the relative turbulence and precipitation intensities are characterized as being negligible to light. Therefore, these data show that the presence and location of lightning do not necessarily indicate the presence and location of hazardous precipitation and turbulence.

It is felt that most, if not all, of the direct strikes which have occurred to the F-106B airplane were intercloud strikes or upward branches of cloud to ground flashes, rather than the core channel of cloud to ground flashes, which conveys the entire flash charge to the ground. If this is the case, the peak amplitudes of current and charge should be relatively low in comparison to the published full-threat values (4 and 5) which are based on ground-based measurements of currents in the cloud to ground channel, and this has proven to be the case to date (6). However, some current rates of rise have proven to be very high (6), which implies a potential threat to aircraft electrical and avionics systems from lightning-induced voltages.

Finally, there is strong evidence that a number of the direct strikes to the F-106B

airplane were triggered by the airplane (15), even when the airplane was in areas with high natural lightning flash rates. If this is the case, lightning detection devices may not be capable of warning an aircraft flight crew of a lightning threat. This fact, coupled with the poor correlation of lightning occurrence with hazardous precipitation and turbulence shown in the Storm Hazards Program, implies that lightning warning/detection devices may not be sufficient as the sole cockpit device to guide aircraft flight crews around hazardous thunderstorm areas.

LIGHTNING ATTACHMENT PATTERNS - In the preceding section of this paper, the occurrence of aircraft lightning strikes with respect to the general features of the thunderstorm has been discussed. In this section, the discussion focuses on the locations of the lightning attachment points on the exterior of the F-106B airplane. Four general patterns have been found in the lightning attachment patterns: swept flashes along the entire length of the fuselage; swept flashes which sweep back across the midspan areas of the wing; strikes in which the initial entry and exit points occur at the same extremity; and strikes in which the entry and exit points are confined to the aft extremities. With any of these patterns, it is possible for the swept flash channel to rejoin behind the airplane after the airplane has flown through the channel as shown by the aft-facing lightning movie camera, and described below.

The first lightning attachment point pattern is the typical nose-to-tail swept flash seen on many aircraft. The strike used as an example of this pattern (strike 16 of 1982) also is an example of a swept flash which rejoins behind the airplane after the airplane has flown through the channel. At the time of this strike, the crew called a strike down the right side of the fuselage. The lightning attachment points for strike 16 are shown plotted on an isometric view of the airplane in Fig. 7. The initial entry occurred at the nose boom with the initial exit occurring at the left wing tip. As the airplane flew through the channel, the entry point swept aft along the right side of the fuselage to the vertical tail and the exit channel trailed aft from the wing tip. The general orientation of the channel shows the strike attaching to the airplane downward from the right, and exiting downward to the left off the wing tip. Four of the ten successive frames taken by the aft-facing movie camera are shown in Fig. 8. To aid in the interpretation of these data, it should be noted that the airplane travels approximately 15 m (50 ft) between the center time of each frame, and also travels 7.5 m (25 ft) during the time the shutter is open for each frame. In Fig. 8(a), the entry point has already swept back along the entire length of the fuselage to the vertical tail, with the exit point trailing from the left wing tip. The view shown in Fig. 8(a) remains essentially unchanged for the first four frames

(frame rate of 14 frames/sec). In the fifth frame, Fig. 8(b), the airplane apparently has flown out of the channel, as two pieces of the channel can be seen faintly behind the airplane. The sixth frame is blank, but in the seventh frame, Fig. 8(c), the lightning channel can be seen clearly behind the airplane. There is a displacement of the channel which was caused, apparently, by the airplane movement while the airplane was still a part of the channel. Frames 8 and 9 are blank. Finally, the tenth frame, Fig. 8(d), shows a burst in the vicinity of the afterburner which was counted as a restrike, although it may have been an entirely new strike. This film sequence shows that it is possible for an airplane to fly out of a live lightning channel. In this case, the airplane was out of the channel in about 0.3 sec (4 frames).

The second pattern, in which swept flashes sweep back across the midspan areas of the wing, is illustrated in Fig. 9. In this figure lightning attachment points for strike 2 of 1980 are shown plotted on an isometric drawing of the F-106B airplane. This strike is also an example of the third pattern, in which the initial entry and exit points occur at the same extremity (nose boom in this case) without involving any other extremity until the flash sweeps aft. The lightning strike scenario which follows was deduced from the geometry of the lightning attachment points and the pilot's comments at the time of the strike. (The lightning movie cameras were not installed during 1980.) The initial entry and exit points are presumed to have occurred on the nose boom. As the airplane moved forward, the entry point swept down the right side of the fuselage and beneath the right wing across the midspan area. The exit point, on the other hand, swept back to the left wing, where the flash branched. One branch swept down the leading edge to the wing tip and the other branch swept across the top of the wing in the midspan area. The general orientation of the channel gave an entry from below and to the right of the airplane, with an exit off the extremities upwards to the left. The exit points were presumed to be on the left wing because more severe damage was found on the left elevon and wing tip than was found on the trailing edge of the right elevon. A more detailed description of this strike can be found in (3). This is one of several strikes which have occurred in which the flash swept back across the midspan area of the wing with no upstream initial attachment point such as an engine nacelle. The flash would normally be expected to sweep back along the wing leading edge to the wing tip (see (25)).

The fourth pattern of lightning attachment points that has been found consists of those strikes in which the entry and exit points are confined to the aft extremities of the airplane. A photograph of such a strike is shown in Fig. 10, taken from the aft-facing movie camera on the left side of the airplane. This strike

(number 15 of 1982) was detected only by the movie camera, indicating that this strike was confined to the vertical tail and right wing tip, as shown in the lightning attachment point diagram, Fig. 11. The exit point is presumed to have occurred at the right wing tip because of the physical damage found there. (The right wing tip is not in the field of view of the camera.) This strike is one of several filmed in 1982 in which the attachment points were confined to the vertical tail, wing tips, and afterburner. In fact, evidence of lightning attachment points have been found up to 36 cm (14 in.) inside the afterburner nozzle.

The lightning attachment point data have provided further insights into the validity of the assumptions used in establishing lightning strike zones on aircraft by showing the manner in which an airplane interacts with a lightning strike channel, especially the manner in which flashes sweep aft from initial lightning attachment points. These data confirm that initial entry and exit points frequently occur at airplane extremities, in this case the nose boom, the wing tips, the vertical-fin cap, and the afterburner. Swept-flash attachment points were observed along the full length of the fuselage, as is common in other airplanes of this general size, following initial strikes at the nose. Unexpectedly, several flashes swept aft across the midspan surfaces of the delta wing. Swept-stroke attachments across unswept wings on airplanes without upstream attachment points such as engine nacelles or drop tanks are extremely rare (25), and only a few midspan strikes to other delta-wing airplanes have been reported.

The swept-flash attachment paths and burn marks found in this program indicate that the midspan areas of swept-wing airplanes may be more susceptible to lightning attachment than is currently believed. If so, careful attention to lightning protection may be required for the external wing surfaces of integral wing fuel tanks in swept-wing airplanes now being designed, especially when composite materials and adhesive bonding will be used.

In addition, the lightning attachment points found inside the afterburner indicate that instrumentation installed in the exhaust sections of engines cannot be presumed to be immune from lightning damage because of their location. Rather, lightning hardening procedures may be required for such installations.

SUMMARY OF RESULTS

During the NASA Langley Research Center Storm Hazards Program, 419 thunderstorm penetrations were made from 1980-1982 with an F-106B airplane in order to record direct lightning strike data and the associated flight conditions. This study produced the following results:

1. The mean strike altitude was 8.7 km (28,400 ft); the mean strike temperature was $-32^\circ C$. The peak strike rate occurred at ambient temperatures between $-40^\circ C$ and $-45^\circ C$, whereas most previously reported strikes have occurred at or near the freezing level ($0^\circ C$).

2. For the thunderstorm areas studied in the Storm Hazards Program to date, lightning strikes have been encountered at nearly all temperatures and altitudes in the vicinity of the storms, usually where the relative turbulence and precipitation intensities are characterized as being negligible to light. Therefore, the presence and location of lightning do not necessarily indicate the presence and location of hazardous precipitation and turbulence.

3. The data confirm that initial entry and exit points of strikes frequently occur at airplane extremities, in this case the nose boom, the wing tips, the vertical-fin cap, and the afterburner. Swept-flash attachment points were observed along the full length of the fuselage, as is common in other airplanes of this general size, following initial strikes to the nose. Unexpectedly, several of the flashes swept aft across the midspan surface of the delta wing. Evidence of lightning attachment points were found up to 36 cm (14 in.) inside the afterburner.

REFERENCES

1. Bruce D. Fisher and Norman L. Crabill, "Summary of Flight Tests of an Airborne Lightning Locator System and Comparison With Ground-Based Measurements of Precipitation and Turbulence." 1980 Aircraft Safety and Operating Problems, Joseph W. Stickle, compiler, NASA CP-2170, Part 1, 1981, pp. 251-277.

2. Bruce D. Fisher, Gerald L. Keyser, Jr., Perry L. Deal, Mitchel E. Thomas, and Felix L. Pitts, "Storm Hazards '79 - F-106B Operations Summary." NASA TM-81779, 1980.

3. Bruce D. Fisher, Gerald L. Keyser, Jr., and Perry L. Deal, "Lightning Attachment Patterns and Flight Conditions for Storm Hazards '80." NASA TP-2087, Dec. 1982.

4. "Protection of Aircraft Fuel Systems Against Lightning." AC No. 20-53, FAA, Oct. 6, 1967.

5. SAE Committee AE4L, "Lightning Test Waveforms and Techniques for Aerospace Vehicles and Hardware." Soc. Automot. Eng., Inc., June 20, 1978.

6. F. L. Pitts, M. E. Thomas, K. P. Zaepfel, G. B. Finelli, and L. D. Lee, "Statistical Analysis and Interpretation of Direct Strike Lightning Data." NASA TM-84653, 1983.

7. Greg J. von Bokern, "In-Flight Lightning Data Measurement System for Fleet Application-Flight Test Results." Proc., National Aero. and Elec. Conf., Dayton, OH, Vol. 1, May 1982, pp. 25-31.

8. William E. Howell and Bruce D. Fisher, "Observations of Severe In-Flight Environments on Kevlar/Epoxy and Graphite/Epoxy Composite Structural Components." SAE Paper No. 830767, Apr. 1983.

9. G. K. Parks, B. H. Mauk, R. Spiger, and J. Chin, "X-Ray Enhancements Detected During Thunderstorm and Lightning Activities." Geophys. Res. Lett., vol. 8, no. 11, Nov. 1981, pp. 1176-1179.

10. Joel S. Levine and Edwin F. Shaw, Jr., "In-Situ Aircraft Measurements of Enhanced Levels of Nitrous Oxide Associated With Thunderstorm Lightning." Nature, vol. 303, pp. 312-314.

11. Perry L. Deal, Gerald L. Keyser, Bruce D. Fisher, and Norman L. Crabill, "Thunderstorm Hazards Flight Research - Program Overview." AIAA-81-2412, Nov. 1981.

12. B. D. Heady and Keith S. Zeisel, "NASA F-106B Lightning Tests." NASA CR-166057, Jan. 1983.

13. M. E. Thomas, "Direct Strike Lightning Measurement System." AIAA-81-2513, Nov. 1981.

14. R. J. Doviak, ed., "1980 Spring Program Summary." NOAA Tech. Mem. ERL NSSL-91, Apr. 1981. (Available from NTIS as PB81-234940.)

15. Vladislav Mazur, Bruce D. Fisher, and John C. Gerlach, "Conditions Conducive to Lightning Striking an Airplane in a Thunderstorm." Proc., Int'l. Aero. & Ground Conf. on Lightning & Static Elec., Ft. Worth, TX, June 1983.

16. D. S. Zrnić and J. T. Lee, "Pulsed Doppler Radar Detects Weather Hazards to Aviation." AIAA-81-0235, 1981.

17. D. M. LeVine, "Lightning Electric Field Measurements Which Correlate With Strikes to the NASA F-106B Aircraft (July 22, 1980)." NASA TM-82142, 1981.

18. Robert E. Carr and John C. Gerlach, "Wallops Severe Storms Measurement Capability." Preprint Vol. - Fifth Symp. on Met. Obs. and Instr., Toronto, Canada, Apr. 1983. Amer. Met. Soc. & Canadian Met. & Oceanographic Soc.

19. William Gracey, "Measurement of Aircraft Speed and Altitude." NASA RP-1046, May 1980.

20. Franklin A. Fisher and J. Anderson Plumer, "Lightning Protection of Aircraft." NASA RP-1008, 1977.

21. Donald R. Fitzgerald, "USAF Flight Lightning Research." Lightning and Static Electricity Conference, 3-5 December 1968 - Part II. Conference Papers, AFAL-TR-68-290, May 1969, pp. 123-124. (Available from DTIC as AD 693 135.)

22. Donald R. MacGorman, A. A. Few, and T. L. Teer, "Layered Lightning Activity." Jour. Geophys. Res., vol. 86, no. C10, Oct. 1981, pp. 9900-9910.

23. William L. Taylor, "Lightning Activity Characteristics From VHF Space-Time Mapping." Prog. & Abstracts, Joint URSI/IEEE/NEMP National Radio Science Meeting, Univ. of New Mexico, May 1982, p. 130.

24. Vladislav Mazur, John C. Gerlach, and W. David Rust, "Lightning Flash Density Versus Altitude and Storm Structure From Observations With UHF- and S-Band Radars." Proc., Int'l. Aero. & Ground Conf. on Lightning & Static Elec., Ft. Worth, TX, June 1983.

25. J. Anderson Plumer, "Further Thoughts on Location of Lightning Strike Zones on Aircraft." Lightning Technology, Suppl. NASA CP-2128, FAA-RD-80-30, 1981, pp. 81-98.

(a) Location of electromagnetic sensors

(b) Location of additional research sensors and equipment

Fig. 1 - NASA Langley Research Center Storm Hazards '82 research vehicle

(a) Plan view of F-106B airplane showing field of view coverage

(b) Sketch of aft camera view

Fig. 2 - Field of view of aft lightning movie camera

Fig. 3 - Aircraft lightning strike incidents as a function of altitude. From (20)

Fig. 4 - Thunderstorm penetrations and lightning statistics as a function of pressure altitude for Storm Hazards '80-'82
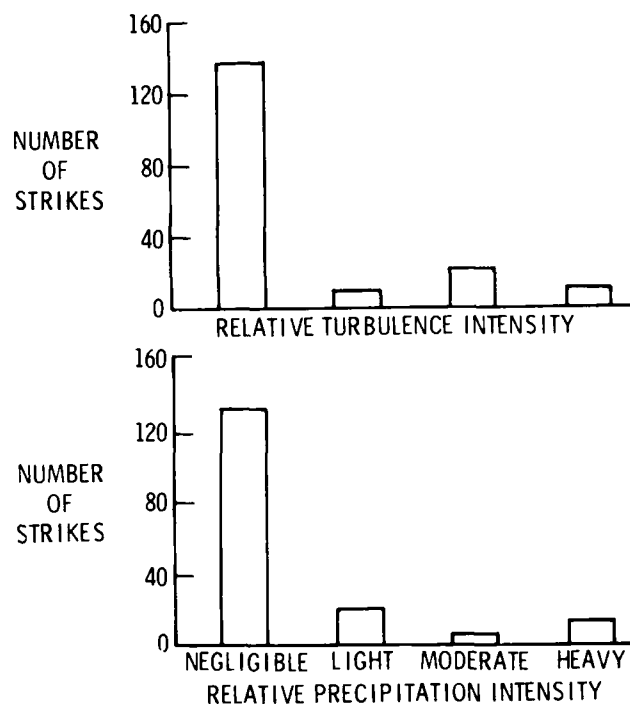
Fig. 6 - Relationship of lightning strikes to relative turbulence and precipitation intensities
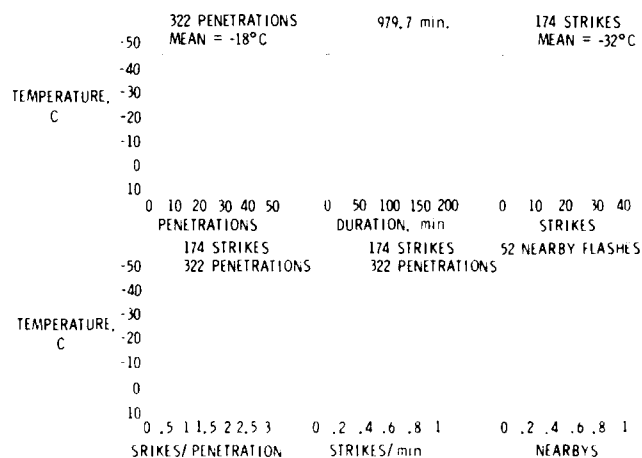
Fig. 5 - Thunderstorm penetrations and lightning statistics as a function of ambient temperature for Storm Hazards '80-'82
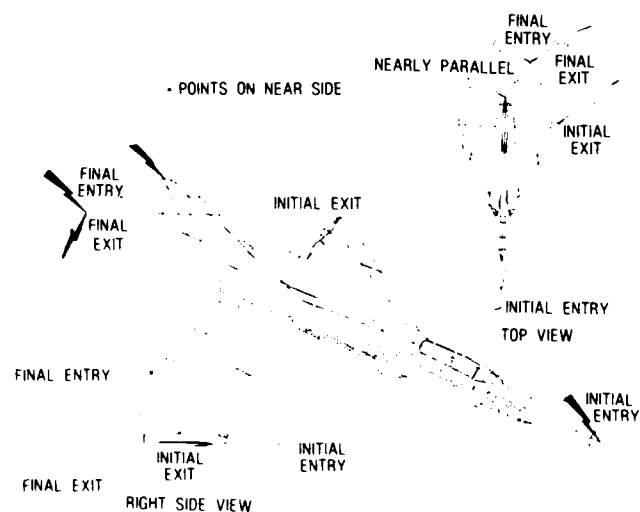
Fig. 7 - Lightning attachment points and strike scenario for strike 16 of 1982; flight 82-017; June 5, 1982; 18:39:46.8 GMT. (Points shown are a composite of the points·from strikes 4-17 in 1982)
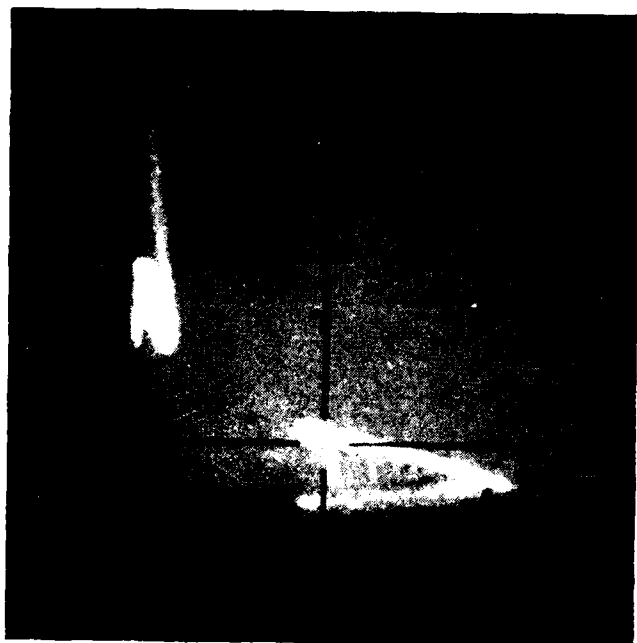
(a) Frame 1 of 10

(c) Frame 7 of 10

LIGHTNING CHANNEL
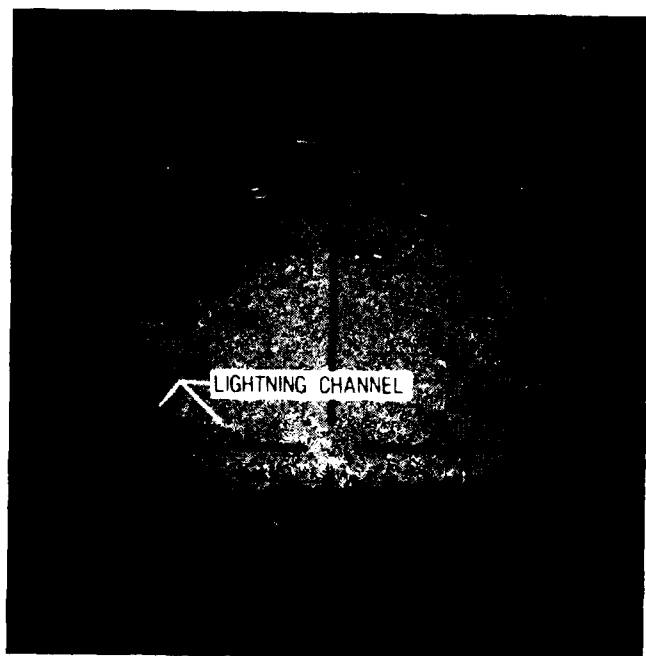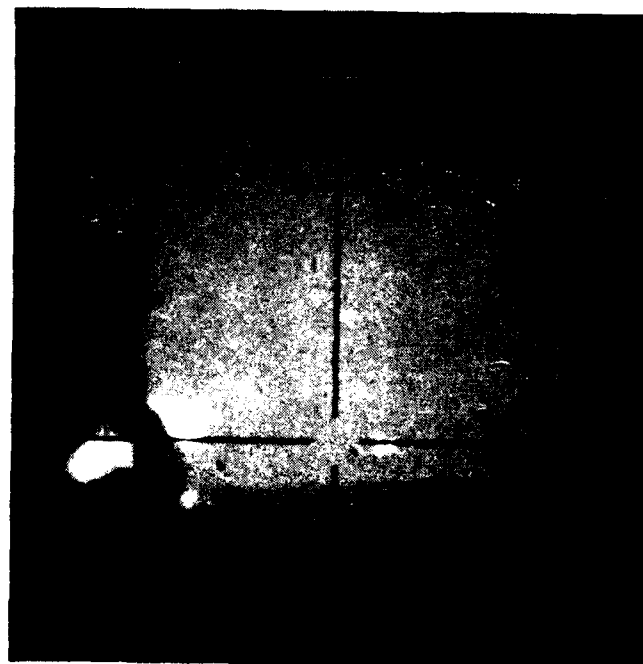
(d) Frame 10 of 10

Photograph of direct strike to vertical
stabilizer and tip of F-106B airplane for aft
swept lightning strike 2 of 1983 flight 83-037.

Fig. 9 - Lightning attachment points and strike scenario for strike 2 of 1980; flight 80-019; June 17, 1980; 22:28:36 GMT. From (3)
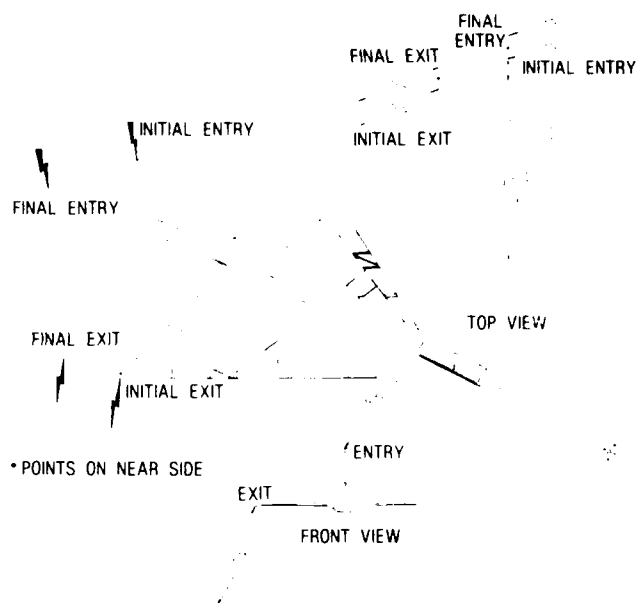
Fig. 11 - Lightning attachment points and strike scenario for strike 15 of 1982; flight 82-017; June 5, 1982; 18:35:27.8 GMT
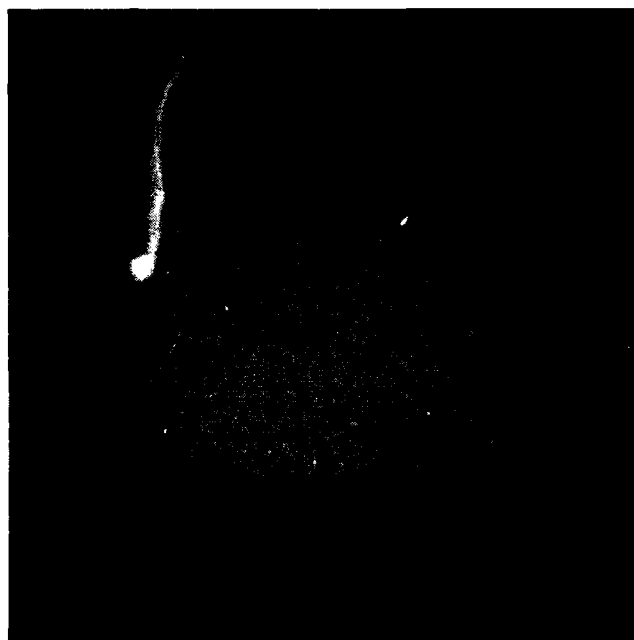
Fig. 10 - Photograph of direct strike to vertical tail of F-106B airplane from aft movie camera. Strike 15 of 1982; flight 82-017; June 5, 1982; 18:35:27.8 GMT. First of three frames

26-12

Table 1 - Summary of Fifteen Airborne Experiments in 1980-1982

Experiment	Data system (See Fig. 1)	Organization	Key ref.	Year
Direct-strike lightning measurements	DLite system	NASA	6	1980-1982
Direct-strike lightning measurements	Data Logger	Boeing Commercial Airplane Co.	6 & 7	1980-1982
Effect of lightning on composite materials	Fiberglass vertical-fin cap flame sprayed with aluminum Graphite/epoxy fin cap Kevlar-Thorstrand/epoxy fin cap with shunt output to Data Logger	NASA	8	1980-1982
Measurement of lightning optical waveforms	Lightning optical signature sensor	NOAA-NSSL	None	1980-1982
Measurement of lightning X-ray emissions	Lightning X-ray detector	Univ. of Washington	9	1980-1982
Measurement of trace gases from lightning- Atmospheric Chemistry Experiment	Atmospheric chemistry air sampler system	NASA	10	1980-1982
Lightning attachment point determination	F-106B	NASA	3	1980-1982
Turbulence and wind shear measurements	Aircraft Instrumentation System (AIS) Inertial Navigation System (INS)	NASA	None	1980-1982
Storm hazards correlation	Airborne lightning locator Airborne X-band radar Cockpit voice recorder Outside-air temperature gauge AIS INS	NASA	1	1980-1982
Measurement of thunderstorm electric fields	Field mills	NASA & AFGL	6	1981-1982
Photography of lightning attachments	Two - 16 mm movie cameras	NASA	6	1981-1982
Evaluation of passive lightning protection techniques	Four commercially available diverter strips	Lightning Technologies Inc.	None	1982
Evaluation of X-band weather radar for storm avoidance	Airborne X-band radar Airborne lightning locator Video recorder	NASA	None	1982
Qualitative assessment of character of water film on a radome	16 mm color movie camera in pod under left wing	NASA	None	1982
Determination of feasibility of detecting rain and ice with a simple indicator	Metal patch bonded to leading edge of vertical tail	NASA	None	1982

Table 2 - Summary of Seven Ground-Based Experiments in 1980-1982

Experiment	Data system	Organization	Key ref.	Year
Turbulence measurement with Doppler radar	1. NOAA-NSSL Doppler at Norman	NOAA-NSSL	16	1980–1981
	2. NASA Wallops SPANDAR	NASA Langley AFGL	None None	1982 1981–1982
Turbulence measurement with airborne Doppler radar	NASA Langley Doppler in NASA Wallops Skyvan airplane	NASA Langley	None	1981–1982
Measurement of fast and slow field changes from lightning	Fast and slow antennas installed at NASA Wallops	NASA Goddard	17	1980–1982
Measurement of locations of cloud to ground lightning	LLP system with sites at Hampton, VA; Wallops Island, VA; and Dahlgren, VA	NASA Langley NASA Wallops NASA Goddard SUNY-Albany	18	1982
Measurement of locations of lightning	LDAR system installed at NASA Wallops	NASA Wallops	18	1980–1982
Radar detection of lightning	NASA Wallops UHF radar	NASA Wallops Univ. of Oklahoma	15 & 24	1982
Passive radar detection of lightning	NASA Wallops telemetry antenna	AFGL	None	1982

Table 3 - Summary of Lightning Events and Penetrations and Associated Data

(a) Direct strikes

		Number of strikes with –					
Year	Totals	Recorded (DLite) waveforms	Recorded (Date Logger) waveforms	Camera views	Crew calls	Altitude data	Temperature data
1980	10	8	0	(a)	9	10	9
1981	10	0	1	0	9	10	10
1982	156	107	12	77	131	155	155
Totals	176	115	13	77	149	175	174

(b) Nearby flashes

1980	6	6	(b)	(a)	0	6	5
1981	22	22	(b)	0	2	22	22
1982	26	26	(b)	0	5	25	25
Totals	54	54	–	0	7	53	52

Notes: (a) Cameras not installed
(b) Data Logger sensors respond to direct strikes only

(c) Penetrations

		Number of penetrations with –	
Year	Totals	Altitude data	Temperature data
1980	69	69	46
1981	111	111	59
1982	241 (a)	241	217
Totals	421 (a)	421	322

Note: (a) Includes two cloud passes

ELECTROSTATIC CHARGING OCCURRING IN A VORTEX TRAILED

FROM THE TIP OF A LIFTING SURFACE

John W. Daugherty

Owens Corning Fiberglass
Granville, Ohio

Henry R. Velkoff

Department of Mechanical Engineering
The Ohio State University
Columbus, Ohio

ABSTRACT

A program was undertaken to investigate the vortex geometry, particle distribution and electric field distribution in a trailing vortex shed from an airfoil tip placed in a dust laden flow. A differential airfoil, positioned in a subsonic wind tunnel, generated the trailing vortex. Dust conditions, typical of a helicopter landing zone, were simulated by seeding the wind tunnel flow.

A vaned probe was used to measure the vortex geometry. A particle impact probe and a miniature field meter were used to map the particle distribution and electric field distribution across the trailing vortex. The particles in the trailing vortex created a quasi-steady, electric field with contours of constant electric field similar in appearance to the particle distribution contours.

INTRODUCTION

Static charge buildup on aircraft has always been a nuisance with regard to in-flight transmission and reception of radio messages. In the case of a helicopter, static charge buildup is a severe problem because it also presents a personnel and material handling hazard. An individual loading sling loads from a hovering helicopter becomes an integral part of the discharge path for the static charge on the

surface of the helicopter. The resultant discharge causes violent shocks to the unloading personnel; and in situations where the stores are flammable or explosive arcing from the helicopter to these stores can result infires and/or explosions.

Due to the hazard associated with electrostatic charging of helicopters, studies have been carried out to determine means of eliminating or dissipating of this build-up charge. Definitions of the precise charge-generating mechanisms are still nebulous. There have been attempts to credit the large deposits of static charge on helicopters to ions in the engine exhaust gases, to contact charging (triboelectrification) occurring when suspended particles in the air (water droplets, mist, dust, snow flakes, ice crystals) impact the surface of the helicopter, and to movement of the helicopter through varying electrostatic fields.

A fundamental aspect of the fluid field associated with the flight of a helicopter, which does not occur with fixed wing aircraft, is that the trailing vortices shed from each rotor tip flows downward in a helical path and bathes the surface of the helicopter. The trailing vortices shed from the tips of fixed wing aircraft, flow downstream and eventually become dissipated in the atmosphere.

The purpose of this research was to study the charge-generating and separation capabilities of a trailing vortex system and to determine if the trailing vortex system can create a stable electric field and if so to determine the parameters which control the strength of this field. To accomplish this, an experimental program was initiated to measure the strength, geometry, and charging capabilities of a trail-

ing vortex produced due to lift on an airfact placed in the test section of a low-turbulence, subsonic wind tunnel. To measure the rotational velocities present in the trailing vortex system, a non-rotating type vortex meter was designed and fabricated. A homogeneous mixture of particles was seeded in to the flow field in such a way as to simulate helicopter dusty landing zones. A miniature electric field mill was used to measure the electric field in seeded flow. An impact probe was developed which was used to map the particle density distribution throughout the flow field.

Experimental measurement of the trailing vortex geometry and strength was made throughout a plane normal to the flow direction at several locations downstream of the trailing edge of the airfoil. Measurements made with the electric field mill and density probe were made at the same locations as the vortex measurements. This permitted comparion of flow field geometry versus electrostatic charging.

BACKGROUND ON ELECTROSTATIC CHARGING OF HELICOPTERS

The hazards of static buildup on helicopters were mentioned briefly in the introduction. To illustrate the seriousness of this problem, one has only to refer to a publication by M.E. Rodgers (1) where it is reported that rescue operations were being jeopardized by the frequent electrical shocks received by winchmen and survivors. In some cases severe shocks had been experienced, and concern was expressed about the possible consequences to survivors in poor physical condition. Attempts to provide conductive paths through the winchmen's clothing proved largely ineffective, and trailing wires for earthing purposes represented greater hazards than the static buildup under certain conditions.

The various mechanisms leading to static electrification of helicopters in flight have been cited in References (1) and (2). These mechanisms are precipitation charging, spray electrification charging by induction, and charging from engine exhaust gases. In Reference (3), the main rotor blades of helicopters are said to be the chief contributors to the electrostatic charge on helicopters. The remainder of this paragraph will be devoted to discussing the details of these charging mechanisms.

1. Participation charging -- occurs when charge-carrying particles, such as dust, water droplets, snow flakes or ice crystals strike some part of the helicopters's surface. The charging currents depend upon the space charge density, interception surface area, and velocity of impact.

2. Spray Electrification -- occurs due to the shattering of the surface liquid film of water droplets on impact with some part of the helicopter surface. The shattering of the droplet causes the electrical double layer to break and results in separation of parts having dissimilar charges.

3. Charging by induction -- occurs due to the helicopter passing through regions of varying electric field. The absolute charge on the helicopter remains relatively unchanged while the potential field of the surrounding varies.

4. Charging from the engine-exhaust gases takes place due to the thermally generated ion pairs in the combustion chamber of jet engines. If ions of either polarity preferentially recombine, the remaining charges of like sign will yield a charging current.

EXPERIMENTAL PROGRAM

This section of this paper describes briefly the experimental equipment employed in the measurement of the vorticity contours, and the particle density contours. Most of the equipment discussed in this section was designed and fabricated specifically for the experiments which were performed during the course of this study. The equipment required to produce the seeded flow field and the trailing vortex system were a subsonic wind tunnel into which a differential airfoil was mounted, a particle feed system, and a filter system.

WIND TUNNEL AND DIFFERENTIAL AIRFOIL - A low turbulence subsonic wind tunnel was used to obtain a flow field for the experimental tests. The wind tunnel is 45 feet long (13.7 m) from inlet to the end of the turning box located at the tunnel exit and has the capability of developing test section velocities of 187 ft./sec. (57 m/sec). The test section is 10 feet long (3.05 m) with a 2 x 1.5 ft. (.61 x .46 m) cross section and is constructed of wood coated with non-pigmented varhish for dielectric properties. The trailing vortex system was generated in the wind tunnel through the use of a differential airfoil. A differential airfoil is made up of two airfoil sections of equal span length and chord. It was mounted tip-to-tip across the wind tunnel test section. The airfoil sections were positioned so that the angle-of-attack of one section was equal and opposite to that of the other. The airfoils were supported in the wind tunnel at their quarter-chord position by a steel support rod positioned 2 feet (.61 m) aft of the contraction section exit. The differential airfoil was used in this work because it produces a stable vortex whose position in the wind tunnel test section is independent of the flow velocity, the airfoil angle of attack, and the distance aft of the airfoils.

PARTICLE FEED SYSTEM - The wind tunnel flow field was seeded with particles which are blown against the wind tunnel inlet screen by a nozzle. The particles were stored in a spring-loaded hopper capable of holding 50 pounds (22.7 kg) of particles. The hopper was equipped with a dial indicator to indicate the flow rate of particles from the hopper. The particles were drawn from the hopper by a venturi located beneath the hopper. The spout of the hopper was connected to the throat of the venturi. Air passing through the venturi mixed with the particles and carried them to a mixing chamber in the back on the nozzle.

The nozzle, which directed the particles against the wind tunnel inlet screen, consisted of a cylindrical mixing chamber section, a converging-diverging section, and a hollow sting running down the center of the nozzle. At the end of the sting was mounted a deflecting cone. The mixing chamber received the mixture of air and particles from the venturi and also un-seeded air from the primary air supply. This mixture was exhausted through the converging-diverging section toward the wind tunnel inlet.

A third air-supply line was attached to the hollow sting. Air passing down the sting was exhausted through jets located in the base of the cone. The main purpose of the cone was to reduce the core velocity of the nozzle exhaust. The air jets at the base of the cone helped to shape the nozzle exhaust plume.

FILTER SYSTEM - The wind-tunnel flow exited into a large turning box which directed the flow of air and seed particles up toward the laboratory ceiling. A system to filter the particles from the flow without creating a severe pressure drop, was used to prevent the particles from blowing throughout the laboratory and to collect the particles for reuse. The system selected was a large 18-ft. high, 12-ft. diameter (5.5 by 3.7 m dia), filter bag which is made of cotton flannel.

VORTEX PROBES - The vortex-sensing probe designed and fabricated for the measurement of the vorticity in the trailing vortex system was capable of determining the geometry and magnitude of rotation of a trailing vortex by traversing a plane normal to the axial direction of the vortex. The non-rotating type vortex meter used senses the rotation of the fluid by means of strain gages. The output signal from the strain gages (either in millivolts or frequency) corresponds to a stress in the sensing element due to twist which is caused by the rotating fluid acting on the probe vanes. The angular motion in the fluid due to vorticity was sensed by the action of the flow over a set of vanes spaced as a cross. The vanes have dimen-

sions of 1/2" x 1/4" (.64 cm x 1.27 cm). A strain gage bridge was used to pick up the torseon signals received. Figure 1 shows a typical probe-vane arrangement.
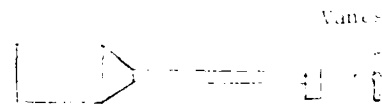
Figure 1. Vortex Probe Schematic

The calibration of the vortex probes was carried out by rotating the vortex probe in a uniform flow attained in the wind tunnel facility. The rotation of the probe caused torque to be produced on the vanes which caused a change in stress in the sensor. This change in stress changed the frequency of the radio signal being transmitted from the calibration system to a receiver located outside the wind tunnel. This frequency was visually displayed on an oscilloscope or monitored with a digital frequency counter. The probe was rotated over a range of angular velocities, and a plot of frequency versus angular velocity was obtained. Figure 2 presents results from the calibration.
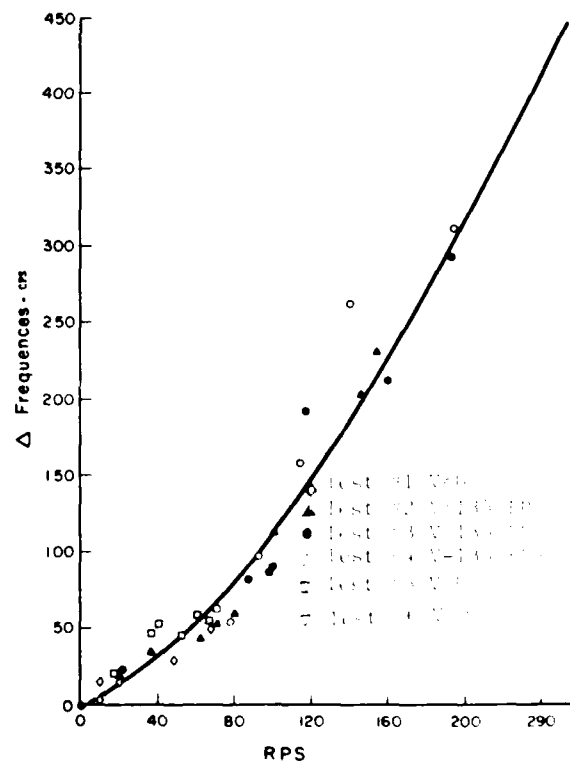
Figure 2. Vortex Probe Calibration

TEST PARTICULATES - The particulates used for seeding the flow were poly-vinyl-chloride, (PVC) pellets, and sand. The poly-vinyl-chloride pellets were used to seed the wind tunnel flow for most of the experiments to avoid excessive wear of the equipment.

Poly-vinyl-chloride (PVC-pellets) - The PVC pellets were spherical in shape, white in color and chemically inert. The physical properties were:

Sp. Gr. (resin) 1.4
Bulk density . . . . . 0.47 - 0.58 gm/cc
Vol. resistivity . . . 10^{14} ohm/cm
Dielectric constant. . 3.7
Specific Heat . . . . 0.25 cal/gm - °C

The results of a sieve analysis for three samples of PVC as supplied and the results obtained during the course of this study are given for comparison in Table L.

Table 5 -- PVC Sieve Analysis Results

Sieve Size	Supplied Distribution % Retained			Measured Distribution % Retained	
(Microns)	Test #1	#2	#3	Test #1	Test #2
420 μ				.45	2
250 μ		Trace		69.50	55
210 μ		1			
177 μ	0		0	11.40	21.6
149 μ	9	41	31	16.25	19.0
105 μ	45	40	49	1.10	2.1
100 μ	15	6	8		
74 μ	12	3	5	0.19	
50 μ	19	9	7	1.08	.3

#120 PETRO SAND AND #3 GLASS - The #120 Petro Sand and 3# glass granules were generally spherical although the surface is very rough. The materials are 99.9% silicon dioxide. The particle distribution for each material is given in Table 2.

Table 6 -- Particle Distribution of the 2 Sands / #120 and #3

	% Retained #120 Sand		#3 Glass	
Sieve Size (microns)	Supplied Dist.	Measured Dist.	Supplied Dist.	Measured Dist.
841 μ			1.2	
580 μ			10.0	
420 μ	Trace	1.27	29.5	35.5
280 μ	0.50		30.5	
250 μ		8.90		53.00
200 μ	6.60		20.0	
177 μ				7.20
149 μ	40.00	68.50	7.0	2.20
105 μ	38.20		1.5	1.50
74 μ	12.80	18.75	.2	0.25
50 μ	1.90	2.57	.1	0.45

It was necessary to simulate the conditions of a typical helicopter landing zone. Reference (5) was used to obtain typical helicopter dust concentration and particle size distribution of particulates recirculated through the rotor of a hovering helicopter at a typical helicopter landing zone. The PVC pellets and #3 glass had particle size distributions similar to that in the Phillips Drop Zone. The particle size distribution for the #120 sand fill between that of the terrain and the distribution obtained at a one-foot hover height.

ELECTROSTATIC SENSING-DEVICE - This section describes the instrument used and results obtained from them in conducting measurement of the particles and the electric field set-up by the swirling particles in the trailing vortex. A difficulty, associated with using these instruments, was the lack of knowledge about the order-of-magnitude of electric field levels, voltage gradients and charging rates to be expected.

ELECTRIC FIELD MILL - An electric field mill was constructed (6) which was used to measure the electric field distribution in a plane normal to the wind tunnel flow. The electric field meter sensor consisted of a set of fixed conductive vanes and a second set of rotating vanes, geometrically similar to the first, which were grounded. The grounded set of vanes was positioned directly above the conducting vanes on an insulated shaft which prevented charge flow from one set of vanes to the other. The rotating vane periodically shielded and exposed the insulated probe to the electric field in which the field meter has been placed.

The field meter used in this work was modified so it could operate in the seeded flow field in the wind tunnel. A grounded cone was attached to the field mill sensor in front of the rotating vane. This cone deflected the particles away from the conducting plate of the field mill sensor.

The sensor plate output of the field mill was connected to a model 610C Kiethley electrometer. The electrometer functioned as a pre-amplifier and impedance matching device. The output of the Kiethley electrometer then passed through a high-low band-pass filter to an amplifier. The output of this amplifier was then monitored with a digital counter for statistical analysis and a light-beam oscillograph for continuous recording of the field mill signal.

The electric-field mill probe was inserted into the x-y positioning device, and the output from the sensor recorded as it traversed vertically through the trailing vortex. Vertical traverses were run at several horizontal locations in the vortex. The field mill was also used to determine

32-4

the statistical distribution of voltage pulses recorded at discrete locations in the vortex. A drawing of the electric field mill is shown in Figure 3.
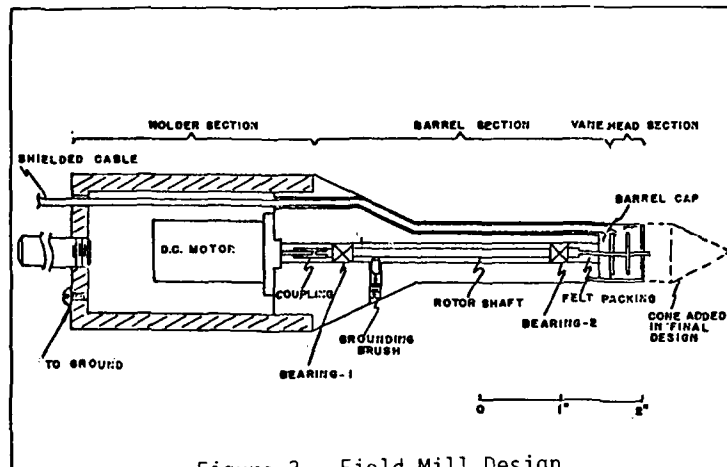
Figure 3. Field Mill Design

ELECTROSTATIC DENSITY PROBES - To determine the density distribution of particles throughout the wind tunnel flow field, electrostatic density probes were fabricated similar to those described in References (8, 9, and 10).

The results of the previous designs of electrostatic density probes indicated that, with the paticulates used in this work, probes which require the passage of particles through them, are susceptible to clogging. An impact probe used inthis work had a small brass cylinder, 0.125 inches in diameter and 0.1875 inch long (.05 cm dia and .074 cm). These dimensions were chosen to minimize disturbances to the flow and yet permit local measurements in regions of minimum particle density, such as the vortex core. The brass cylinder was soldered to the center wire of a co-axial cable. A 10^7 ohm resistor was inserted into the probe lead between the probe tip and ground. Particles impacting the probe caused a current to flow through the resistor which resulted in a voltage pulse across the resistor. Each voltage pulse was amplified by an battery powered isolated amplifier with a 20 mega-ohm input impedance and an overall gain of 1,000. The output of the amplifier was connected to a digital counter which recorded the individual pulses and displayed the running total. The background noise level of the amplifier was less than a microvolt. The amplifier was contained within a grounded metal case to eliminate pickup of stray signals.

CALIBRATION OF THE IMPACT PROBE - The impact probe was initially tested in the exhaust of a small nozzle. Particles were introduced upstream of the nozzle and through impacts with the duct walls became charged. To increase the probability of

particle impacts prior to exiting from the nozzel, pieces of screen were placed in the duct to increase the turbulence and increase the probability of particles impacting the duct and/or the screens. The approximate number of particles per sample was determined from the sample distributions. The weight of each sample used in these calibration tests was 0.2 gm. As a check on the number of particles per sample a ring probe soldered to the impact probe was located at the exit of the nozzle. The diameter of the circular loop was slightly larger than the exist diameter of the nozzle. The particles were introduced into the calibrations system over a 4.0 minute time interval. Eighteen samples of each of the three particulates were used for these tests. The total number of particles sensed by the ring probe was monitored by a digital counter. The results of these tests indicated the number of particles per sample sensed by the ring probe agreed with the number calculated using the measured distribution for the PVC pellets and was more than 50% low for the #3 glass and #120 sand samples. The error between the number of particles sensed by the ring probe and that calculated from the distributions of the sand samples was probably due to low charge levels residing on the sand particles.

The circular wire was removed from the cylindrical probe tip and the cylindrical impact probe was then positioned 0.5 inches (1.27 cm) from the nozzle exit in line with the nozzle exhaust. The pulses induced in the probe due to particles impacting the probe and particles passing close to the probe surface were recorded. Histograms of the results of these tests are also shown in Figure 4. The mean value and standard
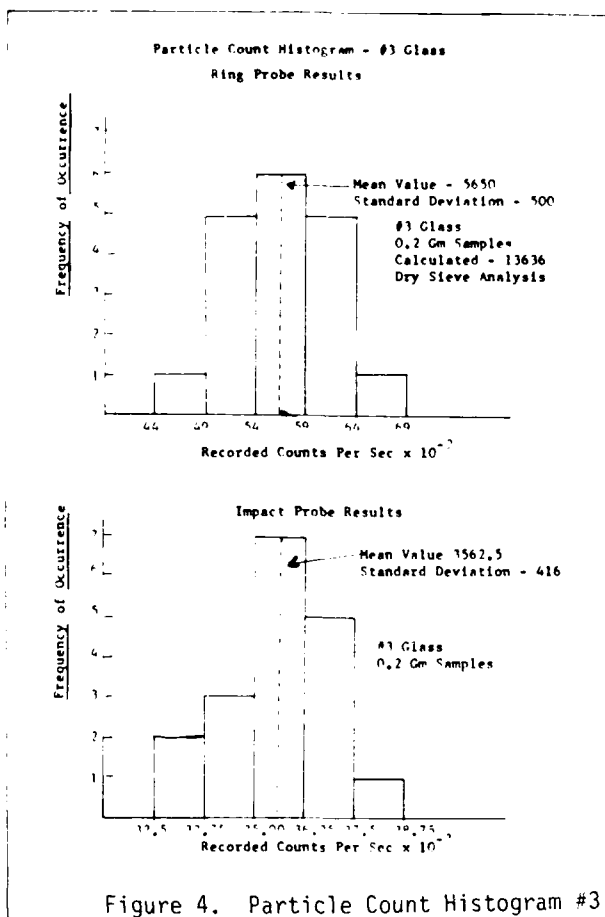
Figure 4. Particle Count Histogram #3 Glass

deviation of the measurements are indicated in each figure. The results of these tests were used in determining the effective diameter of the probe.

X-Y POSITIONER - The x-y positioner is an electromechanical device capable of locating probes accurately within the wind tunnel test section. The x-y positioner located the probes in a plane aft of the airfoil trailing edge. The positioning device was moveable and could be positioned at any point in the wind tunnel test section. The probe support hub of the device was capable of supporting any and all of the instruments used in the course of this work. Separate power trains drove the probe support vertically or horizonally to a positioning accuracy of better than 0.01 inch (.004 cm).

EXPERIMENTAL RESULTS

EXPERIMENTAL PROCEDURE - The experimental measurements obtained cover three separate phases; vortex data, electric field distribution, and particle density distribution. All the results discussed in this section regarding electric field measurements and density distributions are for PVC seed particles only.

The vortex probe was used to measure the vorticity distribution at several locations aft of the airfoil trailing edge. The probe was moved to the wind tunnel center line which coincides approximately with the vortex center. Frequency readings were taken over ten second intervals. At least two and often three frequency readings were taken at each point. The probe was then repositioned at various locations in a plane normal to the wind tunnel flow. After recording the frequency readings at the desired locations in the vortex, the probe was then moved far from the vortex, but not into the wind tunnel boundary layer, and a background reading obtained. To make a vorticity map at another location aft of the airfoils, the tunnel was shut down. Then the x-y positioner was repositioned at the desired location aft of the airfoils and the vortex probe repositioned on the wind tunnel center line. The tunnel flow velocity was brought back up to the desired velocity and, as previously outlined, frequency readings recorded at various locations in a plane normal to the flow. Vortex data was obtained for two flow velocities and two angles of attack at various locations downstream from the airfoils.

The electric field meter tests were performed after the vorticity measurements were completed. The electric field measurements were made at five transverse locations in the plane of the trailing vortex. The field meter was positioned at a transverse location, then continuously moved vertically through the vortex; the output of the field meter was recorded continuously on a light-beam oscillograph. The field meter was then positioned at five vertical locations over which the continuous trace was taken. At each vertical location, the magnitude of the electric field was monitored. The output of the field meter was connected to a digital counter with a variable voltage threshold. By varying the counter threshold level, the voltage pulses below a specified level did not register on the counter. The results of the statistical measurements were plotted on probability graph paper and from this plot the mean field strength was obtained.

The particle density distribution was the last phase of the experimental tests. The baseline particle distribution was measured without airfoils in the wind tunnel. The mass flow indicated by the particle density probe was compared against the know mass flow from the particle feed system. The particle density probe was then used to map the density distribution throughout the trailing vortex at several locations aft of the trailing edge of the airfoil.

VORTEX PROBE RESULTS - The vortex probe results are shown in Figures 5 and 6. The center of the wind tunnel is at 0-horizontal and 0-vertical. The results are plotted as lines of constant angular velocity, which is equal to half the vorticity. Although the wind tunnel flow was stopped completely from test to test, the vortex location and geometry was not noticeably altered.
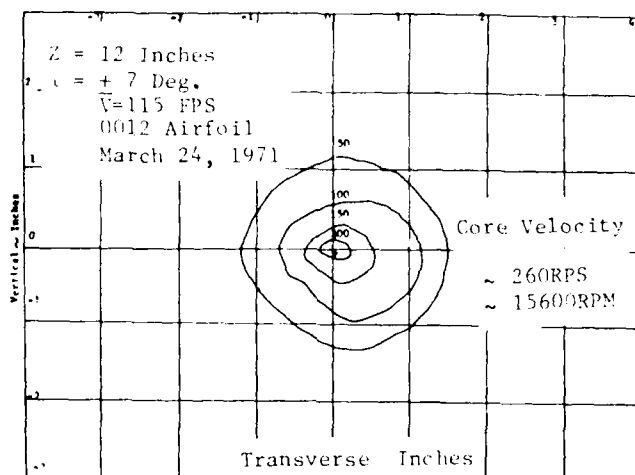
Figure 5. Angular Rotation Contours - rps
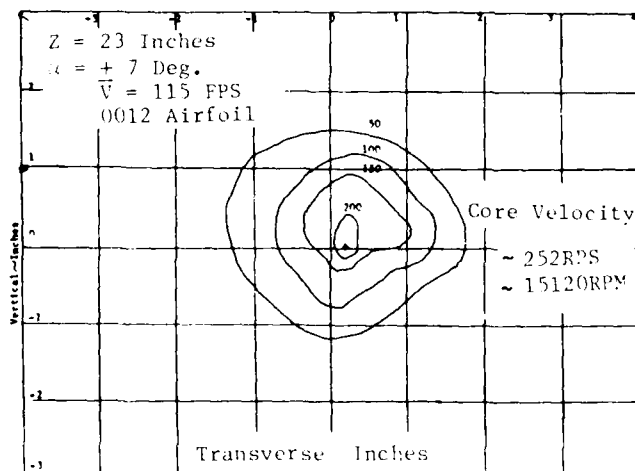
Figure 6. Angular Rotation Contours - rps

The vorticity measurements downstream of the 0012 differential airfoil at ±7 degrees angle of attack were run with the wind tunnel flow at 115 fps (35 m/s). Care was taken to insure that the airfoils were set at equal and opposite angles of attack.

These contour plots shown in Figures 5 and 6 indicate that the geometry of the vortex is well defined as close as 12 inches (.305 m) aft of the airfoils. Study of all data taken revealed that the differential airfoils produce a stable vortex whose position in the wind tunnel test section is independent of the angle of at-

tack, the flow velocity, and distance downstream of the airfoils within the range of the test.

ELECTRIC FIELD METER RESULTS - Electric field data was taken at $Z = 12$ inches (.305 m) and $Z = 24$ inches (.61 m). In each case, the angle of attack of the airfoils were set at ±7 degrees and ± 12 degrees. When the meter was located in the proper axial position, it was then positioned at the desired horizontal and transverse location with the x-y positioner. The wind tunnel flow was then brought up to speed and the particle feed system turned on. The electric field meter then traversed a vertical path through a portion of the vortex, beginning 3.5 inches (8.9 cm) above the vortex center line and ending 3.5 inches (8.9 cm) below. At six locations spaced vertically across the vortex (4.0 and 1.5 inches (10.2 and 3.8 cm) above, at the center, 1.5 and 2.5 inches (3.8 and 6.4 cm) below, the electric field meter output was monitored statistically. Due to the limited capacity of the particle feed system, the flow of particles was stopped as the meter was repositioned between statistical readings and during transverse movement of the meter. It was necessary to shut down the wind tunnel flow completely several times during the mapping of the electric field in order to collect the particles and refill the particle-feed hopper.

The flow field in the absence of the airfoils was traversed vertically with the electric field meter at five horizontal locations across the wind tunnel test section. Visual observation of the oscillograph traces for these traverses indicated a slight decrease in the electric field level near the south wall of the wind tunnel test section.

The output signal of the electric field meter was fed into suitable amplifiers and to the oscillograph or the digital counter. The oscillograph was used for obtaining continuous traces. The digital counter was used during the statistical monitoring of the electric field. The mean value of electric field was obtained from probability plots.

The electric field data and the voltage distribution curves for $\alpha = ±7°$, $Z = 12$ and 23 inches is shown in Figures 7 and 8. The complete electric-field contours were obtained by linear interpolation between the locations where the electric field measurements were made. The dotted portions of the contours were added on the basis of trends indicated by the other contours.

PARTICLE DENSITY DISTRIBUTION - The particle density probe was traversed vertically and horizontally in a plane normal to the wind tunnel flow. At each location, the number of particles impacting the probe

was recorded over two ten-second intervals. The average reading was then taken as the particles per second passing that point in the wind tunnel.

The result of these measurements are shown in Figure 9 which is a plot of the particle density distribution without the airfoils in the test section. The particle density distribution, with no airfoils in the test section, indicates a density
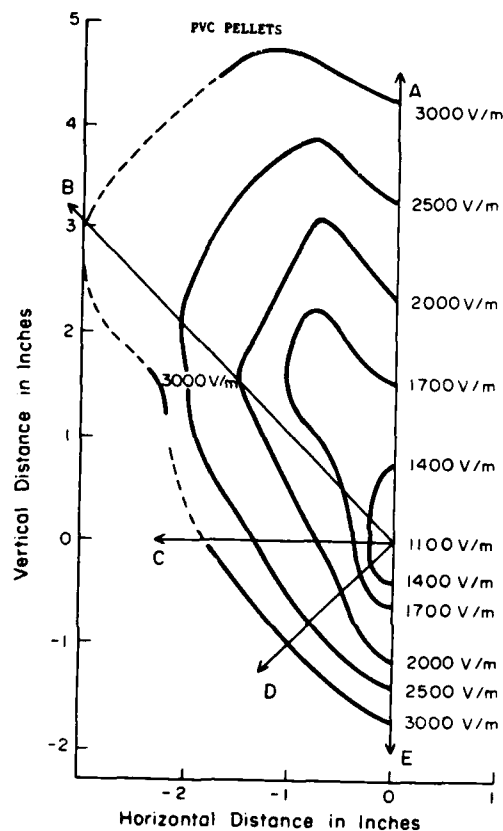
Figure 7. Electric Field Distribution
(Volts/m) = ±7° Z = 12 inches

gradient from the top of test section toward the bottom. This is to be expected due to the gravita-
tional force on each particle. It must be emphasized that the gravitational effect on the particles occurs during the time the particles are leaving the feed nozzle plume and being accelerated in the wind tunnel inlet from a velocity of 13 ft/sec (4.0 m/sec) to a velocity of 115 ft/sec (35 m/sec). After the particles enter the test section inlet, the effect of gravity is negligible compared to the drag force due to the flow velocity. The average particle density across the test section is 250 particles per second. With the differential airfoil installed in place, the particle density probe was traversed vertically and horizontally over a plane aft of the airfoil. At each location, particle counts were taken twice over ten second intervals.
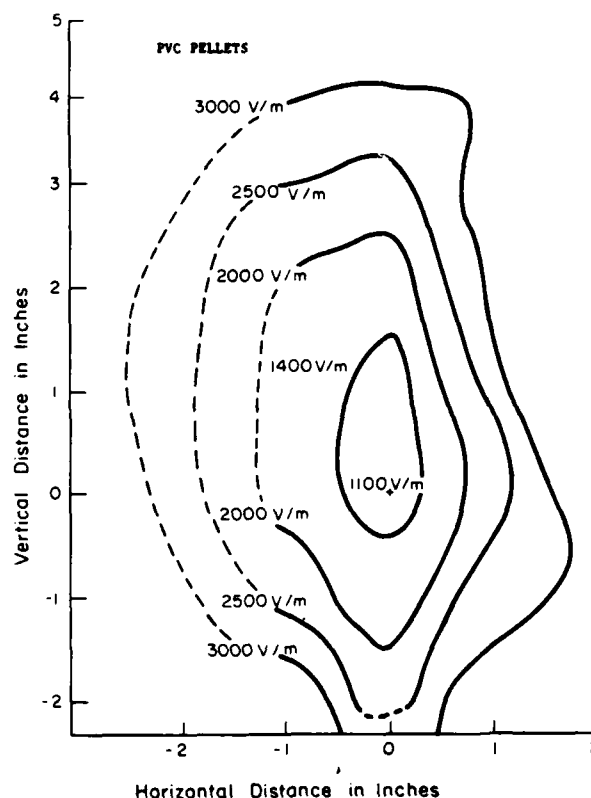
Figure 8. Electric Field Distribution
(Volts/m) = ±7° Z = 23 inches
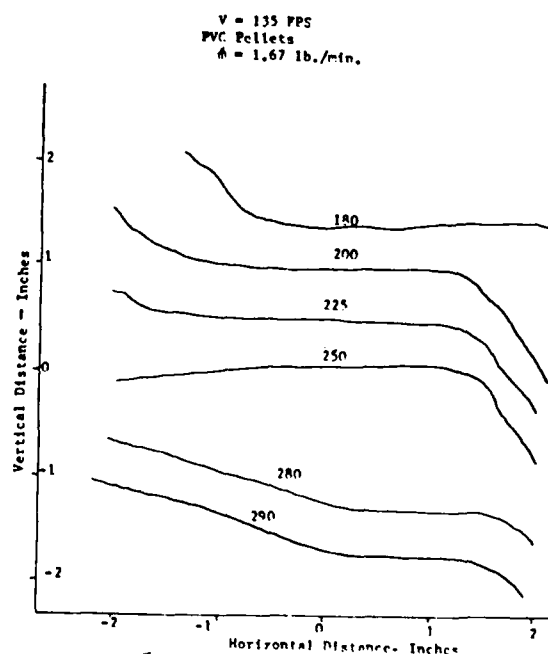
Figure 9. Particle Density Distribution

The readings were averaged. The density distribution at Z = 12 inches aft (.305 m) of the airfoils for ±7 degrees angle of attack are shown in Figures 10 and 11. The particle density contours were obtained by linear interpretation between measured values.

Due to the limited capacity of the particle feed system, the wind tunnel had to be shut down several times during the measurement of the density distribution over the entire plane of the flow field in order to collect the particles and refill the particle feed hopper. Each time this was done, the last monitored point in the flow recounted to insure there was no variation in the particle feed rate or vortex geometry.

EXPERIMENTAL TESTS WITH SAND IN FLOW FIELD - Measurements of the electric field, density distribution and particle charge were made in the wind tunnel flow seeded with sand. The procedure for making the measurements is the same as discussed previously for tests run with the wind tunnel flow seeded with PVC pellets. Due to the abrasive characteristic of the sand, only one vertical trace through the core of the vortex with the field meter and density probe was made for each type of sand. The magnitude of the electric field was ana-
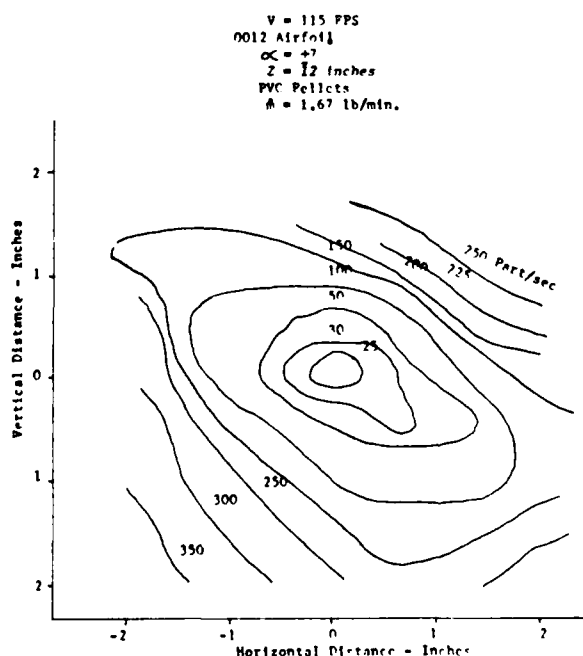
Figure 10. Particle Density Distribution

lyzed statistically at five locations over which the continuous trace had been run. Particle charge was measured at several locations over the same vertical path through the vortex core. All measurements made with sand in the flow field were taken 12 inches (.305 m) aft of the airfoil.
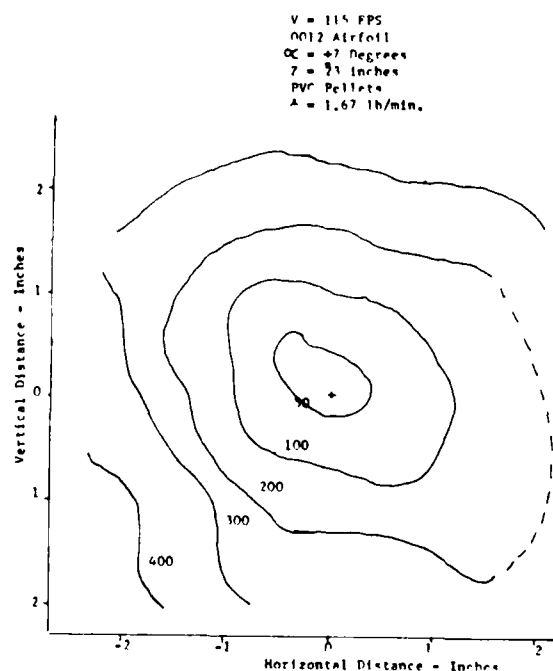
Figure 11. Particle Density Distribution

A plot of the particle density and electric field strength, 12 inches (.305 m) downstream of the airfoil with the wind tunnel flow seeded with #120 petro sand, is shown in Figure 12. The magnitude of the electric field was measured statistically at five locations on a vertical path through the midpoint of the trailing vortex The flow velocity is 115 fps (35 m/sec) with the differential airfoil set at ±7 degrees.

DISCUSSION OF EXPERIMENTAL RESULTS

VORTEX PROBE RESULTS - The vorticity contours are shown in Figures 5 and 6 at a plane 12 inches aft of the airfoils for a velocity of 115 ft/sec (35 m/sec) with the airfoils set at ±7 degrees angle-of-attack. It should be noted that the magnitude of the vorticity contours are specified in terms of angular rotation and that this value should be doubled to obtain the magnitude of the vorticity.

ELECTRIC FIELD METER RESULTS - The electric field contours for the conditions α = ±7°, Z = 12 inches and Z = 23 inches (.305 m and .58 m) are shown in Figure 7 and 9 respectively. The wind tunnel flow was seeded with PVC pellets for which m = 1.67 lb/min (.76 kg/min). The shape of the electric field contours at Z = 12 appears similar to the vorticity contours for a vortex which is not completely rolled up. The electric field contours at Z = 23 indicate a weakening of the field strength relative to that at Z = 12 in the vicinity of

X Volts/m~E   ●—Part/Second

Approximate
Curve Based
upon tests

#120 Sand
0012 Airfoil
= + 7 deg.
Z = 12 inches

Centerline
of Vortex
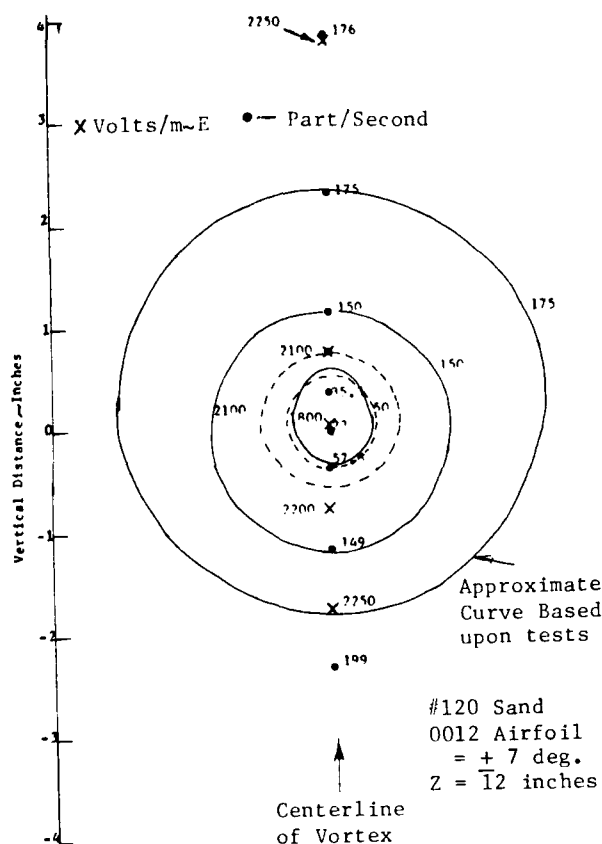
Figure 12.   Electric Field and Particle
Density - Sand

the center of the vortex. This is to be
expected since the charge-carrying parti-
cles, which are creating the electric field,
are moving with time (or axial distance)
away from the center of the vortex. This
movement, of the particles out of the vor-
tex center, is due to the centrifugal force
on the particles caused by the fluids rota-
tional motion. It is interesting to note
that the electric field intensity at z = 23

increases in the upper left-hand region.
This indicates that the particles, in this
region at Z = 12 are still under the influ-
ence of vorticity bearing fluid which has
not completely rolled up into the trailing
vortex. However, this is not in agreement
with the vorticity results which indicate
that, for the condition $\alpha = \pm 7°$, the shed
vorticity has completely rolled up at a
distance Z = 12. A possible explanation
for this occurrence is that the particle
being heavier than air tends to lag
slightly behind the fluid due to their
inertia and, therefore, roll up into the
vortex at a slightly slower rate than the
fluid particles.

The magnitude of the electric field at
Z = 12 inches was plotted against radial
distance along rays A, B, B, D, and E,

Figure 7. The results indicated that where
the flow has rolled up, the electric field
distribution is nearly axisymmetric.

The electric field contours for $\alpha = \pm 7°$
at Z = 23 is shown in Figure 3. These con-
tours are similar to what one would expect
from flow of charged particles in a free
vortex. When the charged particles reach
their equilibrium radius, where they are no
longer under noticeable influence of the
rotating fluid, the particle distribution
that should result is one with most of the
particles in the outer region of the vortex
and progressively fewer particles nearer
the vortex center. The individual parti-
cles carry electrostatic charge; hence, the
electric field would be expected to in-
crease as one moves away from the vortex
center.

PARTICLE DENSITY PROBE RESULTS - The
particle density probe results are shown in
Figures 9 through 11 as contours of
particle density (in particles per second).
The background density recorded with no
airfoils in the test section indicates a
homogeneours mixture of PVC pellets in
horizontal planes within the wind tunnel
test section but some stratification from
top to bottom of the flow. This vertical
density variationis probably due to the low
speed at which the particles enter the wind
tunnel prior to the acceleration into the
wind tunnel test section. A second possi-
bility is that the plume from the feed noz-
zle may have been directed too low on the
wind tunnel inlet screen. The number of
particles traveling through the entire
plane of the 3 ft. sq. (0.8 sq.m.) test
section was calculated to be 0.8×10^7
particles per second. This number compares
well against the number of particles being
fed into the test section from the feed
hopper which is 0.57×10^7 an average
particle diameter (200 μ).

The particle density contours for the
conditions $\alpha = \pm 7$ degrees at Z = 12 and
Z = 23 are shown in Figures 10 and 11. The
contours at Z = 12 have an appearance simi-
lar to vorticity contours taken somewhat
closer to the airfoils. The density con-
tours at Z = 23 are similar in shape to the
vorticity contours obtained when the vortex
is completely rolled up, Figure 3, however,
enclosing a much larger area.

The variation of the density along
radial lines was plotted versus distance
for several angular positions. The varia-
tion of density was nearly linear and
indicated the distribution of particulates
in these test could be assumed axisymme-
tric.

RESULTS OF TESTS WITH #120 SAND - The
electric field measurements and particle
density variations for the #120 petro sand
is given in Figure 12. The electric field
profile for the #120 petro sand shows that

the electric field varies from 1,800 volts/m at the vortex center to 2,250 volts/m outside the vortex core. The particle density distribution shows that the particles are being thrown out of the vortex core due to centrifugal force. The particle density distribution indicates a slight stratification of particle density similar to that with PVC pellets in the flow. The electric field is somewhat lower than that which occurred with the PVC pellets. This is probably due to the difference in the electrical characteristics of the two materials. The major variation of electric field intensity occurs near the vortex core which is also where the major variation in particle density occurs. This result agrees with the that obtained from tests with PVC pellets. The field gradients for the PVC tests were greatest near the edge of the vortex core, Figure 7, where the density gradient is greatest.

The electric field gradient in the #120 petro sand is greatest near the vortex core also where the largest variation in density gradient occurs. This pattern tends to verify that the electric field meter is actually measuring the electric field set up by the flowing particles.

CONCLUSIONS

The major conclusions which can be drawn from the results of this study are:

The differential airfoil generated a stable vortex whose position in the wind tunnel seemed independent of the wind tunnel flow velocity, angle of attack and distance downstream. The core of the vortex appeared to be turbulent. The trailing vortex system in a flow seeded with particles established a quasi-static electric field distribution due to the charged particles. The electric field and particle density distributions downstream of the airfoils are approximately linear with radial distance from vortex center and roughly axisymmetric at each downstream station in the region of measurements.

The shape of the curves of vorticity and particles distribution were quite similar which indicates a direct dependence of the particle distribution on the vorticity field. The shape of the electric field was quite similar to that of the particle distribution. The electric field in turn depends on the charged particle distribution and hence in turn on the vorticity distribution. The results of the work do confirm the hypothesis that charge separation and an electric field do indeed result as a consequence of the trailing vorticies created by lifting surfaces in the presence of dust or particulate laden air.

It should be noted that in corrolary work selective charge deposition does indeed occur with bodies placed downstream in a particulate loaded vortex (11).

REFERENCES

1. Rogers, M.E. and Minihan, E.B., "Interim Report On Investigation of Static Buildup On Helicopter." R.A.E. Report, 1967.

2. Born, G.J., and Durbin, E.J., "An Investigation of Electrical Charging and Discharging of Aircraft in Flight," Princeton University Inst. and Control Lab., Report No. 593, (Dec. 1961).

3. Trecom Tech. Report 64-14, "Measurement Program To Determine Static Electricity Charging In Helicopter Main Rotor Blades," June, 1964, Ft. Eustes, Virginia.

4. McMahon, M.C., "A Non-Rotating Vorticity Meter," NASA CR-887.

5. Rodgers, S.J., "Evaluation of the Dust Cloud Generated By Helicopter Rotor Downwash," USAAV LABS., Tech. Report, 67-81, Ft. Eustes, Virginia.

6. Evans, J.E., "The Design, Test and Evaluation Of An Electric Field Meter Commonly Referred To As A Field Mill," M.S. Thesis, Mechanical Engr. Dept., Ohio State University, March, 1971.

7. Gunn, P., "Electric Field Meters," Rev. Sci. Inst., Vol. 25, No. 5, pp. 432-437, May, 1954.

8. Cheng, L., Tung, S.K., and Soo, S.L., "Electrical Measurement of Pulverized Coal Suspension," J. Engr. for Power, April, 1970.

9. Hendricks, C.D., Jr., Journal Colloid Science 17, 249 (1962).

10. Min, K., Chao, B.T., and Wyman, M.E., "Measurement Of Electro-Static Charge On Solid Gas Suspension Flow," Rev. Sci. Inst., Vol. 34, No. 5., pp. 529-531, (May, 1963).

11. Bohl, Philip & Velkoff, H.R., "Electrical Charging Of A Cylinder By A Seeded Vortex," IEEE-IAS Conference, Chicago, Illinois, Oct., 1976. Also M.S. Thesis, Mechanical Engineering Dept., Ohio State University, Columbus, Ohio 1972.

12. Daugherty, John W., "Study of the Electrostatic Field and Charge Distribution in a Vortex Seeded with Dust". Ph.D. Dissertation, The Ohio State University, Columbus, Ohio, 1972.

EFFECTS OF SIMULATED LIGHTNING CURRENTS ON THE
TENSILE STRENGTH OF GRAPHITE/EPOXY

William E. Howell
NASA Langley Research Center
Hampton, VA

ABSTRACT

An investigation of the effects of high amplitude simulated lightning currents on the tensile strength of T300/5208 graphite/epoxy has been conducted. Tests were conducted on both unidirectional [0], and quasi-isotropic, [+45, -45, 0, 90]$_s$, laminates. Current, ranging from 3.4 kA to 48.0 kA, was conducted through tensile test specimens and the specimens were then tested to measure residual strength. Some test specimens were conditioned to a moisture level of approximately one percent prior to being subjected to high amplitude current. In addition, some specimens were strained to 4000 μcm/cm prior to being subjected to the test current. Residual strengths are compared with baseline strengths and the results are reported herein.

LIGHTNING STRIKES TO AIRCRAFT are a major concern because of the potential damage to avionics, fuel systems, and the airframe. Thus, the aircraft must be capable of sustaining lightning strikes without incurring significant damage. The effects of lightning on aircraft can be catastrophic. Localized damage due to intense heat can occur; however, widespread damage may also occur due to current dissipation away from the strike attachment point. Airplane damage from lightning strikes is described in references (1-4)*. Helicopters are also susceptible to lightning strike damage, and some of the associated problems are discussed in reference (5). The certification peak current of 200 kA and the associated waveform are described in reference (6).

The introduction of advanced composites as an aircraft structural material has stimulated interest in aircraft lightning protection. The high strength, high stiffness, and low density of composite materials make them attractive for aircraft structural applications. However, the electrical properties of composites and metals are significantly different. Graphite/epoxy (Gr/E) has a relatively high electrical resistivity compared to aluminum. The resistivity of Gr/E is 6.0×10^{-3} ohm-cm, whereas the resistivity of aluminum is 2.8×10^{-6} ohm-cm. The energy absorbed from a lightning current is a function of the resistivity of the material through which it flows. Therefore, Gr/E will tend to absorb orders of magnitude more energy than will aluminum which may cause a significant temperature rise and physical damage.

The effects of simulated lightning strikes on composites are reported in references (1) and

*Numbers in parentheses designate References at end of paper.

(7-11). The visible effects of natural lightning on two composite materials are reported in reference (12). However, information on the residual strength of composites after simulated lightning strikes is limited (ref. 11).

The purpose of this paper is to report on the effects of simulated lightning currents on the tensile strength of graphite/epoxy composite materials. The test currents were conducted through the specimens with no arc gap in the circuit. These tests, therefore, were different from tests conducted by arcing the current across an air gap to a test panel and then tensile testing specimens machined from the panel. Tensile test specimens were exposed to current levels ranging from 3.4 to 48.0 kA to determine the onset of strength degradation. Tests were also conducted to determine the effects of moisture and tensile load on the residual tensile strength after a simulated lightning strike.

Identification of commercial products in this report is to adequately describe the materials and does not constitute official endorsement, expressed or implied, of such products or manufacturers by the National Aeronautics and Space Administration. All units of measure used in this report are given in the International System of Units.

TEST SPECIMENS

All of the specimens were machined from 8-ply laminates fabricated from T300/5208 Gr/E pre-impregnated tape. Specimens with unidirectional, [0], and quasi-isotropic, [+45, -45, 0, 90]$_s$, orientations were evaluated. The specimen geometry is shown in (fig. 1). Each specimen was 30 cm long to accommodate electrical clamps and mechanical grips. A summary of the conditioned test specimens is given in (table I).

EXPERIMENTAL PROCEDURES

Each specimen was mounted in the series RC circuit represented in (fig. 2(a)). The test procedure consisted of conducting a high amplitude simulated lightning current through each specimen. A representative test waveform used in the experiments is shown in (fig. 2(b)). A specimen mounted in the test circuit is shown in (fig. 3).

In order to determine the effects of moisture, one set of quasi-isotropic specimens was dried in a vacuum furnace at 71°C. A second set of specimens was moisture conditioned in a chamber at 100 percent relative humidity and 32°C. The specimens were removed from the chamber and weighed every 30 days until the weights stabilized. It took 90 days to dry the first set of specimens and 120 days were required to condition

the second set of specimens to approximately a one-percent moisture content. A third set of specimens was tested in the as-received condition, (approximately 0.5 percent moisture). After the specimens were exposed to a test current, they were loaded in tension to failure. A small sample was cut from the failed as-received specimens and dried in the vacuum furnace for moisture determination.

Three specimens were exposed to high amplitude currents of 3.4, 6.9, and 15.8 kA, respectively, while being subjected to a static tensile load. Figure 4 shows a specimen mounted in the electrical circuit and the load frame. Each of the specimens was mounted in the load frame and loaded in tension to a strain level of 4000 μcm/cm, which is representative of the present design allowables for composite aircraft structures (refs. 13 and 14). The load frame was then connected in the circuit and the specimen exposed to the test current.

A photograph of each current waveform was obtained from an oscilloscope trace. The data obtained from the photographs were used to calculate the test current and the associated action integral. The action integral is defined as

$$\int i^2 dt \tag{1}$$

where i is the instantaneous current and t is the time associated with that current. The action integral is a measure of the energy associated with the electrical discharge.

After the tensile tests were completed, samples from several specimens were used to determine if the temperature rise from resistance heating had caused oxidation of the resin in the composite. The samples were evaluated by diffuse reflectance-FTIR as described in reference (15). The purpose of this test was to determine if any strength degradation could be explained by oxidation of the composite matrix.

RESULTS AND DISCUSSION

Unidirectional Gr/E specimens were tested to obtain baseline strength data. Although this is not a realistic aircraft structural laminate, this ply orientation was evaluated as a control set. The tensile failure of unidirectional laminates is fiber-dominate instead of matrix-dominate as is the case for cross-ply laminates (ref. 16). The data obtained for these tests are presented in (fig. 5). There was no strength degradation until a current density of 155 kA/cm^2 was applied to the specimen which was sufficient to cause the specimen to ignite and burn. The remains of the burned specimens were not adequate to grip and perform tensile tests, hence a zero tensile strength is shown in (fig. 5). There was no visible damage to the specimens exposed to high amplitude currents less than that required to cause matrix ignition. The results shown in (fig. 5) indicate an onset of strength degradation, for the [0]$_8$ laminates, of greater than 144 kA/cm^2 and 18 kA^2-s.

Several of the quasi-isotropic specimens, after exposure to various levels of current, are shown in (fig. 6). In (fig. 6(a)), specimens 1 and 14 are visibly undamaged but specimens 17 and 45 are delaminated. An edge view of delaminated specimens is shown in (fig. 6(b)). The delaminated specimens were not tensile tested because they were assumed to have minimal residual strength due to the severe damage. Three of the quasi-isotropic specimens that burned are shown in (fig. 7). The severity of the visible damage increased with increasing moisture content. A visual inspection indicated that the matrix was burned away from the zero degree plies of fibers. This was expected since the zero degree fibers carry current continuously end to end.

The residual strengths of the quasi-isotropic laminate tests are presented in (fig. 8). The effects of moisture are readily apparent. The dry specimens were the least affected by current in that the onset of strength degradation was at an action integral of 5.0 kA^2-s. The as-received specimens exhibited an onset of strength degradation at about 2.5 kA^2-s and a 31 percent degradation at 4.25 kA^2-s. For the specimens with 1 percent moisture, the onset of strength degradation was at about 2.0 kA^2-s and a 31 percent degradation at 3.0 kA^2-s.

The data in (fig. 8) indicate that the residual strength was significantly affected for the specimens that were loaded to a strain level of 4000 μcm/cm and simultaneously subjected to high amplitude current. The loaded specimens exhibited a 6 percent strength degradation at an action integral of 0.25 kA^2-s and a 31 percent degradation at about 1.7 kA^2-s. These results indicate that strain increases the susceptibility of Gr/E composites to damage by simulated lightning current.

The strength data from (fig. 8) are plotted as a function of current density in (fig. 9). The onset of strength degradation occurs at a current density of 55 kA/cm^2 which is in agreement with data in reference (7). At this current density, 55 kA/cm^2, moisture did not cause a strength reduction; however, the specimens strained to 4000 μcm/cm had a strength reduction of 31 percent.

The matrix is exposed to higher shear loads in the quasi-isotropic laminate than it is in the unidirectional laminate. A comparison of the residual tensile strength data for the two laminates indicates that a quasi-isotropic laminate, (fig. 9), is more susceptible to current damage than is a unidirectional laminate, (fig. 5).

A comparison of the data in (figs. 8 and 9) with data from reference (1), (fig. 10), indicates visible damage is not a reliable indicator of the extent of strength degradation. Figure 10 shows data for simulated lightning strikes whereas the data presented in this paper are for current conduction tests. Data shown in (fig. 10) indicate that only superficial surface damage occurs at an action integral value of 250 kA^2-s. This is two orders of magnitude higher than the onset of strength degradation values presented in (fig. 8). The residual tensile strength of the

quasi-isotropic specimens, excluding the loaded specimens, was degraded at action integral values ranging from 2.0 to 5.5 kA^2-s.

The results of the diffuse reflectance-FTIR tests were inconclusive. Some of the specimens had an increase in oxygen while others did not. The measurements were made over the specimen thickness which may have masked possible matrix oxidation at the matrix-fiber interface. Such oxidation would destroy the bond but may not have been detected by the FTIR. More detailed analysis and photomicrography are required to determine if the failure mechanism is mechanical cracking, oxidation, or a combination of the two.

Using the assumption of a 200 kA lightning strike to an 8-ply Gr/E laminate, the curve faired through the as-received specimen data in (fig. 9) was used to develop the plots in (fig. 11). The curves for the 16- and 48-ply laminates were generated from the 8-ply curve. The change in the number of plies changed the laminate thickness while all other parameters remained constant. This simply changed the current density for a given radial distance from the assumed lightning strike attachment point. In (fig. 11), the tensile strength is shown as a function of radial distance from the point of the assumed lightning attachment point. Although the current flow is dependent on ply orientation and lightning attachment points of the aircraft, the current was assumed to be conducted uniformly away from the attachment point.

The results indicate that, for the 8-ply (0.12 cm thick) laminate, the residual strength is zero out to a radial distance of 2.75 cm. Approximately a 10 percent strength degradation is indicated at a radial distance of 3.5 cm. This radius of damage is less than the 7-cm radius for a 100 kA strike used in the calculations presented in reference (10). The action integral density reported in reference (10), however, is 20 times greater than that indicated in this report to cause strength degradation.

Data presented in reference (7) indicate that for a 100 kA simulated lightning strike, matrix cracking may occur 3 cm from the attachment point. This current density level is similar to that of the 16-ply curve in (fig. 11). The 16-ply curve indicates that strength damage would be initiated approximately 4 cm from the attachment point. This may indicate that the residual tensile strength was degraded at a radial distance greater than the visible damage reported in reference (7).

SUMMARY OF RESULTS

An investigation of the effects of high amplitude simulated lightning currents on the tensile strength of unidirectional and quasi-isotropic graphite/epoxy laminates has been conducted. The results of this investigation are as follows:

1. Onset of strength degradation for the 8-ply unidirectional laminates occurred at an action integral value greater than 18 kA^2-s.

2. Onset of strength degradation for the 8-ply quasi-isotropic laminates occurred at action integral values of 5.0, 2.5, and 2.0 kA^2-s, respectively, for the dry, as-received, and moisture conditioned specimens.

3. Onset of strength degradation for the quasi-isotropic laminates occurred at significantly lower values of action integral than in arcing tests reported by previous investigators.

4. The strength degradation for the quasi-isotropic laminates loaded to 4000 μrm/cm was higher than the strength degradation experienced by the unloaded laminates.

REFERENCES

1. F. A. Fisher and J. A. Plumer, "Lightning Protection of Aircraft." NASA Reference Publication 1008, October 1977.

2. J. A. Plumer, "Investigation of Severe Lightning Strike Incidents to Two USAF F-106A Aircraft." NASA CR-165794, September 1981.

3. P. T. Hacker, "Lightning Damage to a General Aviation Aircraft-Description and Analysis." NASA TN D-7775, September 1974.

4. B. D. Fisher, G. L. Keyser, Jr., and P. L. Deal, "Lightning Attachment Patterns and Flight Conditions Experienced During Storm Hazards '80." NASA TP-2087, November 1982.

5. P. D. Pettit, "Helicopter Lightning Strikes." United States Army Aviation Digest, pp. 10-13, October 1978.

6. SAE Committee AE4L, "Lightning Test Waveforms and Techniques for Aerospace Vehicles and Hardware." Soc. Automot. Eng., Inc., June 20, 1978.

7. E. H. Schulte, "Effects of Lightning Current Waveform Components on Graphite/Epoxy Composite Material." Trans. SAMPE, Vol. 23, May 1978, pp. 1024-1038.

8. J. T. Kung and M. P. Amazon, "Lightning Conductive Characteristics of Graphite Composite Structures." Trans. SAMPE, Vol. 23, May 1978, pp. 1039-1053.

9. J. G. Belani and L. J. Broutman, "Moisture Induced Resistivity Changes in Graphite-Reinforced Plastics." Composites, October 1978.

10. S. D. Schneider, "Lightning Protection Considerations for Graphite/Epoxy Aircraft Structures." AGARD Conference Proceedings No. 228, April 1980, pp. 14-1 to 14-6.

11. J. Rouchon and D. Gall, "Evaluation du Comportement a la Foudre de Structures en Materiaux Composites Haut Module." AGARD Conference Proceedings No. 228, April 1980, pp. 13-1 to 13-14.

12. W. E. Howell and B. D. Fisher, "Observations of Severe In-Flight Environments on Airplane Composite Structural Components. SAE-830767, April 1983.

13. J. E. McCarty and W. G. Roeseler, "Durability and Damage Tolerance of Large Composite Primary Aircraft Structure." Paper presented at the Sixth Conference on Fibrous Composites in Structural Design, New Orleans, LA, January 24-27, 1983.

14. C. F. Griffin, "Fuel Containment and Damage Tolerance in Large Composite Primary Aircraft Structures." Paper presented at the Sixth Conference on Fibrous Composites in Structural Design, New Orleans, LA, January 24-27, 1983.

15. P. R. Young, B. A. Stein, and A. C. Chang, "Resin Characterization in Cured Graphite Fiber Reinforced Composites using Diffuse Reflectance-FTIR." Paper presented at the 28th National SAMPE Symposium and Exhibition, Anaheim, CA, April 12-14, 1983.

16. S. W. Tsai and H. T. Hahn, "Introduction to Composite Materials." TECHNOMIC Publishing Co., Inc., 1980.
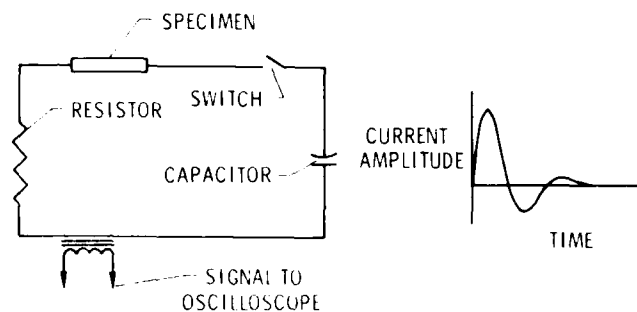
(a) Test circuit   (b) Damped waveform used to test composite

Fig. 2 – Circuit and waveform used to test the T300/5208 graphite/epoxy specimens

Table I – Summary of Test Specimens and Conditions

SPECIMEN CONDITION	LAMINATE LAYUP	EXPOSED TO CURRENT	NUMBER OF SPECIMENS TESTED
AS-RECEIVED	$[0]_8$	YES	5
DRY	$[+45, -45, 0, 90]_s$	YES	7
1 PERCENT MOISTURE		YES	8
AS-RECEIVED (0.5 PERCENT MOISTURE)		YES	5
DRY		NO	3
1 PERCENT MOISTURE		NO	2
AS-RECEIVED (0.5 PERCENT MOISTURE)		NO	2
AS RECEIVED (0.5 PERCENT MOISTURE) LOADED TO 4000 µcm/cm		YES	3
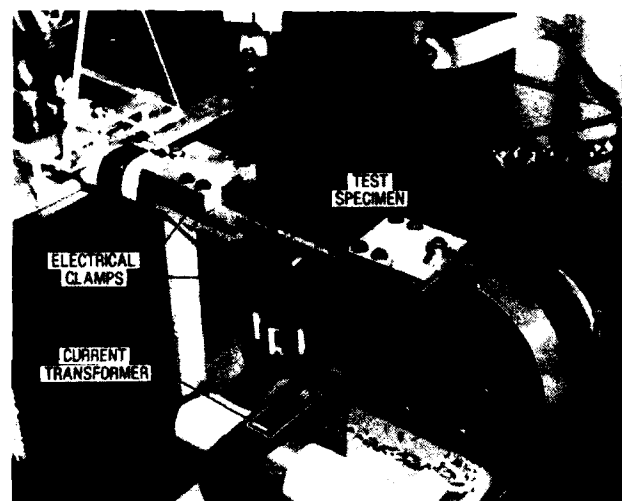
Fig. 3 – Specimen mounted in electrical circuit

(a) Unloaded specimen

(b) Loaded specimen
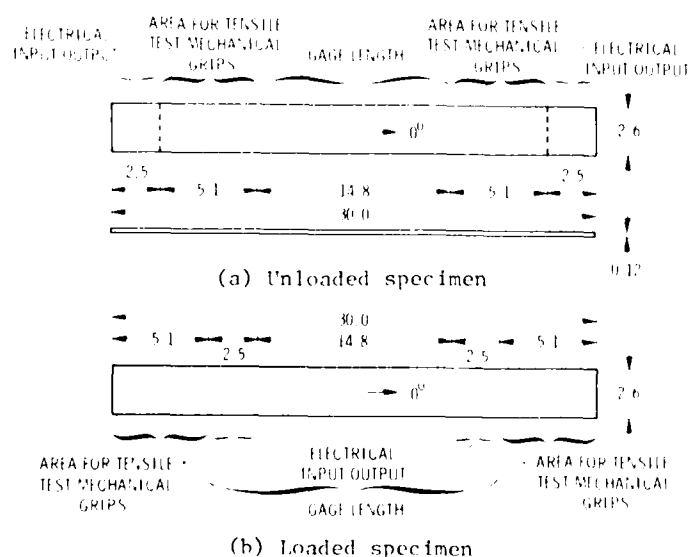
Fig. 1 – Test specimen geometry. Dimensions are in centimeters
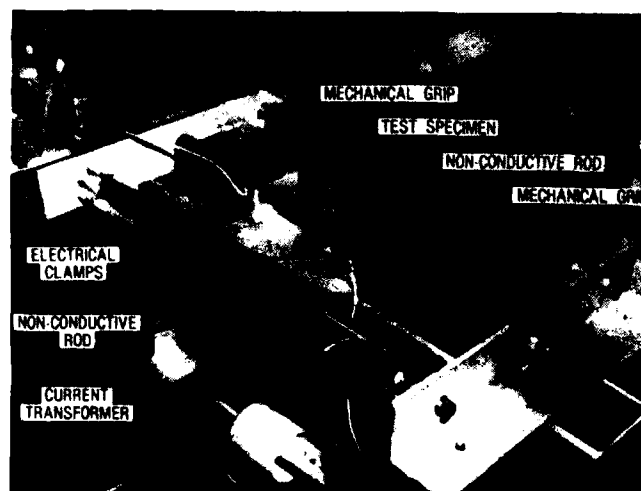
Fig. 4 – Specimen mounted in load frame and electrical circuit
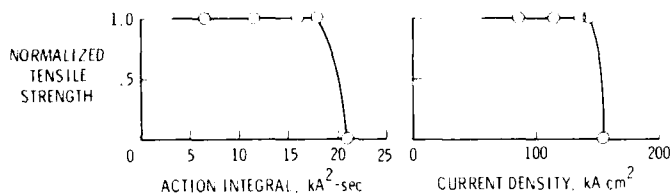
(a) Effect of action integral (b) Effect of current

Fig. 5 - Effect of action integral and current on the tensile strength of uni-directional T300/5208 graphite/epoxy laminates
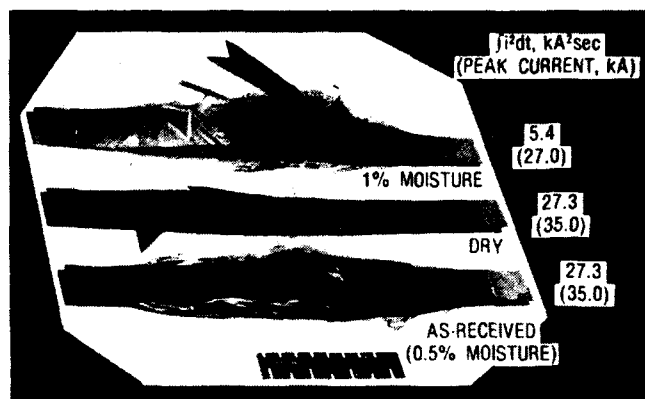
Fig. 7 - The most severe damage caused by current for the quasi-isotropic laminates
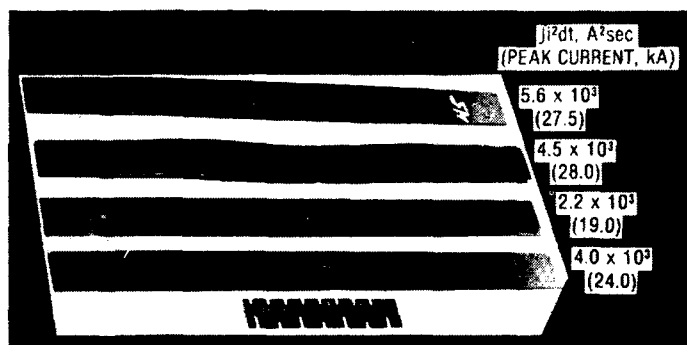
(a) Overall view

Fig. 6 - Specimens after exposure to simulated lightning current

Fig. 8 - Effects of action integral on the residual tensile strength of dry, as-received, moisture conditioned, and loaded quasi-isotropic T300/5208 graphite/epoxy laminates

(b) Edge view of visible damage

Fig. 6 - Concluded
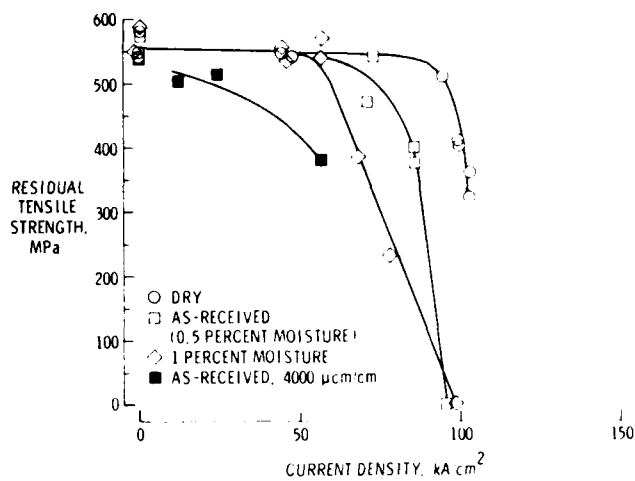
Fig. 9 – Effects of current on the residual
tensile strength of dry, as-received,
moisture conditioned, and loaded quasi-
isotropic T300/5208 graphite/epoxy laminates
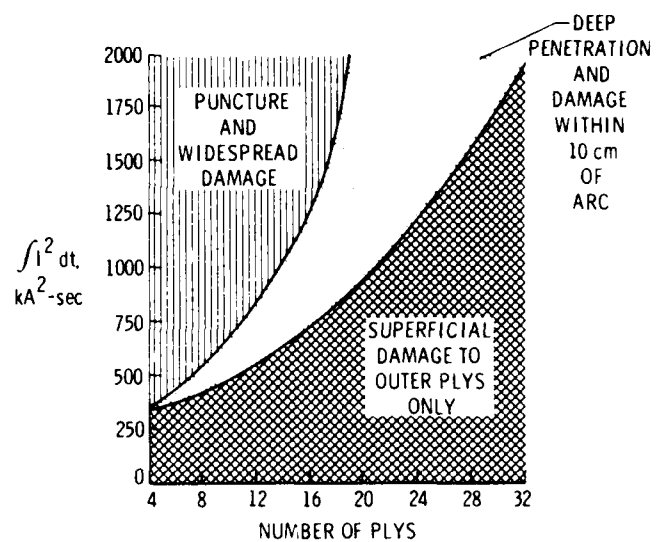
Fig. 10 – Estimated visible damage to un-
protected graphite composites. Figure
7.39, p. 238, of reference 1
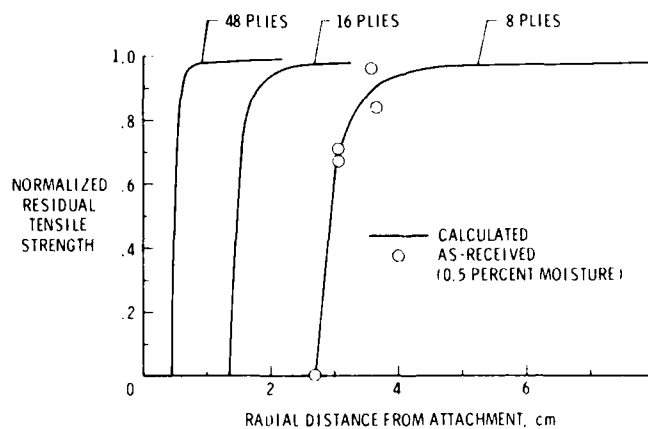
Fig. 11 – Tensile strength degradation as
a function of radial distance from lightning
attachment point.

The Streamer to Spark Transition

by

J.A. Bicknell and B.Y. Humood

Physics Department, UMIST, PO Box 88, Manchester M60 1QD, ENGLAND

ABSTRACT

The critical energy required for the positive streamer-spark transition has been measured using an electrode geometry which allows the streamer to propagate in a uniform field. The energies are 1mJ/cm for breakdown paths in the range 2-11 cm. Much longer delay times have been recorded than those observed in short point-plane gaps and these correlate well with the dark current. The occurrence of these long delay times allows the possibility that the molecular vibrational energy may contribute to the breakdown

FROM AN ELECTROSTATIC POINT OF VIEW, aircraft are commonly regarded as small capacitors subject to a charging current, produced by p-static or other means, as a result of which the aircraft potential is raised to tens or hundreds of kilovolts whilst total stored energy remains small. The corona which ensues limits the ultimate potential achieved and this may occur by design at well-located passive dischargers or otherwise. Tanner and Nanevicz (1)* and Boulay (2) have demonstrated how the electromagnetic coupling between the corona occurring at strategically placed discharges and avionics can be minimised. The aircraft is usually negatively charged so these discharges exhibit negative corona displaying characteristic high frequency Trichel pulses. By contrast, Nanevicz (3) in a comprehensive review has identified the source of a number of spurious coronas many of which may develop into an arc-like discharge. As Taillet (4) has indicated, these transient discharges exhibit much larger currents i and rates of change di/dt than simple corona; he suggests 10^2A and 10^8As^{-1} respectively in times ~ 100 ns. Such events can give rise to very strong coupling. The so-called streamering that can be seen at a dielectric surface is an example. In this case, negative charge accumulates on the surface creating large tangential surface fields. Positive streamers can then develop at adjacent conducting sections of the airframe and propagate into the negative charge centre. It is the transition of the low current, low conductivity streamer channel into an arc or surface discharge that gives rise to the large and rapidly varying currents referred to by Taillet. Some of the critical parameters required for this transition are considered here.

BACKGROUND

Positive streamers often represent the first stage of the electrical breakdown of an insulating gaseous medium. Unlike their negative counterpart, they propagate in relatively modest ambient fields ($\sim$4kV.cm^{-1} at STP) forming tree-like structures as they do so. Fig.1. shows a Lichtenberg figure of such a structure; this appears to be a faint glow to the naked eye which cannot resolve the individual branches. Once formed, these branches or channels have a radius $\sim$30μm and a free electron density $\sim 10^{14}$ cm^{-3} corresponding to a resistance 1MΩcm^{-1}. Because of this low channel conductivity the linking of two electrodes or charge centres by a streamer system is not the sole requirement for breakdown. In order for this to occur a further increase in electron density to 10^{17}cm^{-3} is required otherwise, particularly in electronegative gases such as air/oxygen, a reduction in density and, therefore, conductivity takes place because of electron attachment

($\alpha-\eta < $o).

A number of criteria have been proffered as being crucial in the transformation of a streamer channel to a spark i.e. the glow-to-arc transition. These include a minimum streamer charge in long gaps: Renardiers Group (5) and short gaps, Gibert and Dupuy (6), a maximum current (i_p in Fig. 3.). Marode (7) and critical streamer energy, Sigmond and Goldman (8). This last criterion is related to and supported by the hydrodynamic model of Marode, Bastien and Bakker (9) who suggest that a rise in temperature of the channel, produced by the energy released, leads to a decrease in neutral gas density at constant E-field so that E/N (N = number density) is increased to the point where $\alpha-\eta > $o and the subsequent increase in impact ionisation leads to the required electron density for breakdown. The critical streamer energies reported by Sigmond and Goldman were obtained using small point-plane gaps (< 15mm) and single channel repetitive breakdown streamers. The preliminary measurements reported here involve a somewhat different electrode configuration which extends the streamer range to 11 cm. and attempts to simulate streamer growth in a uniform field.

EXPERIMENTAL

The electrode arrangement is shown in Fig. 2 . Positive streamers develop at the needle point located at the centre of a small hole in the ground electrode and propagate across the gap to the upper cathode. The electrodes of 42 cm. diameter provide a uniform field in the gap which is variable up to 13 cm; the surrounding chamber gives provision for gas and pressure variations. A 50Ω system connected between point x and ground monitors the conduction currents flowing in the streamer system. For breakdown studies these currents may be examined directly with an oscilloscope or indirectly using a 20 MHz Transient Recorder. The latter is particularly useful in the study of air breakdown when pre-breakdown streamers can occur prior to the breakdown streamer itself so that the initial streamer or associated luminosity cannot be used as a trigger. In such cases, the pre-trigger mode allows the use of the breakdown current as a trigger so that the required pre-breakdown currents are recorded.

RESULTS AND DISCUSSION

The time dependence of the breakdown streamer currents in gaps up to 11 cm. all exhibit the same basic profile shown schematically in Fig. 3. The positive primary streamer travelling at velocities $> 5 \times 10^7$ cm/s crosses the gap in a time which is usually small compared to the breakdown time T_B. The low conductivity channel, or more accurately because of streamer branching, channels which now link the two electrodes give rise to a current maximum, i_p, which occurs after a few hundred nanoseconds followed by a decay governed by the electron attachment rate coefficient ν of the gas; a large ν will provide a large negative ion density in the channel. The subsequent non-luminous period preceding the breakdown is characterised by a dark current i_c which, in the larger channels, may flow for a time $t < T_B$. The measured values of i_c imply a channel resistance varying from $0.2M\Omega/cm$ in short gaps to $3M\Omega/cm$ in the larger gaps. The breakdown behaviour in the present electrode geometry can be compared and contrasted with that observed in short point-plane gaps referred to earlier.

CRITICAL ENERGY FOR STREAMER-SPARK TRANSITION Because of the uniform field geometry employed, the energy per unit length of gap W is

$$W = E_B \int_o^{T_B} idt \qquad (1)$$

The values of W obtained in gaps up to 5 cm using room air at a pressure of 300 torr are shown in Fig. 4. as a function of gap size; the minimum breakdown field for all gaps is 4kV/cm.

The applied field was increased manually so that, in the absence of a starter electron near the needle point, the recorded breakdown field could exceed the minimum. Apart from the smallest gap of 2-3 cm. the unit critical energy is approximately constant at $\sim$ 1mJ/cm. This value can be compared with those of Sigmond and Goldman (8) using point-plane electrodes and humid air where they found critical energies of 70 μJ/cm at 1 cm rising to 110 μJ/cm at 1.4 cm suggesting a parabolic relationship between total energy and gap size. The present figure of 280 μJ/cm at 2 cm is consistent with this behaviour but clearly as the gap increases a linear rather than a parabolic relationship develops. An explanation of this initially rapid rise in unit critical energy may be provided by the nature of the streamer systems in the two cases. Whereas Sigmond and Goldman were confident they were using single channel, repetitive streamers the present measurements were made, as Fig. 1. makes clear, with a heavily branched system. Clearly, once branching occurs, the average energy input will rise because some will be dissipated in channels that do not form part of the path of the final arc. Tang (10) has reported an almost

linear increase in streamer numbers with propagation distance in a uniform field which would support the concept of a constant unit critical energy. Since branching is unavoidable in most practical circumstances any realistic estimate of the breakdown energy required must include the associated losses. Although not included in Fig. 4. some recent measurements at 11 cm. confirm the working value of 1mJ/cm.

PEAK CURRENT i_p AND BREAKDOWN TIME T_B. Marode (11), again working with small (1-1.5 cm) point-plane gaps, established a definitive relationship between i_p and T_B which takes the form

$$\frac{i_p - i_o}{i_o} = \frac{A}{T_B^{\alpha}} \qquad (2)$$

where i_o is a minimum current for breakdown and A, α constants. ($A = 8 \times 10^{-3}$, $\alpha = 1.62$ provided T_B is measured in ns). This has not been confirmed by the present measurements, indeed the breakdown time is independent of i_p, which is almost constant and independent of gap size with a value of 60 - 70 mA.

If one ignores the small charge injected prior to the attainment of peak current then a good approximation to the unit critical energy W may be obtained as

$$W = \frac{E_B i_p}{\nu} \left[1 - \exp\left(-\nu T_B\right) \right] \qquad (3)$$

For $T_B > \frac{1}{\nu}$ and assuming a constant value for W then i_p should be independent of T_B. For air, $\nu \sim 10^6 s^{-1}$ so that, provided the breakdown time is greater than $\sim$1 μs, a constant i_p provides some support for the energy criteria. Using the values given above $W \sim 0.25$mJ/cm., in reasonable agreement with the measured value bearing in mind the dependence of W on the value of ν which itself is a sensitive function of E/N at the magnitude relevant to this experiment (i.e. E/N $\sim$ 50 Td). Of course, if $T_B < 1/\nu$ then with the same assumption of constant W, the reverse argument applies and i_p will be dependent on T_B. Marode's experimental results (equation 2) confirm this behavious, so that is is reasonable to conclude that the maximum current criteria is a manifestation of that based on energy.

DARK CURRENT i_c AND BREAKDOWN T_B. Although the unit critial energy is independent of the gap size, considerable variation in the breakdown time is apparent; generally this time increases with gap size. The 2 cm gaps exhibit times of 1-2 μs, as observed by Sigmond and Goldman and others, but at 5 cm times of 50 μs or more are common. If the gap is overvolted then shorter breakdown times result.

These times show a marked dependence on the magnitude of the dark current i_c (Fig. 5.) Although the dark currents tend to be grouped according to gap size with large currents

usually occurring in the smaller gaps, the occasional short time for a given gap is associated with an above average dark current (e.g. points A in Fig. 5.)

The origin of the dark current is not entirely clear although it must be electronic since ion mobilities are too low to sustain currents of a few milliamps. The prevailing experimental conditions suggest electron drift velocities of $\sim 5 \times 10^6$ cm/sec so any electrons created in the channel during the primary streamer transit will either have been swept out by the ambient field or attached to an electronegative molecule, such as O_2 to form a negative ion. Thus the electrons which constitute the dark current must either be generated within the channel itself, possibly by a detachment process, or injected from the cathode. Marode (7), drawing an analogy between a streamer channel and a glow discharge, suggests a high field cathode fall may be responsible for electron injection from the cathode. A small number of secondary electrons emitted at the cathode are multiplied by collisional ionisation before entering the channel proper; he finds a cathode fall of $\sim 400V$ over 3μ. However, in the absence of a cathode (e.g. surface streamers on a wind-shield or the corona-leader structure in long gaps) some internal mechanism, such as detachment, must be viable to ensure the breakdown. Gallimberti (12) has shown that the detachment lifetime of electrons from O_2^- decreases from $50\mu s$ at $700K$ to $1\mu s$ at $1000K$ when the degree of detachment is about 5% of of the negative ion population and rises rapidly with temperature. Marode et al (9) and Bastien and Marode (13) have calculated the anticipated channel temperatute in specific cases to be several hundred degrees which is sufficient to allow some contribution by detachment to the dark current. Of course, maintaining a dark current of a few mA does not explain the onset of the breakdown. The channel conditions during the dark period suggest an electron density of between 10^{13} -10^{15}cm.$^{-3}$ whilst 10^{17} cm.$^{-3}$ is considered the minimum for breakdown. The most promising explanation for this sudden increase is that of Rogoff (11) for hydrogen and Marode, Bastien and Bakker (9) for air which depends upon a decrease of the channel gas density N following an expansion of the neutral species due to the energy released in the channel. At constant field this causes an increase in E/N so that $\alpha-\eta > o$ and collisional ionisation leads to the final current growth. For this to occur a certain minimum energy must be supplied to the channel which provides at least qualitative justification for the critical energy concept. Ignoring losses due to radiation and conduction a simple estimate of the rise in channel temperature ΔT is

$$\Delta T = \frac{fW}{\pi a^2 \rho s} \qquad (4)$$

where a is channel radius, ρ gas density and s specific heat. f is the fraction of the available energy which contributes to the translational and rotational energy of the gas molecules and hence the gas temperature. In the short gaps for which calculations have been made, $f < 0.05$; the bulk of the remainder being stored in the vibrational states of the molecule. With $f = 1$ and $a = 30\mu$ equation (4) yields $\Delta T \sim 1500K$ using the minimum value for W of $50\mu J/cm$. so that when the vibrational energy is made available a substantial temperature rise should occur. The time constant for vibrational relaxation $T_v >> T_B$ for short gaps which effectively prevents the vibrational energy contributing to the breakdown process. At 600K this relaxation time is $\sim 50\mu s$ and falls with increasing temperature which suggests that large amounts of energy may be dumped in the channel provided dark currents continue to flow for such a time and thus maintain the channel temperature. As seen from Fig. 5. this is possible for streamer channels >3cm.

CONCLUSIONS

The energy required to give a positive streamer-spark transition has been measured and, for breakdown paths greater than 3 cm. is proportional to the length of the path; at 300 torr the energy required is $\sim 1mJ/cm$. Breakdown time T_B increases with length and correlates well with the magnitude of the dark current. For $T_B < \nu^{-1}$ the breakdown time depends on the amplitude of the initial streamer current but is independent of this current for $T_B > \nu^{-1}$. This suggests that the shorter breakdown times occur when there is initially a sufficiently large energy input to achieve the required rise in channel temperature otherwise the breakdown is delayed until the molecular vibrational energy is available.

REFERENCES

1. R.L. Tanner and J.E. Nanevicz, Proc. IEEE, 52,1, 1964
2. J. Boulay, La Recherche Aerospatiale (1979), p. 101.
3. J.E. Nanevicz AGARD-LS-110, 12-1. 1980.
4. J. Taillet, AGARD-LS-110, 11.1, 1980.
5. Renardiers Group, Electra 23, 53-157, 1972.
6. A.Gibert and B. Dupuy, J. Phys. D. 43,21,1983.
7. E. Marode, J. Appl. Phys. 46, 2005-2015,1975
8. R.S. Sigmond and M. Goldman, Proc.III Int. Symp on Gaseous Dielectrics, Knoxville Pergamon, New York, 1982
9. E. Marode, F. Bastien and M. Bakker, J.Appl. Phys. 50, 140-146 (1974)
10. T.M. Tang. Ph.D. U.M.I.S.T., Manchester 1982.
11. G.L. Rogoff, Phys. of Fluids, 15, 1931-1940, 1972
12. I, Gallimberti, Journal de PhysiqueColloque C7 Supplement, 40, 193, 1979.
13. F.Bastien and E. Marode, private communication.
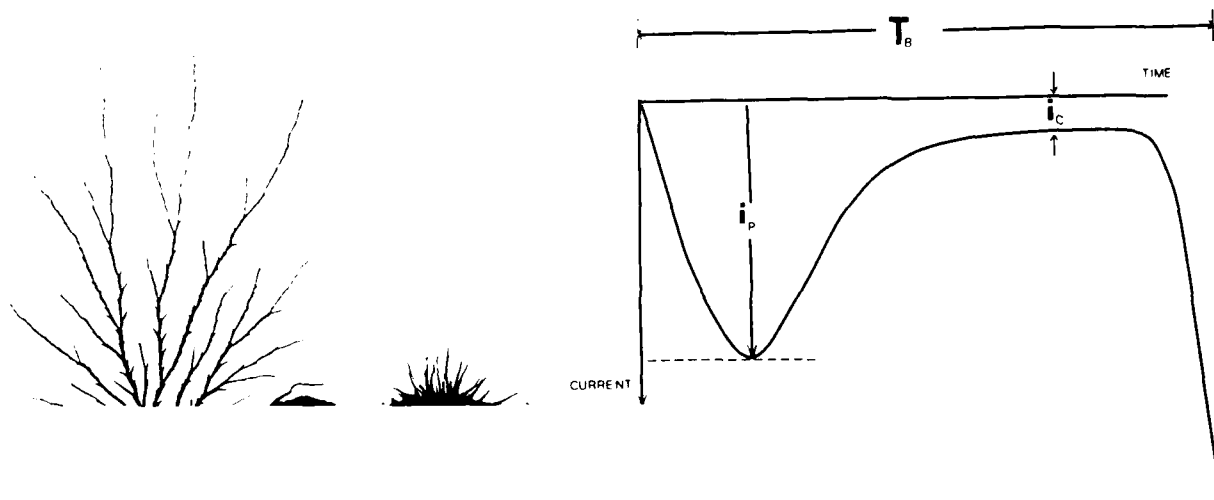
Figure 3
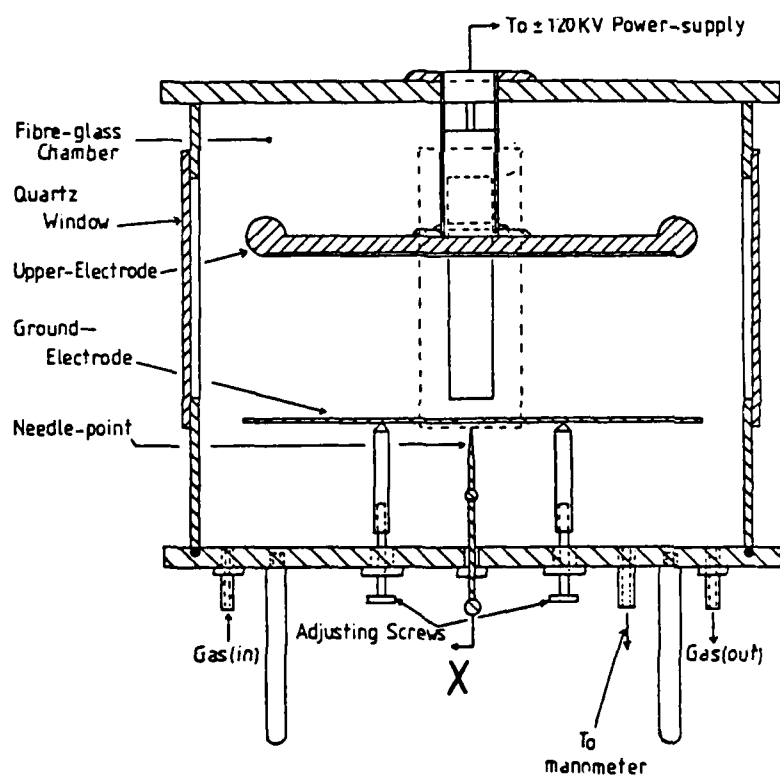
Figure 2

Figure 5

Figure 4

42-6
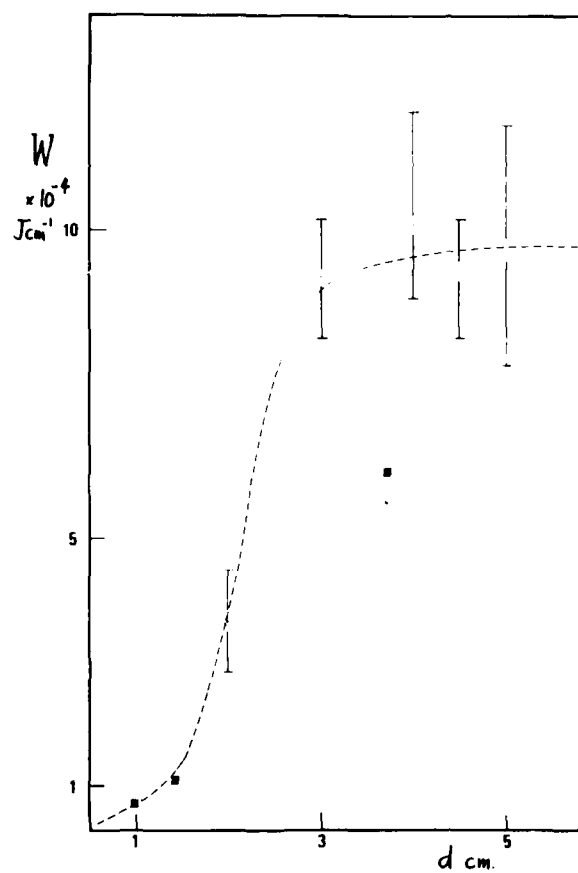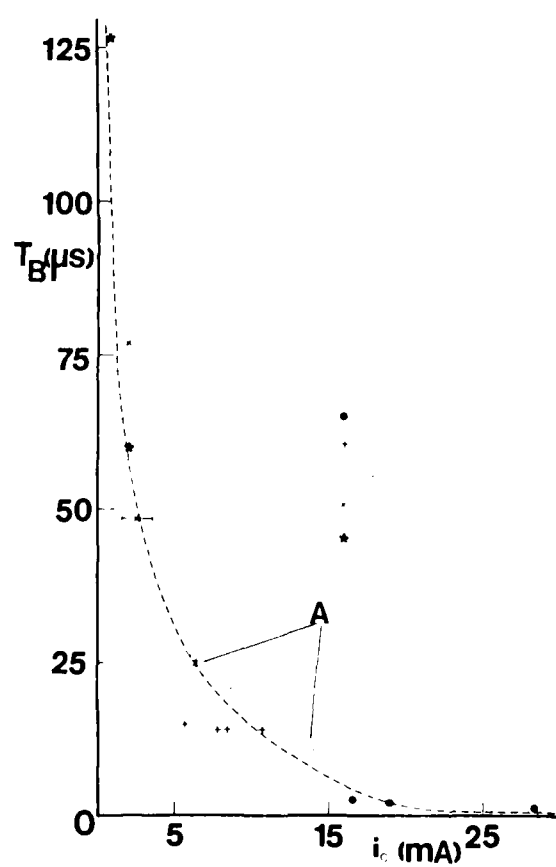
LIGHTNING SHOCKWAVE EFFECTS ON AIRCRAFT FUEL VENT LINES

By

T. S. LEE

University of Minnesota, Minneapolis, Minnesota, U.S.A.

and

J. D. Robb

Lightning and Transients Research Institute
St. Paul, Minnesota, U.S.A.

ABSTRACT

Earlier studies of lightning effects on aircraft fuel vents have shown evidence of very high flame propagation rates suggesting the presence of combined ignition-detonation waves. Substantial mechanical damage has been done to the vent outlets indicating abnormally high pressures. This problem has been evaluated in terms of basic shock phenomena in relation to possible hazards to fuel vents on aircraft. The results of this investigation showed that lightning strikes need to be separated as widely as possible from fuel vent outlets in order to prevent "Run-up" phenomena in which a combustion wave from the vent outlet increases in velocity to a fully developed detonation wave with its associated extremely high pressures and temperatures.

IN LIGHTNING STRIKE RECORDS for commercial airliners accumulated over the last eighteen years, no known commercial airliner losses have been attributed to lightning effects on aircraft fuel vents. However, fuel systems remain of primary concern as they properly should, particularly with the new composite materials and construction. One phenomenon which remains to be more fully investigated, even though no problems have been noted in aircraft accident or incident reports, is that of lightning shockwave effects on fuel vents.

An early paper (1)* suggested very large shock pressures from nearby lightning strokes based on the spectral analysis of natural lightning and the assumption that most of the channel thermal energy was converted into shock pressure. Shock pressures sufficient to break up brick walls were postulated from 30,000 ampere natural lightning discharges at distances of a few meters. LTRI tests with 200,000 ampere laboratory lightning discharges showed no such large effects and reasons for the reduced pressures measured in the laboratory discharges as shown in (Fig. 1) were postulated (2). These included possibly increased equilibration times and most probably less-than-total energy conversion into shock pressures. Energy balance considerations have been more recently addressed in (3) by R.D. Hill.

Earlier tests of lightning strike effects on

----
*Numbers in parentheses designate References at end of paper.

aircraft fuel vents (4) have shown the existence under some circumstances of extremely high pressures sufficient to cause extensive mechanical damage to a vent outlet as shown in (Fig. 2). Studies were carried out which suggested that shock wave-detonation interaction could be primarily responsible for such pressures. The basic mechanisms of shock propagation have been studied in relation to mechanical damage to the vent systems and to the effectiveness of flame arresters as discussed in this paper.

Flame arresters operate on the principle of absorbing more heat out of the flame front region by conduction into the arrester grid than is generated in the flame front. The flame front passing into the arrester is quenched by heat transfer into the flame arrester walls. The effectiveness of any flame arrester depends on the velocity of flame travel through the grid as a result of fuel tank breathing or ignition in the vent outlet, as well as the flame front temperatures. Fast passage of the burning vapor through the grid requires a greater depth of grid than does a slow front velocity because of the reduced heat transfer at the higher velocity.

Most flame travel occurs in free and non-turbulent air at less than 75 miles per hour. The older wire-mesh-screen type of flame arrester may be adequate for stopping the flame fronts with relatively low velocities. Burying the simple screen arresters a few feet inside of a vent, however, results in arrester failure as the flame becomes driven by the heated gas and passes

too quickly through the screen to transfer sufficient heat for quenching the flame.

Also, even if the flame screen is mounted at the outlet and a stationary flame is held at the grid, the flame can continue to burn and heat up the simple grid to a temperature at which ignition occurs on the back side of the screen. The flame can then continue into the vent.

The modern honeycomb type of flame arrester can be sufficiently deep that the heat flow into the long walls is sufficient to quench a flame as discussed in (5) and illustrated in (Fig. 3). This type of arrester can therefore withstand substantially greater flame front velocities than can the simple screen arrester and it has much improved flame holding properties as well.

A major question that has been raised is that of possible over-pressures from a lightning-induced detonation wave which might exceed the capability of a honeycomb type arrester. The theoretical survey and analysis of shock-detonation interaction, as presented in the Appendix and illustrated in (Fig. 4), suggest that an over-driven detonation wave will generally attenuate down to a detonation wave.

A recent study of the effect of shock detonation waves, in flame arresters have indicated that some arresters do indeed prevent the passage of detonation waves (6). The flame arresters do appear to be effective in providing complete protection if they are properly installed with no gaps around the outside of the arrester which could permit flame passage around the outside. Presumably the detonation wave triggered by a lightning shock wave would decay, even if the initial pressures exceeded that of the detonation wave, into a normal detonation wave after some distance of propagation. However, this point needs to be experimentally resolved in view of the extreme pressures and damage reported in aircraft fuel vents from this combination of lightning shock waves and detonation (1).

CONCLUSIONS

There has been a good record of aircraft fuel systems in the presence of lightning over the past 18 years. However, the new materials and construction of aircraft with composites suggest that a basic understanding of lightning shock interaction with flame fronts at a vent outlet is required to assure that no new problems are introduced by the new materials and construction techniques.

The basic recommendation for vent location remains unchanged. Until vent phenomena such as lightning shock-detonation interactions are better understood, vent outlets should continue to be located as far as possible from lightning direct attachment points in order to minimize possible generation of overdriven detonation-shock waves in vents.

APPENDIX

DETONATION AND SHOCK WAVES

The modern hydrodynamic theory of combustion and detonation is well established, both theoretically and experimentally (7). To briefly illustrate the essential concepts germane to the problem under consideration, (Fig. 4) shows, in a pressure-inverse density $(P - 1/\rho)$ diagram, a Hugoniot curve, for a given reaction heat release per unit mass and for a given initial state (P, ρ).

There are two ranges of this curve in which reaction wave propagation is physically possible - the upper corresponding to detonation waves and the lower corresponding to deflagration waves (flames). The upper range is limited by Rankine lines labelled 1 and 3 and the lower range is limited by Rankine lines labelled 4 and 6. The part EF of Hugoniot curve implies unphysical mass fluxes and is hence without physical interest.

Consider the intermediate Rankine line labelled 2. It cuts the Hugoniot curve at two points, A and B, suggesting two possible detonation states. Point B denotes a weak detonation whereas A denotes a strong detonation. As the slope of line 2 is reduced, A and B approach one another to finally coincide at I as the mass flux approaches that corresponding to line 3. Point I is known as Chapman-Jouget (C-J) detonation state. Similarly, when the mass flux is low, for any Rankine line falling between 4 and 6 there occur two possible (C and D) deflagration states. The lower state is known as weak deflagration and the upper one, strong. As the mass flux is gradually increased, these finally approach the C-J flame state at point II. From entropy considerations, it could be shown that states of weak detonation and deflagration corresponding to sections of the Hugoniot curve, between I and E and below II respectively, are unstable and are physically unattainable.

In the hydrodynamic or Zeldovich-von Neumann picture of a detonation wave, at first compression and heating of the medium by means of a shock wave take place, then ignition and burning of the mixture. The cause of the chemical reaction is the heating of the medium being compressed by the shock wave. In the case of shock compression, both pressure and temperature are much higher than for ordinary adiabatic compression. They are even higher yet for a higher wave velocity. The detonation wave travels at a supersonic velocity. On the other hand, a normal flame propagates at a subsonic velocity and its associated pressure differentials are typically negligible.

It is well known experimentally that an overrich or overlean mixture will not support a stable flame. There exists an inflammability

range to the mixture concentration. The concentration range allowing propagation of the detonation wave, i.e., within which the mixture has the ability to sustain an already created wave, defines the limits of detonability. The limits are naturally narrower than the ordinary limits of inflammability. For hydrogen-air mixtures, for example, the lower limit of inflammability is about 9% and the lower detonation limit is about 18-20%.

Flames propagate at subsonic velocities. As such, the flame front is capable of emitting compressive wavelets ahead of it, giving rise to the possibility that a shock wave may be formed in finite time as a result of nonlinear wave accumulation.

Detonation does not always occur. For it to begin, the mixture must be detonable and the required physical conditions must exist. As to the latter, two separate ways of creating detonation are to be distinguished: the spontaneous development of detonation during normal burning, say in the case of a flame propagating in a long tube, and the creation of a detonation wave due to the action of a powerful shock wave. In the first case the concentration limits within which spontaneous detonation may occur have been called the explosion limits or explosion range; in the second case, the limits of detonability or detonation range. These are, conventionally, more loosely referred to as conditions for self-ignition and forced ignition.

Self-ignition, i.e., transition to detonation from a flame, has recently been investigated by Bjorkland and Ryeson (6). They have developed empirical data on the predetonation distance for flowing mixtures of gasoline and air in 6 inch diameter piping at atmospheric conditions. This 'run-up' distance was found to be on the order of 11 meters. Also, they found that only a small fraction of the flame cases lead to self-ignition. We note that this result is in agreement with the recognition that the limits of explosion are in general narrower still than the limits of detonation.

Let us return now to (Fig. 4) for a closer examination of the physically allowed detonation waves. It is seen that the C-J condition (point I) represents the slowest possible detonation. It is noteworthy that data on limits of detonability have all been confined to the C-J type of detonation wave. Detonation waves moving with higher velocities all belong to the class called strong or overdriven detonation (IA and up). In contrast to the C-J detonation for which postdetonation products expand sonically, these strong detonation waves have the ensuing products moving away subsonically. Hence, the local condition resembles that found immediately behind a shock wave driven by a pistonlike source. As the pulse driving weakens progressively, the postdetonation state approaches the sonic

condition gradually. In the limit, the C-J detonation is reached and the front velocity falls down to its stable detonation value (usually referred to as the detonation velocity).

Hydrodynamic phenomena which have the character of an explosion also arise in air in connection with spark discharges. These were studied by Mandel'shtam and his coworkers (8 - 13). We present here the general picture of the process. A thin electrically conducting column is formed in the air between the electrodes immediately after the discharge. As a result of Joule heating the air in this column is heated to temperatures of the order of many tens of thousands of degrees and is strongly ionized (at least singly). Propelled by thermal expansion, the column expands and acts on the surrounging air like a piston, sending into it a cylindrical shock wave. (After the shock wave travels a distance far exceeding the column length, it gradually becomes spherical.)

In the early stages the air density distributions with respect to radius have a character appropriate to a cylindrical blast wave. Dolgov and Mandel'shtam (11) measured these distributions at successive times by interferometric methods, according to the following electrical circuit parameters in the experiment: C = 0.25 µf, L = 2 µh, V = 10 kv and a discharge gap of 5 mm. The conclusion was that, at the beginning when the shock wave is still strong (the velocity > about 2 km/sec) the density distribution corresponds to that in a strong line explosion (14). At a later stage, the wave weakens and the counter pressure of the air ahead of the shock wave begins to have an effect. In this case the density at the periphery of the blast wave does not differ greatly from standard density, while in the central regions the density is very low. Since the pressure behind the blast front is, roughly speaking, equalized spatially, the temperature in the central regions is very high. This central, strongly rarefied and high-temperature core is the electrically conducting column. The average density of air in the column is approximately 10-3 of that in the undisturbed air, and the average temperature is approximately 40,000 degrees K. Spectroscopic measurements give consistent results. (Thermodynamic equilibrium in the column is established quite rapidly (12,13), making it possible to determine the actual gas temperature by spectroscopic means.)*

The theory of the explosion wave due to a spark discharge was developed by Drabkina (9). It should be noted that the flow differs somewhat

---

*It should be noted that Hill and Robb (15) have argued against the assumption of electron thermal equilibrium in the lightning discharge column, implicating a much lower effective temperature and hence a much reduced mechanical effect during column expansion.

from that which takes place with an instantaneous energy release, since in the given case the time for Joule heat generation, which is determined by the half-period of the discharge, is comparable with the time over which the shock wave is observed. With this taken into account, the rate of energy generation was determined experimentally from shock trajectory data.

Phenomena which are similar to those investigated in the laboratory, but which take place on a much larger scale, are encountered in a storm. Lightning is simply an electrical discharge and the thunder is produced leading to a shock wave which is formed and which degenerates into an acoustic wave at large distances. Zhivlyuk and Mandel'shtam (1) measured by spectroscopic means the average temperature in a lightning column, and found it to be approximately equal to 20,000 degrees K. This value is in agreement with calculations based on formulas given by Braginskii (16) assuming for typical values of the current and time the values 30 kamp and 100-1000 usec (the radius of the lightning column is 10 cm). Estimates of the pressure behind the shock front were found to be such that at distances of the order of several meters the thunder can be quite destructive.

It is possible to give a rough quantitative estimate to the extent of front propagation after which the counter pressure effect begins to weaken the leading shock wave. In line with the second-order cylindrical blast wave decay theory (14), we have in the physical problem a characteristic length.

$$R_1 = (E / P_0)^{1/2} ,$$

where E is the effective lightning blast energy per unit length and P0 is the atmospheric air pressure. Typically E is on the order of 30 to 300 Joules/cm for a lightning strike. The corresponding length scale R is on the order of 70-200 cms. Until the propagation expansion is beyond R1, the shockwave remains strong.

Strong radial expansion of a lightning column in a detonable mixture can be approximately likened to a pistonlike driving pulse. The principal physical phenomenon is hydrodynamic in nature. In the early phases when the detonation wave is heavily overdriven, the heat released at the detonation wave front is unimportant when compared with that deposited in the lightning column core and the classical blast wave theory provides a good description. Subsequently, this heat becomes more and more important as the core expansion slows down, until eventually the detonation wave becomes self-sustaining and C-J in character.

The C-J condition corresponds to the limit of the progressive process of a core-rarefactive effect overtaking a driven detonation front from

behind. If the predetonation mixture has a mass density and a latent chemical energy available for release W per unit mass, then, a second physical length scale

$$R_2 = (E / W)^{1/2} ,$$

say, exists in the problem. At this extent of cylindrical expansion, the total energy released chemically through detonation becomes comparable in importance to the energy deposited by the lightning pulse. Thus, it may be regarded as the minimum distance it would take for a storing blast wave to gradually settle down to a mode of stable detonation propagation. Typical values appropriate for a detonable hydrocarbon mixture at standard atmospheric pressure and temperature lead to range of 10-25 cms for R_2.

We now reemphasize the relative limits of explosion, detonation and flame in mixture concentration in a practical situation. From the qualitative exhibit of (Fig. 5), we recognize that only a fraction of inflammable mixture concentrations are inherently capable of shock-triggered detonation. Within the latter class, only a portion are inherently capable of self-explosion (flame to detonation transition). Conversely, a mixture free of self-explosion possibilities may still be vulnerable to the detonative initiation of a driving shock wave. For aircraft fuel vent lines, there is the question of possible over-pressures from a lightning-induced detonation wave which might exceed those of the simple C-J detonation wave for which the conventional flame arresters have been tested. In light of the foregoing discussions in the present section, several aspects of that question can be addressed:

1. When atmospheric conditions are such that there is spatial gradation of fuel-mixture concentration along the tube, leaner toward the vent opening, there is the possibility of flame ignition by shock wave somewhere inside the tube. If the tube length is large enough, greater than a few meters, say, there further exists the possibility of having detonation waves generated by self-ignition.

2. If concentration around the vent opening is already detonable, a detonation wave can be expected as a result of a lightning-induced shock wave emitted from a strike point within meters away from the vent. In this case, a near-stable detonation wave may propagate into the vent tube through the opening.

3. If the strike point is very near (within a quarter of a meter or so, say,) and if the atmospheric conditions of detonability happen to prevail out to a few meters from the vent opening, then the detonation wave resulting from the lightning-induced column expansion can be highly overdriven. It is conceivable that the process of slowing down to a stable C-J

detonation on the part of the overdriven detonation wave may not have reached completion before wave entry into the vent tube. In this case, the detonation wave would continue to travel in the tube in an overdriven state over some additional distance. It is important to note that data on the effectiveness of flame arresters as supressors of overdriven detonation waves are lacking in the literature.

In conclusion, we observe that the probability of development and propagation of lightning-initiated detonation waves in the vent tube, even overdriven ones, cannot be discounted outright. Questions concerning possible schemes of prevention or suppression in an existing vent tube-flame arrester system warrant more detailed investigations.

REFERENCES

1. Zhivlyuk, Yu. N., and Mandel'shtam, S.L., "On the temperature of lighting and the force of thunder" JETP 13, 338-340 (1961).

2. Robb, J.D., "Lightning protection of dielectric composites" SAE, 14th Stapp Car Crash Conference, December, 1971.

3. Hill, R.D., "A survey of lightning energy estimates" Rev. Geophysics and Space Phys. 17,155 (1979).

4. Newman, M.M., Stahmann, J.R., Robb, J.D., "Airflow Velocity Effects on Lightning ignition of Aircraft Fuel Vent Efflux" Federal Aviation Administration Report No. DS-67-9, Project No. 520-002-05X, Contract No. FA66WA-1486, July 1967.

5. Bolta, C.C., Friedman, R., Griner, G.M., Markels, Jr., M., Tobriner, M.W., and von Elbe, G., "Lightning Protection Measures for Aircraft Fuel Systems; Phase II" Federal Aviation Agency Report No. FAA ADS-18, Contract No. FA64WA-4955, May 1964.

6. Bjorklynd, R.A. and Ryeson, P.R., "Detonation-Flame Arrester for Gasoline Cargo Vapor Recovery Systems" Final Report JPL 80-18 for U.S. Department of Transportation (Jet Propulsion Laboratory, California Institute of Technology, 1980).

7. Khitrin, L.N., The Physics of Combustion and Detonation, Office of Technical Services, U.S. Department of Commerce, Washington, D.C., 1962.

8. Abramson, I.S., Gegechkori, N.M., Drabkina, S.I., and Mandel'shtam, S.L., "The passage of a spark discharge" Zh. Eksperim. i Teor. Fiz. 17, 862-867 (1947).

9. Drabkina, S.I., "The theory of the development of a spark discharge column" Zh. Eksperim. i Teor. Fiz. 21, 475-483, (1951).

10. Gegechkori, N.M., "Experimental investigation of a spark discharge column" Zh. Eksperim. i Teor. Fiz. 21, 493-506 (1951).

11. Dolgov, G.G., and Mandel'shtam, S.L., "Density and temperature of a gas in a spark discharge" Zh. Eksperim. i Teor. Fiz. 24, 691-700 (1953).

12. Mandel'shtam, S.L., and Sukhodrev, N.K., "Elementary processes in a spark discharge column" Zh. Eksperim. i Teor. Fiz. 24, 701-707 (1953).

13. Sukhodrev, N.K., "On excited spectra in a spark discharge" Tr. Fiz. Inst., Akad. Nauk SSSR 15, 123-177 (1961).

14. Sakurai, A., "Blast Wave Theory" in Basic Developments in Fluid Dynamics, Vol. 1, Ed. M. Holt (Acad. Press, 1965).

15. Hill, E.L., and Robb, J.D., "The pressure pulse from a lightning stroke" J. Geophy. Res. 74, 3426-3430 (1969).

16. Braginskii, S.N., "Theory of the development of a spark channel" JETP 7, 1068-1074 (1958).
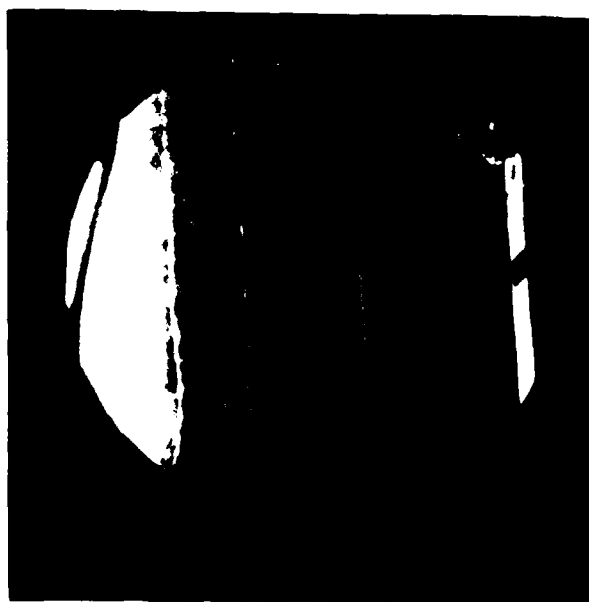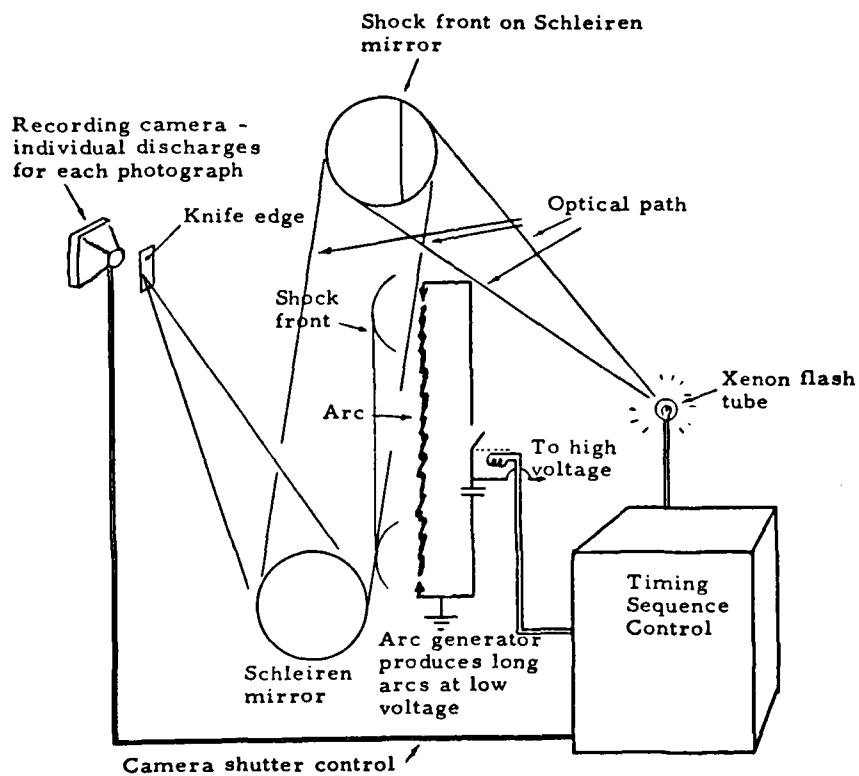
Fig. 1a – Schlieren measurments of labortory lightning shock (from reference 2)
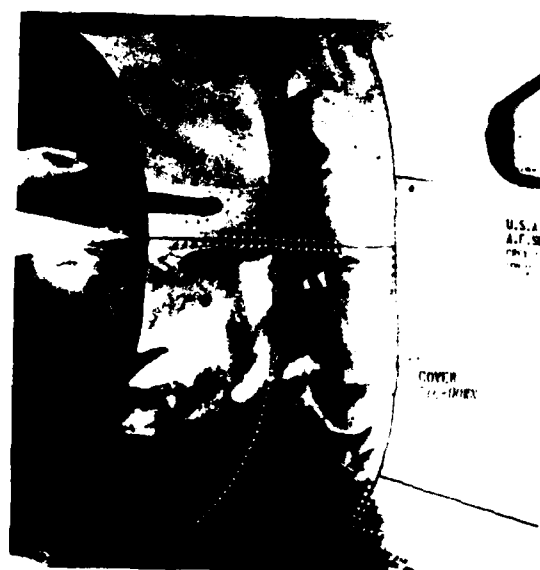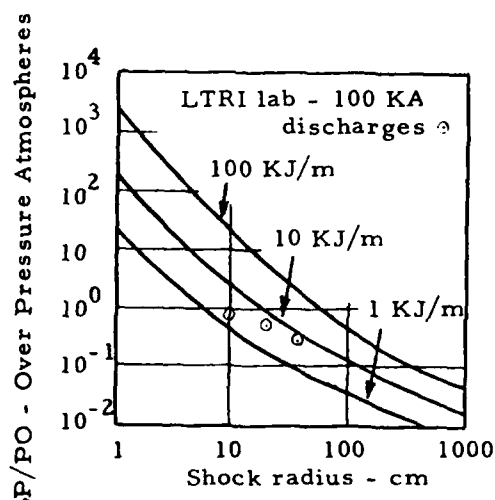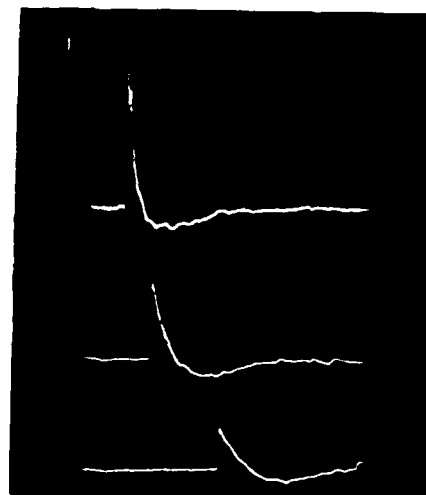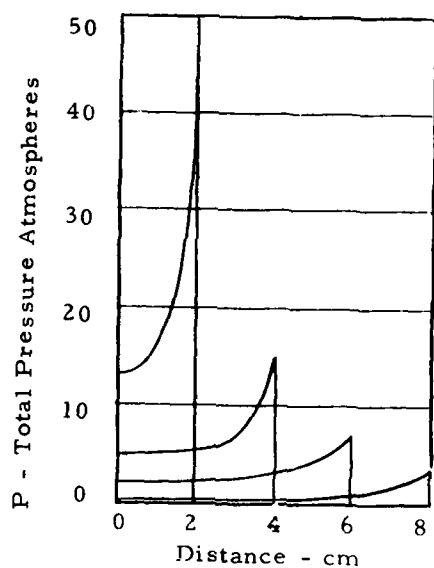
Figure 1b.   Theoretical and Experimental Shock Profile Measurements
in the Laboratory Compared with In-flight Aircraft Damage.

Fig.   2a   – Normal   vent   tube   outlet   before   Fig. 2b – Close-up of vent tube outlet slot after
explosion   explosion
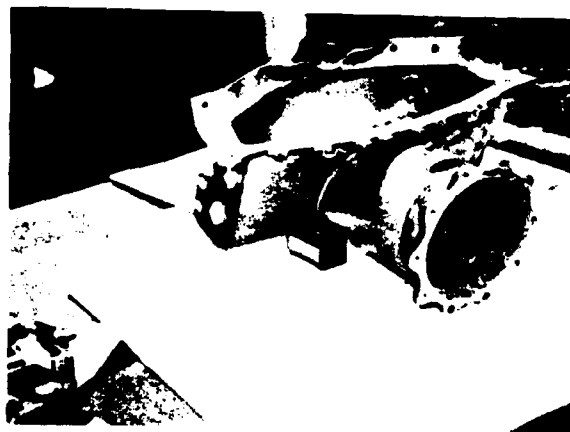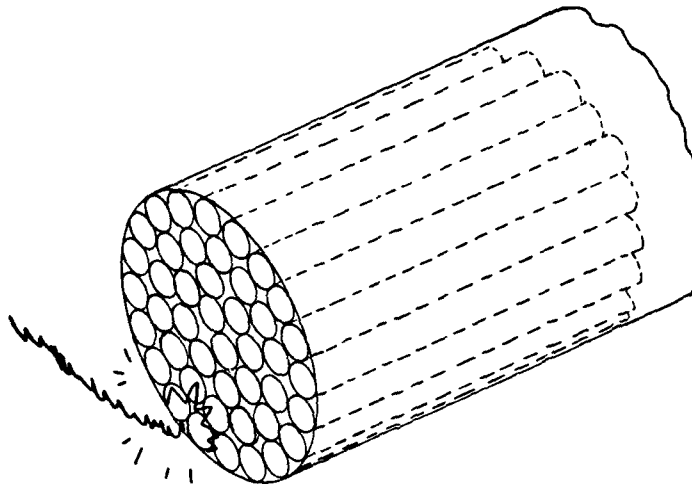
Fig. 3 - Honeycomb type of flame arrester has deep section to absorb heat and quench flame more efficiently - arrester may be located at outlet or deep in vent
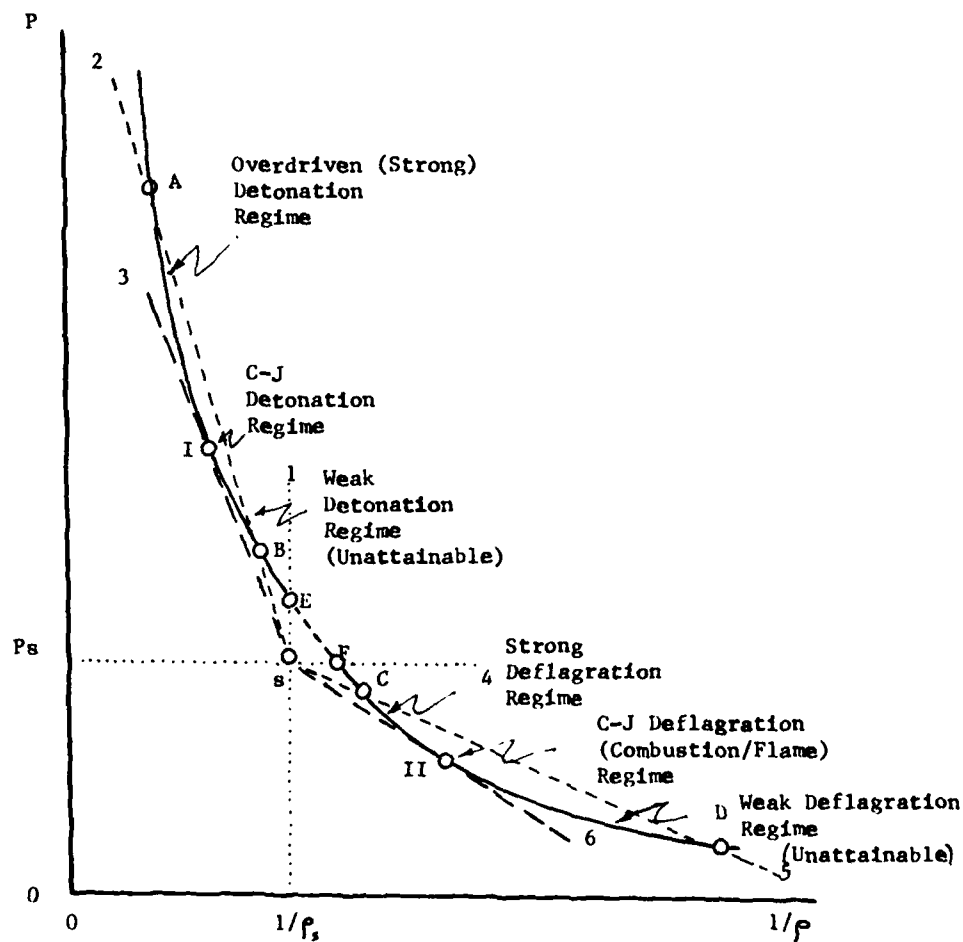
Fig. 4 - Hugoniot curve on a P vs $1/\rho$ plane to distinguish between detonations and flames
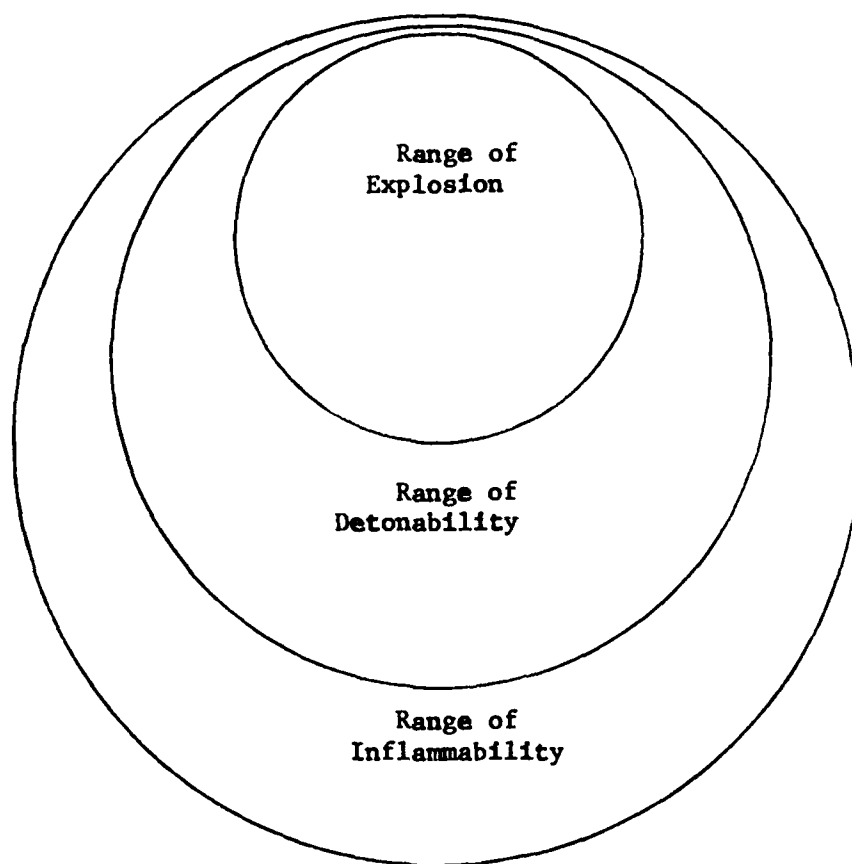
Figure 5. The Relative Ranges of Inflammability, Detonability and Explosion in Mixture Concentration.

AN OVERVIEW OF THE F-14A AND F/A-18A LIGHTNING TESTS

R. A. Perala and C. C. Easterbrook
Electro Magnetic Applications, Incorporated, Denver, Colorado

ABSTRACT

During the spring and summer months of 1982, various low
and high level current injection tests were accomplished on the
F-14A and F/A-18A aircraft. The intent of this paper is to present
an overview of the tests and a summary of some of the more signifi-
cant results. The low level tests included swept CW, a fast (~300 ns)
risetime test, and a nuclear EMP related test referred to as the
Surface Current Injection Technique (SCIT). High level pulses up
to 173 kA with a 10-90% risetime of 1.7 μsec were injected into a
powered up active aircraft. Shock excitation tests were also
performed with voltages on the aircraft on the order of 1 MV.
Comparisons between low and high level, fast and slow risetime,
and CW and pulse responses are summarized. In addition, because
the two aircraft afford an opportunity to compare metal and carbon
fiber composite (CFC) construction, comparisons between the two
aircraft are given.

.

This paper was not available for incorporation into this book.

UHF INTERFEROMETRIC IMAGING OF LIGHTNING

by P. Richard, A. Delannoy, G. Labaune, P. Laroche

Office National d'Etudes et de Recherches Aérospatiales (ONERA)
BP 72 92322 CHATILLON CEDEX

ABSTRACT

ONERA has operated in Ivory Coast in 1981 and in the United States in 1982 a lightning imaging system. This system is an UHF interferometer which gives the location of the emitting sources all along the various phases of the lightning discharge. The corresponding set-up is described with emphasis on the means used for increasing the accuracy. Examples of results obtained both with natural and triggered lightning strokes, and correlation of these results with E field measurements will be presented.

AN ELECTROMAGNETIC LIGHTNING IMAGING SYSTEM using interferometric measurements was developed at ONERA (Office National d'Etudes et de Recherches Aérospatiales). This equipment was first experimented in 1981 during the COPT (Tropical Deep Convection) campaign in Ivory Coast, in complement to a field meters network for monitoring the global electrical activity of storms. In 1982, the system was used at the Langmuir Laboratory, Socorro, New Mexico for the observation of triggered lightning flashes.

We will present here typical results obtained during these two campaigns, with particular emphasis on the phenomenology ; the analysis has been obtained through correlations with E field measurements.

DESCRIPTION OF EXPERIMENTS

INTERFEROMETRIC SYSTEM – In its principle, the interferometric location is based on the measurements of the phase difference of an incident plane wave upon a couple of antennae. The angular location of a source is obtained with two interferometric couples constituted by a three antennae system. The interferometer is built with two complementary systems : a large one with a 10λ baseline for an accurate but ambiguous location of sources (since phase measurement is obtained with a 2π ambiguity), and a small system with a λ baseline for ambiguity removal. At our receiving frequency (300 MHz), the baselines are thus 1 and 10 m long (Fig. 1).

The system optimization has been performed taking into account the instrumental and source parameters [1][*]. A basic assumption is the "point source hypothesis" i.e that within our time resolution, the source can be considered as a unique point source within to the angular resolution. It is anticipated that this condition is fullfilled with a 1 μs time resolution.

Among instrumental parameters influencing phase measurements accuracy, particular emphasis was devoted to the coupling between antennae for the small system, to instrumental phase errors associated with cables and electronics and to baseline dimensional uncertainties. All these errors were reduced at the data processing phase either through corrections (for coupling), or calibration for other instrumental errors. The nominal resulting angular accuracy is 5.10^{-3} in direction cosine.

The principal source parameters are the signal nature and the source size when not a point source. Provided the condition $(b/\nu_0)(D/\lambda) << 1$, it can be shown that phase errors due to the loss of correlation between antennae, depending on signal nature (noise waveform, pulses), is negligible compared to other contributions (b is the receiving bandwidth, ν_0 the central frequency and D/λ the baseline size in wavelength unit). Extended sources, within a μs, would be plotted as a point source at the source center of mass.

Independence with respect to the signal nature is one of the most important feature of the interferometric measurement : while other location methods such as hyperbolic location or DTOA (Difference in Time Of Arrival) depends on amplitude and shape of the signal for correlations leading to delay measurements [2, 3, 4, 5], the interferometric location uses only the phase information of signals, thus permitting a high dynamic acquisition (80 dB in our case through the use of limiter amplifiers) leading in a continuous way, unlike other methods, to the source location with a 1 us time resolution.

An example of data processing is presented in figure 2 ; we can see the different steps, from the raw phase data (in sine and cosine), to the image reconstruction ; we see in particular the

[*] Numbers in parentheses designate References at end of paper.

improvement when reconstruction uses the large system data.

Performances limitations are :

- sensitivity limited to 1 µV/m.kHz at 300 MHz

- problems of ambiguity : still the small system has three remaining ambiguities ; in a few cases, ambiguity removal was not possible when we observed scattered successive sources all over the celestial sphere,

- lack of distance information ; nevertheless in some cases, this information is brought back by charge location from the E field sensor network, which is used for the calculation of propagation velocities of emission phenomena, (the minimum velocity inferred from this distance measurement is given in each case).

In 1982, the system has been improved by removing the ambiguity : - a (λ/2) baseline was used, and in 1983, the sensitivity is being increased up to 10^{-2} µV/m.kHz ; a real time digital data acquisition and pre-processing sub-system is being added ; 3-dimensional location will be possible using two 10 km apart interferometric systems, both giving angular images of lightning.

E FIELD SENSORS NETWORK - A ten stations network for E field measurements at ground level was implemented, during the COPT experiment, within a 32 x 32 km area (Fig. 3). Each station comprised a field mill sensor with a $\pm$30 kV/m dynamic range, and a capacitive antenna with data acquisition at 3 different sensitivities : $\pm$ 30, $\pm$ 300 and $\pm$ 3000 V/m (the damping time constant had been set to 10 s). All signals were sampled at a 800 Hz rate. These measurements have been mainly used during two phases of the lightning flash : first, for the analysis of the slow charge evolution within thunderstorm clouds ; secondly, for the modelization of lightning discharges either with unipolar model for cloud-to-ground stroke, or dipolar model for intracloud activity. [6]

The results have been correlated to the interferometric locations of electromagnetic sources at 300 MHz ; we will essentially present here the observed phenomena related to the different phases of the lightning discharge.

2. RESULTS ANALYSIS

For the COPT experiment data processing, our attention was focused on two events representative of the different types of thunderstorms in this region : a storm resulting from diurnal convection, and a squall line storm. A total number of 23 discharges has been studied, most of them of the intracloud type. Though we cannot pretend to an exhaustive phenomenologic description of lightning with such a limited number of events, some characteristic electromagnetic phenomenon have been observed in the different discharge phases leading to interesting comparisons with E field variations and neutralized charges locations.

GENERAL REMARKS - The signal appears to be made of a series of pulses, with pulse width usually not exceeding the time resolution (1 µs).

According to the pulse rate, the emission phases can be classified on two types : either low rate pulse radiation, or high rate pulses bursts.

Low Rate Pulses Radiation (Fig. 4) is characterized by less than 15 pulses/ms ; this radiation can last up to several hundred ms ; it is mostly associated with spread out sources presenting low drift angular velocity, and are observed usually during breakdown phases of both cloud-to-ground and intracloud discharges. They are simultaneous to slow E field variations of large amplitude (up to several tens of kV/m) corresponding to intracloud neutralizations.

Pulses Bursts (Fig. 4) - At 300 MHz, these phenomena appear as the most intense radiation ; they usually last several hundred µs with a mean time between pulses of 2 to 4 µs. These bursts are associated with fast propagation of sources (10^6 to 7.10^7 m/s) over large distances (up to 10 km) either within the cloud or between cloud and ground. All propagations are observed in only one direction at a time. They occur in all phases of a lightning (breakdown, leader, dart leader, intracloud), and are always associated with small E field steps of the order of 100 V/m corresponding to small amounts of charge transfer or neutralization. When associated to large E field slow changes, they frequently occur after the largest variations.

TYPICAL OBSERVATIONS ASSOCIATED TO THE DIFFERENT PHASES OF THE DISCHARGE -

Intracloud Activity - Both types of radiation are observed during this type of discharges. During the first few hundreds ms, we observe a low rate radiation simultaneous to large E field variations. The associated UHF sources locations are spread out over distances which can be estimated from a km to several km and present apparently slow drift velocities ($\sim 10^4 - 10^5$ m/s). Usually, bursts are observed in the last hundreds ms of the discharge, following large E field variations ; the associated sources propagate at high speed ($>10^7$ m/s) within the volume concerned by the previous breakdown processes (Fig. 5).

From their similitudes in electromagnetic and E field signatures and chronology, these phenomena can be compared to the K process [7, 10] associated to recoil streamers. It is interesting nevertheless to point out the difference, of an order of magnitude, between estimated velocities for electromagnetic sources ($\cdot 10^7$ m/s) and velocities currently presented for recoil streamers ($1-4.10^6$ m/s) [7]. Similar phenomena qualified as "Q noise" [8] or "solitary pulses" [4] have been observed and also present velocities up to 3.10^7 m/s.

Breakdown Processes and Leader in Cloud-to-Ground Flashes - In precursor to a cloud-to-ground flash, processes have been observed to last from a few tens ms to several hundreds ms. The shorter events can be associated to a leader activity with a preponderance of short bursts, this activity being preceded for long precursors by processes usually within the cloud and typical in some cases of intracloud discharges.

In one of this case of cloud-to-ground flash, we observe a 625 ms intracloud activity preceding a 25 ms leader. The first 350 ms presented a low rate

pulse radiation (10-15 pulses/ms) associated with a spread-out activity expending throughout the cloud ; corresponding slow E field variations (total of 30 kV/m) are associated to large vertical dipolar neutralizations between altitudes of 4 km (negative charges) and 7 km (positive charges). The last 275 ms are a superposition of the intracloud discharge and breakdown processes prior to the cloud-to-ground flash. During the weakening of the low rate activity, we observe 4 bursts (Fig. 6) corresponding to rapid propagations of sources over large distances (probably between 5 and 10 km). All propagations are observed to converge towards the charge that will be neutralized by the first return stroke. Final paths of bursts 1, 3 and 4 seem to follow the same downwards trajectories ; respective velocities are 10^6, 5.10^7 and $1.5.10^7$ m/s. These downwards trajectories seem to be limited within the cloud. A last burst (4) corresponds to the beginning of the leader phase ; the pulse emission rate increases during this phase and is associated with a large number of sources scattering from the breakdown volume. Due to the large extent of the activity over the remaining ambiguities of the small interferometric system, it was not possible in this particular case to differentiate radiation within the cloud from possible downwards radiation associated with the leader.

Other cloud-to-ground discharges are not superimposed on such an intracloud activity, and it was possible to locate electromagnetic sources during leader phases. Prior to that, we observed either short or long breakdown ; an example of the last type is a 300 ms activity previously to a 50 ms leader (Fig. 7). The radiation is of the short burst type, several tens of ms apart, and is localized along a vertical path. In the first hundred of ms, sources are shown to be close to the ground, below the cloud base, and present in one case, 230 ms before the return stroke, a propagation to ground with a velocity of 7.10^7 m/s. The overall topology of breakdown associated electromagnetic sources will then be the place of leader and subsequent dart leader sources propagations. Figure 7 presents E field variations on four stations and the associated electromagnetic sources locations for the breakdown and leader phases. Radiation during the leader is observed only during E steps and corresponds for the first burst (b) to a downwards propagation to the ground (2.10^7 m/s) and for the following bursts either to localized in-cloud radiation or upwards propagations (2.10^7 m/s). E field steps can be modelized as long intracloud horizontal dipolar discharges driving negative charges away from the location of first stroke (similar observation is presented in [9], intersteps E field evolutions do not give any detectable emission, they correspond to similar but slower charge transfers. Charges models indicate that during all this leader, horizontal discharges are predominant compared to vertical transfer usually associated to leader advance. The low time resolution of E field measurements cannot give us informations on the chronology, within the ms, of charges transfer in the cloud and propagation of UHF sources below the cloud. Nevertheless, in this case, observations suggest a different image of a

precursor phenomenon where the breakdown activity is already associated to UHF sources defining parts of a cloud-to-ground channel. This channel is then the place, during leader phase, of propagating sources at high speed ($> 10^7$ m/s) well above usual leader mechanisms velocities, and associated to the transfer of charges within the cloud.

In a third case of cloud-to-ground flash, no noticeable breakdown activity can be observed. E field measurements indicate the start of a leader 10 ms prior to the return stroke ; though the distance of the activity (12 km) and the resulting imprecision on interferometric location at low altitude, electromagnetic sources present a propagation towards ground in the first 3 ms of the leader activity, subsequent sources for the remaining 7 ms are mostly located in altitude (Fig. 8). E field measurements show an usual leader phenomenon lasting 10 ms [11]. Timing difference again suggests that UHF radiation mechanisms are not strictly related to a leader progression. In these 3 examples of cloud-to-ground lightning, we have noticed from weather radar data that every case of low elevation activity, below the cloud base, is associated to heavy precipitations.

Dart Leader – Dart leader radiation is of the burst type ; all data either from triggered or natural cloud-to-ground lightning flashes show a 100 to 300 μs long phase of sources, propagation to ground, with velocities between 10^7 and 5.10^7 m/s ; dart leader radiation does not come from the cloud but from sources descending towards ground (Fig. 9). The return stroke is sometimes observed with a delay (up to several hundred μs) ; the sources are localized within the cloud, usually away from the leader starting point ; this suggests that the observed delay (or part of it) is associated with the upwards and intracloud propagation time of return stroke

Return Stroke – At 300 MHz, the return strokes radiation present a large dynamic, going from no noticeable radiation to levels comparable to burst type radiation. The study of its location shows either spread out sources, or more compact groups of sources away from locations of precursor activity. Some of these phenomena could be explained, from an instrumental point of view, if we were in presence of strong simultaneous sources all along the return stroke channel ; their location would in this case appear to be a point-source, their center of mass, moving apparently in an incoherent way. Nevertheless, return stroke radiation is not continuous and usually not strong, and thus instrumental effect cannot explain all the observations. Such lack of spatial correlation between return stroke associated VHF-UHF sources and precursors has already been mentioned in the case of other location methods [4].

While in two cases of first stroke sources appear spread out around leader trajectories, in most other cases or first or subsequent strokes, they are located within the cloud. This suggest that UHF emission during return stroke does not come essentially from the current wave, but is induced by the effect of this wave either around the channel or within the cloud (Fig. 9).

CONCLUSION

300 MHz radiation from lightning flashes appears impulsive at the one μs time scale. It can be classified according two types :

- a low rate pulse radiation associated to slowly drifting spread out sources, occuring mainly during breakdown phenomena and intraclouds presenting large charge transfers ;

- a high rate pulse radiation or bursts lasting several hundreds μs and characterized by unidirectional propagation of sources with velocities up to 7.10^7 m/s. This last type of radiation is the most powerfull in the studies frequency range.

Bursts are observed in all phases of a lightning and are always simultaneous with E field steps associated with small dipolar neutralizations. For some phases, such as J process and intracloud discharges, they can be associated to K changes, though presenting higher velocities. But they are also present in precursor phenomena such as breakdown, and leader, where they are observed to follow identical trajectories (in some cases to ground) well before it could be supposed from E field variations with usual models. Observed velocities, in the range 10^7 m/s, are, excepted in the dart leader case, higher than currently measured with other diagnostics, and constitute an additionnal argument suggesting a difference between UHF radiation mechanisms and the phenomena observed usually, in particular, the current wave. These bursts seem to be located either within cloud or in heavy precipitation zones when observed going to ground. This rises the question of understanding the relationship between the discharge and its environment ; on the one hand, the UHF radiation mechanisms, and, on the other hand, its propagation.

REFERENCES

1. P. Richard, G. Auffray, "VHF-UHF Interferometric Imagery, Applications To Lightning". Submitted to Radio-Science.

2. D.E. Proctor, "A Hyperbolic System for Obtaining VHF Radio Pictures of Lightning". J.G.R., Vol. 76, n° 6, pp. 1478-1489, Feb. 20, 1971.

3. J.W.Warwick, C.O.Hayenga, J.W.Brosnahan, "Interferometric Directions of Lightning Sources at 34 MHz". J.G.R., Vol. 84, n° C5, pp. 2457-2468, 1979.

4. P.L. Rustan, M.A. Uman, D.G. Childers, W.H. Beasley, C.L. Lennon, "Lightning Source Locations from VHF Radiation Data for a Flash at Kennedy Space Center". J.G.R., Vol. 85, n° C9, pp. 4893-4903, 1980.

5. W. D. Rust, W.L. Taylor, D. Mac Gorman, "Preliminary Study of Lightning Location Relative to Storm Structure", AIAA Journal, Vol. 20, pp. 404-409, 1981.

6. P. Laroche, M. Metzger, F. Roux, J. Testud, J. Chauzy, "Electric Field Variations Produced by Natural and Triggered Lightning and Related Radar Measurements". Presented at 6th International Conference on Atmospheric Electricity, Manchester (G.B.), August 1980.

7. Golde. "Lightning". Vol. 1, Academic Press, 1977.

8. D.E. Proctor, "VHF Radio Picture of Cloud Flashes". J.G.R., Vol. 86, n° C5, pp. 4041-4071, May 20, 1981.

9. P.R. Krehbiel, M. Brook, R.A. Mc Crory, "An Analysis of the Charge Structure of Lightning Discharges to Ground". J.G.R., Vol. 84, n° C5, pp. 2432-2456, May 20, 1979.

10. M. Brook, N. Kitagawa, "Radiation from Lightning Discharges in the Frequency Range 400 to 1000 Mc/s", J.G.R., Vol. 69, N° 12, pp. 2431-2434, June 15, 1964.

11. W. Beasley, M.A. Uman, P.L. Rustan Jr, "Electric Fields Preceding Cloud to Ground Lightning Flashes", J.G.R., Vol. 87, n° C7, pp. 4883-4902, June 20, 1982.

$$\Delta\phi_{12}=2\pi\frac{D\alpha}{\lambda}\cos\varphi\sin\Theta=2\pi\frac{D\alpha}{\lambda}U=(\Delta\phi_{12})\text{ measured}$$
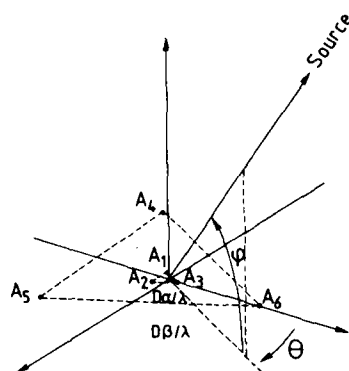
$$\Delta\phi_{13}=2\pi\frac{D\alpha}{\lambda}\cos\varphi\cos(\Theta\frac{\pi}{6})=2\pi\frac{D\alpha}{\lambda}\frac{u+\sqrt{3}v}{2}=(\Delta\phi_{13})\text{ measured}$$

$$\Delta\phi_{45}=\frac{D\beta}{D\alpha}\Delta\phi_{12}=(\Delta\phi_{45})\text{ measured}+2k_{45}\pi$$

$$\Delta\phi_{46}=\frac{D\beta}{D\alpha}\Delta\phi_{13}=(\Delta\phi_{46})\text{ measured}+2k_{46}\pi$$

Fig. 1 - Principle of interferometric measurement
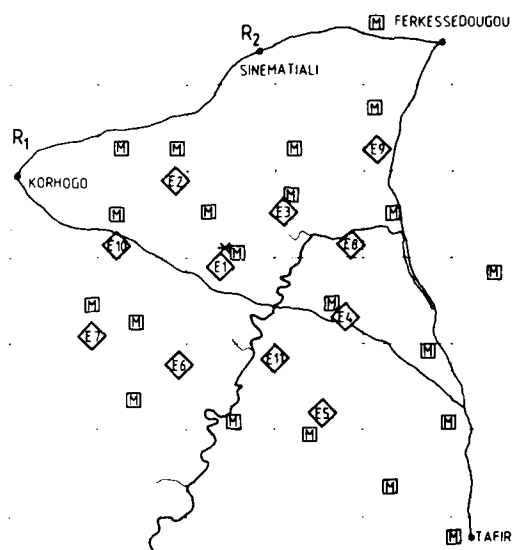
Fig. 3 - COPT 81 : Locations of experiments
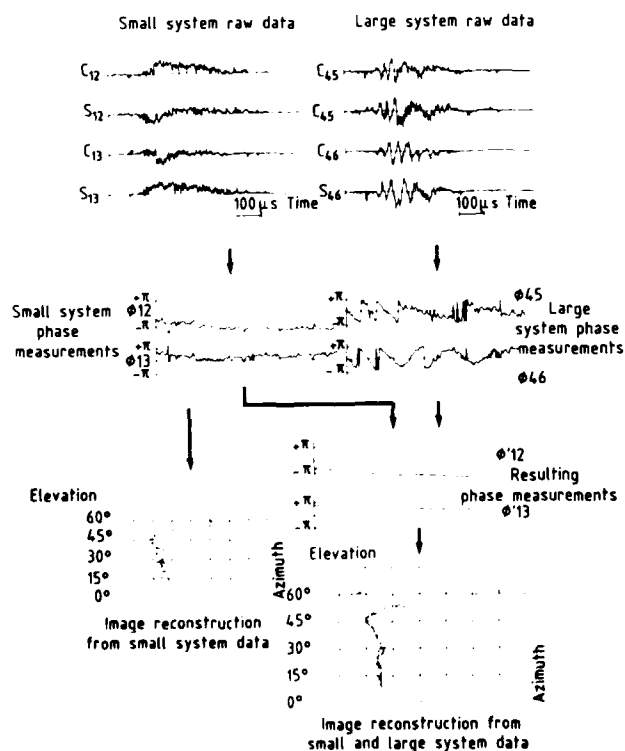
Fig. 2 - Example of data processing in lightning image reconstruction
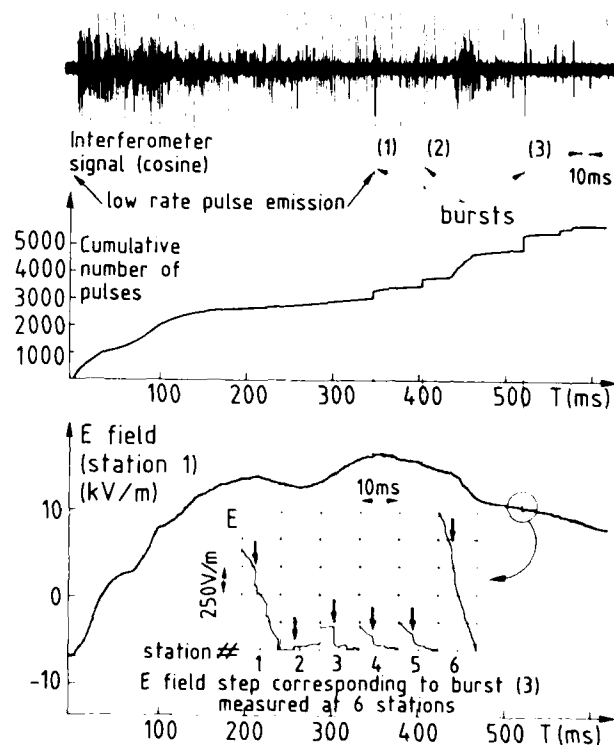
Fig. 4 - Examples of low rate pulse emission and bursts during an intracloud activity
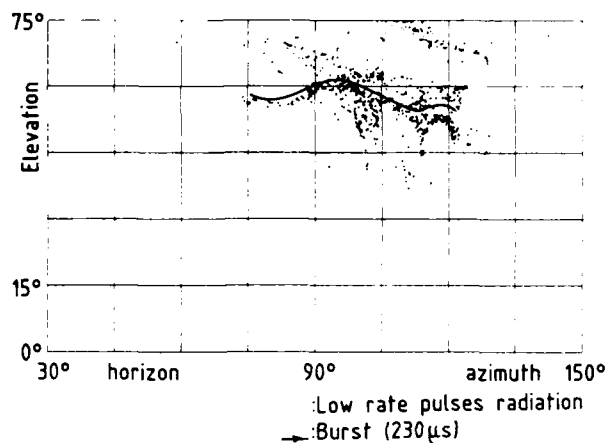
Fig. 5 – Intracloud activity. Low rate pulses radiation (120 ms) :. Burst (230 μs) : __

75°

Elevation

15°

0°

30° horizon   90°   azimuth 150°

:Low rate pulses radiation
→:Burst (230μs)

E field evolutions

280 Station ≠ 7   1200 Station ≠ 2
V/m   V/m

0   0

3680 Station ≠ 10   2400 Station ≠ 1
V/m   V/m

0   0

100   320 t(ms)   100   320 t
Breakdown   Leader   Breakdown   Leader (ms)

Breakdown phase   Leader phase

UHF sources
locations

15°   15°

0°   0°

– 45° Azimuth   – 45° Azimuth

Elevation
50°

a   b   c   d   Mean time
(96)   (278)   (310) (316) (ms)

Elevation
versus time

10°

0°
Average : 7 10⁷   2 3 10⁷   2.2 10⁷ 2 5 10⁷ t
velocities (m/s)   100 μs

Fig. 7 – Breakdown and leader activity in precursor to a cloud-to-ground flash

Timing (ms)
(from beginning of activity)
burst 1 · 359.257 – 363 412
burst 2 · 417.263 – 417.816
burst 3 · 533.850 – 534 333
burst 4   645.414 – 646 295

75°

Elevation

15°

0°
horizon   0°   azimuth 45°

✝ Location of charge neutralized by the cloud
  to ground stroke (-12 C)

Fig. 6 – Intracloud bursts in precursor to a cloud-to-ground stroke

E field (station ≠ 8)
kV/m

0

–5

2   12   t(ms)

30°

Elevation

10°

0°
0 1   5   10   t (ms)

(average downward)
(velocity: 1.5 10⁶m/s)

Return
stroke

Fig. 8 – E field and UHF sources elevation versus time during leader phase of a cloud-to-ground flash
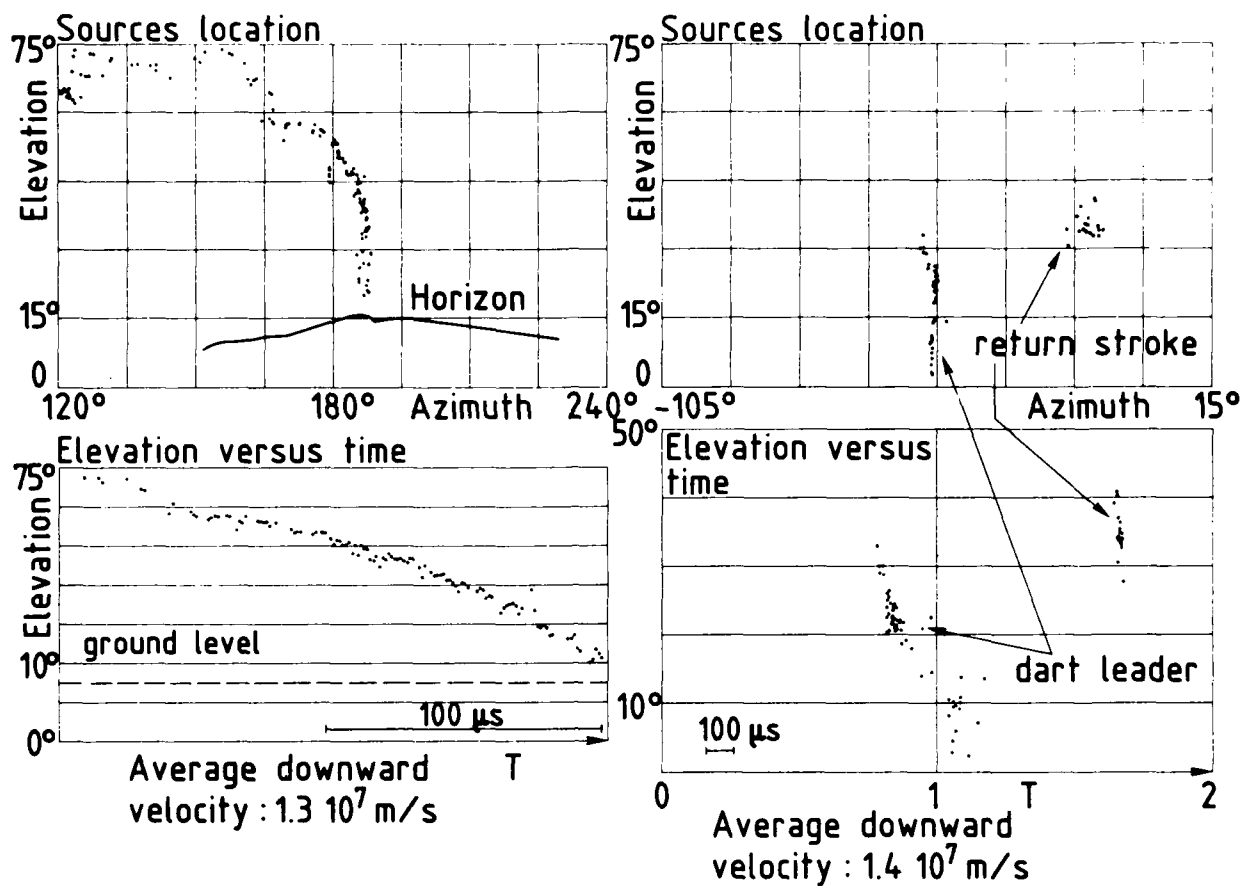
Fig. 9 - Examples of dart leader
Left : triggered lightning
Right : natural lightnin
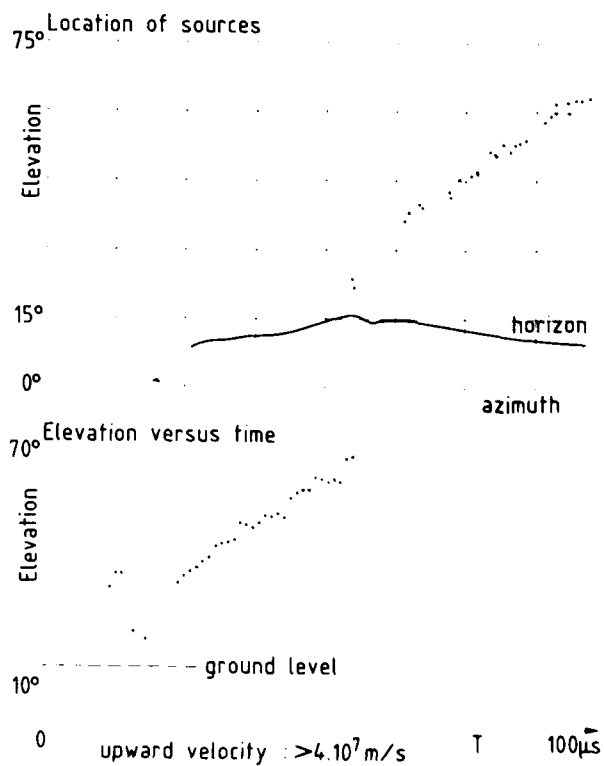
Fig. 10 - Return-stroke associated sources (triggered lightning)

58-7

MAGNETIC FORCE AND SHOCK DAMAGE RESULTING FROM LIGHTNING STRIKES

C JONES, G REID, CULHAM LABORATORY,
ABINGDON, OXFORD OX14 3DB, ENGLAND

ABSTRACT

The problem of aircraft radome protection is of particular importance as this is an area where considerable damage has been experienced. The probability of a strike to a radome is increased in the case of supersonic aircraft (which carry pitots on the front of the radome) yet such aircraft can least afford to lose the radome because of the adverse aerodynamic effects. Some of the problems have been discussed by A W Hanson (1) and of particular interest in that paper was the consideration of swept arcs and the interaction between such arcs and solid conductors carrying lightning currents. Various experiments in the furtherance of that work are described here in which the movement of arcs were studied as well as the forces they produced. This has also lead to a theoretical appraisal of the impulsive nature of magnetic forces generated by lightning currents and the effective mechanical forces they produce. This theory has been used to compare predicted forces with actual forces calculated from the deflection of a simple mechanical system over a limited range of operating conditions.

The paper starts with a review of the various mechanical effects which can result from lightning strikes.

MAGNETIC FORCE AND SHOCK EFFECTS may be

encountered in lightning interactions with aircraft from a number of sources and through several mechanisms. The major contributions to the problems are:

1) Magnetic forces (including pinch effects and magnetic interaction).
2) Mechanical shock waves associated with arc attachments.
3) High current arcs in confined and semi-confined spaces.
4) Fusing conductors.
5) Hydraulic shock in fuel tanks.

MAGNETIC FORCES - These forces arise from the interaction of magnetic fields generated by lightning current pulses flowing in conductors. Being peak current and time dependent, magnetic force effects are most damaging where geometrical considerations constrain current to flow in small conductors, and where current carrying conductors are routed at acute angles in close proximity to each other. This is a common situation where, for instance, a braid is attached to a conducting surface by a tag and bolt. Here, currents in the di/dt phase of a lightning pulse are encouraged by inductive effects to flow as close to each other as

*Numbers in parentheses designate References at end of paper.

possible creating maximum magnetic forces. A similar situation nearly always arises where a narrow conductor (e.g. a diverter strip) is attached to a larger structure (e.g. an aircraft fuselage). These magnetic forces are not confined to two or more conductor geometries: a single conductor carrying an impulse current is subject to its own magnetic forces (called pinch effect). Hence flat braid will tend to compress into a nearly cylindrical form after a lightning current pulse as will then flat foil strips. Even cylindrical conductors like conduits can be affected; lightning simulation tests at Culham Laboratory have demonstrated reductions in outer radius of copper conduit from 2.5mm to 2mm after a 200kA, $2 \times 10^6 A^2 s$ pulse, involving compressive forces of $\sim 320 MN/m^2$ (21 tons/in^2). Magnetic interaction forces are the subject of the main part of this paper.

MECHANICAL SHOCK WAVES ASSOCIATED WITH THE ARC ATTACHMENT - This effect is usually observed at the lightning arc attachment ppints on the airfract. It is caused by the explosive expansion of gas in the arc channel in the longitudinal direction producing a shock wave during the early part of the first return stroke. Resulting damage can vary from denting 2mm thick aluminium sheet to splitting 0.5mm thick aluminium or breaking a hole through carbon fibre panels less than about 0.7mm thick. The mechanism is peak current and action integral dependent, hence only component A of the lightning waveform is significant.

HIGH CURRENT ARCS IN CONFINED AND SEMI-CONFINED SPACES - High impulse current arcs produce radial shock waves and very large gas overpressure through rapid heating and expansion. In confined spaces this can cause considerable damage as in cases of punctured radomes etc. It can also cause debonding or blow-outs when such arcing occurs in voids in insulating layers or in glue lines. The severity of the problem is dependent on peak current and action integral so component A of the lightning waveform is again the main culprit.

FUSING CONDUCTORS - A conductor embedded in a non-conducting material will fuse if sufficient energy to vaporise it is dissipated in it. When it vaporises an arc replaces the conductor as the carrier of the current. As in the above paragraph, considerable damage can be done by the explosive expansion of gasses in such a case. Further damage may be done directly by the heating and expansion of the conductor and nearby materials before and during vaporisation, for instance by the vaporisation of epoxy in a carbon fibre member. A case in point might be a long thin propeller blade constructed with a carbon fibre completely encased in glass fibre. Puncture to and subsequent lightning current conduction through the carbon will, if insuffi-

cient carbon is present, cause the structure to split open.

A similar effect occurs when a conductor is confined only on one side as in the case of a radome diverter strip. If a fuseable strip is used as a diverter strip, on fusing while carrying a lightning current impulse, the surface to which the strip is affixed may be split. This effect appears to depend on action integral, peak current, the quantity of material vaporised and on the mechanical properties of the supporting material.

HYDRAULIC SHOCK IN FUEL TANKS - As observed above, an explosively fusing conductor produces a shock wave in the surrounding gas. Similarly, a fusing conductor immersed in a fluid will produce a shock wave in the fluid and this may in certain circumstances have great potential for causing damage. Unlike fuel vapour explosion or detonation, this effect is more likely to occur when fuel tanks are full.

The remaining part of this paper is concerned with the first of these damage mechanisms as described above, and is chiefly directed to the problem of magnetically induced forces associated with radome protection. The results should, however, reflect on any impulse magnetic force problems.

ARC INTERACTION WITH RADOME DIVERTER STRIPS

The problem of magnetic interaction between a lightning arc channel and lightning conductor strips has been discussed previously by A W Hanson in "Lightning Protection Techniques for Radomes having Forward Mounted Pitots",(1). There he considers a step leader attaching to the pitot boom when there will be some delay between the initial leader attachment and the time of arrival of the first return stroke. During this delay the aircraft will have moved forward and hence sweeping of the leader channels will occur. The interval between the initial leader attachment and arrival of the return stroke could vary from 0.5ms to 60ms according to the altitude of the aircraft: the altitude determines how much further the step leader must propagate before the channel is complete for the first return stroke to occur. With aircraft speeds in the range 66-200m/s the aircraft may have travelled between 0.033m and 12m. Hence it is possible that a leader be swept over the surface of a radome prior to the first return stroke in which time re-attachment may be impossible because of the dielectric surface. Parallel or near parallel current paths are created by the arc and the radome protection strip carrying current back to the fuselage. The results of this effect (illustrated in Fig. 1) are believed to have been seen by the author in at least one damaged radome.

In these circumstances magnetic forces will exist between the arc channel and the current carrying conductor pushing them apart, (Fig. 2). Effective forces as high as 22kN/m (1500lb/ft) with a conductor spacing of 33mm have been produced in laboratory experiments using solid conductors and lightning simulation current waveforms. As one of the conductors in practice may be an arc, a key question is then whether the arc moves appreciably in the time-scale of interest as this might greatly reduce the effective force between an arc and a fixed conductor. If an arc does display some "inertia", what will be the time resolved displacement of the arc and hence what reaction does it provide for the forces acting on a protection strip attached to a radome wall?. Experiments were devised to investigate these questions.

ARC MOVEMENT

To investigate this phenomenon it was necessary to generate long arcs with high (100kA) currents. Initiating such arcs is a problem because high current capacitor banks do not in general produce very high voltages. The simplest method is to use a fine fuse wire of metal or carbon across the gap where an arc is required. A few kilovolts are then enough to initiate the breakdown by fusing the fuse wire in the early, low current phase of the discharge. Early tests described in (2) on the 100kV capacitor bank at CLSU (shown diagrammatically in Fig. 3) and using an Imacon image converting camera framing at 2.5×10^4 frames/sec (40μs between images) showed problems in recording fuse wire initiated arcs. This was due to the intense illumination produced by the fusing of the wire and subsequently in the vapour from it. Other methods of triggering long arcs had then to be sought. Sophisticated techniques using high powered lasers do exist (3) but the cost and complexity are prohibitive. Further tests compared trigger electrode initiated arcs with fuse wire using the circuit shown in Fig. 4. The Imacon photographs of this experiment are shown in Fig. 5. As can be seen from the photographs, the lower arcs show much more detail than the upper fuse wire initiated arcs. The important feature to observe from the pictures is that the arc does not move or break-up significantly until frame 5 or 6, i.e. 200-240μs after the striking of the arc.

FORCES PRODUCED

Direct investigations were then made of the forces produced by the arc with the arrangement shown in Fig. 6. It was very similar to that used in Fig. 4, but a single fuse wire gap was used for convenience. The important parameter to monitor here was the movement of the parallel return conductor for which an optical technique was used.

This displacement monitor was required to measure the movement of the return conductor fairly accurately and with microsecond time resolution. This had to be achieved in the presence of large magnetic and electric fields. A system using a focused light beam was developed (4). This comprised a microscope lamp, two condenser lenses and a large area photo-sensitive diode with additional circuitry to give a voltage output proportional to the amount of light falling on the surface of the diode (Fig. 7).

Basically the idea was to put an opaque flag of minimal inertia on the return conductor and arrange the light beam to focus to a point just beyond the tip of the flag. The second condenser then focused the beam onto the photo-diode surface. Experiment established that the output of the photodiode circuit was linearly proportional to the observation of the light beam by the flag over the distances of interest. The sensitivity of the device could be altered by moving rhe focus of the beam towards or away from the flag, and the dynamic range by adjusting the intensity of the light source.

Tests were done using the above apparatus applying currents with peaks ranging from 60kA to 85kA, with various load impedances to produce different fundamental frequences and both damped, sinusoidal and clamped unidirectional waveforms. A typical damped sinusoidal current waveform is shown in Fig. 8a with the displacement in the lower trace, while a clamped waveform and dis-placement curve is in Fig. 8b.

RESULTS OF EXPERIMENTS

The results are presented in Table 1. They have been assembled in ascending values of capacitor voltage and added circuit inductance. Results from using a solid conductor in place of the arc have been tabulated adjacent to the arc test results for direct comparison. Direct comparison is not straightforward because of the difference in total circuit resistance between arc and solid conductor tests and between clamped and ringing waveforms. This is more fully discussed later.

The "effective" force on the return cond-uctor may be expected to depend on the square of the current (of the force between two current varying conductors) and on the time for which the current pulse lasts. The value of "effective" force is defined as the force which, when applied slowly and continuously, would produce the same strain in the mechanical system as the transient force. This is calcu-lated using standard mechanical deflection equations. Accordingly, the maximum deflection has been plotted against the action integral of the current pulse ($\int i^2 dt$) for each test discharge and this is shown in Fig. 9.

It should be noted that for the ringing waveforms, the test circuit included the fault limiting resistance (R_c in Fig. 3) in the capa-citor bank which dominated the change from the static resistance of a solid conductor to the time varying resistance of the arc. Thus the two lines representing ringing waveform tests are very close. In the case of the clamped discharges, the fault limiting resistance of the bank is removed at peak current so the decay is dominated by the load resistance. Thus to obtain the same action integral in the arc as in the solid conductor, a higher current was used for the arc tests.

From the graph it may be concluded that:

1) For similar current waveshapes, the effects of an arc and solid conductor on the movement of a return conductor are of a similar

order. Hence the arc has an effect much the same as a mechanically stiff conductor over these timescales.

2) Changes in the current waveshape produce widely differing effective forces for similar action integral. Hence action integral does not combine the important parameters in a suit-able way to produce an overall proportionality.

3) For a given current waveshape, the action integral does display approximate pro-portionality to return conductor deflection.

4) To obtain overall proportionality the effect of waveshape must be included with the action integral parameter.

THEORETICAL CALCULATION OF CONTINUOUS EQUIVALENT FORCE

The waveform produced by lightning can be approximated to a double exponential with a fast rise time of the order of a few micro-seconds and a much larger decay time τ from 100µs to several milliseconds.

The type of forces resulting from light-ning type waveforms have been discussed by T E James and J Phillpott in (5). Conductors will be subject to high initial impulsive forces, followed by a slower and much smaller decaying component. The maximum mechanical stress will occur at the maximum deflection when all the kinetic energy is converted into strain energy.

If we consider a simple mechanical system which has an angular frequency 'ω' subject to a rapidly applied force P_o (being the maximum magnetic force at peak current) which decays exponentially in a time $\tau/2$. This is related to what is termed an "effective transient force" P_t which would produce the same stress in the mechanical system when applied slowly but continuously.

A relation can be derived between the ratio of the effective transient force (P_t) and the peak applied force (P_o), i.e. P_t/P_o, and the product of the natural angular frequency of the mechanical system 'ω' and the exponential decay time of the current pulse τ, i.e. $\omega\tau$.

This relationship for a fast rise time and exponentially decaying pulse was originally derived in 1959 by T E James and subsequently by R H Evans in (6) from simple mechanical considerations and is reproduced here as Fig.10.

Using this curve, the effective mechanical forces for fast, intermediate, and long types of lightning pulses with the characteristics shown in Table 2 have been composed. This is shown in Table 3. The values of force P_o are relative and have been normalised to a value of 1.0 for a peak current of 50kA. Value of the angular frequency 'ω' of the mechanical structure have been assumed to lie between 10^3 rads/s for a heavy flexible system and 10^4 rads/s for a lighter stiff one. It can be seen from Table 3 that the maximum effective force is produced by the fast high current component due to the much greater peak force P_o which is produced.

More general conclusions may be drawn

from the curve in Fig. 10: it is clear that in the curved central area of the graph that $\omega\tau$ critically affects the effective force and in a non-linear function, hence effective force will not be a function of action integral alone. At the bottom end of the graph, effective force is approximately a linear function of $\omega\tau$ so it may be expected that mechanical systems with very low ω will respond according to action integral levels. At the top end of the graph the effective force ratio tends to a constant factor of 2, so above a certain level of $\omega\tau$ one may expect effective force to scale with peak current only.

COMPARISON BETWEEN THEORETICAL FORCE AND MEASURED FORCE

In the case of the clamped circuit test discharges it is possible to compare the effective force calculated from the relationship plotted in Fig. 10 with the effective force calculated from the measured displacement of the conductor. This latter calculation gives the uniform loading along a simple supported beam as used for the return conductor, which would produce the same maximum deflection as measured while passing the high current impulse through the circuit. The natural angular frequency (ω) of the conductor may be found directly from the frequency of the displacement oscillations.

The results of these calculations are shown in Table 4. It can be seen that there is reasonable agreement between the practical results and the theoretical calculations.

Figure 11 shows displacement calculated from the theoretical equivalent force (P_t) plotted against peak current squared for each of the values of τ in Table 4 plus some additional values (ω is kept constant). Also plotted are the measured displacements numbered to refer to Table 4. Agreement is quite good as some inaccuracies would be expected for the following reasons:

1) The waveforms used only approximated to exponential decay especially in the case of arc conductors.

2) The mechanical model of the arc/rod and return conductor was very simplified assuming simple support and uniform loading throughout.

3) No allowance was made of arc movement at long timescales.

CONCLUSIONS

During the experiments very large forces were recorded resulting from the magnetic interaction between arcs and current carrying conductors in close proximity. These were up to 70% of the forces between two solid conductors at similar spacing and carrying currents of similar magnitudes and waveshape. From this it may be concluded that similar design considerations must be given to forces arising from possible magnetic interaction with arcs as is given to magnetic interaction between solid conductors.

Calculations of forces using the theory derived for exponentially decaying impulse currents have given reasonable agreement with those calculated from conductor displacement in experiments. It is reasonable to conclude therefore that the exponential decay theory may be used to indicate the level of forces that might be expected in practice at least over a limited range of mechanical systems.

The experimental results confirm that in the range of the $\omega\tau$ product used (0.2 to 2 rads) action integral alone is insufficient as a measure of mechanical deflection; therefore waveshape also must be taken into consideration. However the results indicate that for $\omega\tau < 0.2$ the deflection would be a linear function of action integral. This is supported by the theory as the graph of effective force against $\omega\tau$ illustrates. In general, to predict peak magnetic forces it is necessary to know peak current, current waveshape and the anular frequency of the mechanical system.

REFERENCES

1 A W Hanson, 'Lightning Protection Techniques for Radomes having Forward Mounted Pitots' Symposium in Lightning Technology, Hampton Va 1980.

2 C C R Jones, J G Talboys, C Chessum, 'Experiments with Fusewire and Electric Pulse Triggered Arcs', CLSU Memo 101, November 1981.

3 J R Greig, R F Fersler, P P Murphy, R E Pechacek, J Penn, M Raleigh, 'Laser-Guided Electric Discharges in the Atmosphere', 7th International Conference in Gas Discharges and their Application, London 1982.

4 C C R Jones, J G Talboys, C Chessum, S E V Warder, 'Development of a Technique for Monitoring Solid Conductor Displacement as a Function of Time', CLSU Memo 106, June 1982.

5 T E James, J Phillpott, 'Simulation of Lightning Strikes to Aircraft', CLM-R111 HMSO 1971.

6 G W Reid, C C R Jones, R H Evans, 'Theoretical Considerations in Assessing the Mechanical Forces Produced on Conductors due to Lightning Strike Currents', CLSU Memo 110, November 1982.

Table 1 - Results of Arc and Rod Tests

Arc or Rod	Capacitor Voltage kV	Clamp or Ringing	Added Circuit Inductance µH	Decay Time τ µs	$\hat{I}$ kA	$\int I^2 dt$ x 10^6 A^2s	Maximum Bar Deflection mm	Period of Bar Oscillation ms
Arc	25	Ringing	0	-	79	0.1	0.85	1.9
Rod	25	Ringing	0	-	83.7	0.12	0.88	1.68
Arc	25	Clamp	0	62	78	0.19	0.6	-
Rod	25	Clamp	0	360	83	1.24	1.45	2.2
Arc	25	Ringing	1.6	-	59	0.1	.78	1.9
Rod	25	Ringing	1.6	-	60	0.1	1.1	1.68
Arc	25	Clamp	1.6	200	59	0.36	0.68	1.79
Rod	25	Clamp	1.6	576	61.8	1.1	1.3	2.14
Arc	35	Ringing	1.6	-	85	0.2	1.3	1.9
Rod	35	Ringing	1.6	-	80	0.16	1.7	1.9
Arc	35	Clamp	1.6	250	85	.72	1.25	1.94
Rod	35	Clamp	1.6	554	76	1.61	1.6	2.4
Arc	35	Ringing	4.3	-	64	.156	.16	1.79
Rod	35	Ringing	4.3	-	71.6	.28	.28	2.04
Arc	35	Clamp	4.3	-	74	1.4	2.5	2.0
Rod	35	Clamp	4.3	-	68	.92	2.1	2.0

Table 2 - Maximum Effective Parameters for Composite Current Waveform

Component		Negative Discharge	Positive Discharge
(1) Fast			
Peak current I	(kA)	200	200
di/dt	(kA/μs)	80	8
Pulse time τ	(μs)	10	100
Coulombs	(C)	2	20
I^2t	$10^6(A^2s)$	0.2	2.0
(2) Intermediate			
Peak current I	(kA)	50	50
Pulse time τ	(ms)	0.4	2
Coulombs	(C)	20	100
I^2t	$10^6(A^2s)$	0.5	2.5
(3) Continuing			
Peak current	(kA)	1	1
Pulse time	(ms)	200	200
Coulombs	(C)	200	200
I^2t	$10^6(A^2s)$	0.2	0.2
Total coulombs (C)		~220	~320
Total I^2t	$10^6(A^2s)$	0.9	4.7

Reproduced from "Simulation of Lightning
Strikes to Aircraft" (reference 5)

Table 3 - Effective Transient Magnetic Force P_t

I (kA)	τ (ms)	Coulombs (C)	I^2t $10^6(A^2s)$	P_o (Relative) (Units)	P_t/P_o		P_t (Relative Units)	
					$\omega=10^3$	$\omega=10^4$	$\omega=10^3$	$\omega=10^4$
200 (Fast)	0.1	20	2.0	16.0	0.05	0.45	0.8	7.2
50 (Int)	2.0	100	2.5	1.0	0.75	1.73	0.75	1.73
1.0 (Long)	200	200	0.1	.0004	2.0	2.0	0.0008	0.0008

Reproduced from "Simulation of Lightning Strikes to Aircraft" (reference 5)

Table 4 - Comparison of Force on Conductor from Maximum Deflection and Calculation of P_t for Clamped Shots

	Arc or Rod	Capacitor Voltage kV	Decay Time μs	$\hat{I}$ kA	$\int I^2 dt$ × 10^6 A²s	Maximum Bar Deflection mm	Peak Force P_o kN	ωτ using mean period of 2ms rads	P_t/P_o	Theoretical Effective Force P_t kN	Effective Force Calculated from Deflection P kN
1	Arc	25	62	78	0.19	0.6	3.7	0.19	0.1	*.36	.93
2	Rod	25	360	83	1.24	1.45	4.1	1.13	0.5	2.1	2.3
3	Arc	25	360	59	0.36	0.68	2.1	1.13	0.51	1.0	1.1
4	Rod	25	576	61.8	1.1	1.3	2.3	1.8	0.7	1.6	2
5	Arc	35	250	85	0.72	1.25	4.3	.785	.35	1.5	1.9
6	Rod	35	554	76	1.61	1.6	3.5	1.74	0.65	2.3	2.5

* Anomalous result created by complex current waveform departing appreciably from assumed exponential decay

Note: 10kN ≈ 1 ton (to 0.36%)
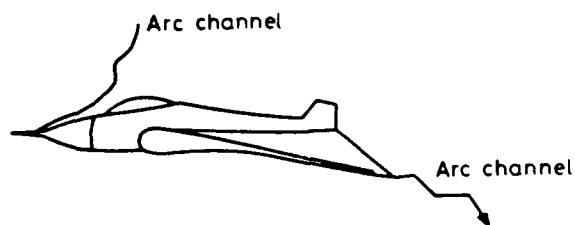
Fig. 1 - Maximum Arc Channel
Interaction Condition
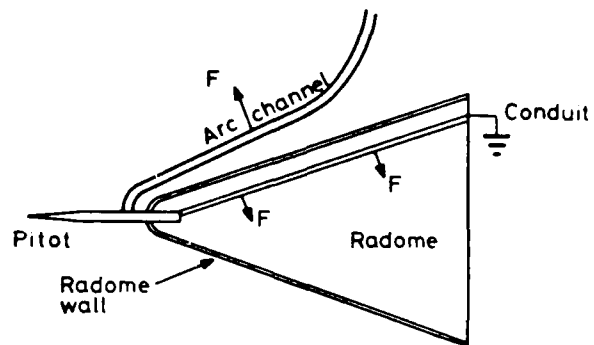
Fig. 2 - Magnetic Forces Acting on a simple
Conduit Protection System for Maxi-
mum Arc Channel Interaction Conditions
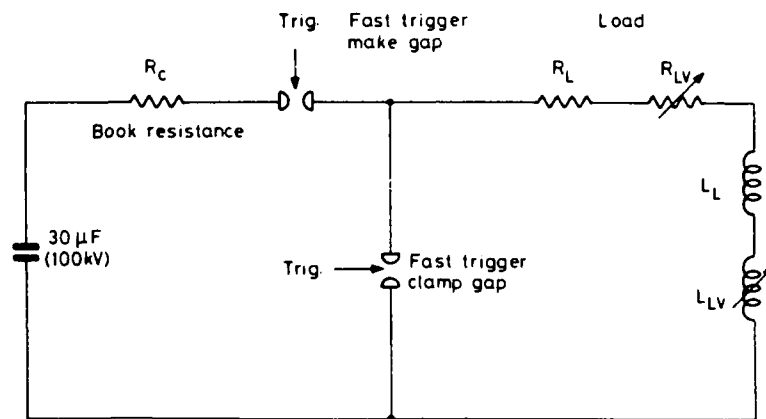
Fig. 3 - Circuit Arrangement for Forces Tests
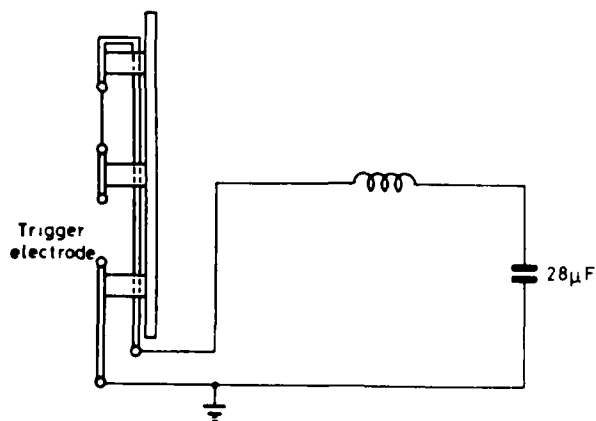
Fig. 4 - Test Rig for Double Arc Experiment
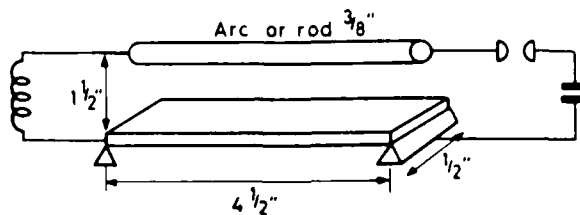
Fig. 6 - Test Rig for Displacement
Measurements

Fig. 5 - Double Arc Experiments

Plate 1

Plate 2

1 3 5 7 9 11

Trigger initiated arc

Carbon filament initiated arc

2 4 6 8 10 12

Trigger initiated arc

Copper fuse-wire initiated arc

2 4 6 8 10 12
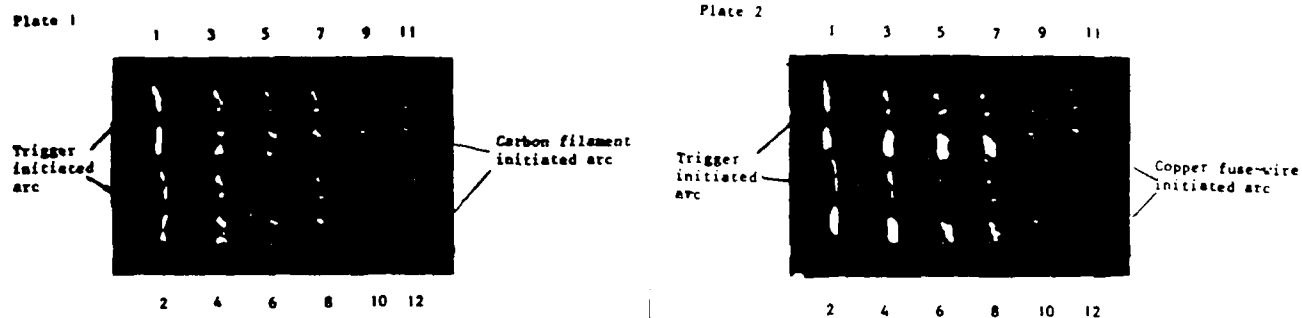
40µs Time Interval between Frames

Framing Camera Pictures and Double Arcs (see Fig. 4)

Arc or fixed rod

Return conductor

Insulation

Light source

Flag attached to return conductor

Large Photo Diode Detector

Monitor oscilloscope
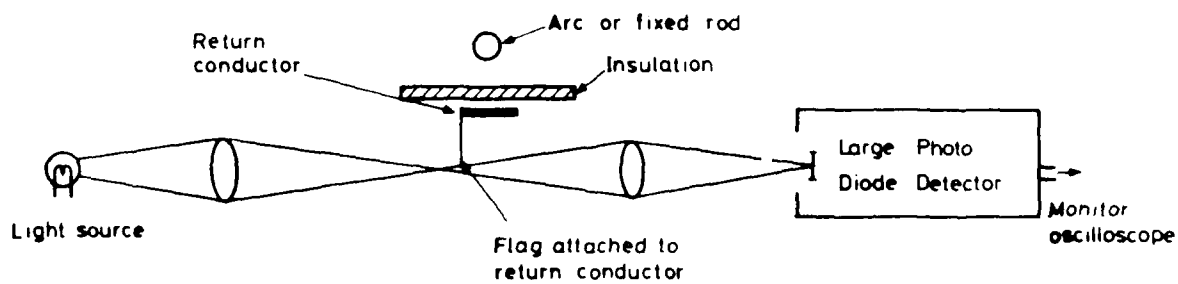
Fig. 7 - Return Conductor Displacement Monitor
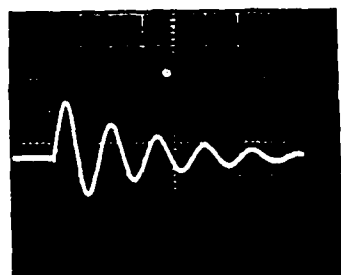
Current Waveform (50us/div)
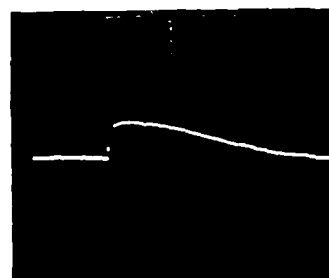
Current Waveform (0.1ms/div)
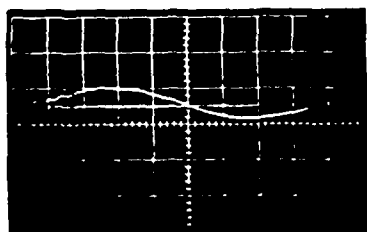
Fig. 8 - (a) Ringing Waveform Return Conductor Displacement Waveform (0.2ms/div)
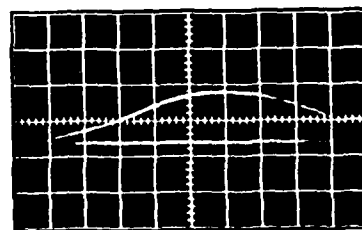
Fig. 8 - (b) Clamped Waveform Return Conductor Displacement Waveform (0.1ms/div)
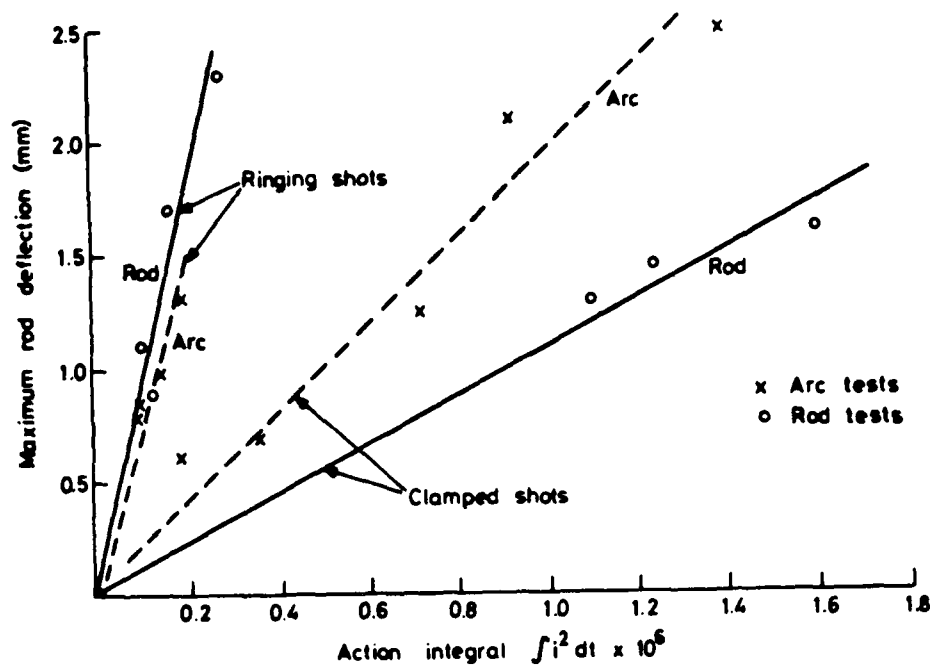
Fig. 9 Plot of deflection against action integral for experimental discharges.

P_t = Effective transient force

P_o = Peak applied force

τ = Current decay time constant

ω = 2π × Natural frequency of the system
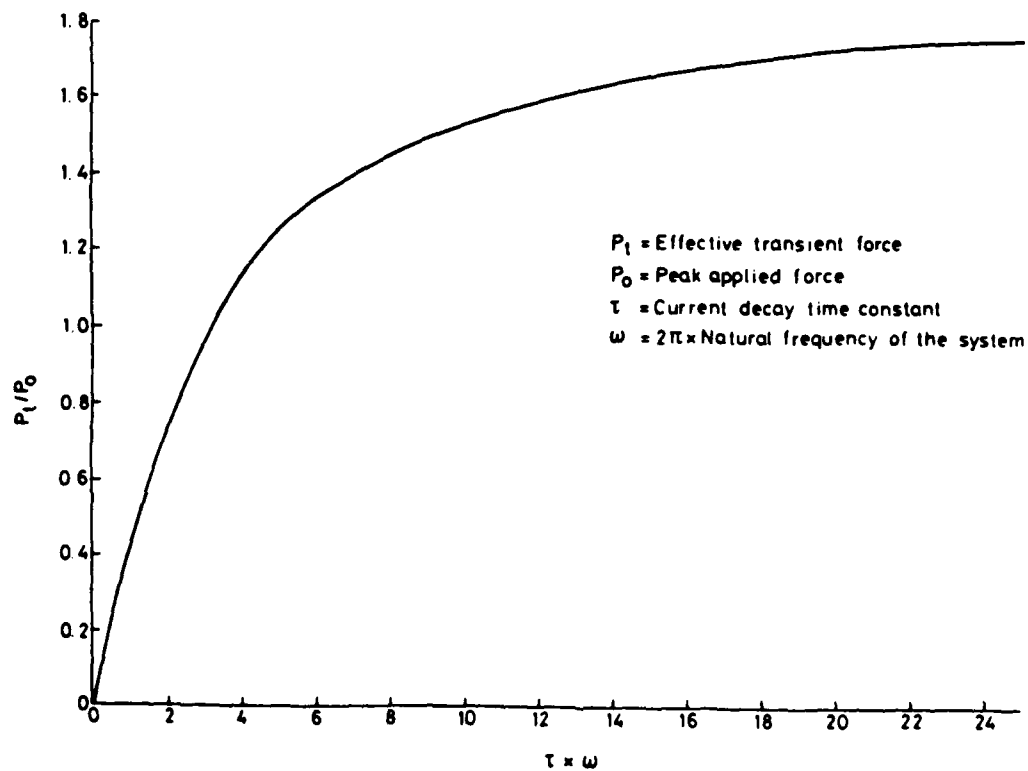
Fig. 10. Curve for calculating effective force from experimental impulse force
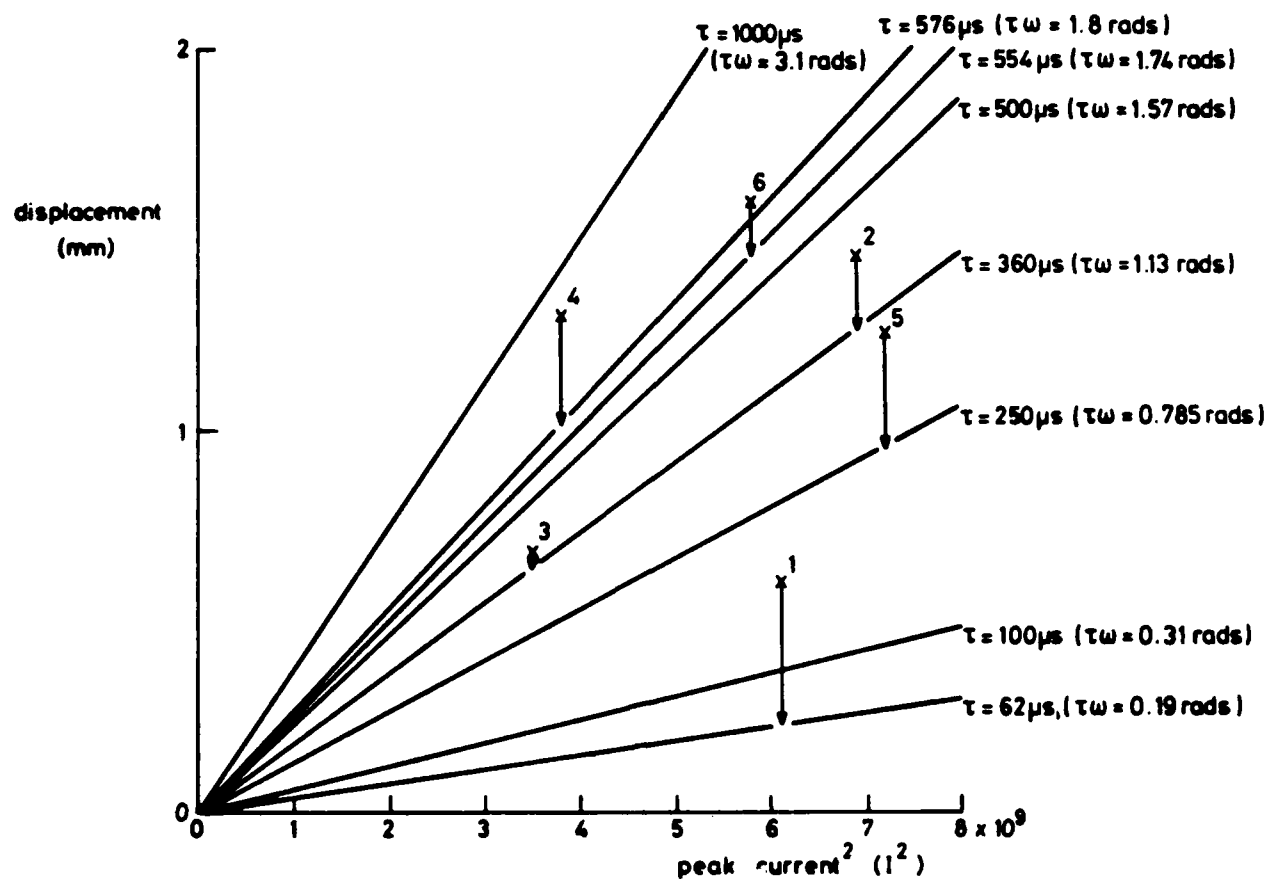
Fig. 11 – Displacement against Peak Current Square for Different Values of
τ ($\omega = 3.1 \times 10^3$ rads/s). Full lines are the theoretically predicted
values. The experimental results (x) are related to the corresponding
theoretical value by an arrow and to Table 4 by numbers 1 to 6.

The Lightning and Electrostatic Control Effort
For the Apache/AH-64 Helicopter

By

G. A. Booth and H. M. Hoffart
Hughes Helicopters Inc.
Culver City, CA 90230

ABSTRACT

The primary flight pattern of the AH-64 Helicopter will subject the vehicle
primarily to cloud-to-ground lightning discharges as well as cloud-to-cloud. Other
considerations are the tribo-electric effects. To effect control, a concerted
review of the vehicles lightning and charging aspects was performed. Deleterious
effects were examined and corrective measures described in this paper will assure
greater personnel and vehicle safety while complying with the vehicles mission
requirements.

The AH-64 Apache Helicopter uses a four blade main rotor and a four bladed
tail rotor driven by two gas turbine engines to meet the required flight and per-
formance characteristics. The main and tail rotors, in addition to sections of
the vehicles body, include composite materials in their design and construction.
Composite materials are also used for structural support as well as for aerodynamic
covers for some of the avionics equipment as well as for the gas turbine engines.
The extensive use of composite materials in the AH-64 vehicle design impacted on
the control efforts for lightning attraction and discharging plus the problems
associated with possible lightning penetration into on-board avionics equipment.
Other areas associated with electrostatic discharging included electromagnetic
interference/electromagnetic compatibility requirements and effective eletrical
bonding control for all electrical-electronic units used in the vehicle. To effec-
tively implement the above areas, whatever control measures were exercised,
the control effort impact was considered for each of the areas outlined above.
Wick static dischargers are used extensively. Including blade tip static discharge
wicks, to dissipate vehicle electric potential charges to limit vehicle potential
levels to only a few thousand volts. Blade wicks also reduce pulse discharge
levels. The lower peak energy levels per pulse can effect a 20dB to as much as
100dB of quieting for the vehicles communications equipment. Thus, an improvement
in electromagnetic compatibility is realized, though the initial effort pertained
to the reduction of vehicle electrification potential levels. Streamer currents
are also reduced because of the use of multiple wick static dischargers. Elec-
trical bonding designed into the structure and surfaces and effectively implemented,
will reduce arcing that would otherwise be present due to high potential levels and
high level streamer currents.

The paper will therefore delineate the controls and measures employed to
reduce the effects of lightning, static electrical charging and the interaction of
electromagnetic interference control and electrical bonding.

This paper was not available for incorporation into this book.

The Sandia Lightning Simulator

By

James C. Bushnell and J. G. Kostas
Sandia National Laboratories
Albuquerque, New Mexico 87185

ABSTRACT

Sandia has developed a lightning simulator to produce currents equivalent to
those of severe natural lightning, (99 percentile), on external loads on the order
of 8 microhenries. The simulator can produce from 1 to 4 pulses, with the first
pulse having peak current of 200 kiloampere, rising to this value in 2 microseconds,
with an e-folding decay time on the order of 75 microseconds. The interpulse
spacing may be varied over a wide range. A continuing current on the order of 300
amperes for 1 second may also be included. The total action integral is as high
3×10^6 ampere^2 - second, and total charge transfer 300 coulombs. The design and
implementation of this facility and associated instrumentation will be discussed.

THIS PAPER DESCRIBES the Sandia Lightning Simulator, which has been built at Sandia National Laboratories, Albuquerque, New Mexico to provide a test capability for severe lightning current threat levels to large as well as small test objects. This simulator is of a design rather different from most other simulators, and provides the following capabilities:

- peak current of 200 kiloamperes
- second pulse of 100 kiloamperes
- rise time to peak current 2 microseconds
- decay time constant 75-300 microseconds
- peak rate of rise on the order of 200 kiloamperes per microsecond
- multiple pulse operation at arbitrary time delays
- continuing current of 300 amperes for 1 second
- total action integral in excess of 2 million amp-squared seconds
- total charge transfer in excess of 300 coulombs

The simulator is based on the use of a crowbarred Marx generator and provides a lightning test capability difficult to produce by more traditional means.

The simulator is based on the use of crowbarred Marx generator and provides a lightning test capability difficult to produce by more traditional means.

The basis for the design requirements is the report by Cianos and Pierce (1) which surveys the knowledge of natural lightning available up to the time of its writing in 1972, and the detailed rationale for the design parameters of the Sandia simulator, which is not discussed here, is largely derived from this report.

A number of simulators for natural lightning have been built in recent years. Most of these simulators are based on the use of some variant of the linear R-L-C circuit, either under-damped, critically damped or overdamped. It is not the purpose of this paper to discuss in detail the characteristics which may be obtained by such circuits, but some preliminary comments may help to provide a framework for the decisions which have been made in the design of the Sandia simulator.

It is possible to obtain fast current risetimes using an underdamped RLC circuit, with the resulting waveform being a damped sine wave. Such a waveform has dominant frequency components in the vicinity of the fundamental frequency, and hence pre-ferentially exites those resonances in a system under test near this frequency, In addition, such a waveform is bipolar, whereas natural lightning is unipolar. The critically damped waveform is unipolar, but the waveform produced exhibits either longer rise times or shorter decay times than expected from natural lightning if the other para-meter is maintained at typical values.

Of the three linear RLC circuit types, the overdamped ciruit is capable of most nearly simulating natural lightning rise and decay times, and in priciple any combination of rise and decay times may be obtained by suitable choice of the parameters. The basic difficulty with the overdamped circuit is that the requirements for a short rise time and a long decay time imply that a relatively large damping resistance, well in excess of that inherent in most tests, must be included to generate typical lightning waveforms. The energy requirement for an overdamped circuit is determined by the value of the damping resistance.

An example may suffice to demonstrate the problem. Suppose that it is desired to produce a 200 kiloampere peak current into an external load of 5 microhenries, with a 10-90% risetime of 2 microseconds and an e-folding time constant of 75 microseconds. An over-damped circuit yielding these parameters must have a capacitance of 15.9 micro-farads charged to 1.03 megavolts and a resistance of 4.8 ohms, with total stored energy of 8.4 megajoules. Such a circuit is both economically prohibitive and probably technically infeasible. With more modest requirements on the peak current, for example, such as the ability to simulate typical lightning peak curents of, say, 20 kiloamperes rather than those which may be expected in extreme lightning environments, it is possible to build such a simulator, and several have been constructed for this regime.

The remainder of this paper is divided into several sections. The second section gives a more detailed description of the design characteristics. The third section describes the basic design which was chosen as a result. The forth section is an overall descrip-tion of the high voltage components which are included in the simulator. The fifth section gives a more detailed description o the crowbar switch. The sixth section describes the building and exterior area in which the simulator is housed. The seventh section discusses

the instrumentation which is incorporated in the simulator and used for tests, and the last section is a summary of the paper.

DESIGN CHARACTERISTICS - The design characteristics of the Sandia lightning simulator have been chosen to match the 99%-ile levels of natural lightning, with the exception of the number of strokes. Present technology does not allow the production of lightning flashes at this level for all the pertinent characteristics, and a choice must be made to give a design which is both technologically and economically feasible.

A combination of basic and derived parameters may be used to represent lightning flashes. Those used here are: the stroke rise time, number of strokes per flash, peak current in a single stroke, action integral (the integral of the square of the current with respect to time), and total charge transferred. Other combinations of parameters are possible, but it is preferable to choose a set of parameters which are nominally statistically independent. The large statistical variability of natural lightning is also important, and it is desirable to provide for the simulation of nominal lightning strikes as well as those very severe. There is only limited knowledge available on the statistical correlations between the above parameters. In the absence of such knowledge, it was deemed desirable to be able to produce all of these major parameters simultaneously. Simultaneous production of these parameters is important because there may be important synegistic effects occurring in the combined environment which do not occur in the individual environments taken one at a time.

This set of parameters is reasonable for describing the severity of lightning damage effects. The rise time is important because the coupling through apertures increases with decreasing rise time and correspondingly greater high frequency content. The number of strokes is important because of the synergistic effects which may occur because the first of a series of strokes produces initial effects which allow significant damage to occur on later strokes. The peak current is important because it determines the maximum magnetic forces which a structure may experience. The action integral is important because when resistive

heating damage effects are expected, the action integral times the resistance gives the deposited energy. Finally, the total charge transferred is important in such phenomena as burnthrough when a plasma is formed at a surface, since in this case the energy deposited is proportional to the total charge times the plasma voltage drop.

The design characterisics which result from these considerations along with technological and economic considerations are also shown in Table 1.

The estimated voltages between cloud and ground are on the order of 100 megavolts prior to the lightning flash, and initiate the stepped leader precursor to the return stroke. The electric fields which exist just before initiation of the return stroke can be quite large, and are certainly major contributors to the aperture coupling to systems, but are perhaps less important in direct-strike lightning damage than the return stroke currents. It is for this reason that emphasis is given in the simulator design on the return stroke simulation. The electric fields present immediately before the return stroke have similarities to NEMP, and EMP tests may be expected to be pertinent to this kind of vulnerability.

There has been considerable recent work on the possibility of lightning risetimes in the submicrosecond regime, which is largely subsequent to the fixing of the design parameters of the Sandia simulator. The Sandia simulator in its present form is not capable of submicrosecond rise times, although exploratory work in this area is in progress.

BASIC DESIGN - The capability to produce the levels shown in Table 1 is made possible by a circuit concept due to F. W. Neilson for lightning simulation(2) which has not previously been used for this purpose, although the general concept has been studied extensively for other purposes. The key to the circuit used in the Sandia lightning simulator is the use of a crowbar switch across the Marx generator used to supply th high voltage required to produce the high current levels in an external load. The use of a crowbar switch produces an essentially nonlinear circuit in which, before closure of the crowbar switch, the circuit is a lightly damped L-C circuit, while after crowbar switch closure the circuit becomes an L-R circuit. The basic

circuit concept is shown in Fig. 1.

With this design, the lightning current rise time is dependent upon the product of the source capacitance and the total circuit inductance, which is a series combination of the external load inductance (equipment under test), the intrinsic source inductance, the interconnection inductance, and any inductance deliberately added to provide the desired current rise time.

The decay time of the current is then determined by the ratio of the total circuit inductance to the total circuit resistance. With a total circuit inductance on the order of 10 microhenries, a total circuit resistance on the order of 0.1 ohms is required to give a decay time on the order of the desired value of 75 microseconds. This low a value turns out to be well within acheivable ranges. The principal interest in lightning effects is for structures which are largely metallic or contain substantial metallic paths, and in almost all cases the resistance is rather low. The restriction that the circuit resistance must be low has not proved to be a significant limitation.

The circuit used for the Sandia lightning simulator is qualitatively different from those used in most other lightning simulators. The essentially nonlinear nature of the circuit used in the Sandia lightning simulator eliminates the requirement for a large damping resistor, and the resulting energy efficiency is aproximately two orders of magnitude better than an overdamped circuit with essentially the same output characteristics.

The crowbar circuit requires a low inductance voltage source to drive the peak current through the external load inductance, since the peak current obtainable is the initial voltage times the square root of the ratio of source capacitance to total circuit inductance.

The principal requirements for implementation of such a circuit concept are a low inductance high energy capacitance and a suitable crowbar switch. The obvious choice for energy storage is a Marx generator which will be briefly described for those not familiar with the concept.

A Marx generator is a high voltage generator consisting of a number of capacitors which are charged in parallel and connected in series by spark gaps. Initially the spark gaps are open circuits, and an external power supply is used to charge the capacitors to a common voltage. When the Marx generator is fired (erected) one or more spark gaps are triggered, and the untriggered spark gaps are rapidly fired by overvoltage. The resultant configuration is a series configuration in which the capacitance is the series combination of the capacitors, and the voltage is the original charging voltage times the number of capacitors connected in series. A voltage multiplication is thus realized, allowing high voltage output with relatively low voltage input.

The air-insulated Marx generators extensively used for lightning simulation, for example in lightning attachment point studies can easily provide the voltages required, but their large physical size, which is due to the requirement for sufficient voltage standoff leads to a rather large inductance, and the peak currents which can be obtained do not reach the levels required by the design goals.

Sandia Laboratories has been engaged in high voltage research for approximately 20 years, principally for electron beam acceleration for a variety of radiation simulation purposes. the latest in the series of machines which have been built is the Particle Beam Fusion Accelerator (PBFA) (3), which contains 36 oil insulated Marx generators, each producing an open circuit output voltage of 3.2 megavolts. A relatively simple modification to the connection used for the PBFA Marx generators allows their use for the Sandia lightning simulator at 1.6 megavolts. Since these Marx generators were built at Sandia at the time the lightning simulator was being built, the Marx generators for the lightning simulator were constructed on the same assembly line. This occurrence was a very significant advantage in being able to build the Sandia lightning simulator.

Another principal component of the simulator is the continuing current generator (CCG). The CCG must produce a relatively low voltage on the order of 1 kilovolt to sustain an arc to a load, and produce output current on the order of 1 kiloampere to supply the required continuing current of 300 amperes to the load. The sources we considered were a bank of storage batteries, an electrical substation of 1 megawatt capacity and a motor-

generator set with inertial energy storage. The storage battery concept requires the lowest initial capital investment, but was rejected because of the substantial maintenance requirement and the safety hazards inherent in their use. The substation alternative requires an infrequently used continuous capacity and the capital costs were believed to be excessive, and the solid state rectifiers which are the obvious choice were expected to be unduly subject to damage from high voltage breakdown in the event of a malfunction. For these reasons, the first alternatives were rejected, and a motor-generator set is used in the simulator.

The original conception of the simulator did not anticipate a possible requirement for testing large objects such as airplanes, but it has proved possible to adapt the basic design for such purposes. More details are provided in the paper being presented by R. A. White(4) at this conference.

A circuit diagram of the principal high voltage and continuing current sections is shown in Fig. 2. Fig. 3 is an artist's drawing of the Sandia lightning simulator.

HIGH VOLTAGE COMPONENTS - The high voltage components are located in two oil tanks, with two of the four Marx generators in each oil tank.

The two oil tanks are each 12 feet wide, 21 feet long, and 10 feet high in inside dimensions. Each tank was built as three 12' by 7' by 10' sections welded together after installation. The pump and drain connections are through holes in the bottom of the tanks. The capacity of each tank is approximately 17,000 gallons.

The principal components inside the oil tanks are the Marx generators, the crowbar switches, the make-up inductances used to set the total circuit inductance, the trigger generators used for erection of the main Marxes and the crowbar switches, gas isolation switches to minimize interaction between different Marx generators, and the isolation/interconnection circuit between the high voltage components and the CCG.

The Marx generators are physically all the same size, two each of two different capacitance values. Each Marx generator has 32 capacitors of 0.7 or 1.3 microfarad nominal capacitance with a maximum

charge voltage of 100 kilovolts for a total stored energy of 112 or 208 kilojoules per Marx, or 640 kilojoules for all four Marx generators. The 32 capacitors are arranged when erected as two parallel stacks of 16 capacitors, providing an open circuit voltage of 1.6 megavolts with an effective capacitance of 87.5 or 162.5 nanofarads. The Marx generators are charged with dual polarity power supplies, because in this configura.ion one spark gap switch is required for every two capacitors, while with single polarity power supplies a spark gap is required for each capacitor. The internal Marx inductance for each Marx is approximately 1 microhenry and is appreciably lower than would be possible with single polarity charging.

The Marx spark gaps are of symmetrical construction with a midplane field distortion triggering electrode. With the +/- charging scheme, the DC voltage across each spark gap is 200 kilovolts, with the mid-plane triggering electrode initially at ground potential. The spark gaps are pressurized with sulfur hexafluoride at a pressure dependent upon the charge voltage, but typically on the order of 30 psi gauge. The trigger generator which initiates the Marx erection is itself a small 6-stage Marx with a nominal open circuit output voltage of 480 kilovolts and actual output voltage of 400 kilovolts when connected to the main Marx gaps. The Marx trigger voltage is fed to each gap through 2 kiloohm resistors. The trigger Marx generators are located inside the oil tanks near the main Marx generators.

Using a single 32 capacitor Marx with initial charge voltage of 100 kilovolts and a total circuit inductance of approximately 9 microhenries, a peak output current of 100 kiloamperes may be obtained with the sine wave current waveshape rising to its peak value in 2 microseconds. In principle, a single Marx with a total circuit inductance of 9 microhenries can produce output currents of 140 kiloamperes peak with a rise time of 1.4 microseconds. It is desirable to operate Marx generators at lower than their rated voltage capacity in order to provide longer life and decreased likelihood of catastrophic breakdown.

The design peak output current of 200 kiloamperes is obtained by the parallel connection of two Marx generators with a total circuit inductance of 9 microhenries. When

the full output current is desired, three pulses rather than four are obtainable because two of the Marxes are required to produce the first 200 kiloamperes pulse. At present, although four pulses are possible, limitations in available equipment allow a maximum of two pulses. The Marx generators are paralleled in pairs to produce the two pulses.

The series inductance of the Marx generators, the interconnection inductance and the load inductance is normally less than the desired value of 9 microhenries. In order to give a total circuit inductance of 9 microhenries, a make-up inductance is normally included in series with the output connection. This inductance is also located in the oil tank, and is chosen as appropriate depending on the external circuit inductance. The make-up inductance is constructed either of copper tubing, or of stainless steel when a resistive inductor is required to give the desired L/R decay time. The fact that in many cases the intrinic inductance and resistance of the system are low gives valuable flexibility in testing.

Since in multiple pulse operation of the lightning simulator all Marxes used must be charged before erection of the first one, it is necessary to provide isolation between the Marx generators so that the erection of one Marx does not in turn cause erection of other Marxes which are to be erected at the inter-pulse spacing of approximately 35 milliseconds, or damage due to the discharge of one Marx through unerected Marxes.

To provide this isolation, switchs are placed in series with the output connection from each Marx generator. The switch design is the same as the crowbar design except that no trigger is used. The switches operate in a self-break mode. The pressure in the isolation switches is set so that switch breakdown occurs due to overvolting when the Marx to which it is connected is fired, while the voltage across the isolation switch due to firing of a different Marx is insufficient to cause its breakdown due to inductive voltage division.

The final item included in the oil tanks is the isolation/interconnection circuit between the continuing current generator (CCG) and the output. This circuit provides for protection of the CCG from the high voltages produced by the Marx generators and for proper operation of the CCG itself. The interconnection circuit is composed of a shunt load of 1 ohm, a series resistance also of 1 ohm to provide current limiting of the continuing current, and a series inductance of four 100 microhenry inductors for isolation of the CCG output from the high voltage transient occurring when the Marxes fire. Without this inductive isolation, arc-over and damage to the armature windings are to be expected. The shunt and series resistors are salt water resistors to allow large energy handling capacity, and the isolation inductors are single layer solenoids wound on forms approximately 8 inches square and 12 inches long.

CROWBAR DESIGN AND TRIGGERING – The major innovation in the Sandia simulator is the use of a crowbar switch across the Marx generator, and a significant amount of the effort in the development of the simulator has been applied to the design and triggering of the crowbar switch.

The requirements on the crowbar switch are fairly stringent. The main requirements are that the crowbar must (a) withstand the full open circuit Marx voltage, (b) be command triggerable externally at much lower voltage, (c) have low inductance and resistance when closed in order to minimize coupling between the Marx generator and the external circuit, and (d) be able to carry the full charge of the main stroke for a reasonable number of shots.

Several different possibilities were considered for crowbarring, such as explosively driven foil switches, or water, oil or gas dielectric switches, operated with timing controlled by natural breakdown phenomena in a self-break mode, or by external triggering. As a result of consideration of such additional requirements as flexibility of operational conditions, avoidance of shock damage effects, and reusability, it was considered that the gas dielectric switch was most promising, and preliminary experiments conducted by R. L. Parker(5) showed that the electrically triggered sulfur hexafluoride switch appeared to be feasible. All the crowbar switches constructed have been gas dielectric switches with either electrical or laser triggering.

The Marx generator used as the primary energy store has an open circuit voltage of 1.6 MV to obtain the desired rate of rise of current. At two microseconds after Marx erection, the current

in the circuit has reached its peak value, with low voltage across the Marx generator, and at this time the crowbar switch should be triggered. In order to have low inductance and resistance, the crowbar switch should be physically small. With a desired time to peak of 2 microseconds, the allowable jitter in crowbar triggering is on the order of 100-200 nanoseconds. In many other uses of gas dielectric switches, the switch is operated near the self-break threshold, and the allowable jitter is substantially smaller than that for the lightning simulation application.

The most desirable gas for use as an insulator sulfur hexafluoride, as it has a breakdown strength several times that of air at the same pressure, and the crowbar switches used in the Sandia simulator have used either pure sulfur hexafluoride, or a mixture with other gases.

The crowbar switches are approximately 24 inches long and 24 inches in diameter. The end electrodes are insulated from each other by lucite rings with aluminum spacers to provide capacitive grading of the voltage. The end plates are of aluminum, and the electrodes have hemispherical ends made of stainless steel and are 3.5 inches in diameter. The crowbar design is essentially the same as used for the isolation switches in PBFA.

The original crowbar design was a trigatron, in which a trigger electrode is mounted in one of the switch electrodes with its tip flush with the surrounding electrode, and a 400 kilovolt trigger pulse is applied between the trigger electrode and the surrounding electrode. After a delay on the order or 100 nanoseconds which is dependent on the instantaneous voltage applied to the main gap, the arc produced by the trigger pulse causes a breakdown of the main gap, crowbarring the Marx generator and converting the circuit to the L-R decay mode. The gap used was on the order of 92 mm, with pure sulfur hexafluoride as the dielectric at a pressure of 90 psi gauge. Using this crowbar design, the design goal of 200 kiloamperes with the appropriate rise and decay times was first achieved. There were however some difficulties in reliability of operation and switch lifetime, principally due to erosion of electrodes due to the large charge transfer on each shot, amounting to 15 coulombs for a 200 kA pulse with

a decay time of 75 microseconds. The operating voltage range of this switch was somewhat limited at a fixed gap spacing, and operation at lower voltages required use of a smaller gap.

The alternative to the electrical triggering originally used is the use of a pulsed laser for switching the crowbar, in which the laser beam enters the gap through a hole in one electrode, with a lens being used to focus the light at or near the opposite electrode to initiate the breakdown of the main gap. Both IR and UV lasers, as well as visible lasers are possible candidates for this purpose, and we have used both Nd-doped glass IR and KrF excimer lasers.

The crowbar configuration used for laser triggering is very nearly the same as used for electrical triggering except that no trigger electrode is present, and the hole in one electrode is used instead for entry of the laser light. The laser is mounted outside the oil tank, and the laser output light is focused by a lens mounted inside the electrode so that the focal point is in the gap between the two electrodes. The laser beam produces ionization of the gas in the gap, initiating closure of the crowbar switch.

The IR laser approach was first used. The laser is a Pockels cell Q-switched Nd-glass laser, with an output energy of approximately 3.5 joules. The beam divergence of the laser is approximately 5 milliradians, appreciably larger than the diffraction limit. The laser must be mounted close to the crowbar switch to limit beam spreading and consequent loss of light transmitted through the limited aperture in the crowbar switch. In order to avoid sympathetic triggering of the laser electronics on erection of the main Marxes, the laser flash lamp power supplies and thyratron Q-switching electronics are located in the control room. Operation at full voltage is not possible with pure sulfur hexafluoride gas, and a mixture of 10% SF6, 50% N2 and 40% A is used at a pressure on the order of 180 psi gauge to allow triggering by the laser while avoiding self breakdown of the switch when the Marx generator. At present, the IR laser approach is still being used for production of the second lightning pulse.

It is advisable to operate the switch so that the peak Marx voltage is as far below the self-break threshold of the switch as possible. Since this

also means that the voltage at which the switch is to be operated is low, a tradeoff is necessary. The delay between laser pulse incidence and closure of the switch is a rather strong function of the instantaneous voltage across the switch. Since the voltage across the switch is a consine wave passing through zero at the most desirable time for switch closure, the delay between the laser pulse and switch closure may become so long that a failure to switch occurs, leading to an underdamped sine wave current waveform rather than the desired fast rise and slow decay.

Operation using a KrF UV excimer laser at 248 nm affords several advantages over the IR laser, the main ones being the fairly easy availability of low beam divergence lasers, and the ability to trigger in pure SF6 at lower pressure rather than the high pressure mixed gas required for the IR laser. The low beam divergence of about 200 microradians allows one to locate the laser remotely from the crowbar and use mirrors to align the beam with the crowbar switch. The capability for triggering with pure SF6 gas allows operation at lower pressure and with smaller gap spacings, affording greater safety and lower jitter operation. The output energy of the laser is approximately 0.5 joules, and only half of this energy ' applied to the crowbar switch to avoid laser damage to the crowbar switch windows.

BUILDING AND EXTERIOR AREA – The building (Sandia Laboratories Building 888) was constructed specifically to house the lightning simulator. It consists of five rooms: the high bay containing the high voltage components and the test object, the control room housing the computer and data acquisition and display equipment, the CCG room containing the CCG and associated equipment, the pump room housing pumps and oil filtration equipment, and a light lab and desk space for some of the personnel working in the facility.

A 150 foot by 300 foot are has been reserved east of the simulator building for tests which cannot be conducted indoors. A 50 foot by 90 foot concrete pad has been poured immediately outside the east rollup door to support heavy test objects. The concrete pad is made of high-strength concrete over highly compacted earth and is capable of supporting the main landing gear wheels of a F-14A airplane with their standard footprint.

A scale drawing of the coaxial line is shown in Fig. 4. The center of the output bushing is located 7 feet above the concrete pad. The high bay has interior dimensions of 50 feet by 60 feet by 30 feet high. A bridge crane of 6 ton capacity and a maximum hook height of 22 feet above ground level can traverse essentially the entire high bay floor area. In the high bay are located the two oil tanks containing most of the high voltage components; the load ring where experiments are mounted; the high voltage power supplies for charging the Marx and trigger generators; gas handling equipment or pressurizing the Marx generator gaps and crowbar switches; and a 10' by 7' screen room for collecting some of the data relating to facility operation. The high bay is lined with metal screening to reduce emanations from the high voltage equipment to the outdoors when the simulator is fired.

The control room is also lined with metal screening and in addition has an interior 10' by 20' screen room which holds the computer for data acquisition, analysis and display. There are four plastic conduits running underneath the floor, three of which connect to the high bay area with the fourth connecting to the CCG room. The CCG room houses the CCG itself, its motoring supply and the contactor used for conection to the high voltage circuitry.

The pump room contains two independpent pumping and filtration systems for the oil tanks, with connection to two external buried tanks each of 20,000 gallon capacity for oil storage when the high bay tanks must be drained for maintenance or circuit changes. Valving is included so that either pumping and filtration system may be used with either high bay oil tank. Emptying of the high bay oil tanks by gravity takes about 25 minutes, while filling is done through the pumps and takes about 2 hours.

The current outputs from the Marxes in the oil tanks must be combined and fed to the equipment under test outside the oil tanks. The load ring is used for this purpose. The two oil tanks are located with their 21 foot lengths parallel and 11 feet apart. Oil-insulated high voltage coaxial lines of 16 inch outer conductor diameter and 6 inch inner conductor diameter are connected between each oil tank and the load ring. The load ring is hexagonal of which and height approximately 4 feet. A roughly hemispherical lucite dome 30 inches in diameter is mounted on top of the load ring, and the output electrode, 6 inches in diameter, protrudes through

the lucite dome approximately 12 inches. The output electrode is connected to the center conductors of the coaxial lines from the oil tanks inside the load ring, which is also filled with oil. The inner conductors of the coaxial lines between the oil tanks and the load ring are supported by teflon cones mounted on the oil tank walls and inside the load ring.

Three bakelite pads are located on top of the load ring outside the hemispherical dome. The equipment under test is supported by a tripod arrangement which provides both mechanical support and electrical continuity for the ground return of the lightning current in a roughly coaxial configuration to minimize inductance and to equalize currents around the circumference of test objects. current viewing resistors (CVRs) are mounted adjacent to the three bakelite pads to complete the electrical circuit and provide for the measurement of the current waveform delivered to the load.

Tests have been conducted on objects too large to be mounted above the load ring. In order to conduct these tests, an additional high voltage oil insulated coaxial structure has been built to mount on top of the load ring to conduct the current to such objects. This structure allows test objects to be located out of doors, and incorporates an SF6 insulated high voltage bushing at the output end capable of withstanding approximately 1 MV, and a dummy load section in which may be mounted an inductor simulating the external load inductance which may be used for checkout off the simulator immediately before tests. The oil-air transition is made in two stages: first is an oil-sulfur hexafluoride transition in which the allowable fields in the sulfur hexafluoride gas are somewhat greater than in air, and in which the center conductor increases from the 6 inch diameter in the oil section to a 24 inch diameter to reduce corona and breakdown in the external air insulated region. The sulfur hexafluoride/air boundary is a fiberglass/epoxy cone with diameters at the ends of 48 and 24 inches and axial length of 48 inches.

The continuing current generator (CCG) must supply a load current on the order of 300 amperes for 1 second. Of the possible alternatives for such a source, the motor-generator alternative was chosen. The CCG consists of two diesel locomotive traction motors mounted with coupled shafts. The motor armature windings were rewound to produce the desired characteristics. In operation, one of the motors is driven by a power supply to drive the combination to a maximum speed of 1800 rpm using separate field and motoring supplies. After they are up to the desired speed, the motoring supply is disconnected and the field supply is set at maximum current. In the generator mode, the outputs of the two motors used as generators are connected in parallel using blocking diodes so as to prevent one generator from driving the other due to the unavoidable small differences in output voltage.

The source of electrical energy from the CCG is the inertial stored energy of approximately 2 megajoules in the rotation of the armature, so that the generators slow down during the continuing current phase as mechanical energy is converted into electrical energy.

The armature inductance of each generator is on the order of 20 milli-henries. With a 1 ohm load, the output current rise time from the CCG is on the order of 20 milliseconds. The open circuit voltage of approximately 1 kilo-volt from the CCG is insufficient to initiate an arc over the distance of several inches used to separate the simulator from the load when arcing to it is desired. Because of the exponential decay of the current produced by the Marx generator/crowbar circuit, the load arc would extinguish well before the CCG output rises in this problem is to establish an output current through the CCG armature inductance into a dummy load before the Marx generators are fired. When the first Marx generator is fired, the load arc forms, and a fraction of the shunt dummy load current transfers to the load arc in a time short compared to the intrinsic 20 millisecond time constant.

A mechanical contactor is used to make the connection between the CCG and the shunt load. This contactor as well as the CCG power supplies is located in the CCG room. Heavy duty cables are used to route the CCG output through a hole in the wall of the CCG room to a bushing on the oil tank wall through which the CCG output is fed to the isolation/interconnection circuit.

the initiation of the load arc by the high voltage from the Marx generators is an integral part of the switching of

the CCG. If a hard-wired connection were made with no arc, the continuing current would begin prior to the high current, giving an unrealistic simulation. It is possible, but substantially more complicated, to include a series switch in the CCG circuit to avoid the use of a load arc, particularly since such an arc may be included away from the load if a hard-wired connection is required.

The CCG output capacity is roughly 1 kilovolt at 1 kiloampere for 1 second. As the CCG slows down, the continuing current decreases until the CCG voltage is no longer sufficient to sustain the arc, which then extinguishes. This occurs at a voltage on the order of several hundred volts depending on the length of the load arc.

INSTRUMENTATION AND CONTROL - The instrumentation for the lightning simulator is comprised of numerous transducers for sensing, fiber optics transmitters, cables and receivers for data transmission, hard-wire coaxial cables for data transmission, oscilloscopes and transient digitizers for data acquisition, and a minicomputer for overall control, data analysis and data display.

The sensors used are principally CVRs and current probes for current measurement, high voltage dividers for voltage measurement, and special purpose sensors for incorporation inside equipment to be tested.

Four channels of 150 MHz fiber optics made by the Nanofast Corp. are available at present for monitoring of experimental outputs and facility characteristics. Two simultaneous 8 channel 25 MHz fiber optic transmitters are also available Coaxial cable connections may be made between sensors and recording instrumentation, although this must be done with concern for safety and avoidance of ground loop problems.

The data acquisition equipment consists of 5 Tektronix 7844 85 MHz bandwidth oscilloscopes with dual beams and dual time bases, three 2 channel Tektronix 7612D 200 MHz maximum sample rate 8 bit digitizer, 7 LeCroy 2256A 20 MHz maximum sample rate 8 bit digitizers, 2 LeCroy 8210 1 MHz maximum sample rate 10 bit digitizers each having 4 channels with a common time base, and 8 LeCroy 8830 33 MHz 8 bit digitizers with up to 8K storage.

A PDP-11/34 minicomputer with 128K 16 bit memory is used for data acquisition and analysis and inter-faced to all of the transient digitizers. The terminal is a Tektronix 4014 with full graphics capability and hard copy output. A line printer allows detailed printout of test results. An industry standard tape recorder is used for permanent storage of data and transmittal to other laboratories.

The software is written principally in Tektronix SPS BASIC, and implements remote setup and control of digitizers where possible, and rapid computation and display of test outputs such as current and vltage waveforms and action integral and charge transfer as well as relatively easily written data analysis programs. A file system for easy storage and retrieval of individual test results has been written.

Digital delay generators with 100 ns time resolution are used to provide the delays necessary for proper timing of the sequence of events in operation of the simulator.

SUMMARY

The Sandia Lightning simulator has proved to be successful for a variety of tests, both within the scope of its original design definition, and for a number of tests not originally conceived. Fig. 5 shows waveforms obtained in actual tests with peak currents above 200 kiloamperes. Although the entire development process is not yet complete, the simulator has been used for a number of tests on Sandia systems and for tests on two Navy aircraft, the F-14A and F/A-18, which are reported at this conference.

design and implementation of the
effort, and M. J. Landry has been
instrumental in the use of UV lasers
in triggering the crowbar switch.
P. Thullen of the Los Alamos
National Laboratory was very helpful
in our use of motor-generators for
continuing current generation.
T. H. Martin and numerous other
people associated with the Sandia
Particle Beam Fusion Accelerator
have provided valuable assistance
without which this simulator could
not have been built.

REFERENCES

1. N. Cianos and E. T. Pierce, "A Ground-Lightning Environment
    for Engineering Usage." Stanford Res. Inst. Techn. Rep. No. 1,
    Project 1834, Aug. 1972.
2. F. W. Neilson, "An Extreme Lightning Test Facility."
    Unpublished internal report, Sandia Laboratories, 1977.
3. T. H. Martin, J. P. VanDevender, G. W. Barr, S. A. Goldstein,
    R. A. White and J. F. Seamen, "Particle Beam Fusion
    Accelerator-I (PBFA-I)." 1981 Particle Accelerator Conference,
    Washington, D.C., March, 1981.
4. R. A. White, "Full-System Tests using the Sandia Lightning
    Simulator," this conference.
5. R. L. Parker, "Feasibility Studies for Crowbarring One
    Megavolt on the LILI Facility." Sandia Laboratories, SAND
    78-1700, April, 1979.

SANDIA LIGHTNING
SIMULATOR
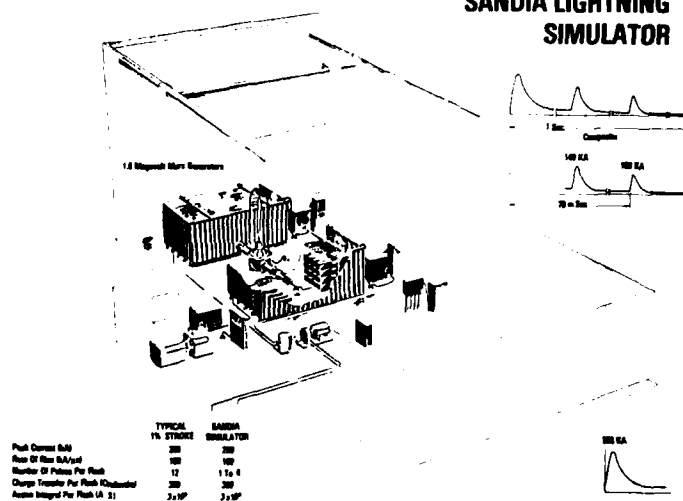
Fig. 3 - Sandia Lightning Simulator

$$R_L << 2\sqrt{\frac{L_L}{C_M}}$$
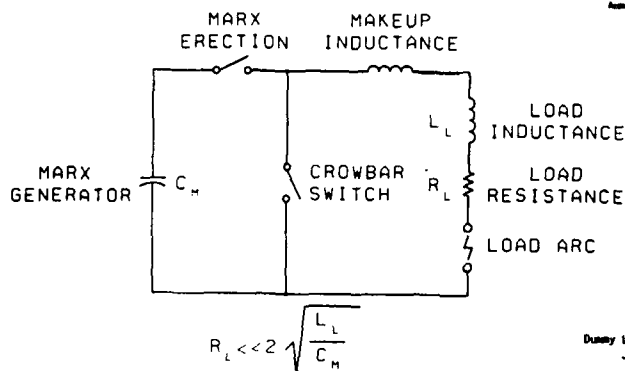
Fig. 1 - Basic Crowbarred Circuit
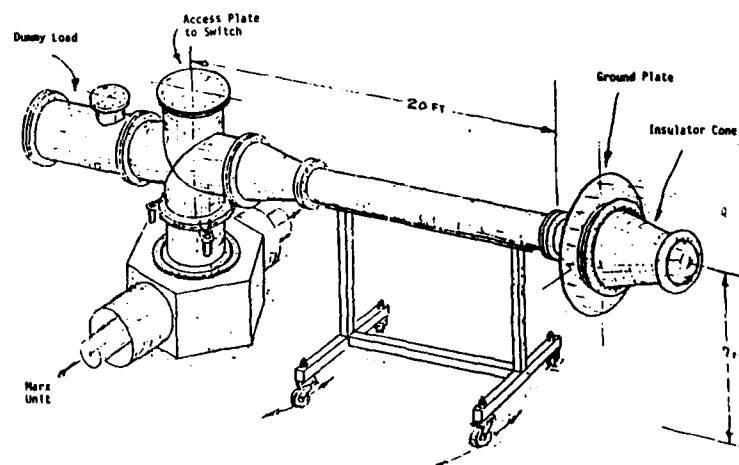
Fig. 4 - Coaxial Transmission Line
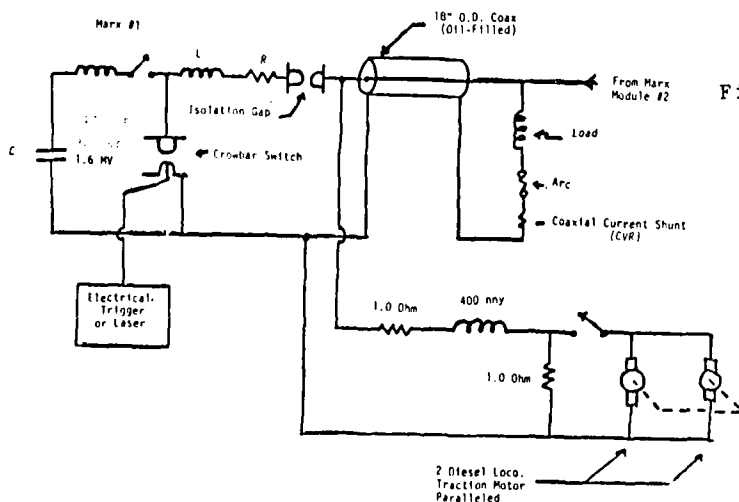
Fig. 2 - Lightning Simulator Circuit
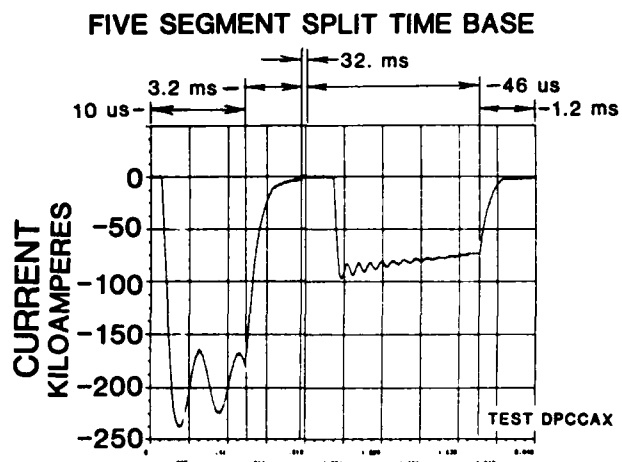
FIVE SEGMENT SPLIT TIME BASE

Fig. 5 - Simulator Current Waveforms

Fig. 7 - High Voltage Components
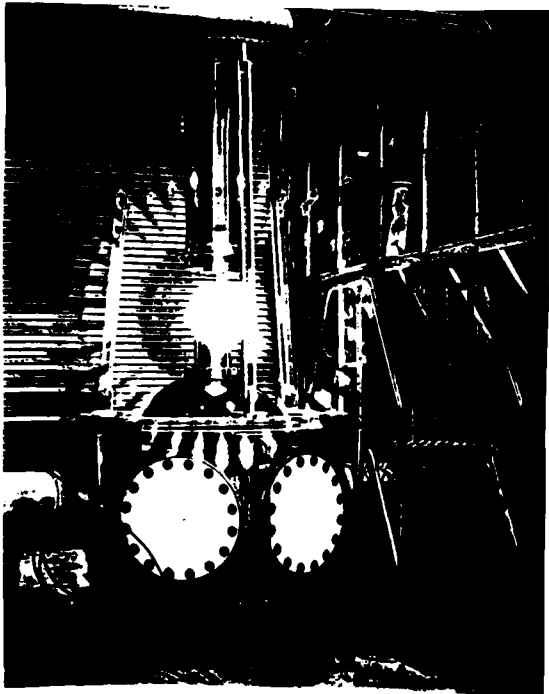

Fig. 6 - Weapon System Under Test
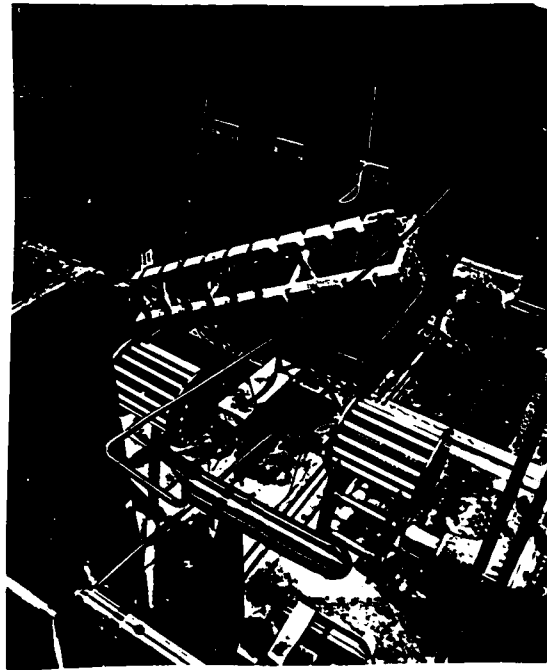
COMPONENT LIGHTNING TEST FOR THE AFTI/F-16
DIGITAL FLY-BY-WIRE SYSTEM

K. G. Wiles and R. T. Zeitler

General Dynamics
P. O. Box 748
Ft. Worth, TX 76101

ABSTRACT

A fly-by-wire flight control system with triple-redundant digital computer implementation is utilized on the Advanced Fighter Technology Integration/F-16 (AFTI/F-16) aircraft. Since flignt safety is contingent on a complex array of electronic circuitry, comprehensive lightning susceptibility testing was performed on the interface circuits to design-in protection against lightning induced transients. Criteria designation for this program was patterned after circuit-level testing completed on the F-16 aircraft (analog system) but was expanded in scope and depth to answer questions of functional upset as well as damage threshold requirements.

The objective of this paper is to present an overall summary of the component lightning susceptibility test program performed for the AFTI/F-16 Digital Flight Control System. This summary will include a description of the test criteria and procedure, an overview of test results, and a discussion of our conclusions and recommendations for future testing. In this manner, we hope to provide an insight into lightning susceptibility testing and hardening techniques for sensitive aircraft equipment.

INDIRECT EFFECTS FROM LIGHTNING STRIKES have always been of major concern for the F-16 flight control system because of its fly-by-wire design. This concern resulted in a development program to study these effects and to define hardness levels for electronic circuitry. As a result of the program, and data collected during lightning transient analysis (LTA) tests, a lightning hardness criteria was developed for use on the F-16 analog flight control system (1)*. This criteria was a rectangular pulse whose amplitude and duration represented the maximum amplitude and duration of the test data scaled to a 200-kiloampere threat level.

Subsequent studies utilized the F-16 LTA test data, and data from other aircraft, to establish a damped sinusoid criteria which more closely represented the natural phenomena. This criteria was also selected to represent the maximum amplitude and duration of full threat levels. The fundamental frequency of the damped sinusoid was selected from expected aircraft resonant frequencies with some safety margin added to assure maximum energy content.

Differences between the energy content of the rectangular and damped sinusoid pulses prompted considerable controversy. As a result of this controversy, both criteria were applied to the AFTI/F-16 Digital Flight Control System (DFCS). The results of this testing is presented and discussed in the following paragraphs.

TEST CRITERIA

Application of both test criteria to the DFCS interface circuitry followed the same format utilized on the F-16 analog system in which all interface circuits were reduced to a minimum number of worst case generic forms. Hardness evaluation of the selected generic circuits to lightning-induced, hard-failure damage was accomplished utilizing the rectangular and, to some extent, the damped sinusoid pulse criteria. Both pulses were compared for relative hardness levels and failure mechanisms when sufficient devices were available.

In addition to hardness evaluations, functional upset analyses were performed with the damped sinusoid. Expected variations in device protection and interface components were tested when dramatic changes in response were anticipated. This resulted in additional testing but helped to identify worst case responses. The salient features of both pulse criteria are as follows:

*Numbers in parentheses designate References at end of paper.

Rectangular Pulse Criteria

o Each generic interface circuit must withstand four unipolar rectangular pulses in each polarity.

o Each test pulse shall have an open circuit voltage of at least 500 volts and a source impedance of less than 100 ohms.

o Pulse width shall be at least 5 microseconds in duration with a rise and fall time not greater than 100 nanoseconds.

o Each test of rectangular pulses shall be applied between each line and equipment ground (common-mode) and also between the wires of any parallel pairs (transverse-mode).

o Four samples of each generic test circuit, where feasible, shall pass this criteria or hardening techniques shall be evaluated.

Damped Sinusoid Criteria

o Each generic interface circuit must withstand 15 damped sinusoid voltage pulses in a time period of one second or less. This step was used primarily as a comparison to the 500-volt rectangular pulse criteria; the energy content of one rectangular pulse is roughly equivalent to that of 15 damped sinusoid pulses.

o Each test pulse shall be a damped sinusoid waveform with a frequency of 1 Megahertz (+50%), an initial peak voltage of 500 volts (+10%), and a second peak voltage of greater than or equal to -300 volts with a generator source impedance of 100 ohms at 1 Megahertz.

o Initial rise-time shall be less than or equal to 100 nanoseconds.

o Each series of 15 voltage transient spikes shall be applied between each line and equipment ground (common-mode) and also between the wires of any parallel pairs (transverse-mode).

o Four samples of each generic test circuit, where feasible, shall pass this criteria with power applied or hardening techniques shall be evaluated.

Figure 1 illustrates the difference in the applied pulse criteria waveforms. The similarity in high frequency spectrum content and amplitude of each pulse is shown in figure 2. The major difference between waveforms is the dc component of the rectangular pulse which usually produced the thermal breakdown in the devices tested.
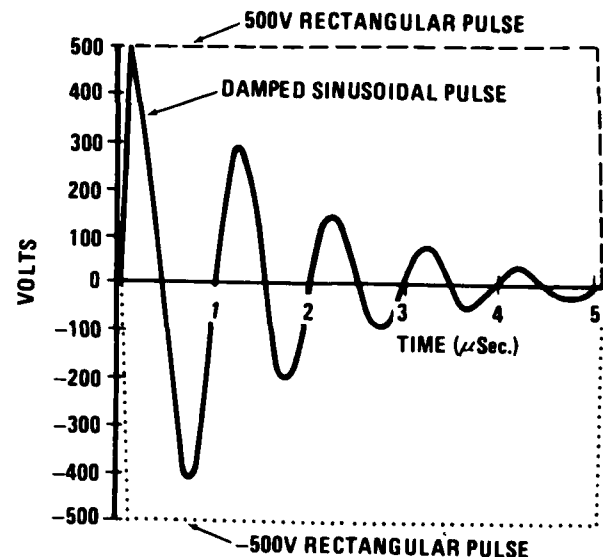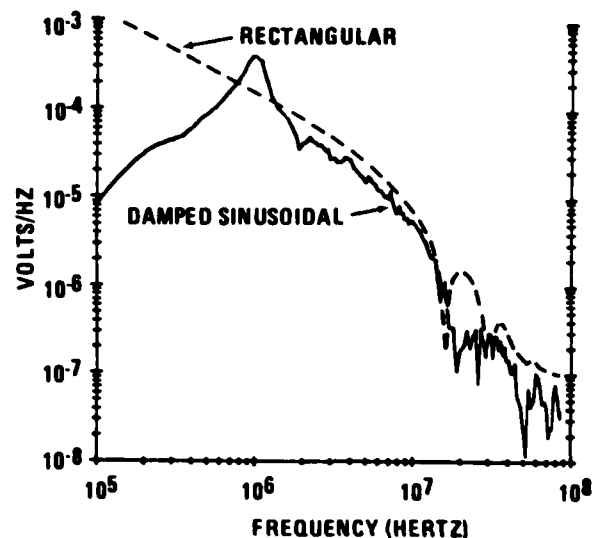
Fig. 1 – Pulse criteria waveforms

Fig. 2 – Relative spectral content of applied pulse criteria

TEST SETUP AND PROCEDURE

Each generic circuit was mounted in a printed circuit board and plugged into an interface box which provided access to circuit power, the pulse generator, and monitoring points. This interface box was then connected to the appropriate pulse generator test load as shown in figure 3. After each test, this arrangement was used to evaluate the pass/fail status of the circuit.

The schematic of figure 3 identifies the voltages monitored with a 100-MHz, differential oscilloscope. V_G was used to establish the applied pulse amplitude while V_L identified the voltage developed across the generic circuit interface. An 80-ohm current limiting resistor, which provided the source impedance, was used to stabilize the generator output and maintain the proper waveform throughout the test load dynamic range. This test arrangement made the pulse generator relatively insensitive to test circuit impedances, allowing the generator to see 31 ohms for a short circuit test load and 50 ohms for an open circuit test load.

Since V_G was a known applied quantity (i.e., the applied pulse), all pertinent circuit quantities could be determined from the transient response of V_L or V_R. The decision as to which of the two voltages would be measured was based on which voltage was anticipated to have the smallest peak amplitude since this would provide the best resolution of the test voltages. The

known transient voltage of V_G and the measured transient voltage of V_L or V_R were numerically combined and integrated by trapazoidal methods to evaluate the energy dissipated over the pulse duration. These voltage and energy manipulations were easily applied for the rectangular pulse; however, phase changes and waveform distortions created by the test circuit made the damped sinusoid pulse calculations too tedious except for general approximations.

In general, the basic test procedure involved applying the four-pulses/500-volt rectangular criteria in each polarity and, when device quantities permitted, applying the 15-pulse sinusoid criteria. This step was accomplished for each interface junction at 100-volt increments up to 500 volts. Pretest and posttest functional checks were performed after each pulse to determine the pass/fail status of the device. If a failure occurred, appropriate protection was devised based on allowable design constraints and testing was repeated.

After successfully demonstrating the required damage survivability, the circuit was tested for functional upset using the sinusoid criteria. Upset responses could not be eliminated on most circuits due to design constraints; consequently, these upsets were reported for evaluation to the flight control designers and provisions were made for system level tests in a lightning pulse chamber.
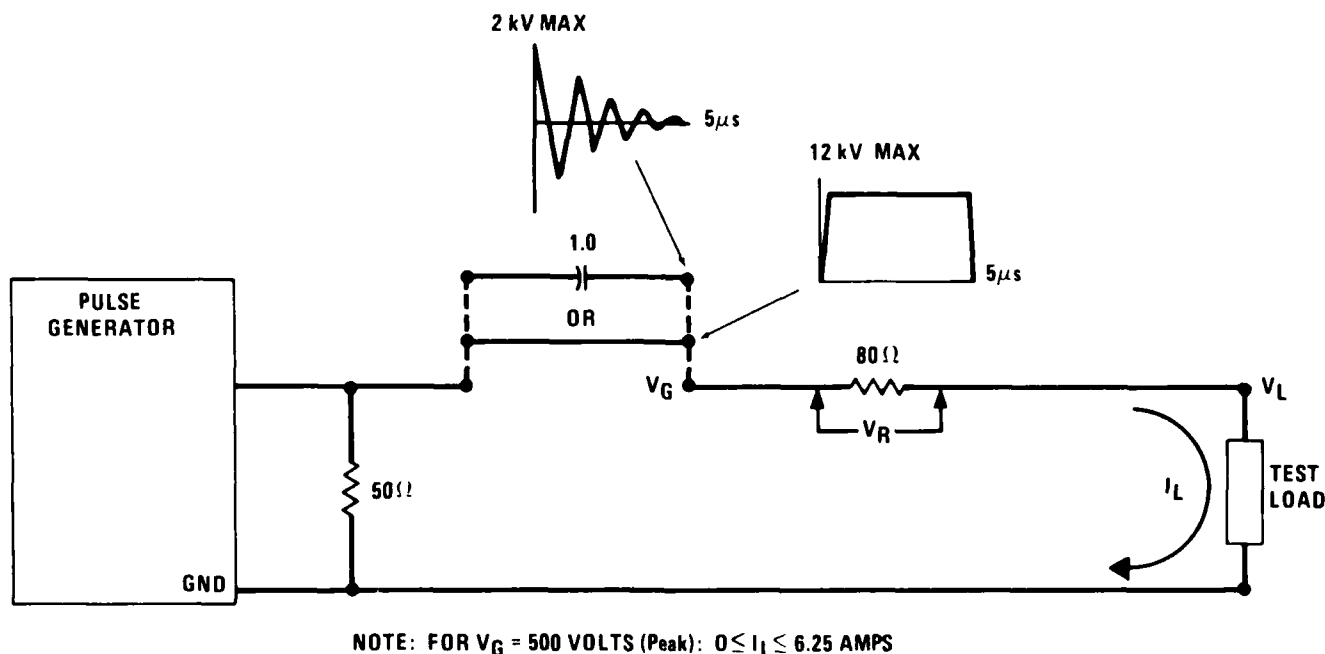

NOTE: FOR V_G = 500 VOLTS (Peak): $0 \leq I_L \leq 6.25$ AMPS

Fig. 3 - Basic test configuration

Table 1 – Generic Circuit Test Results
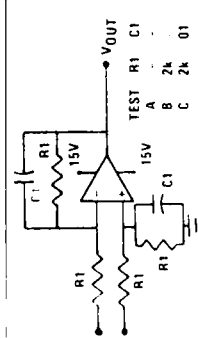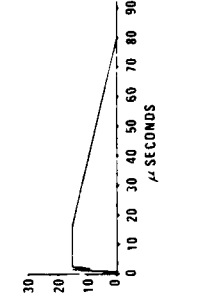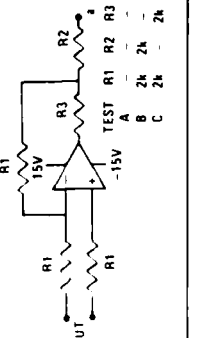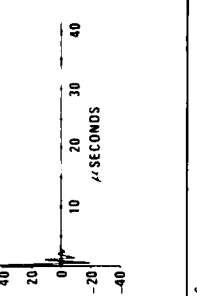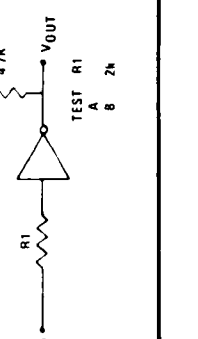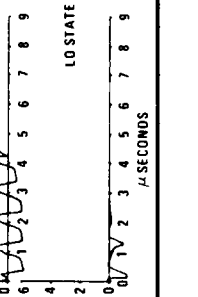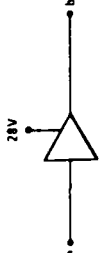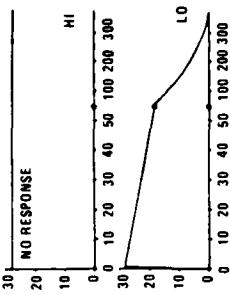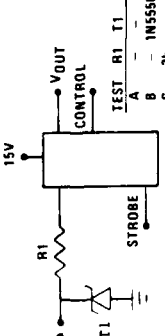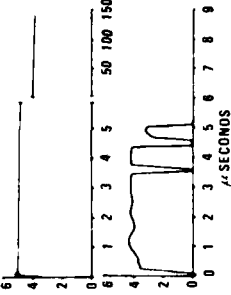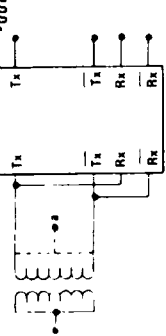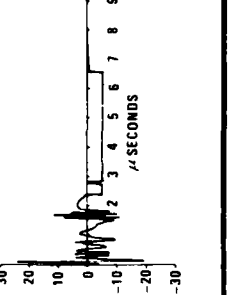
GENERIC CIRCUIT DESCRIPTION	TEST	TEST POINTS INPUT	TEST POINTS COMMON	SUSCEPTIBILITY 500 VOLT CRITERIA RECTANGLE	SUSCEPTIBILITY 500 VOLT CRITERIA SINUSOID	MAXIMUM RECT. PULSE TESTED & PASSED (VOLTS)	MAXIMUM RECT. PULSE TESTED & PASSED (AMPS)	V_{OUT} WORST CASE RESPONSE TO SINUSOIDAL PULSE CRITERIA
CIRCUIT 1 – LM124 OP AMP – INPUT	A1	a	b	FAIL	FAIL	100	—	(waveform, 0–90 μSECONDS)
	A2	b	a	FAIL	—	200	0.25	
	B1	a	b	PASS	PASS	510	0.24	
	B2	b	a	PASS	PASS	510	0.43	
	B3	ab	GND	PASS	—	510	0.49	
	B4	GND	ab	PASS	PASS	510	0.24	
	C1	a	b	PASS	—	520	0.24	
	C2	b	a	PASS	PASS	520	0.37	
	C3	ab	GND	PASS	PASS	520	0.37	
	C4	GND	ab	PASS	—	520		
CIRCUIT 2 LM124 OP AMP OUTPUT	A1	a	GND	FAIL	—	200	2.1	(waveform, μSECONDS to 40)
	A2	GND	a	FAIL	—	400	4.7	
	B1	a	GND	PASS	PASS	520	0.24	
	B2	GND	a	PASS	—	520	0.24	
	C1	a	GND	PASS	—	520	0.37	
	C2	GND	a	PASS	PASS	520	0.37	
CIRCUIT 3 – ULS2002H – INPUT	A1	a	GND	PASS	PASS	500	5.7	HIGH STATE / LO STATE (waveforms, μSECONDS)
	A2	GND	a	FAIL	—	125	1.3	
	B1	a	GND	PASS	PASS	510	0.23	
	B2	GND	a	PASS	—	510	0.25	

67-4

Table 1 – Generic Circuit Test Results
(continued)

GENERIC CIRCUIT DESCRIPTION	TEST POINTS			SUSCEPTIBILITY 500 VOLT CRITERIA		MAXIMUM RECT. PULSE TESTED & PASSED		V_{OUT} WORST CASE RESPONSE TO SINUSOIDAL PULSE CRITERIA
	TEST	INPUT	COMMON	RECTANGLE	SINUSOID	(VOLTS)	(AMPS)	
CIRCUIT 4 – UDN2981A DISCRETE – I/O	A1	a	GND	PASS	PASS	500	5.8	
	A2	GND	a	PASS	–	530	5.6	
	B1	b	GND	PASS	PASS	530	6.0	
	B2	GND	b	PASS	–	510	6.2	
CIRCUIT 5 – LS12793310-1 DISCRETE INPUT	A1	a	GND	FAIL	–	200	0.18	
	B1	a	GND	PASS	PASS	530	6.0	
	B2	GND	a	PASS	–	540	6.6	
	C1	a	GND	PASS	PASS	530	0.18	
	C2	GND	a	PASS	–	540	0.20	
CIRCUIT 6 – CT3231 MUX TRANSCEIVER – I/O	A1	a	GND	PASS	–	1200	13.6	
	A2	GND	a	PASS	–	500	5.4	
	B1	b	GND	PASS	PASS	1200	–	

TEST SUMMARY AND RECOMMENDATIONS

Test results on a few of the interface circuits are summarized in Table 1. In each case, device damage protection was achieved with little impact on circuit design. Most of the circuits used in the DFCS were protected with series resistance and/or shunt capacitance usually already included in the design. Transient suppression devices were only required on circuits where current or frequency requirements prohibited resistors and/or capacitors. In a few cases, devices were able to withstand the criteria pulses in one or both polarities. In these situations, internal damping or suppression accounted for the survivability.

All devices produced some response to the damped sinusoid criteria. Selection of different protection components modified the duration and severity of response. In general, the output response of a device was a variation on the typical output signal and lasted the duration of the lightning transient. The exception to this statement were those devices which could be driven into saturation, such as operational amplifiers. In these cases the saturation recovery time and circuit loading determined the duration of device response.

During the course of the program many observations were made concerning generic circuit testing. These observations and some associated recommendations are listed below:

1) Sudden polarity reversals from the sinusoid produced no observable degradation as originally expected even though devices failed both positive and negative rectangular pulses. The predominate rectangular failures were usually identified by device breakdown late in the pulse, indicating thermal failure. Sinusoid failures were rare but usually occurred on the leading edge of the transient and was duplicated in the rectangular pulse.

2) Comparison of the power on/off states revealed that solid state devices failed at lower generator voltages when power was applied. Typical circuits showed a reduction in load impedances with power applied which resulted in higher current levels into the device.

3) A decoupling capacitor was required in most cases to isolate the device from the low pulse-generator impedances. With device inputs decoupled, the circuit under test was pulsed in each state of operation.

4) "Equivalent" replacement parts do not have equivalent responses to lightning transients. Different manufacturers often use variations in device technologies, chip layout, and manufacturing techniques.

Variations in functional response to the lightning transients were the most common difference between replacement parts. Telltale clues for differences in damage characteristics were individual gate and total package power handling capability, maximum voltage ratings, and average life ratings.

5) Devices with built-in voltage suppression in one or preferably both polarities should be selected. Internal voltage suppression reduced or eliminated discrete component requirements for lightning protection and could reduce the device saturation time experienced with operational amplifiers.

6) Devices which have been tested for static discharge requirements (2) may provide a good source of lightning hardened devices. Static discharge tests usually involve much higher voltages for shorter durations than the lightning test but many of the failure mechanisms would be common to both.

7) Devices which have higher trigger thresholds for state changes and/or use higher operating voltages should be selected. These devices were more capable of dissipating the energy from coupled lightning transients.

8) Avoid the use of multi-port devices in which the exposed interfaces share a common node within the device as with the LSI 2793310-1. In this case a failure of one device input resulted in the loss of four to eight input discretes.

9) High speed devices with low failure voltages and/or wide bandwidth requirements (TTL, ECL, etc...) are difficult to protect from lightning transients. Suppression devices for these circuits must operate very close to maximum voltage tolerances; any significant overshoot from suppression delays can quickly degrade or damage the device. Wide bandwidth requirements minimize the use of filters and series resistances at the required values because they would prevent proper device operation.

The best alternative is to avoid this
type of device in the I/O interface; how-
ever, if nothing else will satisfy system
requirements then the I/O lines should
make use of good twisted-shielded pairs
or coaxial cables. Additional testing
is required in this area of device tech-
nology to investigate available options
and their degree of protection.

CONCLUSIONS

The generic circuit testing of the DFCS was
successfully completed with all interface cir-
cuits protected. No outstanding protection tech-
niques were required and many devices were in-
herently "hard" by the nature of the circuit de-
sign. In fact, most circuits are expected to
show damage survivability to two or three times
the levels applied simply due to the interface
components selected as part of normal design
considerations.

Interface circuit responses to a lightning
transient are expected to cause some problems;
however, these problems only extend to the fact
that a response occurs. Normal system design
usually accounts for unexpected transients at
interfaces by using various hardware and software
filtering techniques, redundancy, and persis-
tance. The final concern then is to assure that
secondary coupling beyond the interface circuit
does not occur above normal logic thresholds.

REFERENCES

1. Dr. Carl S. Droste, Robert T. Zeitler,
   and James L. Dabold, "A Lightning Pro-
   tection Program For The F-16 Fly-By-Wire
   System", IEEE International Symposium
   on Electromagnetic Compatibility, San
   Diego, CA., 1979.

2. DOD-STD-1686, Electrostatic Discharge
   Control Program For Protection Of
   Electrical and Electronic Parts,
   Assemblies And Equipment (Excluding
   Electrically Initiated Explosive
   Devices), 2 May 1980.

ACKNOWLEDGEMENT

LIGHTNING TESTS OF AN ELECTRONIC ENGINE CONTROL
WITH ASSOCIATED WIRING

J. Robb, D. Loncrini, H. Ogasian and P. Geren

ABSTRACT

Impulse and swept CW Lightning tests have been carried out as part of a developmental program on a new Electronic Engine Control (EEC) for the next generation of transport aircraft. The tests were made using an experimental engine as a test bed, and were carried out with the controller and with a variety of wiring harnesses.

Digital electonic engine controls are generally used on modern high bypass engines which have relatively poor shielding. The controller is mounted on the fan case and because of the requirements for easy maintnance and quick access, only a few attachment points, such as hinges and latches, can be used for the fan cowl. This lack of bonding points greatly reduces its shielding effectiveness.

The tests on the Electonic Engine Control (EEC) included (a) both impulse and swept CW tests with open and short circuit measurements of the induced voltages and currents at the controller to determine the basic coupling parameters, (b) low level tests with dummy loads at the controller to provide estimates of the voltages which would actually be seen at the pins of the EEC as a function of lightning current amplitude and rate of raise and (c) upset and damage tests of an operating EEC. Bulk cable currents and magnetic fields about the engine were also measured for correlation with the cable conductor measurements.

Single and double shielded cables and cables with both pigtail and 360 degree backshell to shield connections were studied. The impulse tests were performed with an impulse generator connected both as a simple capacitor bank and as a high voltage Marx impulse generator. The drive current was a 230-kHz damped sinusoid with currents ranging from 200 to 23,000 amperes crest current.

The basic problem and the solution may be summarized as follows. With the fan cowls which have only a few attachment points, the EEC and the wiring are in effect on the electromagnetic exterior of the aircraft and therefore the extra 25 to 45 db of shielding, which would be provided by the aircraft skin if the wiring were inside the aircraft or were under a peripherally bonded metal engine cowl, must be obtained for the exposed wiring on the engine. This can be done by either using double shielding or by adding peripheral bonding and improved shielding to a composite fan cowl.

LABORATORY AND IN FLIGHT PASSIVE
DISCHARGERS CHARACTERIZATION

by J.L. Boulay and P. Laroche

Office National d'Etudes et de Recherches Aérospatiales (ONERA)
BP 72 92322 CHATILLON CEDEX

ABSTRACT

A passive potential discharger, using three complementary methods for electromagnetic radiation reduction, has been defined at ONERA. Characterization in laboratory with a special experimental configuration gives the reference levels for the threshold and the efficiency of the discharger with different applied electrical fields. Several dischargers aircraft implantations have been tested in flight : threshold, current efficiency, hysteresis and electromagnetic radiation behaviour of the dischargers are analysed.

THE ELIMINATION OF RADIATION INTERFERENCE OF ELECTROSTATIC ORIGIN ON AN AIRCRAFT requires the use of passive dischargers whose role consists in transferring to the atmosphere electric charges that accumulate on the structure by triboelectric effects or by the exhaust of the propellers.

A "corona" discharge established directly on the structure will electrically disturb systems on board owing to an important coupling between the discharge zone and the corresponding reception antennae. However, the same "corona" discharge when created on a discharger will introduce a much reduced interference because of decoupling supplied by the configuration of the discharger [1]*.

ONERA has developed a discharger which uses three complementary methods of decoupling and allows reduction of radiation interference.

In the laboratory this reduction is measured to be of the order of -80 dBm compared with a non-decoupled system under the

[1]* Numbers in parentheses designate References at end of paper.

same conditions of electrostatic discharge [2] [3].

The purpose of this presentation is to compare the characteristics of a discharger as obtained both in the laboratory and in flight [4]. Two categories of characteristics will be analysed :

- the first one deals with the properties of current ejection associated with the discharger ; it will be shown that these properties are controlled either by the configuration of the space charge created by the discharge itself, or by electrification phenomena on the aircraft. In flight discharge efficiencies of such dischargers varie considerably because of their operating threshold and because of changes associated with the location of the dischargers on the structure of the aircraft. Hysteresis phenomena will be brought to light in the evolution of the emission current that depends on the potential of the aircraft ;

- the second category is related to the reduction of radio-electric interference observed on an ADF system functioning at 350 kHz. The dischargers are evaluated at various locations on the aircraft. It will be shown that residual interference is basically related to the occurrence of unprotected discharges on the structure rather than to intrinsic performance of the dischargers.

OPERATION OF THE POTENTIAL DISCHARGER

SIMPLIFIED MODEL OF A CORONA DISCHARGE - A potential discharger makes use of local intensification of the electrostatic field at a pointed geometrical structure. This makes possible to establish an electrical discharge of the "corona" type that transfers current into the air.

Physical mechanisms related to "corona" discharges, either positive or negative, are relatively complicated (electronic avalanches, recombinations, attachments, secondary emissions, space charge effects, etc...) [5] [6]. Nevertheless, based on studies of the current and radiation characteristics of

such discharges, we can, by limiting ourselves to the most frequent case encountered on aircraft, i.e. that of the negative "corona", schematize the overall process in the following way :

- first phase (fig. 1a) - A conductor (C) possessing a point A is subjected to an electric field E for example measured at a reference point L. When the field reaches at A a threshold E_0, ionization by electron collision occurs in the high local field near, the point. The positive and negative charges thus created, separate under the influence of the field and form an electric dipole of moment ql. The positive charge follows the field towards the point A, the negative one being carried along towards the exterior of the point ;

- intermediate phase (fig. 1b) - The positive ions are captured by the conductor (C), and secondary emission leads to new electronic avalanches. Negative ions are created by attachment of electrons to electronegative molecules in the low field region away from the point. These move towards the outside and lead to the increase in a negative space charge. The process continues as long as the creation of electrons-ions pairs is maintained ;

- final phase (fig. 1c) - The negative space charge becomes strong enough to reduce the electric field at the point A to values lower than E_0.

This puts an end to the avalanche process. Positive charge is then totally captured by the conductor (C) and negative space charge is still moving towards the outside at a speed $\mu_- E$ where $\mu-$ is the mobility of negative ions.

Another current pulse may reappear when the negative charge drifts far enough from the point A for the field reduction effect to vanish.

The whole process is illustrated by the help of two oscillograms of figure 2 representing the pulses associated with a corona discharge whose mean current i_m is of 70 µA ; the first and intermediate phases correspond to the zone of quick variation of the pulse (zone I, fig. 2a) ; the final phase being visualized by the slow variation of the latter. The oscillogram (b) provides the recurrence of these pulses which is here close to 500 kHz.

The mean current corresponds to the product of the frequency f by the charge q liberated in each pulse. It is roughly represented by a variation law of this form :

$$i_m = K(E - E_s)^2$$

where K is a constant at a given pressure, E_s being the value of E at the threshold of the corona discharge.

From a simplified radiation emission standpoint the "corona" discharge can be assimilated to an electric dipole of moment ql, where q and l are variable parameters in time and whose fundamental frequency of excitation

is the repetition frequency of pulses.

ELECTROMAGNETIC COUPLING BETWEEN AN ANTENNA AND AN ELECTRIC DISCHARGE - We have represented in figure 3 a schematic configuration of electromagnetic coupling between an antenna and an electric discharge : the element (1) is a conductor possessing a preferential zone of "corona" discharge occurrence (point A), the element (2) is the considered antenna. This configuration can be taken into account either for the evaluation of the electromagnetic characteristics of a discharger in the laboratory, or for the determination of interference of a reception system on aircraft with or without potential dischargers ; in this last case the element (1) will represent the aircraft structure itself.

The parasite short-circuit current of the antenna $i_{cc}(.)$ is given by [1] [2] :

$$i_{cc}(.) = \;_L(.).H_{LM}(.) \tag{1}$$

where $\;_L(\cdot)$ is a coupling function representing the transmission between a reference point L of the domain D of the corona discharge and the antenna. $H_{LM}(\cdot)$ is an independent function characterizing the properties of the noise source inside the domain D and evaluated at the same point L.

Tanner [1] has expressed these two functions in terms of the following two relations :

$$\;_L(.) = \frac{E_L(.)}{V(.)} \tag{2}$$

$E_L(\cdot)$ is the component of the radiation field normal at (1) at the point L where a voltage V(.) is applied between the conductors (1) and (2) :

$$H_{LM}(.) = \int_D \frac{\overrightarrow{E_M(.)}}{E_L(.)} \cdot \overrightarrow{j_M}(.)dD \tag{3}$$

$\overrightarrow{j_M}(\cdot)$ is the current density vector of frequency for any point M of the discharge and $\overrightarrow{E_M}(\cdot)$ the corresponding field at M when the tension is applied between (1) and (2).

An almost static condition applies inside the domain D :

$$\frac{\overrightarrow{E_M}(.)}{E_L(.)} = k_{LM}.\overrightarrow{u_M} \tag{4}$$

$\overrightarrow{u_M}$ is unit vector tangent to $\overrightarrow{E_M}(.)$ at the point M, and k_{LM} a scalar.

Under these conditions (3) becomes :

$$H_{LM}(.) = \int_D k_{LM} \overrightarrow{u_M} \cdot \overrightarrow{j_M}(.)dD \tag{5}$$

The function $\;_L( )$ will be determined either for a configuration of tests in the laboratory or, on the aircraft, between a point L of the structure and the antenna being considered. $H_{LM}( )$ can be considered as an intrinsic function of the discharger to be evaluated in the laboratory or on the aircraft.

OPTIMIZATION OF THE DISCHARGER FUNCTION FROM THE ELECTROMAGNETIC RADIATION STAND POINT [2] - Optimization implies minimizing the term $H_{LM}(\omega)$; consequently, the study of relation (5) allows several possibilities :

a) to reduce the scalar k_{LM} ;

b) to obtain an orthogonal configuration $\vec{u_M} \cdot \vec{jM} = 0$;

c) to reduce to negligible values the frequency dependent components of the current $j(\omega)$, which induces us to consider a continuous discharge regime ;

d) to increase in the domain D the number N of elementary discharges so that, for the efficiency of a givin discharge, the respective amplitudes of the N components $j_N(\omega)$ can be reduced due to the fact that the corresponding pulses are not simultaneous.

Reduction of the scalar k_{LM} - The principle of the method consists in moving the zone D from the discharge of the element (1) in order to reduce the inductive capacitive effect of the space charge in motion. On reconsidering the schematization of the coupling in figure 3b, we can examine the case in which the extremity of the conductor is isolated in such a way that a third conductor is created at the level of which the discharge appears. In order to maintain on (3) the presence of a "corona" discharge, it is of paramount importance to keep up between (1) and (3) the electrostatic potential ; this condition is achieved by inserting, between these two elements, an appropriate resistance R.

If we compare again the "corona" discharge with an electric dipole $\vec{P}$, we notice that the quantity of charges displaced by capacitive induction on (1) is reduced, or, in other terms, for the same tension $V(\omega)$ applied between (1) and (2), the electric field $\vec{E_M}(\omega)$ is reduced.

In order to guarantee the radiofrequency decoupling mentioned, the resistance inserted between (1) and (3) can be optimized. For frequencies higher than 100 kHz, a value close to 10 M is obtained.

Orthogonal decoupling - If the vector $\vec{u_M}$ and the current density vector $\vec{jM}(\omega)$ are orthogonal (cf. (5)), the scalar product $\vec{u_M} \cdot \vec{jM}$ is reduced to zero. This condition requires a preferential orientation of the discharge in relation to the radiofrequency field on a level with the discharge. The principle used is schematized in figure 3c : the conductor (3) remains isolated from the element (1) owing to the optimal resistance given above ; the conductor (3) is geometrically located to have its emission point situated in such a way that the dipole $\vec{P}$ appears in a direction perpendicular to the plane of symmetry of (1). We notice that, qualitatively, charges of both signs displaced on (1) by the inductive effect of the dipole $\vec{P}$, are equal in absolute value ; their

sum being reduced to zero, no parasite current flows in the antenna short-circuit.

Considering the decoupling resistance between (1) and (3), the orthodecoupling is complementary to the decoupling by resistance previously observed.

Decoupling by independent multidischarges [2] - The principle considered here does not require any outside intervention in the discharge mechanism ; it only consists in appropriating the emission zone so as to provide a large number of elementary discharges. The conductor (3) (cf. fig. 3d) is made up of a high resistive material and its configuration allows to produce discharges on a circular edge in a plane perpendicular to the axis of the discharger. Placed in an electric field, we notice that the whole circumference of the edge shows a great number of discharges emitting a quasi-continuous total current, which implies, on the one hand, that each discharge emits a small quantity of charges and, on the other hand, that these discharges are decorrelated in time.

This discharger presents therefore three complementary methods of decoupling :

- a decoupling by resistance,
- an orthodecoupling,
- a decoupling by multidischarges decorrelated in time.

It is this type of discharger which has been used in the tests performed in the laboratory and on aircraft and analysed in the two following paragraphs.

The discharger is made up of a resistive cylinder whose total resistance between extremities is of the order of 100 MΩ ; the external part of the cylinder is organized, as shown in the sketch (a) of figure 4, so as to form an emission zone perpendicular to the discharger axis. The picture (b) in figure 4 shows the envelope of corona discharges emitted while the discharger is in operation.

DISCHARGER EFFICIENCY

A discharger efficiency is characterized by two parameters :
- a threshold,
- the amplitude of the mean current emitted.

These parameters are determined in relation to an average electric field applied parallel to the axis of the discharger. We can already notice that the field reference will depend on the experimental configuration considered which will be different for the tests in the laboratory and the tests on aircraft. We will also show that the functioning of a discharger is essentially influenced by the structure of space charge due to its own discharge current ; furthermore the movements of space charge are influenced by the electric field configuration of the experimental set-up.

LABORATORY CHARACTERIZATION - The experimental configuration which is most fre-

quently used is that of point-plan arrangement (cf. "corona" discharge studies [5] [6]). We have used an electric field configuration around the discharger which aims at approximating closely the flight conditions (fig. 5) ; the discharger is installed on a support representing a partial structure of the trailing edge ; this support is connected with the electric ground through a device for measuring the mean discharge current i_d. The electric field is applied by means of an external electrode brought up to a potential V with respect to ground ; the polarization electrode is strapped to coincide with an equipotential surface, considering the trailing edge geometry [1]. The electric field used as reference is measured at a point L of the support surface in front of the discharger location.

This configuration allows to compare the discharger parameters defined previously with a "corona" point used as a reference or perhaps with other types of dischargers. This reference point whose length is similar to that of the discharger, possesses at its extremity a known radius of curvature r and gives the characteristic $i_d = f(E_L)$ corresponding to curve (1) in figure 5. Its threshold is $E_s = 10$ kVm^{-1} and the evolution of i_d vs E_s is quasi quadratic ; this result is in agreement with the relation given by Loeb [5] :

$$i_d = K(E - E_s)^{[2 - \frac{8r}{d}]}$$

(6)

where K is a coefficient related to the geometry of the test and where d is the distance between the point extremity and the polarization electrode. In our case $8r/d \ll 1$ therefore :

$$i_d = K(E - E_s)^2$$

(7)

The physical justification of this variation law is explained by the fact that the quantity of charge Q liberated in each Trichel pulse is proportional to the electric field existing at the point and that the frequency of these pulses $1/\Delta t$ is proportional to the drift velocity of the charges $\mu_- E$ (μ_- : mobility of negative ions) which is also proportional to the field, thus :

$$i_d = \frac{Q}{\Delta t} \backsim \gamma E^2$$

We notice that in the configuration of tests which has been used, the field E very rapidly becomes small and constant outside the extremity of the discharger.

In the configuration of tests which have been used, the threshold E_{s1} for "corona" at the point used as a reference depends only on local pressure.

Under the same experimental conditions we have shown in figure 5, curve 2, the variations of i_d vs E_L for the discharger defined above.

A threshold E_{s2}, measured on the sensor L, of 35 $kV.m^{-1}$, is higher than that of the reference point (10 $kV.m^{-1}$).

This discrepancy is due to intensification of the field which is more important for the first case than for the ring edge of the discharger.

After a first zone of quadratic variation, i_d tends towards a straight line starting at the functioning point P. For the same electric field, the discharger current is lower than that of the reference point.

Since the discharger has multidischarges not correlated in time, the space charge appears in the form of a continuous flood of negative ions driven by a drift velocity μE. The space charge field E_p reduces the production of primary electrons at the discharger tip. From equation (7) :

$$i_d = K(E - E_p - E_{s2})^2$$

E_p being proportional to the current i_d we have :

$$i_d = K(E - \alpha i_d - E_{s2})^2$$

As soon as i_d is sufficiently large we tend towards the linear relation :

$$i_d = \frac{1}{\alpha} E$$

(8)

In the presence of a flow of air with a velocity u, the relation (8) can be written in the form :

$$i_d = \frac{1}{\alpha} E + \varepsilon u E$$

(9)

where ε is a constant [5].

AIRCRAFT OPERATIONS – a) Ground testing

The aircraft used in a Meteor NF11. The instrumentation intented for the evaluation of potential dischargers has already been described in document [4].

The first series of measurements consisted in polarizing the aircraft, on the ground, by means of a high voltage generator and measuring the emission currents of a set of dischargers. These dischargers, here 21 of them, have been installed at the wing extremity (2 x 7), at the elevator extremity (2 x 3) and at the top of the rudder (1) ; the dischargers are spaced 30 cm apart.

The electric field used as a reference is measured at a point A of the structure on the aircraft fuselage.

In figure 6 we show the current variation for the discharger at the top of the rudder i_{dH} vs E_A. Beyond a threshold E_S of the order of 3.3 $kV.m^{-1}$, we observe the expected variation with E_A : a quasi-quadratic variation up to the point P, followed by a linear variation. We must point out a very good reproductibility of measurements in all these tests. Knowing that the threshold E_S measured in the laboratory and on the aircraft are not directly comparable we have indicated in figure 7 the variations of i_d vs E/E_S for both tests ; we can notice between the two types of measurements a very important discrepancy. If we compare the slopes of the linear characteristics, we obtain respectively $1/\iota = 31.76$ $\mu A/kV.m^{-1}$ for the laboratory tests and $1/\iota = 6.90$

$\mu A/kV.m^{-1}$ for the aircraft tests, i.e. a ratio 4.6. This difference is due to the behaviour of the space charge created by the emitted "corona" current ; indeed, both test series being performed at atmosphere pressure and the field conditions around the emission zone of the discharger being identical, only the distribution of electric fields outside the discharger are different ; consequently the drift velocity μE of negative ions changes and therefore, the space charge densities. We reach very rapidly a constant field in the case of the laboratory configuration (not far from the values measured on the discharger support) whereas it tends towards zero in the case of the polarized aircraft. It is therefore the term α of the relation (8) which practically determines the value of the emission current as soon as it becomes important. This result is qualitatively corroborated if we examine the characteristics of the dischargers at the wing extremity (dV) and at the elevator extremity (dE) which have an operating threshold identical to dH for the configuration of the aircraft chosen (3.3 $kV.m^{-1}$ measured at A).

The corresponding characteristics $i_d = f(E/E_s)$ as shown in figure 7 are slightly different from those of the discharger dH. At last, a final result allows to confirm the essential part played by the space charge in the discharge efficiency of a discharger ; if we compare the operating conditions of the seven dischargers placed on the aircraft wings, we notice that the discharger in the middle systematically emits the smallest quantity of current and gives, whatever the field E_A may be, a discrepancy of the order of 60 % in relation to the two dischargers nearby. This median discharger is therefore essentially influenced by the space charge liberated by the other six.

b) Tests in flight - Electric field reference - Measurement of the emission currents associated with the dischargers does not provide any difficulty because of specific instrumentation attached to each discharger. However, the determination of an electric field reference is proving to be much more complicated. Indeed, an aircraft in flight may be affected by the effects of its own electric charge Q due to triboelectric impacts or by the charge due to an external field E for example, the local atmospheric electric field.

We know that if the external electric field may be considered as uniform in a volume greater than that of the aircraft, the evaluation of its own potential $V = Q/C$, (C is the aircraft capacity) and the three components of the field E may be obtained from 4 measurements of the electric field E_i on the structure [4]. In these conditions we have :

$$
\begin{bmatrix} E_A \\ E_B \\ E_C \\ E_D \end{bmatrix} = [M] \begin{bmatrix} E_X \\ E_Y \\ E_Z \\ V \end{bmatrix} \qquad (10)
$$

where M is a matrix with β_i coefficients corresponding to the location of the sensors A, B, C and D on the structure.

In the particular case of an external field equal to zero, the expression (10) is reduced to :

$$
E_i = \beta_i V \qquad (11)
$$

The first test we are going to analyse deals with a flight (No 1) in which the aircraft does not possess potential dischargers ; this flight was performed at high altitude in clouds made of ice particles and without any external field.

In figure 8 we have drawn two curves corresponding to the variations of the impact current SI measured on a capture electrode on the aircraft structure and those of the field E_A vs time.

We notice a strong correlation between the time evolution of both parameters. The values $E_A = 0$ are observed simultaneously with the values $Sl = 0$ thus clearly indicating the absence of any noticeable external field. For the whole sequence we have shown in figure 9 the correlation between the electric field measured at the point A and the value of the potential V of the aircraft calculated by means of the relation (10) ; we clearly observe (cf. curve flight 1) a linearity between both terms, in agreement with the relation (11) ; however the slope $1/\beta_A = 2.783$ m of the straight line is rather different from the theoretical value $1/\beta_{ATH} = 4.149$ m.

The test having been performed without an external field we have to take into account the space charge effects. The fact that the field E_A is proportional to the potential V shows that the aircraft charge is related to charging and emission (discharging) currents of the aircraft.

Indeed, these space charges can have two origins :

- the former corresponds to positive particles liberated after collision with the front structures of the aircraft ;

- the latter is related to the negative ions emitted by discharges appearing on the structure of the aircraft.

Since the aircraft is negatively charged its distribution of charge can be schematized as shown in figure 10. The impact surfaces are acted upon by positive external charge produced in the collisions. It then follows that a part of the negative charge of the aircraft is drawn into these areas ; the trailing edge zones, affected by "corona" discharges, are subjected to the effects of the negative external space charge which

tends to repeal their own charges. These processes have therefore two consequences :

1) to modify the charge density at the point A in relation to the situation of a charged aircraft without space charge effects, therefore to modify the measurement of E_A vs V ;

2) to reduce the discharge efficiency of the dischargers (had they been used).

This phenomenon has been systematically observed for flights with triboelectric impacts ; as an example, we have drawn in figure 9 the curves $V = f(E_A)$ obtained during two other flights without a discharger (Nos 2 and 3). We can notice slopes $1/\beta_A$ slightly different from the previous one. For high potentials a change in the slope of the curve $V = f(E_A)$ may be observed ; this is the case of flight No 2 in which potentials exceeding 300 kV were obtained. As shown in the curve of figure 9 for flight No 2 a change in the slope (point I) is situated around $E_A = 65$ kV.m^{-1} ; this modification may be due to the occurrence of new "corona" discharges in different areas of the structure therefore to a new redistribution of charges on the aircraft.

Functioning of the dischargers – Three flights are analysed that correspond to three different installations of the dischargers. Their main characteristics are summarized in the table below ;

Flight No	Number of dis- chargers	location of dis- chargers	aircraft velocity	local pressure
4	23	V : 2x6 E : 2x4 HD : 2	205 ms^{-1}	495 mb
5	12	V : 2x3 E : 2x2 HD : 2	210 ms^{-1}	643 mb
6	9	V : 2x2 E : 2x2 HD : 1	210 ms^{-1}	808 mb

V : wing
E : elevator
HD : top of the rudder.

The curves $V = f(E_A)$, obtained for these three flights, exhibit the same characteristics as those obtained in situations without dischargers. We can observe again (figure 9) linear evolutions of the potential vs E_A for flights Nos 4 and 5, in which high values of the potential have been recorded. Changes in the slopes (point J) take place at a field value of 42 kV.m^{-1}. Let us notice, however, that the slopes $1/\beta_A$ of these curves are lower than those obtained for flights Nos 1, 2 and 3 without a discharger. This could indicate a greater influence of space charge due to the "coronas" on the dischargers. Furthermore, the changes in the slope observed in all the curves $V = f(E_i)$ (i : B, C and D) clearly coincide with the one observed for E_A showing there-

fore the overall effect of redistribution of space charge for the value $E_A = 42$ kV.m^{-1}. The instrumentation used on the aircraft allows to obtain directly the total current I_T emitted by the whole set of dischargers ; in figure 11 we have drawn three curves giving the variations of I_T vs E_A for flights Nos 4, 5 and 6.

We can notice that the evolutions of I_T are also linear in E_A but with a change in slope (points I) in all three cases. The change of slope detected during flight No 5 corresponds to the value $E_A = 42$ kV.m^{-1} mentioned above.

The general repartition of the current curves $I_T = f(E_A)$ in figure 11 is similar to that for the corresponding voltage curves $V = f(E_A)$ in figure 9. Except that the discharge thresholds are not approximatively related to the values of the local pressure for the three flights considered. Whereas the behaviour of the discharger installations in not notably different at low currents, discharge characteristics tend to vary a good deal at strong currents. For example, comparing flights Nos 4 and 5, we notice a current value of $I_T = 350$ µA corresponding to field values E_A of 50 and 107 kV/m (ratio 2). Since for the three tests, the velocities of the aircraft are close to one another this dispersion is essentially due to the space charge created by the dischargers whose number varies (23, 12 and 9 dischargers) according to the zones of the structure.

Figure 12 allows to illustrate the specific performance of a discharger namely the one dH, at the top of the rudder. The starting thresholds are different from those to be expected by the changes in local pressure particularly for the flights Nos 4 and 6. It must be mentioned that the threshold corresponding to the flight No 5 correlates with the value E_A of 42 kV.m^{-1} already observed, which would mean that the changes in the slope noticed in the characteristics $V = f(E_A)$ or $I_T = f(E_A)$ could be related to the thresholds of the discharges at the top of the rudder ; besides this point coincides also with a change in the slope of the characteristic i_{dH} for the flight No 4.

Another important fact is to be mentioned : it deals with hysterisis of the characteristics $i_d = f(E)$ observed during several tests ; we notice that when the current decreases it exhibits a threshold field value that is lower than the one for its initial onset.

The curve in figure 13 was obtained in another sequence of measurements in flight No 4. It clearly illustrates this hysterisis effect ; for increasing values of E_A, the top of the rudder discharger emits current at a threshold voltage of 32.5 kV.m^{-1} ; this current very rapidly rises at about 37 kV.m^{-1}, and becomes stabilized with a permanent linear characteristic (straigth line A) at the end of the sequence. However,

for decreasing currents the operating point follows at first the same straigth characteristic, but eventually deviates from it and leads to lower threshold field value of 17.5 $kV.m^{-1}$.

The interpretation of this phenomenon must also be explained by the effect of space charge that lowers the discharge onset of the dischargers located at the top of the rudder. The space charge delay the starting of the discharger but modify its discharge efficiency until a new electrostatic balance of the aircraft is obtained.

We can sum up the characteristics of this top of the rudder discharger by means of different curves of figure 14 in which we have described the emitted current i_{dH} in relation to the reduced field E_A/E_S, E_S being the threshold field measured at the point A for each test.

- When the number of dischargers is large (23 for the flight No 4) and for fields larger than E_S, we observe a characteristic current $i = f(E_A/E_S)$ close to that obtained on the ground tests. This result shows an electrostatic configuration around the aircraft which is nearly the same in both cases. The greater observed efficiency is due to the aircraft velocity.

- For a small number of dischargers (9 for flight No 6) the slope of the linear discharge characteristic is close to that obtained in the laboratory, which indicates a relatively homogeneous field in areas remote from the discharger tips.

- For intermediate cases (flight No 5 with 12 dischargers) the discharge characteristic of the discharger will be located between the two extreme operating configurations which have just been defined.

RESIDUAL ELECTROMAGNETIC RADIATION

PERFORMANCE OBTAINED IN THE LABORATORY - We have shown that the current emitted by a "corona" discharge is related to the movements of positive and negative charge that give rise to very brief pulses (of the order of 5 ns) and whose repetition frequency increases according to the intensity of the applied electric field. The radiation noise associated with emission at the reference point defined previously is analysed in relation to frequency by using the setting up described in figure 5. Here the discharger and its support can be considered as the reception antenna itself. The spectral distribution of noise is shown in picture (a) of figure 15 : we see a frequency distribution corresponding to the repetition frequency of current pulses. Experimentally and for average currents exceeding 10 µA, noise can be detected up to 100 MHz.

During the same laboratory tests we have shown that the decrease in radiation noise obtained through a discharger with coupling resistance is of the order of -30 dB and

rises to about -50 dB if an orthodecoupling is added. In the case of a discharger with multidischarges a white noise is practically obtained and we can state that the reduction (by comparison with a "corona" point operating with a similar mean current) goes to -80 dB for frequencies ranging from some 10 Hz to several MHz.

AIRCRAFT TESTS - Radio Electric Noise at 350 kHz - The receiver used is a classical ADF system operating as a detector with dynamic compression. The reception frequency is 350 kHz and the bandwidth is 3 kHz.

The aim of the test is to determine the interference level affecting the receiver in the presence of a "corona" discharge that is well defined and detected (reference point). The aircraft is isolated from ground by insulating blocks. It is connected to the earth by a resistance of 30 MΩ in order to create coupling conditions similar to those in flight, between the discharger and the corresponding antenna.

The reference point is at the wing tip and a suitable polarization device allows to vary the intensity of the average current emitted by this point. The radiation noise measured with respect to the mean current is represented in figure 15. The coupling function between the location of the point and the antenna is small and the noise level is rather low. No clearly established variation can be observed. This demonstrates the impulsional nature of the discharge ; noise maxima are recorded when an harmonic of the repetition frequency of current pulses is situated in the bandwidth of the receivers. This point is ascertained by a discrepancy observed, for the same emission current, depending on whether the latter is obtained in an increasing phase or a decreasing one ; the exact harmonic analysis of pulses shows indeed a frequential discrepancy between both experimental methods.

Discharger Effects on Aircraft - In order to measure the performance of the dischargers from the point of view of radiation we can consider again the three flights (Nos 4, 5 and 6) performed with installation of 23, 12 and 9 dischargers, and we compare the results obtained with reference to flight (No 1) performed without a discharger.

The radiation noise observed corresponds to the levels recorded in the ADF system at 350 kHz and whose detection threshold is of the order of some 10^{-6} V in the case of the aircraft in flight without electrification phenomenon.

Flight No 1 (fig. 17) - For the flight used as a reference, an important increase in noise is observed at a field of the order of 25 $kV.m^{-1}$. This coincides with the threshold for the wing or elevator extremities ; the noise reaches a maximum of 300 µV for $E_A = 40$ $kV.m^{-1}$ and then resumes its equilibrium at a value 100 µV. The highest level detected in the low field re-

gion may be explained by the fact the repetition frequency of the various discharges appearing on the structure are located in the area of the ADF receiver, whereas for higher fields only harmonics of frequency repetitions are taken into account.

Flight No 6 - For $E_A \leqslant 25$ kV.m^{-1}, the discrepancy observed in relation to flight No 1 is not significant ; the noise below 25 kV.m^{-1} is undistinguishable from flight No 1. But, on the other hand, a very rapid evolution of interference at 350 kHz occurs at 35 kV.m^{-1}, explaining the appearance of one or several "corona" discharges strongly coupled with the antenna ; the areas taken into account may be the trailing edges or the top of the rudder. A rapidly decreasing interference depending on the field, clearly indicates the presence of a "corona" source that is very localized and strongly coupled with the ADF antenna. Because of the low level of electrostatic activity observed during this flight, we do not have any data for values of E_A higher than 41 kV.m^{-1}.

Flight No 5 - The installation of an extra discharger on each elevator and at the top of the rudder allows to suppress the overall interference appearing around the value $E_A = 40$ kV.m^{-1}. We can observe a noticeable increase in noise for higher values of the field around 60 kV.m^{-1}. At this level the 12 installed dischargers have almost identical operating conditions. This indicates that the unprotected discharges appear in the strong electric field areas that require an increase in the number of dischargers.

Flight No 4 - Three extra dischargers have been installed on the wings, two on the elevator and one at the top of the rudder. No increase in noise can be noticed up to values E_A reaching 75 kV.m^{-1}. This demonstrates nearly complete radiation protection ; the recorded noise level is very close to the detection threshold of the receiver.

The important conclusions of these tests are expressed on the following statements :

a) Noticeable radiation interference appears in the detection system only it an unprotected "corona" discharge is created on the aircraft structure. This result is ascertained by tests performed on the ground where the establishment of a single "corona" discharge is sufficient to disturb the ADF receiver.

b) In strong electric field areas, the number of dischargers must be sufficient to avoid the formation of discharges directly on the structure. We are of the opinion that we must not exceed a maximal current of 50 µA for each discharger.

c) The performance of a discharger is sufficient if the decrease in radio noise for a current of 50 µA, reaches -50 dBm when compared to an unprotected discharge of the same mean current.

CONCLUSION

The following conclusions can be drawn from this analysis :

a) the electrostatic configuration of an aircraft in flight in the presence of triboelectric impact is very complicated ; in addition to the aircraft potential due to negative charges accumulated on the structure, important local electric fields due to particles charged after collision and negative ions liberated by the "corona" discharges have to be evaluated ;

b) this electrostatic configuration modify the discharge characteristics of the aircraft ; we show that they are linked to the presence of space charge which raise their operating threshold and make the evolution of the emitted current linear vs the potential or vs the electric fields on the structure ; hysteresis phenomenon in the functioning of the dischargers are frequently observed ;

c) electromagnetic radiation interference may be practically suppressed on an aircraft if the number of the dischargers is sufficient ; from the maximal value of the emission current for an aircraft of a given size and speed [1] the number of dischargers may be evaluated by limiting the maximal value of current per discharger to be of the order of 50 µA ;

d) the dischargers must exhibit a radiation coupling of at least -50 dBm in relation to an unprotected "corona" discharge of the same mean current.

REFERENCES

1. R.L. Tanner and al, "Precipitation charging and corona-generated interference in aircraft." AFCRL 336, Technical Report 73. SRI Project No 2494, Contract AF 19 (604), 3468, 1961.

2. J.L. Boulay, "Elimination des perturbations radioélectriques d'origine électrostatique sur avions." La Recherche Aérospatiale, pp. 101-120, n° 1979-2.

3. J.L. Boulay, "Optimization of the reduction of the radioelectric noise created by a corona discharge on aircraft." 3ème Congrès International de l'Electrostatique, Grenoble, 20-22 avril 1977.

4. J.L. Boulay and P. Laroche, "Aircraft potential variations in flight." International Aerospace Conference on Lightning and Static Electricity, Oxford, 23-25 mars 1982.

5. L.B. Loeb, "Electrical "coronas". Their basic physical mechanisms." University of California Press, 1965.

6. E. Nasser, "Fundamentals of gaseous ionization and plasma electronics." Wiley & Sons, Interscience, 1971.
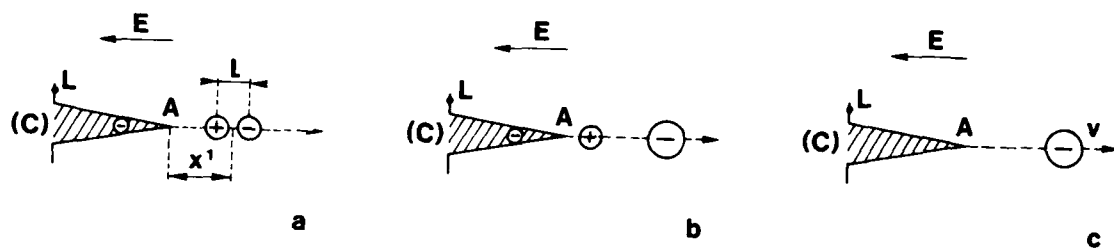
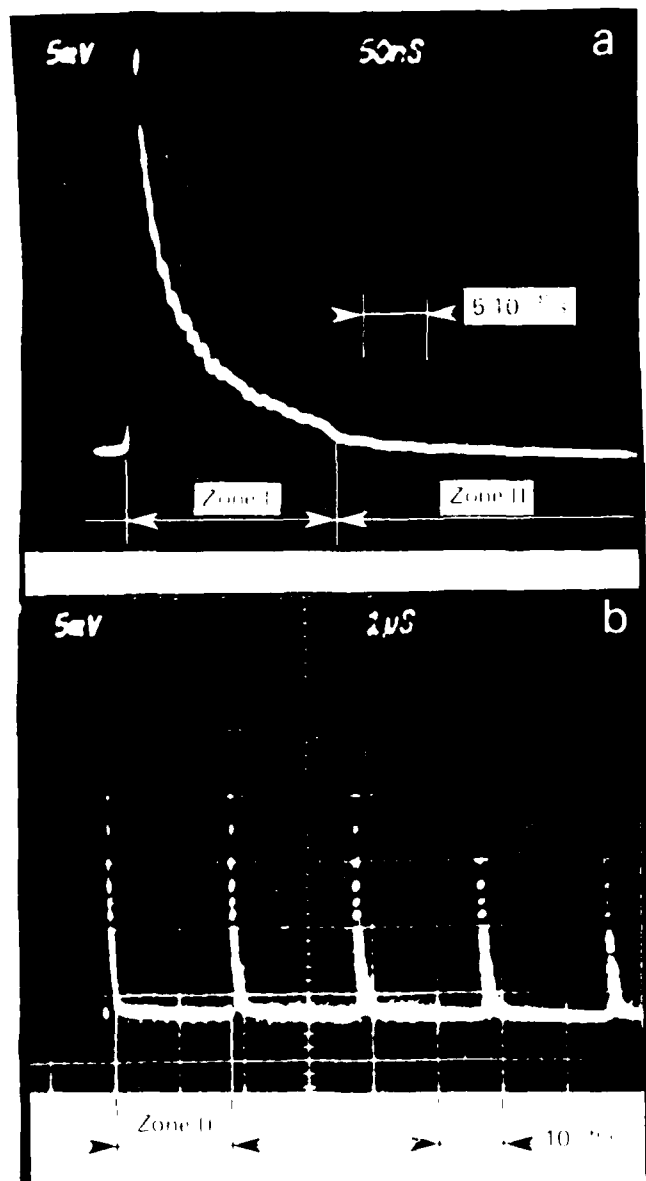Fig. 1 - Negative "corona" discharge model

Fig. 2 - Current pulses associated with a
negative "corona" discharge.
Mean current i_m = 70 μA

a . NO DECOUPLING   b . DECOUPLING BY A RESISTANCE

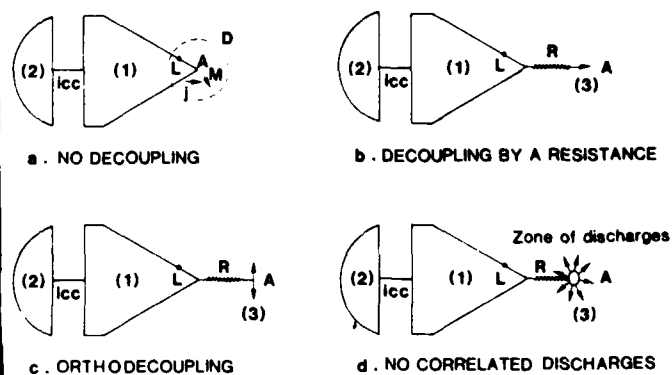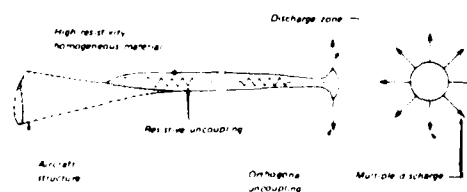c . ORTHODECOUPLING   d . NO CORRELATED DISCHARGES

Fig. 3 - Radiation coupling reduction prin-
ciples :
- without decoupling,
- decoupling by a resistance,
- orthodecoupling,
- decoupling by multidischarges

a | PRINCIPLE

b | VIEW OF THE "CORONA" DISCHARGE ZONE

Fig. 4 - Optimized discharger configuration
a) Principle
b) View of the "corona" discharge zone
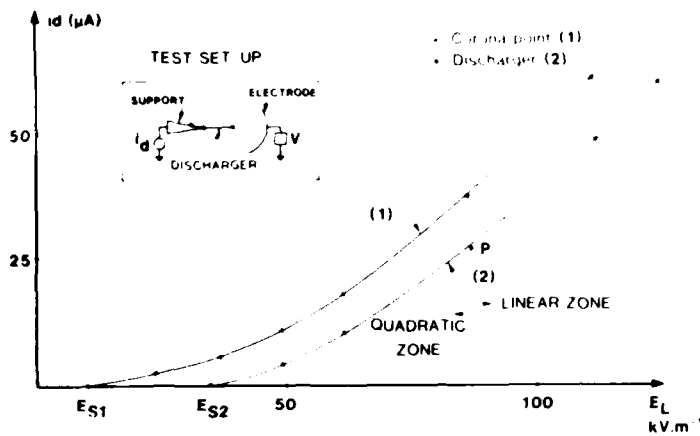
Fig. 5 - Discharge efficiency. Laboratory tests
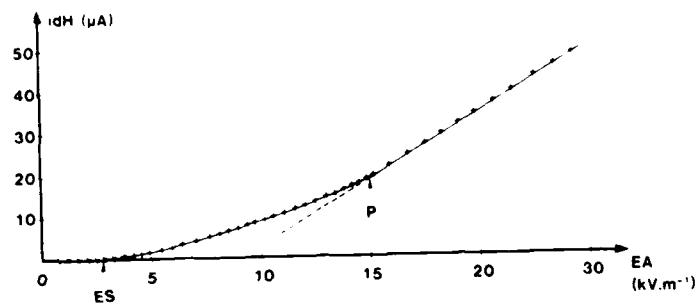
Fig. 6 - Discharge efficiency. Aircraft tests at ground
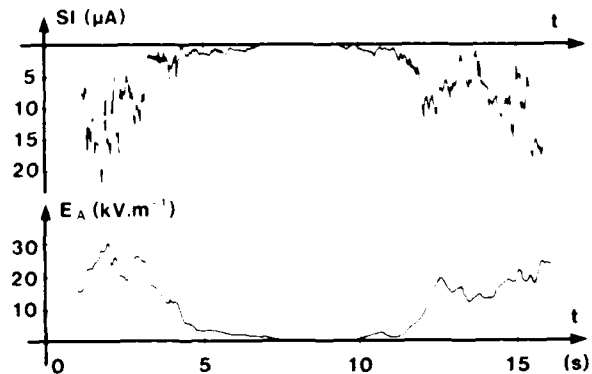
Fig. 8 - Flight No 1 - Impact current and electric field on the aircraft structure
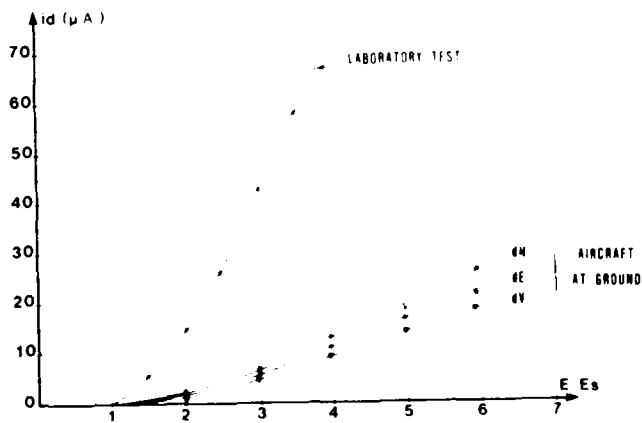
Fig. 7 - Comparison between discharge efficiencies
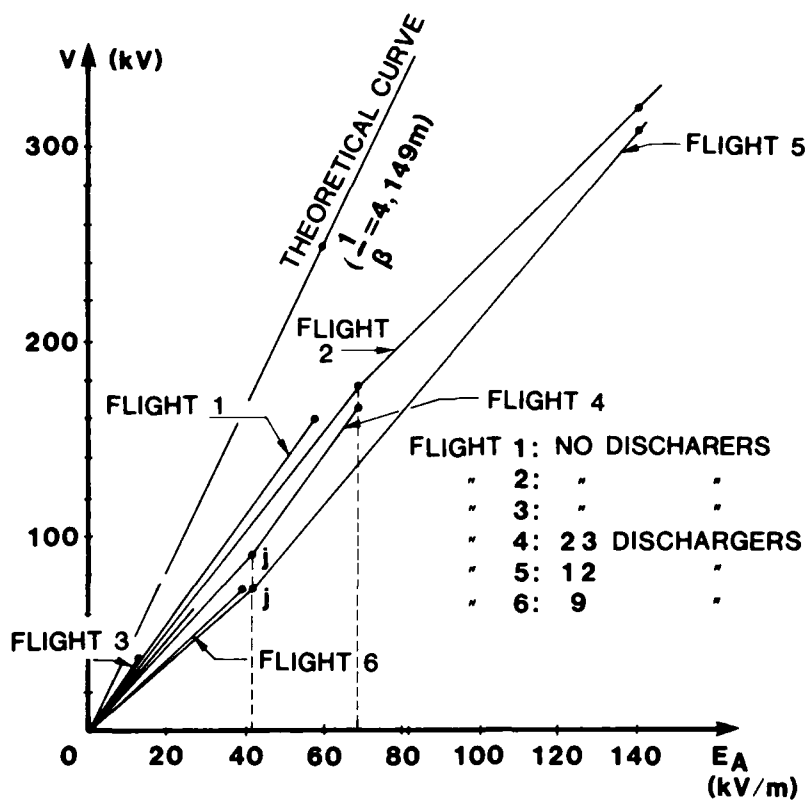
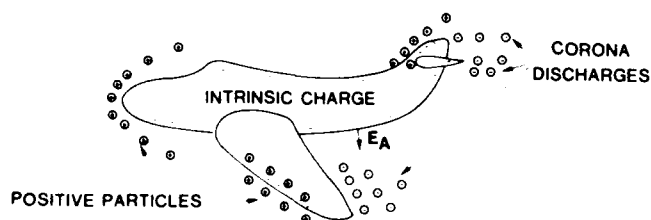Fig. 9 – Aircraft potential and electrical
field on the structure

FLIGHT 1: NO DISCHARERS
" 2: " "
" 3: " "
" 4: 2 3 DISCHARGERS
" 5: 1 2 "
" 6: 9 "

Fig. 10 – Electrical charged aircraft and
space charge. Schematic representation

Fig. 12 – In-flight discharger operation

Fig. 11 – Total current emitted by dis-
chargers
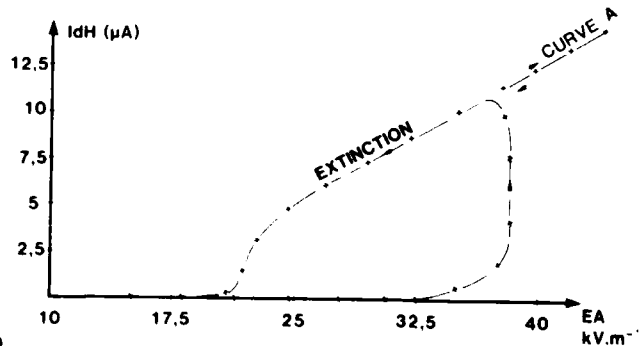
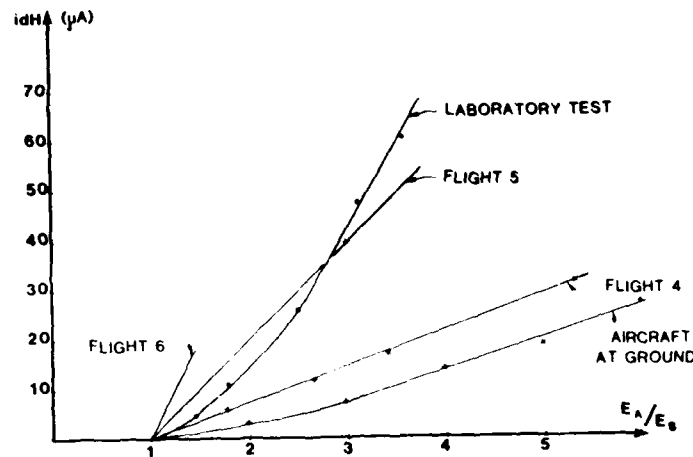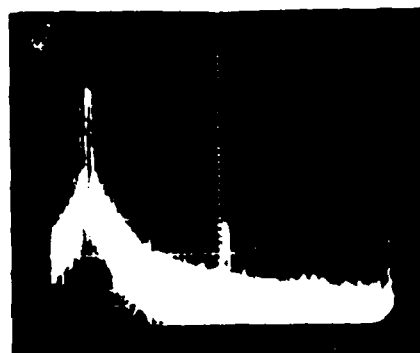Fig. 13 – Hysteresis associated with dis-
chargers

94-11

Fig. 14 - Characteristics of the discharger
at the top of the rudder

Ref   0 dBm   10 dBm div
5 MHz div - B   30 kHz
i m   30 µA

Ref. 30 dBm — 10 dBm div
200 kHz/div — B   30 kHz
i m   30 µA

a) " CORONA " POINT

b) MULTIDISCHARGE SYSTEM
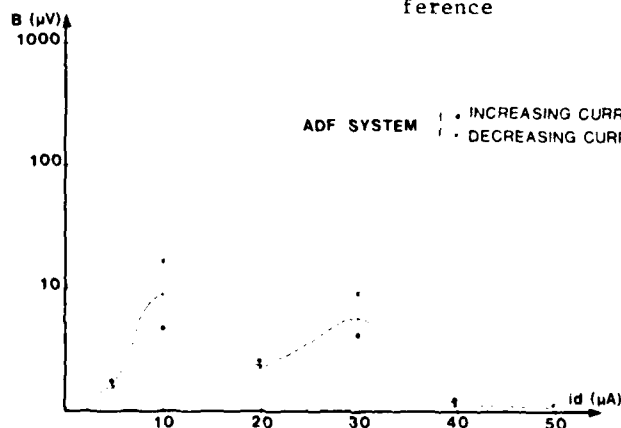
Fig. 15 - Laboratory tests : radiation inter-
ference

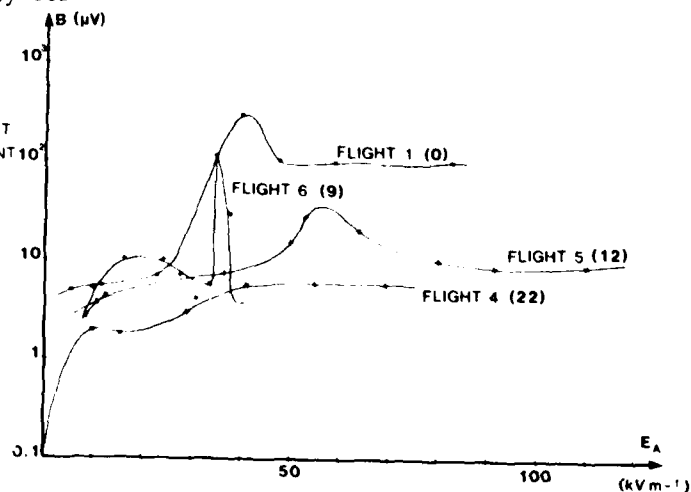Fig. 16 - Aircraft at ground. Radioelectric
noise at 350 kHz

Fig. 17 - In-flight radioelectric noises

Author's Index

Dorcey G. Abshier
Northrop Corp.
4910 St. Andrews Cr.
Buena Park, CA 90621

John W. Adams
NBS, Code 723.04
325 S. Broadway
Boulder, CO 80303

Pierre Alasluquetas
French Aviation
246 Rue Lecourbe 75732
Paris Cedex 15
France

David L. Albright
U.S. Army
2967 Westminster Dr.
Florissant, MO 63033

Dennis Andersh
721 Paseo Del Mar NE
Albuquerque, NM 87123

Robert V. Anderson
Naval Research Lab
Washington, DC 20375

Chuck J. Andrasco
FAA
APM-610
Washington, DC 20591

Paul H. Arnstein
U.S. Coast Guard
Comdt. (G-TES-41)
2100 d St. SW
Washington, DC 20593

Herman W. Ayers
Northrop
4410 W. 231st St.
Torrance, CA 90505

Robert Wm. Baggerman
Georgia Tech
EES/EGSL/CSD
Atlanta, GA 30332

C.G. Baldwin, Jr.
GD/FW
MZ, Box 748
Forth Worth, TX 76101

Carlton F. Barber, Jr.
Aerospatiale Helicopter (EN)
2701 Forum Dr.
Grand Prairie, TX 75051

Dennis Barberi
GS/Land Sys. Div.
P.O. Box 1901
Warren, MI 48090

Rudy C. Beavin
AFWAL/FIEA
Wright Patterson AFB
Ohio 45424

Lewis Becker
Kentron, Intl.
2345 W. Mockingbird
Dallas, TX 75235

Celeste Belcastro
NASA Langley
Research Center
Mail Stop 130
Hampton, VA 23665

Jack L. Bell
FAA - OTFO
250 Richards Rd.
Kansas City, MO 64116

Rodney B. Bent
Atlantic Scientific Corp.
2711 So. Harbor City Blvd.
Melbourne, FLA 32901

David Lee Bernard
Texas Instruments
PO Box 405 MS 75732
Louisville, TX 75067

Saul Bernstein
Dayton T. Brown
555 Church St.
Bohemia, NY 11716

Jean Beteille
SNIAS -France
316 Route De Bayonne
31060 Toulouse
France

Dr. J.A. Bicknell
Univ. of Manchester
60 Gatley Rd.,
Gatley, Cheadle
Cheshire SK8-IQE
United Kingdom

J.A. Birken
NAVAIR
Air-5161D
Washington, DC 20361

Carl R. Bohanan
NOAA-NWS
819 Taylor St.
Fort Worth, TX 76102

Jack A. Bohay
Transport Canada
ABE/A
Transport Canada Bldg.
Ottawa, Ontario, CAN. KIA ON8

Peter Bootsma
De Havilland Aircraft
Garrett Blvd.
Downsview, Ontario Canada M3KIY5

Murray S. Boris
FAA, APM 530
800 Independence Ave. SW
Washington, DC 20591

A. Scott Bottorff
NOAA

Jean Louis Boulay
ONERA
BP 72
Chatillon, Cedex
France 92322

Ernst H. Brehm
BBC, P.O. 351
6800 Mannheim, W. Ger.

Gerald R. Bretts
Northrop
Northrop ASD, Zone E390/3B
3900 E. Washington Blvd
Pico Rivera, CA 90660

Rowan O. Brick
Boeing Co.
362 167th Ave. NE
Bellevue, WA 98003

Audrey Ruth Carlson
TRW, One Space Park
134-8074
Redondo Beach, CA 90274

Don Stanley Cornwall
A.L.P,A.
#6 Goldthread Ct.
Woodlands, TX 77381

George E. Briggs
GTE Products Corp.
77 A. St.
Needham Hts., MA 02194

B. Leonard Carlson
Boeing
516 W. Snoa Rw. Rd. SE
Carnation, WA 98014

Wm. E. (Gene) Cory
Southwest Research Institute
P.O. Drawer 28510
San Antonio, TX 78284

James Brueggeman
ORI, Inc.
Suite 901
1725 Jeff Davis Hwy
Arlington, VA 22202

Thomas J. Carpenter
Dayton T. Brown
555 Church St.
Bohemia, NY 11716

Richard M. Cosel
Florida Inst. of Tech.
150 W. Univ. Blvd.
Melbourne, FL 32901

John S. Bunting
U.S. Dept. of Commerce
1020 15th St.
Suite 2241
Denver, CO 80202

Neil B. Christenson
FAA
PO Box 1689
Ft. Worth TX 76101

William L. Cotton
Boeing
8807 S. 116 St.
Seattle, WA 98178

Brian Burrows
Culham Lightning
Studies Unit (CLSU)
Abingdon, Oxford
OX14 3DB
United Kingdom

Allen Bartlit Church
Sandia National Labs
Division 7132
Box 5800
Albuquerque, NM 87115

Samuel R. Crawford
Ford Aerospace
1260 Crossman Ave.
Sunnyvale, CA 94086

Keith E. Crouch
LTI
10 Downing Parkway
Pittsfield, MA 01201

H. Tom Clark
ROHR Industries
Chula Vista, CA 92012

Henry A. Buschke
Zenith Radio
1000 Milwaukee Ave.
Glenview, IL 60025

Jay D. Cline
Dayton-Granger
P.O. Box 14070
Ft. Lauderdale, FL 33301

Philip J. D'Anna
Northrop
8900 E. Washington Blvd.
Pico Rivera, CA 90660-3737

James C. Bushnell
Sandia Nat. Labs
P.O. Box 5800
ORG 7554
Albuquerque, NM 87185

Daniel G. Coder
Boeing MS 47-13
P.O. Box 3999
Seattle, WA 98124

John L. Dawson
Navair Test Center
Star Rt. Box 83B
Leonardtown, MD 20650

Gregory J. Byrne
Rice Univ.
Dept. of Space P & A
P.O. Box 1892
Houston, TX 77251

Philip D. Collins
Atlantic Richland
6671A Sun Dr.
Huntington Beach, CA 92647

Patrick J. Dowling
Science Applications
2860 S. Circle Dr.
Suite 2400
Colorado Springs, CO 80918

William Byrne
Southwest Research Institute
7110 Wurzbach #911
San Antonio, TX 78240

Wm. W. Cooley
Boeing Co. - MS 41-47
P.O. Box 3707
Seattle, WA 98124

Mark M. Drabkin
LEA
12516 Lakeland Rd.
Santa Fe Springs, CA 90670

Frank A. Cansler
U.S. Army Avns. Rsch. &
Dev. Act. (AVRADA)
Bldg. 2525
Fort Monmouth, NJ 07703

Jack C. Corbin
AF AERO Systems Div.
ASD/ENACE
Wright Patterson AFB
Ohio 45433

Gary A. DuBro
AFWAL/FIESL
Wright-Patterson
AFB, OH 45433

Bob M. Duff
SW Research Inst.
P.O. Drawer 28511
San Antonio, TX 78284

Jerome F. Duffey
PM Blackhawk
DRCPM BH-T
4300 Goodfellow Blvd
St. Louis, MO 63120

James W. Duncan
Xerox
701 S. Aviation Blvd.
El Segundo, CA 90245

Harold F. Ebneth
Mobay Chem.
Penn Lincoln Pkwy. W.
Pittsburgh, PA 15205

George R. Edlin
US Army (MICOM)
Bldg. 8716
Redstone Ars., AL 35898

Roy Francis Ellison, Jr.
Sandia Nat'l. Labs
Albuquerque, NM 87185

Glenn W. Engelhardt
Joslyn Electronics
5341 Highland Ridge Dr.
Baton Rouge, LA 70816

Ronald I. Ewing
Sandia Nat'l. Labs
ORIG 7554 IOAFB East
Albuquerque, NM 87185

Heinz P. Faber
Bell Helicopter Textron
P.O. Box 487, Dept. 81-6
Fort Worth, TX 76101

Richard R. Faullin
GE
14673 Midway Rd., Rm 117
Dallas, TX 75234

Arthur A. Few
Rice Univ.
Space Phics
Box 1892
Houston, TX 77251

Bruce David Fisher
NASA, Langley Research Center
Mail Stop 247/B.D. Fisher
Hampton, VA 23665

Joseph James Fisher
U.S. Navy, Naval Air Systems Command
Washington, DC 20361

Richard J. Fisher
Kaman Sciences Corp.
P.O. Box 7463
Colorado Springs, CO 80933

Tim E. Fitzsimmons
McDonnell-Douglas
16441 Space Ctr. Blvd.
Houston, TX 77058

James E. Foster
NAEC, Code 9452
Lakehurst, NJ 08733

Norman L. Fowler
USAF
HQ AFESC/DEMM
Tyndall AFB, FL 32403

Frank Frankos
Lockhead-Calif. Company
D 7353
Burbank, CA 91520

Harry W. Franz, Jr.
Pacific Missile Test Center
Code 1234
Pt. Mugu, CA 93042

Wm. B. Frazier
Rockwell International
1220 Scenic Dr.
Glendale, CA 91205

Otto Frey
Emil Haefely & Co. Ltd
LeHenmattstr. 353
CH-4028
Basel, Switzerland

Sam K. Frick
FAA
4344 Donald Douglas Dr.
Long Beach, CA 90808

Robert L. Gardner
Mission Research Rd. SE
Albuquerque, NM 87106

John B. Garry
FAA
FAA Technical Center, ACT-120
Atlantic City Airport, NJ 08405

Joseph Geller
U.S. Coast Guard
4443 Ocean Dr. #226
Corpus Christi, TX 78412

John C. Gerlach
NASA
E108, Wallops Flight Facility
Wallops Island, VA 23337

Thomas Patrick Ginand
Gen. Semi-Conductor
Industries, Inc.
2002 W. 10th Pl.
Tempe, AZ 85281

S.N. Glass
Lockheed, Georgia
Marietta, GA 30060

Michael S. Glynn
FAA Technical Center
ACT-340
Atlantic City Airport, NJ 08405

Cyril N. Golub
USAF Eastern Test Range
ETR/RSL
Patrick AFB, FL 32925

J. Goodman
Marshal Space Flt. Ctr.
4713 Ardmore Dr.
Huntsville, AL 35805

Werner Graf
SRI
333 Ravenswood Ave.
Menlo Park, CA 94025

Jim Grandfield
Cessna Aircraft Co.
Pawnee Div., P.O. Box 1521
Wichita, KS 67201

David Gunter
Martin Marietta
Box 179/MS-G5470
Denver, CO 80201

Mitchell A. Guthrie
Naval Surface Weapons Center
Code N42
Dahlgren, VA 22448

Frederick Hall
Northrop
2401 Hacienda Blvd. #202
Hacienda Hts., CA 91745

John Hallett
Desert Res. Inst.
P.O. Box 60220
Reno, NV 89506

Frank E. Hamell
P.O. Box 4175
San Bernardina, CA 92409

Meredith W. Hamilton
NASA
Mail Code NA3
Houston, TX 77058

Arvid Hansen
FAA
AEA 250, Federal Bldg.
JFK Int'l. Airport
Jamaica, NY 11430

Franklin D. Harris
U.S. Naval Wpn Sys
Code 3525
China Lake, CA 93555

Richard Hasbrouck
LLNL
Box 808, L-154
Livermore, CA 94550

Jan Luiken ter Haseborg
Armed Forces Univ.
2 Hamburg
W. Germany Postfach 700822

Egon Hauck
Air Canada
Base 9
Montreal Int'l Airport
(Dorval), Que. H4Y1C2

Paul Hawkins
FAA, Northwest Mtn.
FAA Bldg., Boeing Field
Seattle, WA 98124

Dr. Craig Hayenga
New Mexico Tech
Socorro, NM 87801

Kenneth Heary
Heary Bros. Lightning
Prot. Co., Inc.
11291 Moore Rd.
Springville, NY 14141

Gerald Heiderscheidt
Boeing Vertol
P.O. Box 16858
Philadelphia, PA 19026

Robt. Hendrickson
TRW, Inc.
Skyline One, Suite 1106
5205 Leesburg Pike
Falls Church, VA 22041

Leonard O. Hendry
Beech Aircraft
9709 E. Central
Wichita, KS 67201

Mark M.J. Heseltine
Westland Helicopters
Veovil, Somerset
United Kingdom 20-21B

Harry Heskett
Martin Aeorspace
P.O. Box 179, MSG 5490
Denver, CO 80201

Wm. J. Hillman
Lockheed Cal. Co.
P.O. Box 551 (B-65, PLT AI)
D3OT 7340
Burbank, CA 91520

Mike Hofmeister
McDonnell Douglas
3855 Lakewook Blvd.
Long Beach, CA 90846

Ronald L. Holle
NOAA
325 Broadway
Boulder, CO 80303

Jimmie Honaker
FAA
P.O. Box 1689
Fort Worth, TX 76101

Thomas Horeff
FAA
1543 Farlow Ave.
Crofton, MD 21114

Wm. Edward Howell
NASA-Langley Research Center
MS 188A
Hampton, VA 23665

George L. Huebner
Texas A & M Univ.
Dept. of Meteorology
College Station, TX 77843

Bob Huet
DOW Chemical
Box 150
Plaquemine, LA 70767

Douglas J. Hughes
IITRI
185 Admiral Cochrane Dr.
Annapolis, MD 21401

J. Hughes
ONR 422AT
Arlington, VA 22217

C.B. Huncharek
GD/FW
MZ, Box 748
Forth Worth, TX 76101

Gary K. Ikuma
U.S. Navy Commander,
Naval Air Force,
US Pacific Fleet
NAS North Island
San Diego, CA 92135

Masaru Ishii
Univ. of Tokyo
Inst. Industrial Science
22-1, Roppongi
7 Chome, Minato-KU
Tokyo, 106, Japan

Gary W. Israel
Boeing-Wichita
1232 S. Doreen
Wichita, KS 67207

R. Earl Jobe
Jobe Enterprises
19653 Military Rd. So.
Seattle, WA 98188

Charles P. Johannigmeier
USAAVRAD COM
(Attn: DRDAV-NS)
4300 Goodfellow
St. Louis, MO 63120

John P. Johnson
Sandia Labs - Div. 7132
P.O. Box 5800
Albuquerque, NM 87115

Rollin E. Johnson, Jr.
Martin Denver Aerospace
Martin Marietta MS D6012
P.O. Box 179, Denver, CO 80120

Christopher C. R. Jones
UKAEA Culham Lab.
Abingdon, Oxfordshire
England

Jack Jones
WCAU TV CBS
Philadelphia, PA 19130

Milton (Fred) F. Jones
FAA
DOT/FAA
P.O. Box 1689
Fort Worth, TX 76137

Gajanan Joshi
Raytheon
5 Grove St.
Lexington, Mass. 02173

Clarence Kaiser
FAA - Atlanta
1075 Inner Loop Rd.
College Park, GA 30337

Joseph Kaiser
FAA
601 E. 12 St.
Room 1625
Kansas City, MO 64119

Jerry Kane
ORI, Inc.
6415 Hillside Lane
Alexandria, VA 22306

Heinz Kasemir
Colorado Science Res.
1604 S. Country Rd. #15
Berthoud, CO 80513

G. F. Kavanagh
GD/FW
MZ, Box 748
Forth Worth, TX 76101

Tatsuo Kawamura
Univ. of Tokyo
Inst. of Industrial Science
22-1 Roppongi, 7 Chome
Minato-ku, Tokyo 106,
Japan

Chester Kawiecki
Lightning Protection Corp.
P.O. Box 6086
Santa Barbara, CA 93160

Clyde Keller
Naval Safety Center
NAS Norfolk
Norfolk, VA 23511

Warren Lee Keller
USAF (AFCG)
1842 EEG/EEITE
Scott AFB, IL 62225

Timothy J. Kelly
ORI, Inc.
444 Jacksonville Rd.
Warminster, PA. 18974

Jon R. Kelley
Dayton Granger Inc.
1999 N. Amidon
Suite 100
Wichita, KS 67203

Larry Kelly
FAA
P.O. Box 1689
Fort Worth, TX 76101

Francis Kerr
US Navy
Naval Plant Rep
c/o Hercules, Inc.
Box 157, Magna, VT 84044

Theodore Killen
Canadair, Inc.
Canadair Challenger Service Center
Bradley Int. Airport
Windsor Locks, CT 06095

Charles King
Boeing Commercial Airplane
Box 3707, MS 77-70
Seattle, WA 98124

Erwin Klisch
Airbus Industri
P.O. Box #33
F31700 Blagnac
France

John Kniat
Pratt & Whitney Aircraft
107 Knollwood Dr.
Glastonbury, CT 06033

Henry Knoller
Lockheed Calif. Co.
Box 551
Burbank, CA 91520

Dietrick Konigstein
Hochschule der Bundeswehr
Holstenhofweg 85
D2000 Hamburg 70
W. Germany D2000

Robert A. Kornasiewicz
USNRC
Mail Stop 1130-SS
Washington, DC 20555

Donald Korte
Bendix
2100 NW 62nd St.
Ft. Lauderdale, FL 33310

Dr. Paul Krehbiel
NM Inst. of Mining & Tech.
Res. & Dev. Div.
Socorro, NM 87801

E. Philip Krider
Univ. of Arizona
Inst. of Atmos, Physics
Tucson, AZ 85721

Harry A. Labadorf
Lawrence Livermore Lab.
P.O. Box 808, L-154
Livermore, CA 94550

Gary Allen Lamb
NAVAIR
Naval Air Engineering Center (ESSD)
Code 9313
Lakehurst, NJ 08773

Wayne Langston
FAA
P.O. Box 1689
Fort Worth, TX 76101

Pierre LaRoche
ONERA
BP 72-29
Avenue de la Division Leclere
Chatillion-Cedex
France 92322

James C. Latimer
GTE
1 Research Dr.
Westborough, MA 01581

Jayme E. Lavoie
USAF AFWAL/FIEA
Wright-Patterson AFB
OH 45433

A. J. Ledwig
GD/FW
MZ5488
Box 748
Ft. Worth, TX 76101

Thomas S. Lee
Univ. of Minnesota
Minneapolis, MN 55455

William Lee
Govt. of Canada
26 Starling Cresent
Nepean, Ont, Can D2J229

Marc Leopold
Purvis Systems
6901 Jericho Tpke
Syosset, NY 11791

Christtane Leteinturier
PTT-NTRC
BP40 Route de Tregastez
Lannion, France 22300

David M. LeVine
NASA-GSFC
Code 913
Greenbelt, MD 20771

William Lewis
FAA
1717 Franklin Blvd.
Linwood, NJ 08221

Jack R. Lippert
U.S. Air Force
AFWAL/FIEA
Wright-Patterson AFB,
OH 45433

Raul E. Lopez
NOAA
325 S. Broadway
Boulder, CO 80303

Karl G. L'Overstrand
SAAB Sweden
St. Persgatan 139 C
Norrkoping, Sweden S-60230

James P. Luette
Sandia Nat'l. Lab
Division 7132
Albuquerque, NM 87115

Melvin Luxenberg
FAA
2300 E. Devon
Des Plaines, IL 60018

Walter A. Lyons
R*Scan Corp.
511 11th Ave. So.
Minneapolis, MN 55415

Alexander Mack
Vought Corp.
P.O. Box 225907 M/S REDB
Dallas, TX 75265

Ernie A. Magyar
Magyar & Assoc.
P.O. Box 6027
Wheaton, MD 20906

Thomas L. Mahoney
Harris Corp.
28 Cranbrook Dr.
Centerport, NY 11721

Michael W. Maier
Light. Location & Protection
1001 S. Euclid Ave.
Tucson, AZ 85719

James H. Major
FAA - SW Region
P.O. Box 1689
Ft. Worth, TX 76101

Larry D. Malir
9011 Carter Cr.
Overland Park, KS 66212

Larry E. Marsh
Federal Express
P.O. Box 727
Memphis, TN 38194-0711

Dr. A.R. Martin
Raychem Corp.
Elx Div.
300 Constitution Dr.
Menlo Park, CA 94025

Freddie T. Massey
Fed. Aviation Admn.
Box 20636
Atlanta, GA 30320

Gerald M. Masson
John Hopkins Univ.
Charles & 34th Sts.
Baltimore, MD 21218

John G. Mast
Bell Helicopter
P.O. Box 482
Ft. Worth, TX 76101

W. Joseph Mathews
Vought Corp.
MS Red-14
P.O. Box 225907
Dallas, TX 75265

K.A. Mazur
G/D, Ft. Worth
Box 748
Ft. Worth, TX 76101

Vladislav Mazur
Cimms, Univ. of Okla.
815 Jenkins St.
Norman, OK 73019

Ian Peter MacDiarmid
British Aeorspace
Warton Aerodrome
Preston, PR4 IAX
United Kingdom

Donald R. MacGorman
NOAA/National Severe Storms Lab.
1313 Halley Circle
Norman, OK 73069

Howard J. McGrath
ORI, Inc.
330 E. Bayview Blvd.
Suite 100, Norfolk, VA 23503

Walt McKerchar
Northwest Engineering Service
P.O. Box 1888
Poulsbo, WA 98370

Barbara Melander
Boeing
21018 9th Ave. S.
Seattle, WA 98148

Rick R. Melcher
Joslyn Mfg.
3 S. 504 Shagbark Ln.
Glen Ellyn, IL 60137

David Paul Millard
Georgia Tech
Engineering Experiment Station
Atlanta, Georgia 30332

Eugene P. Miller
DNA
8570 Gynedd Way
Springfield, VA 12153

A. F. Mills
Lockheed Georgia Co.
Dept. 72-05, Zone 80
86 S. Cobb Dr.
Marietta, GA 30060

Irving N. Mindel
IITRI
10 West 35th St.
Chicago, ILL. 60616

Giuseppe Mischi
Italy - Agusta - Samarate (VA)

Jack L. Moe
GD/FW
MZ 1351
P.O. Box 748
Ft. Worth, TX 76101

Jim Moore
Airbus Industries
Avenue Lucien Servanty
Blagnac Toulouse 31700
France

David Moore
Milliken & Co.
Box 1926, M-135
Spartanburg, SC 29304

Bruce Harry Morris
Vought Corp.
Mail Stop TH-57
P.O. Box 225907
Dallas, TX 75265

Quentin L. Morris
Vought
Box 225907
Dallas, TX 75265

John D. Naberhaus
GD/FW, MZ 2884
Ft. Worth, TX 76101

Yoji Y.N. Nagai
Sagami Inst. of Tech.
Fujisawa 251
Japan

Joe E. Nanevicz
SRI
333 Ravenswood Ave.
Menco Pk., CA 94025

James D. Nickum
Ohio Univ.
206 Clippinger Labs
Athens, Ohio 45701

Wolfgang Nobis
Electronics Test Center BW 81
Gartenstr. 44
D-8545 Greding, W. Germany

G.A.M. Odam
Royal Air Estab.
Flt. Sys. Dept.
P69 Bld.
Farnborough Hants
England GV146 TD

Harry Bruce Ogasian
Hamilton Standard Div. of UTC
MS 3-2-36
Windsor Locks, CT 06096

Guy Orion
Brequet Aviation
78 Quai Carnot
St. Cloud 92214
France

Kenneth A. Ostrander
3M, Stormscope
6530 Singletree Dr.
Columbus, OH 43229

W.R. Owens
GD/FW, MZ 2839
Box 748
Ft. Worth, TX 76101

Philip R. Palmer
Simmonds Precision
Panton Road
Vergennes, VT 05491

Prof. George Parker
U.S.C.
3407 Seabreeze La.
Carona Del Mar, CA 92625

Lee W. Parker
Lee W. Parker, Inc.
252 Lexington Rd.
Concord, Mass. 01742

Gerald Walter Parkinson
Sikorsky Aircraft
N. Main St.
Stratford, Conn. 06497

Max Peacock
FAA
16109 SE 175th Street
Renton, WA 98055

Wayne Ray Pecjak
Northrop Aircraft Div.
1 Northrop Ave.
Hawthorne, CA 90250

Warren D. Peele
SCEEE
1101 Mass Ave.
St. Cloud, FL 32769

Dr. Rod A. Perala
Electromagnetic Applications
P.O. Box 26263
Denver, CO 80226

B.L. Perry
British Civil Aviation Auth.
Brabazon House
Redhill, Surrey, England

Herbert G. Peters
FAA, Western Aircraft
Certification Office
15000 Aviation
Hawthorne, CA 90752

Robert A. Peterson
Dorne & Margoun
2950 Veterans Mem. Hwy.
Bohemia, NY 11716

Robert A. Pfeffer
Harry Diamond Labs.
2800 Powder Mill Rd.
Aldphi, MD 20783

Charles Phelps
Whelen Eng. Co.
3 Winter Ave.
Deep River Ct. 06417

William A. Phipps
FAA - P.O. Box 1689
ASW-422
Ft. Worth, TX 76021

Felix Logan Pitts
NASA-LaRC
NASA-Langley, MS477
Hampton, VA 23365

Joseph Pizzirusso
Scott Paper Co.
1500 E. 2nd St.
Eddystone, PA 19013

J. Anderson Plumer
LTI
10 Downing Pky.
Pittsfield, Mass. 01201

Charles Polk
21 Spring Hill Rd.
Kingston, R.I. 02881

Colin G. Pond
Canadair LTD
Box 6087
Montreal Quebec, Can. H3C 3G9

John E. Pryzby
LTI-10 Downing Pky.
Pittsfield, MA 01201

Anton Puhringer
Zentralanstalt fur Meteoroogie
Hohe Warte 38
A 1190 Wien, Austria

Nicholas O. Rasch
FAA Technical Center
ACT-340
Atlantic City Airport, NJ 08405

Abul Rashid
P.O. Box 1310
San Bernardino, CA 92402

Jean S. Reazer
Tech./Scientific Services
P.O. Box 3065
Overlook Branch
Dayton, Ohio 45039

Andrew W. Revay
Fla. Inst. of Tech.
150 West Univ. Blvd.
Melbourne, FL 32901

Tony A. Riley
Bonded Lightening
Protection of Tex., Inc.
11105 Shady Trail #107
Dallas, Texas 75229

Ted Ristoff
Ledex Co.
801 Scholz Dr.
Vandalia, Ohio 45370

John D. Robb
LRTI
2531 W. Summer
St. Paul, MN 55113

Randy Robinson
Beech Aircraft
9709 E. Central
Wichita, KS 67201

Victoria Lee Rondeau
U.S. Air Force/AFWL
12720 Rover Ave. NE
Albuquerque, NM 87112

Dr. Terrence H. Rudolph
Electromagnetic Applications
P.O. Box 26263
Denver, CO 80226

Lothar H. Ruhnke
Naval Research Lab.
NRL Code 4110
Washington, DC 20375

David Rusher
Rockwell Int'l
3370 Miraloma Ave.
Anaheim, CA 92803

W. David Rust
NOAA/NSSL
1313 Halley Circle
Norman, OK 73069

Pete L. Rustan
A.F. Inst. of Tech.
4781 Silveroak St.
Dayton, OH 45424

Fred S. Sakate
Mursak Eng.
P.O. Box 1838
Slidell, LA 70459

Gina R. Salcido
Northrop Corp.
Mail Stop E 722/3E
Pico Rivera, CA 90660-3737

Jerry Albert Sawyer
MITRE - P.O. Box 208
Bedford, MA 01730

Mark E. Schmid
Hopkins-Applied Physis Lab
Applied Physis Lab.
John Hopkins Rd.
Laurel, MD 20707

Stanford Schneider
Boeing - MS 47-31
The Boeing Co.
P.O. Box 3707
Seattle, WA 98031

Donald A. Schroeder
FAA (APM 710)
800 Independence Ave.
SW Wash., DC 20591

Jack Schroeder
Lightning Diversion Systems
17851 Jamestown Lane
Huntington Beach, CA 92647

Adolf Schwab
University of Karlsruhe
78 Bruehlstrausse
7500 Narlsruhe FR. - Germany
W. Germany

Wilfried Siegler
BWB - W. Germany
Dachauer Str. 128
Munich 19 W. Ger. 8000

J. P. Simi
Les Cable-France
65 Rue Jean-Jaures
Bezons 95871
France

T.E. Skelton
GD/FW - Box 748
Ft. Worth, TX 76101

Albert J. Smith
Lockheed Calif. Co.
Burbank CA 91520

William S. Smith, Jr.
FAA
800 Independence Ave. S.W.
Washington, DC 20591

Joseph R. Soderquist
FAA (AWS-103)
800 Indep. Ave. S.W.
Washington, DC 20591

Ross R. Spencer
FAA - 9321 Provincial Lane
Wichita, KS 67212

James R. Stahmann
Planning Research Corp.
PRC 1217
Kennedy Space Ctr., FL 32899

David L. Stanislaw
Cessna
7101 Shade - #617
Wichita, KS 67212

M.J. Stewart
Southwestern Engineering
P.O. Box 278
Comfort, TX 78013

William H. Stewart
Milliken & Co.
P.O. Box 1927
Mail Stop M 420
Spartanburg, SC 29304

Dwight L. Suiter
NASA - 2521 Hillshire
Deer Park, TX 77536

Joseph Svadlenka
Federal Express
P.O. Box 727
Dept. 1512/Safety
Memphis, TN 38118

John D. Swihart, Jr.
FAA
P.O. Box 1689
Fort Worth, TX 76101

Bud Taggart
Nat'l Bur. Stds.
Div. 723.04
Boulder, CO 80303

Joseph Taillet
ONERA
BP 72
Chatillon Cedex
France 92322

Tosio Takeuti
Nagoya Univ.
Research Institute of Atmospherics
442 Toyokawa Japan

Allen Tate
Federal Aviation Admn.
Fed. Bldg. AEW-443
JFK Inter. Airport
Jamaica, NY 11430

C. E. Taylor
Northrop
8900 E. Wash. Blvd.
Pico Riveria, CA 90660-3737

William L. Taylor
Nat'l Severe Storms Lab
1313 Halley Cr.
Norman, OK 73069

Joseph K. Thomas
Northrop Electronics
ORG 3324 N3324/N3-2
2301 West 120th St.
Hawthorne, CA 90066

Mitchel E. Thomas
NASA-LARC
MS 130-Langley Research Center
Hampton, VA 23665

E. B. Thompson
GD/FW
MZ. Box 748
Ft. Worth, TX 76101

Robert James Thompson
Mobay Chemical
Penn Lincoln Pkwy. W
Pittsburgh, PA 15205

Stanley J. Thomson
Planning Research Corp.
PRC 12-17
Kennedy Space Ctr., FL 32899

A.R. Tomme
Vought
605 Colleyville Terr.
Colleyville, TX 76034

Tom Towle
Dayton-Granger
300 Airway Ave.
Costa Mesa, CA 92626

Oren Tranbarger
S.W. Research Inst.
P.O. Drawer 28510
San Antonio, TX 78284

Hauke Trinks
Technical University
Hamburg, W. Germany

Natole J. Tripode
Arco Oil & Gas Co.
P.O. Box 2819
623 IPB
Dallas, TX 75221

Thomas F. Trost
Texas Tech. Univ.
EE Dept.
Lubbock, TX 79409

Robert L. Truax
TCO Mfg. Co.
604 Danley Dr.
Ft. Meyers, FL 33907

Dr. Martin Uman
Univ. of Florida
Dept. of EE
321 Benton Hall
Gainesville, FL 32611

Edward Vance
SRI
333 Ravenswood Ave.
Menlo Park, CA 94025

John Varekamp
Bosen Vaartlaan 40
Amstelreen, Holland

R. Vargas-Vila
GTE Products Corp.
One Research Drive
Westborough, MA 01581

John Varoli
FAA
181 S. Franklin Ave.
Valley Stream, NY 11581

Raymond Vaselich
NAVSEA SYSCOM
8804 Lake Hill
Lorton, VA 22079

Ronald Vavruska
FAA
ANE-153
12 New England Exec. Park
Burlington, MA 01803

Merton Vincent
Boeing
38105 204th SE
Auburn, WA 98002

Aleksandar Vorgucic
Univ. of Nis
1800 Nis
Yugoslavia

John F. Wagner
Booz-Allen-Hamilton
2340 Alamo S.E.
Suite 207
Albuquerque, NM 87106

Wm. T. Walker
U.S. Naval Air Devel. Center
Code 20P4
Warminster, PA 18974

Lawrence Walko
USAF
AFWAL/FIESL
Wright-Patterson AFB
Dayton, OH 45429

Gerald E. Walters
G & H Technology
1649 17th St.
Santa Monica, CA 90404

Thomas C. Wann
USAF HQ AWS/DN
Scott AFB, IL 62225

John P. Warhus
Lawrence Livermore Labs
P.O. Box 808 MS L-153
Livermore, CA 94550

K.A. Wasson
GD/Ft. Worth Div.
Box 748 MZ 2234
Ft. Worth, TX 76101

O. E. Watkins
MF - Box 748
Ft. Worth, TX 76101

Lloyd B. Watts
Fed. Emer. Mgmt. Agcy.
1266 E. Woodman Rd.
Co. Springs, CO 80918

Donald A Weber
B.E.&C. Engineers
625 Andover Park W
Tukwila, WA 98199

Renaud Weber
Aerospatiale
12 Rue Pasteur
92105 SurESNES
Cedex, France

Gus Weinstock
McDonnell Aircraft
Box 516
St. Louis, MO 63166

Jehoshua Weissman
A.D.A. Dep #23 P.O. Box 2250
Haifa, 31021 Israel

Chang-Tai Wen
Texas Tech. Univ.
2118 B. Main St.
Lubbock, TX 79401

Richard P. Wesenberg
NASA
DL-NED-3
Kennedy Space Ctr., FL 32899

Don Whiston
FAA
1126 W. Foster Ave.
Lake Bluff, IL 60044

John J. White
7712 Newington
Springfield, VA 22153

Robert A. White
Sandia Nat. Labs.
Div. 7554 P.O. Box 5800
Albq., NM 87185

Glen B. Whiting
Lockheed Calif. Co.
P.O. 551
Burbank, CA 91520

Howard R. Whitlock
FAA
P.O. Box 1689
Fort Worth, TX 76101

Dan K. Wiener
Federal Express
P.O. Box 727
Memphis, Tenn. 38194

Kenneth G. Wiles
LTI
10 Downing Pky.
Pittsfield, MA 01201

Bobby J. Wilson
Georgia Tech.
347 First St.
Atlanta, GA 30332

John Wilson
ROHR Industries
3240 Casa Bonita Dr.
Bonita, CA 92002

Tom F. Witt
Shell Pipeline
P.O. Box 52163
New Orleans, LA 70152

Gerald W. Wood
Texas Tech. Univ.
P.O. Box 4439
Lubbock, TX 79409

Miles M. Worden
Hq. Air Force/LEEEU
Washington, DC 20330

James A. Wrede
Northrop
8900 E. Wash. Blvd.
Pico Riveria, CA 90660-3737

William E. Wright
General Elec.
Newmann Way
Evendale, Ohio 45215

Richard F. Yotter
FAA
5801 E. 97th Terrace
Kansas City, MO 64134

Joseph A. Zak
USAF HQ 5th Weather Wing
Langley AFB, VA

Keith S. Zeisel
McDonnell-Douglas
P.O. Box 516
St. Louis, MO 63166

Wilfried Ziegler
BWB-ML
Dachauer Str. 128
8000 Munich, W. Germany

Murray A. Ziller
Sikorsky Aircraft
77 Tarinelli Circle
Bridgeport, Ct. 06606

Anthony G. Zimbalatti
Grumman Aircraft Company
MS B25-35
Bethpage, NY 11714